2016-03-01

Development and Application of New Solid-State Models for Low-Energy Vibrations, Lattice Defects, Entropies of Mixing, and Magnetic Properties

Jacob M. Schliesser
Brigham Young University - Provo

Development and Application of New Solid-State Models for Low-Energy Vibrations, Lattice Defects, Entropies of Mixing, and Magnetic Properties

Jacob M. Schliesser

A dissertation submitted to the faculty of
Brigham Young University
in partial fulfillment of the requirements for the degree of

Doctor of Philosophy

Brian F. Woodfield, Chair
James E. Patterson
Daniel H. Ess
Karine M. Chesnel
Jeremy A. Johnson

Department of Chemistry and Biochemistry

Brigham Young University

March 2016

ABSTRACT

Development and Application of New Solid-State Models for Low-Energy Vibrations, Lattice Defects, Entropies of Mixing, and Magnetic Properties

Jacob M. Schliesser
Department of Chemistry and Biochemistry, BYU
Doctor of Philosophy

Low-temperature heat capacity data contain information on the physical properties of materials, and new models continue to be developed to aid in the analysis and interpretation of heat capacity data into physically meaningful properties. This work presents the development of two such models and their application to real material systems. Equations describing low-energy vibrational modes with a gap in the density of states (DOS) have been derived and tested on several material systems with known gaps in the DOS, and the origins of such gaps in the DOS are presented. Lattice vacancies have been shown to produce a two-level system that can be modeled with a sum of low-energy Schottky anomalies that produce an overall linear dependence on temperature in the low-temperature heat capacity data.

These two models for gaps in the vibrational DOS and the relationship between a linear heat capacity and lattice vacancies and many well-known models have been applied to several systems of materials to test their validity and applicability as well as provide greater information on the systems themselves.

A series of bulk and nanoscale Mn-Fe and Co-Fe spinel solid solutions were analyzed using the entropies derived from heat capacity data, and excess entropies of mixing were determined. These entropies show that changes in valence, cation distribution, bonding, and the microstructure between the mixing ions is non-ideal, especially in the nanoparticles.

The heat capacity data of ten Al doped TiO_2 anatase nanoparticle samples have also been analyzed to show that the Al^{3+} dopant ions form small regions of short-range order, similar to a glass, within the TiO_2 particles, while the overall structure of TiO_2 remains unchanged. This has been supported by X-ray diffraction (XRD) and electron energy-loss spectroscopy and provides new insights to the synthesis and characterization of doped materials.

The final investigation examines nanocrystalline CuO using heat capacities, magnetization, XRD, and electron microscopy and compares the findings to the known properties of bulk CuO. All of these measurements show transitions between antiferromagnetic and paramagnetic states in the temperature range of about 150-350 K that are greater in number and higher in temperature than the transitions in bulk CuO. These changes are shown to cause an increase in the temperature range of multiferroicity in CuO nanoparticles.

Keywords: thermodynamics, heat capacity, lattice vacancies, materials, nanoparticles, mixing, characterization

ACKNOWLEDGEMENTS

For formality's sake, this work was funded by the U.S. Department of Energy under grant DE-FG02-05ER15666.

I've had a significant amount of success throughout my PhD studies in terms of research, classwork, and even personal development. None of this success would be possible on my own as my advisor, committee, professors, collaborators, colleagues, family, and BYU's instrument specialists have generously helped me. Thank you all. I need to make special mention of my advisor Dr. Brian Woodfield who kept me going through the difficult and often tedious work. If it wasn't for him, I probably would have given up on the PhD a long time ago, so thank you Dr. Woodfield. You've been an incredible advisor in more ways than you'll ever know.

Above all, I thank God for his grace that has strengthened me more than I ever knew I needed during these past several years. All of my success could be attributed to him and his influence in my life.

TABLE OF CONTENTS

LIST OF TABLES

LIST OF FIGURES

1 INTRODUCTION

Modern materials have become significantly more advanced and refined than the materials of previous generations. Although the general compositions of the materials on a bulk scale are often similar, small changes in structure and composition have turned many common materials into functional and technologically significant materials. Silicon is an excellent example of how a simple material can evolve and expand into new applications. Elemental silicon has traditionally been used in metallurgical fields for making aluminum-silicon alloys, but with the invention of new purification methods such as the Siemens and Czochralski processes silicon has penetrated the fields of solar photovoltaics and electronics.[1-2] Often the small features, such as a few impurity atoms, dopants, or defects, make a material uniquely useful or useless. Advances in materials have created the need for more specialized characterization measurements and modeling to determine chemical and physical properties that contribute to the function of the material.

The field of nanomaterials has received significant attention over the past few decades, and advances with these materials have also introduced new chemical and physical properties that conventional characterization techniques are unable to fully elucidate. These properties include particle size, morphology, surface structure and chemistry, mixing, and localized electronic or vibrational properties. Creating new models and theories to understand the function and significance of such properties is an important area of scientific research.

Traditional theories and techniques can often be used to investigate and explain the basic properties of a material, but extending such models and techniques to accommodate new phenomena is a common and significant aspect of many investigations. The well-established fields of thermodynamics and statistical mechanics have seen many advances that have kept these areas useful for investigations of modern materials. The field of thermodynamics provides a bulk measurement of a system, while statistical mechanics treats a system as a sum of many small systems (like atoms or molecules) with known, or at least predicted, properties that can be averaged over the volume of the system to give bulk properties such as thermodynamics.

The physical principles on which statistical mechanics is based come from the most fundamental sciences. Quantum mechanics has been used to identify the discrete energy levels of many properties for different systems. These energies and their states can be analyzed with statistical mechanics to provide thermodynamic data. In this way, one can link the bulk, measurable properties of a system with the fundamental science and features that occur on an atomic scale.

1.1 Heat Capacities of Solids

Many theoretical models are used to simplify sophisticated systems and produce the internal energies of various states.[3] Although energy can be calculated and predicted for any system, directly measuring that energy and thereby testing the models and predictions is difficult. Heat capacity measurements, however, are quite simple to perform, and because heat capacity is the derivative of the energy with respect to temperature ($C_p = (dH/dT)_p$ or $C_V = (dE/dT)_V$), these measurements provide a method for testing models of microscopic features and their energies.[3-4]

The most common energetic features of a material that heat capacities have investigated include vibrations, electronic character, and magnetic properties.[3-7] Because these properties are common to many materials, it is profitable to introduce their fundamental heat capacity contributions here, though several new models that have similar features to these will be presented later as the bulk of this dissertation.

1.1.1 Vibrational Heat Capacity

Vibrational character is common to all materials due to the atomic and molecular bonds. In a solid, the interactions between the different atoms or molecules are very different from a gas or even liquid. The atoms occupy fixed locations and have strong interactions with their neighbors due to chemical and physical bonds.[3, 5] The atoms and their connecting bonds are often treated as a simple array of balls and springs (see Figure 1-1) in which the atoms are viewed as balls of mass that are all attached to each other with springs, which represent the bonds between the atoms. Although very simplified, this treatment of solid vibrations is typically quite accurate and valid for many purposes.

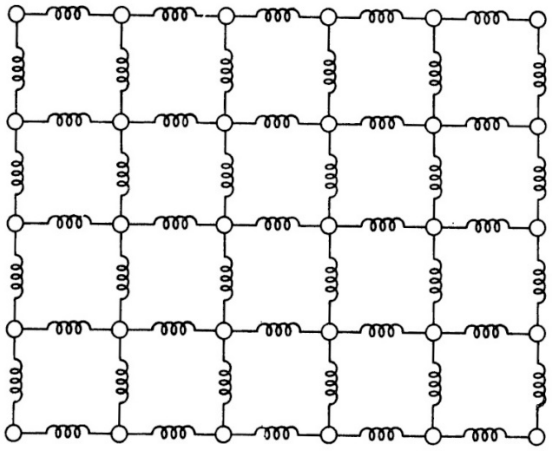

Figure 1-1: 2D Ball and Spring Model of a Crystal Lattice (from McQuarrie[3])

This simple model quantitatively describes the interatomic forces that are exerted on the atoms from the other atoms in the lattice. The atoms occupy low-energy states within a potential well that has steep walls, which typically makes the atomic vibrations small in amplitude. The vibrations about the equilibrium position (minimum energy) of each atom are usually represented as harmonic oscillations, and because the position of each atom influences the neighboring atoms, a solid can be treated as a system of coupled harmonic oscillators.[3]

In a solid with N atoms, there are $3N$ total degrees of freedom (DOF) in which the atoms can move. Three of these $3N$ DOF are given to translational motion, three are given to rotations, and the remaining $3N$-6 are all accounted for with vibrational motion. Because N is large for solids ($O(10^{20})$), the number of vibrational DOF is usually approximated as $3N$.

Through several statistical considerations, the vibrational energy of a solid based on the individual energies of the N atoms can be reduced to the expression:[3]

$$E = U(0;\rho) + \int_0^\infty \left[\frac{h\nu e^{-h\nu/kT}}{1 - e^{-h\nu/kT}} + \frac{h\nu}{2}\right] g(\nu)d\nu \tag{1-1}$$

where U is the potential energy due to atomic displacement, h is Planck's constant, ν is the frequency of oscillation, k is Boltzmann's constant, T is temperature, and $g(\nu)$ is the distribution function or vibrational density of states (DOS). Because the heat capacity is the derivative of the energy with respect to temperature, the vibrational heat capacity of a solid can be derived from Eq. 1-1:[3]

$$C_V = k\int_0^\infty \frac{(h\nu/kT)^2 e^{-h\nu/kT} g(\nu)d\nu}{(1 - e^{-h\nu/kT})^2} \tag{1-2}$$

The complicating feature of this equation is the function $g(\nu)$, which is generally unknown.

The DOS $g(\nu)$ is simply defined as the density of energy states that exist in a given frequency range. Figure 1-2 shows the experimental DOS of aluminum and iron. At low

frequencies/energies the density – or number of states available to be occupied – is small, but as energy increases, the number of available states within a range of energies increases. Typically, the number of states drops back to a low density above a certain energy. The density of states that is lower in magnitude but extends over a wide range of frequencies is typically caused by acoustic phonons or vibrations.[4-5] The sharp peaks in the DOS arise from optical phonons. In many instances, the transverse and longitudinal modes of each of these are distinguishable.[5]

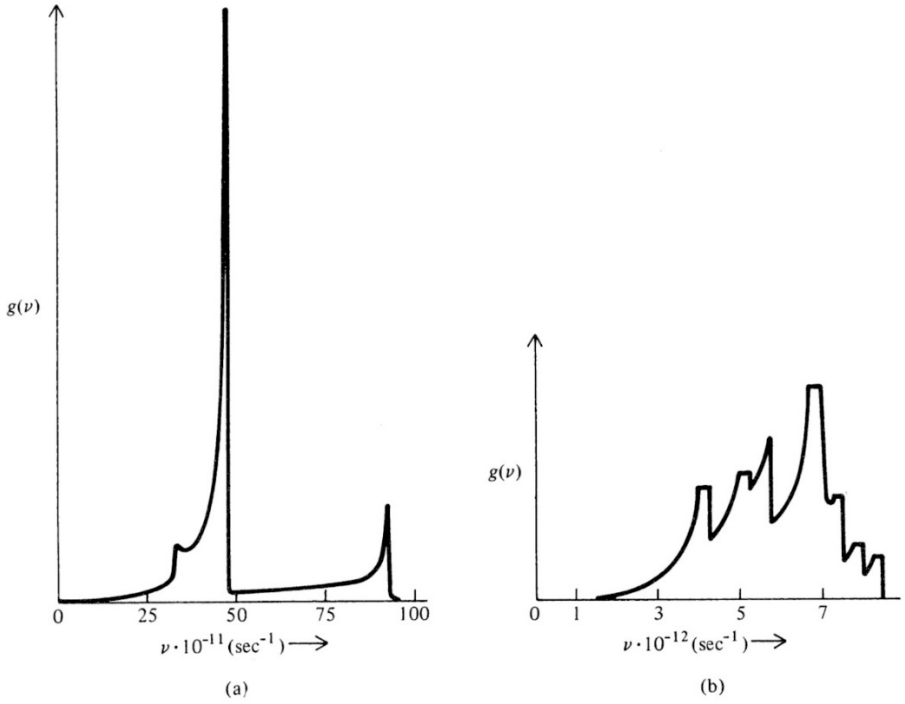

Figure 1-2: Experimental DOS of a) Aluminum and b) Iron (from McQuarrie[3])

The exact DOS as shown in Figure 1-2 can be measured with sophisticated (and typically expensive) techniques, or it can be roughly calculated using lattice dynamics.[3-4] A common method to approximate the features in the DOS is to use simplified models of $g(\nu)$ that are

inserted into Eq. 1-2 with variable parameters; experimental heat capacity data are then fit with the newly simplified Eq. 1-2 to yield information about the different features of the DOS such as maxima or cutoffs. Because these models will be significant for this text, several of the most common models will be presented.

1.1.1.1 The Einstein Model

To produce DOS models, one typically takes a bottom-up approach by modeling the physical properties (such as vibrations) of the individual atoms that make up the solid and then calculating the DOS from the energy levels of these properties. Einstein's approach was the most simple and straightforward and approximates to the vibrational DOS at higher temperatures to a fair degree of accuracy. Before Einstein's contribution, classical mechanics had established that the atoms in a solid behave as harmonic oscillators, which gives a heat capacity of R for each vibrational DOF for one mole of material. This is known as the Dulong-Petit law and produces a predicted heat capacity of $3R$ for monatomic solids, which is independent of temperature and therefore only crudely resembles heat capacity data at high temperatures.

Einstein improved upon this model by removing the classical understanding of vibrations and applying quantum mechanical ideas that had been recently developed by Planck.[8] Einstein treated each atom in a solid as a simple harmonic oscillator that is independent of all the other oscillating atoms in the solid, but his use of quantized oscillation energies produced a heat capacity model that agrees much more with experiment. Because most atoms are in their ground vibrational state at low temperatures (even below a few thousand Kelvin), there is only one appreciable vibrational state of concern in the DOS with this simple model; therefore, the DOS as given by Einstein's model is represented as a delta function at a single frequency.[3-4, 9]

When this DOS function $g(\nu)$ is inserted into Eq. 1-2, the integral can be evaluated in closed-form and produces the heat capacity expression:[3]

$$C_E = 3Nk\left(\frac{\theta_E}{T}\right)^2 \frac{e^{\theta_E/T}}{(e^{\theta_E/T}-1)^2} \tag{1-3}$$

where N is the number of atoms, and the Einstein temperature is defined as $\theta_E = h\nu_E/k$. Thus the Einstein heat capacity of a solid has only one adjustable parameter, θ_E. This value corresponds to the peak in the delta function DOS. Figure 1-3 shows the heat capacity data of copper with an Einstein heat capacity fit. The fit is a decent qualitative representation at temperatures above about 50 K, but the low-temperature data are not accurately modeled with this equation, and a quantitative representation is lacking overall; however, this model has been successful at identifying dispersion in acoustic modes.[10]

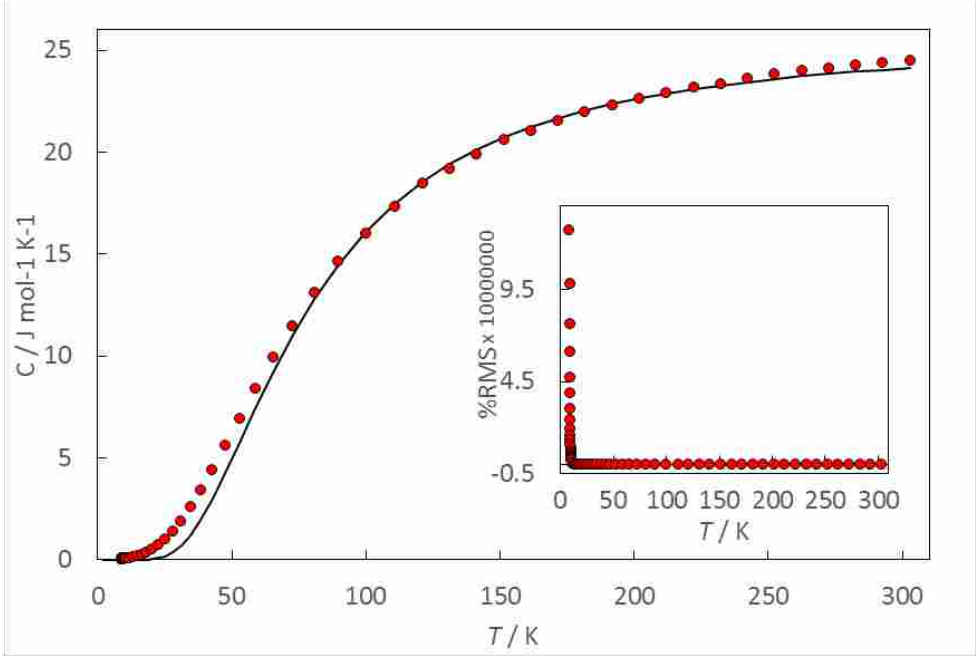

Figure 1-3: Heat Capacity Data of Cu Metal from 0-300 K Fit with an Einstein Function (Eq. 1-3). The inset shows a measure of the deviation of the data from the fit.

1.1.1.2 The Debye Model

The Debye model for vibrational heat capacities is much more robust than the Einstein model, and quantitative agreement between this model and experimental data has been observed for many simple solids. The lengthy derivation will not be given herein, but a qualitative explanation involving the most important features of the model will be presented.

The success of the Debye model comes from treating low-energy atomic vibrations in a solid in an exact manner: as a concerted movement and vibration.[3-4] The normal mode frequencies are not treated for each individual atom but rather as a collective harmonic motion of all the atoms in the solid. Figure 1-4 shows the two extreme normal mode vibrations that a one-dimensional (1D) chain of atoms can have: atoms vibrating against each other, and long chains of atoms vibrating smoothly together to create a long-wavelength/low-frequency vibrational mode. The success of the Debye model is attributed to its accurate treatment of the long-wavelength modes on the bottom of Figure 1-4.

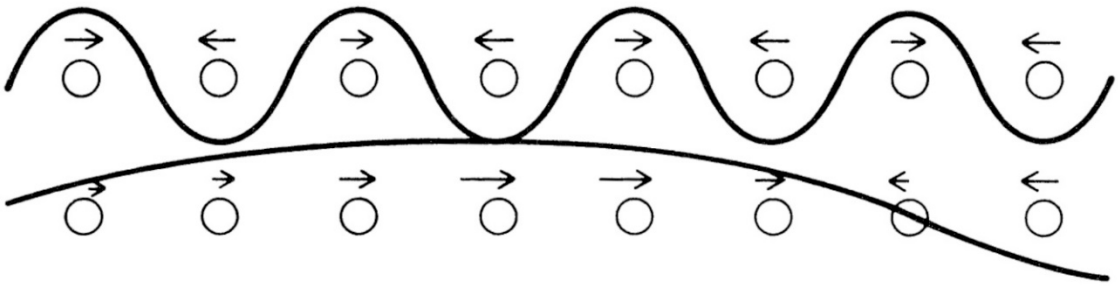

Figure 1-4: Lattice Vibrations Showing the Highest Frequency (top) and a Low-frequency (bottom) Normal Mode (from McQuarrie[3])

Debye recognized that the wavelengths of the lowest energy vibrations in a crystal are very long (theoretically as long as the crystal itself) relative to the atomic spacing of the atoms in

the crystal and therefore treated these vibrations as independent of the atomic character of the material. In other words, he treated the solid body as a continuous elastic body of infinite length. The derivation for the DOS of this model is somewhat similar to the derivation for standing waves in a blackbody and yields the distribution function:[3]

$$g(\nu)d\nu = \frac{12\pi V}{{v_o}^3}\nu^2 d\nu \tag{1-4}$$

where V is the volume, and v_o is the average velocity of the two transverse waves and one longitudinal wave. Because the total number of normal modes is approximately $3N$, the integral of $g(\nu)$ must equal $3N$. Using this correlation and rearranging Eq. 1-4 gives the simplified version:[3]

$$g(\nu)d\nu = \begin{cases} \dfrac{9N}{{v_D}^3}\nu^2 d\nu, & 0 \le \nu \le v_D \\ 0, & \nu > v_D \end{cases} \tag{1-5}$$

where v_D is the characteristic Debye frequency and is observed in the DOS as the cutoff energy for the vibrational modes.

When Eq. 1-5 is inserted into Eq. 1-2, the Debye heat capacity can be generated:[3]

$$C_D = 9Nk\left(\frac{T}{\theta_D}\right)^3 \int_0^{\theta_D/T} \frac{x^4 e^x}{(e^x - 1)^2}\, dx \tag{1-6}$$

where the Debye temperature $\theta_D = hv_D/k$, and $x = hv/kT$. Although this equation cannot be evaluated in closed-form, several approximations can yield simple functions for different temperature regions. At high temperatures, the upper limit of the integral becomes small, and through simple expansions, the integral evaluates to[3]

$$C_D(T \gg \theta_D) = 3Nk = 3R \tag{1-7}$$

which is the classical Dulong-Petit law. At low temperatures ($T \ll \theta_D$), the upper limit of the integral can be assumed to be infinity in which case the integral has a closed-form solution of $4\pi^4/15$, and the heat capacity at low temperatures becomes[3]

$$C_D(T \ll \theta_D) = \frac{12\pi^4}{5} Nk \left(\frac{T}{\theta_D}\right)^3 \tag{1-8}$$

which exhibits the famous T^3 dependence that matches the basic shape of low-temperature data. Thus, the Debye heat capacity function gives a quantitative model of experimental heat capacity data at low temperatures.

Eq. 1-6 can be evaluated numerically at all temperatures, which has become more common practice with the availability of better computers and operators. Figure 1-5 shows the same heat capacity data presented in Figure 1-3 above but with the data fit numerically with the Debye heat capacity function (Eq. 1-6). The data show significantly better agreement than the Einstein model, but there are still drawbacks to this model as seen by the deviation plot in the inset, and a quantitative representation of the data over the entire temperature range is generally unfeasible.

Figure 1-6 shows the measured vibrational DOS of Cu[11] in relation to the DOS determined from the heat capacity data fit with the Einstein and Debye models. As can be seen, both models simplify the actual DOS, but the Debye model represents the DOS significantly better. This amount of agreement between the experimental DOS and the DOS derived from heat capacity data seen in Figure 1-6 is typical of many solids.

As can be seen in Figure 1-5, the Debye model works well at low and high temperatures; however, data at intermediate temperatures are typically poorly modeled by the Debye heat capacity function even when evaluated using numerical methods. The reason for this error will be discussed in chapter 3 herein, but in brief, the Debye temperature, which appears as a constant

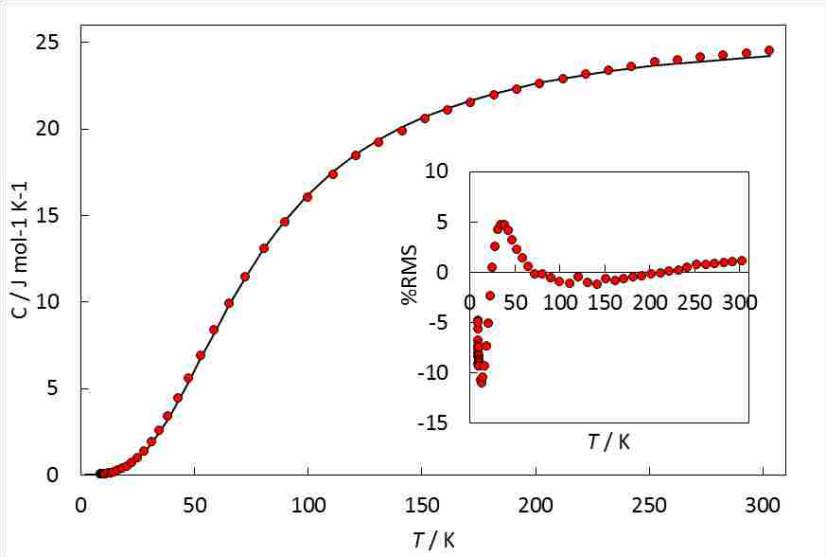

Figure 1-5: Heat Capacity Data of Cu Metal from 0-300 K Fit with a Debye Function (Eq. 1-6). The inset shows a measure of the deviation of the data from the fit.

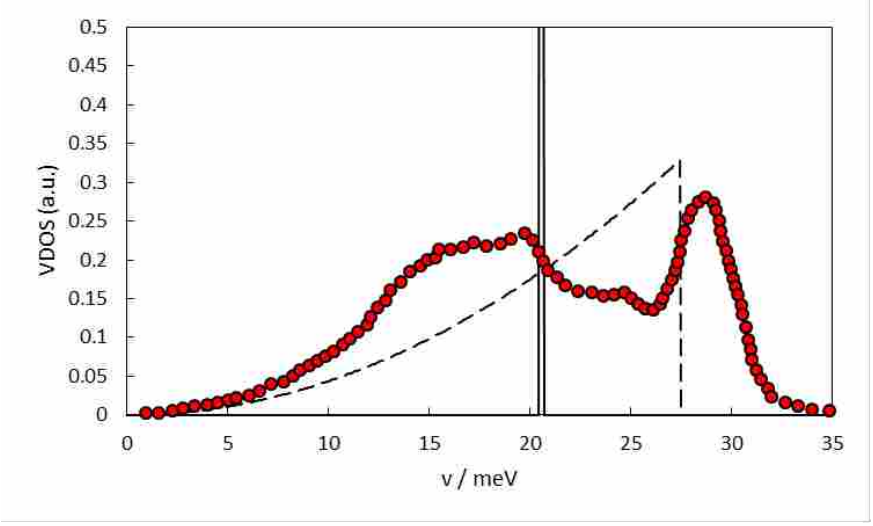

Figure 1-6: Vibrational DOS of Bulk Cu. The points show actual data (from Yildirim et al.[11]), the solid vertical line (just above 20 meV) shows the Einstein DOS, and the dashed line shows the Debye DOS.

in Eq. 1-6, is actually not a constant but is dependent on temperature itself due to various physical properties.[12-13] Figure 1-7 below shows how a typical Debye temperature varies as a function of temperature.[3]

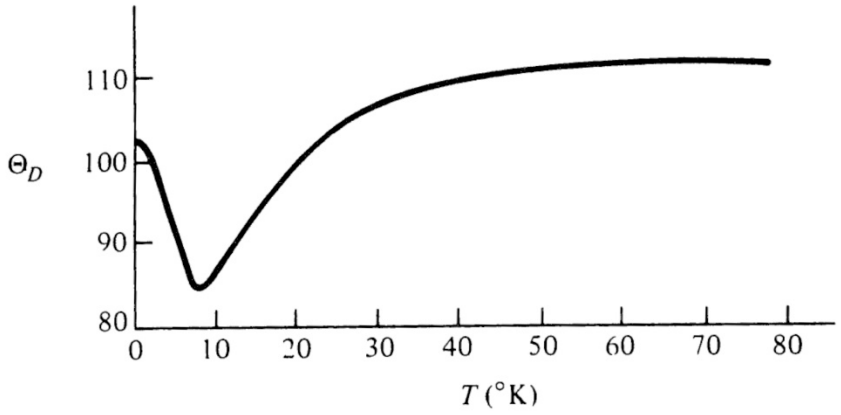

Figure 1-7: Debye Temperature θ_D as a Function of Temperature (from McQuarrie[3])

1.1.1.3 Lattice Dynamics

The use of lattice dynamics to accurately approximate the DOS from first-principle calculations has been extremely significant over the past few decades as computer hardware and software become better and more able to handle complex and laborious calculations.[3] Because lattice dynamics is a field of itself, only brief mention will be made of its use.

The primary focus of lattice dynamics is to calculate a dispersion relation from first-principles. Atoms in a solid are treated as balls (mass) and springs (force), and a set of equations of motion can be obtained from this simple but generally valid approximation. The set of equations is then solved to give the dispersion relation.[3, 5] The one and two dimensional equations (see Figure 1-1) are easily solved with conventional techniques and software, but as the dimensionality increases and the solid to be modeled becomes more complex, sophisticated modeling software becomes required.

Figure 1-8 shows how well lattice dynamics predicts the dispersion relation of graphene.[14] (The dispersion relation is related to the DOS.) The experimental data can be

determined with inelastic neutron scattering experiments, which is not the most accessible technique; nevertheless, this dispersion data could be converted into a DOS, and a more accurate heat capacity could then be predicted.

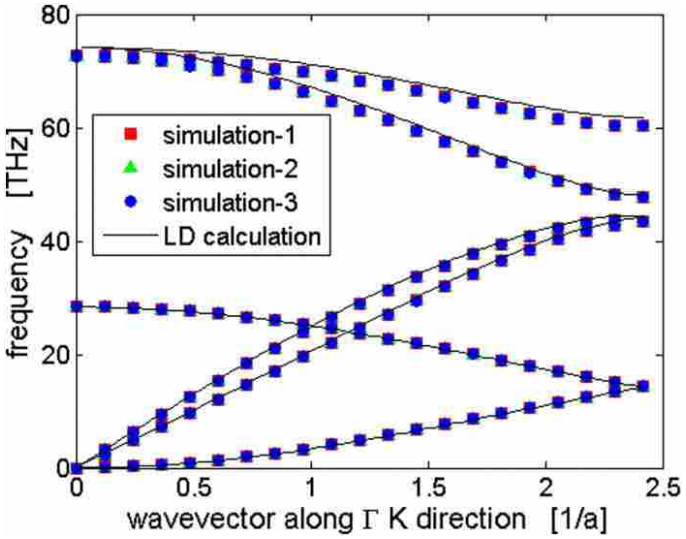

Figure 1-8: Molecular Dynamics and Lattice Dynamics (LD) Simulations of Graphene (from Wei et al.[14])

1.1.2 Electronic Heat Capacity

The contribution to the heat capacity from the free-electron gas can also be derived from basic principles. The conducting electrons in metals are the valence electrons of the metal atoms that experience an essentially constant Coulombic potential throughout the entire lattice and are free to migrate throughout the metal.[3, 5, 15] The free-electron gas is composed of individual electrons that each occupy a defined state of energy, but because electrons are fermions (i.e. they cannot occupy the same state) they fill in increasing energy states starting from the lowest energy. Figure 1-9 shows the occupancy of these states at temperatures from 500 K to 10^5 K.[5] The occupancy at 0 K would be similar in shape to that of the occupancy at 500 K, but there

would be no rounded edges at the Fermi level (5×10^4 K in Figure 1-9) meaning that all electrons would occupy states below this energy level.

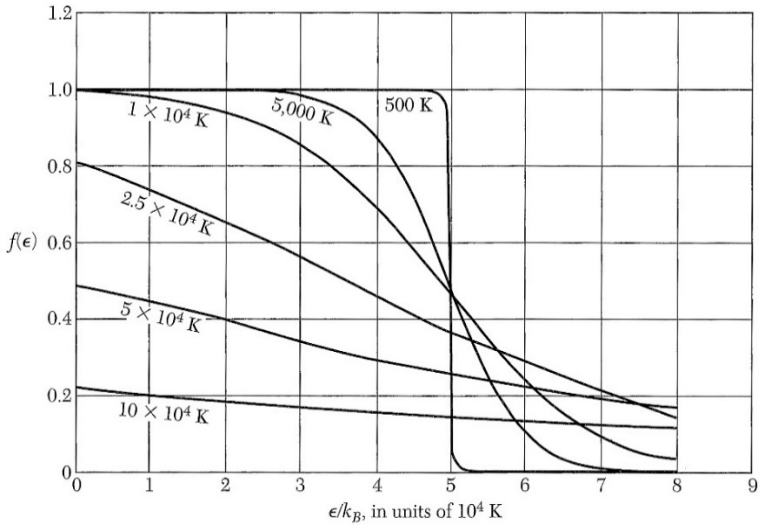

Figure 1-9: Fermi Level and Electronic State Occupancy at Various Temperatures (from Kittel[5])

Note that even at thousands of Kelvin only a small amount of the electrons would be in an excited state above the Fermi level. At 0 K all electrons are in the lowest energy configuration below the Fermi level, and the energy of the electrons in this state can be derived from a combination of quantum mechanics and statistical mechanics:[3]

$$E_o = \frac{3}{5} N \mu_o \tag{1-9}$$

where N is the number, and μ_o is the Fermi energy. Because heat capacity is the temperature derivative of the energy, and this energy has no temperature dependence, the heat capacity would be zero.

To produce a non-zero electronic heat capacity consistent with observations, some of the electrons must be in excited states above the Fermi level even at temperatures as low as a few K.

Although the number of electrons that have enough thermal energy to populate these excited states is very small, they produce a measurable and even significant heat capacity, especially at low temperatures. The distribution of such small populations appears similar to the 500 K distribution shown in Figure 1-9 but with even less spillover or rounding around the Fermi level. The electronic heat capacity is derived from these few excited electrons. The steps of the derivation are beyond the scope of this dissertation, but the result is well-known and turns out to be:[3]

$$C_V = \frac{\pi^2 NkT}{2(\mu_o/k)} = \frac{\pi^2}{2} Nk \left(\frac{T}{T_F}\right) \tag{1-10}$$

where T_F is the Fermi temperature which is directly related to the Fermi level.

This contribution to the heat capacity is small (on the order of $10^{-4} \cdot T$ J·mol^{-1}·K^{-1}), so it is typically too small to distinguish from the relatively massive vibrational contribution; however, at very low temperatures (T < 10 K), where the vibrational heat capacity drops off as T^3, this term becomes significant and observable. Figure 1-10 shows a linear electronic heat capacity contribution to the total heat capacity, which has been plotted as C/T vs T^2 to show the magnitude of the linear term at the y-intercept.[16]

Although a linear contribution to the heat capacity is determined for the free-electron gas typical of metals, many other materials have shown a linear heat capacity at low temperatures.[7, 17-19] This will be the subject of chapter 4 in which other linear heat capacity models will be discussed, and a new linear heat capacity model that is generally applicable to all materials with lattice vacancies will be introduced.[7]

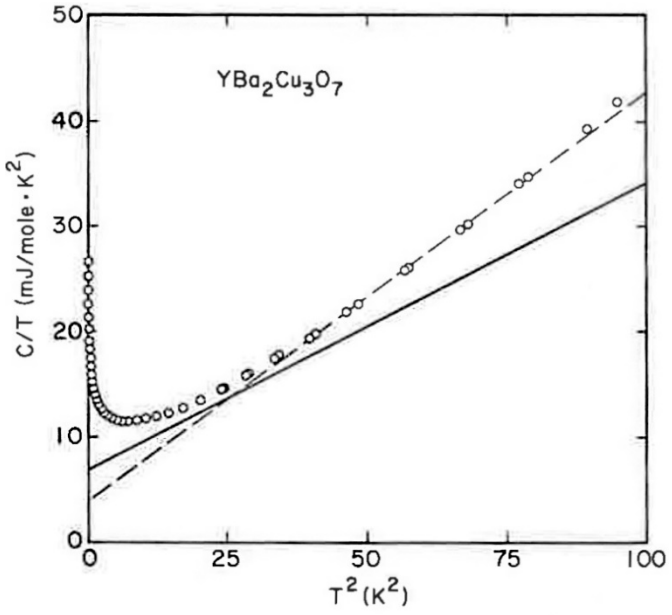

Figure 1-10: Heat Capacity Data of the Superconducting $YBa_2Cu_3O_7$ (YBCO) Plotted as C/T vs T^2 Showing the Electronic Contribution. The solid line represents a least-squares fit of the data including electronic and vibrational terms (the y-intercept gives the magnitude of the linear contribution). The dashed line shows a simple straight line fit (from Fisher et al.[16])

1.1.3 Magnetic Heat Capacity

A magnetic heat capacity for solids is understandably only present when there are magnetic properties in the material, but since many significant materials are magnetic (including those investigated herein), the basic concepts of magnetism as well as various magnetic contributions to the heat capacity of solids will be introduced.

Diamagnetism occurs when there are no unpaired spins in a material. Although these materials have a slight interaction with a magnetic field, they exhibit no magnetic heat capacity behavior. Paramagnetic materials have unpaired spins that are randomly oriented with respect to each other making the overall magnetic moment of the material null.[15] Although paramagnetism

itself is quite uninteresting in terms of the heat capacity analyses used herein, paramagnetic materials typically have very interesting heat capacity features.

The function of magnetism was explained in 1928 by Werner Heisenberg, who showed that a quantum mechanical exchange interaction exists between neighboring electrons and tends to align the spins.[20] When thermal energy becomes insufficient to disrupt this weak interaction and the alignment of the electron spins, a paramagnetic material can transition into a new magnetic state with spins oriented in a specific way. The temperature at which this change occurs is called the Curie temperature T_C or the Néel temperature T_N depending on the type of magnetic state reached below the transition and varies from less than 1 K to over 1000 K depending on the material.[5] Figure 1-11 shows the heat capacity on one such transition.[21]

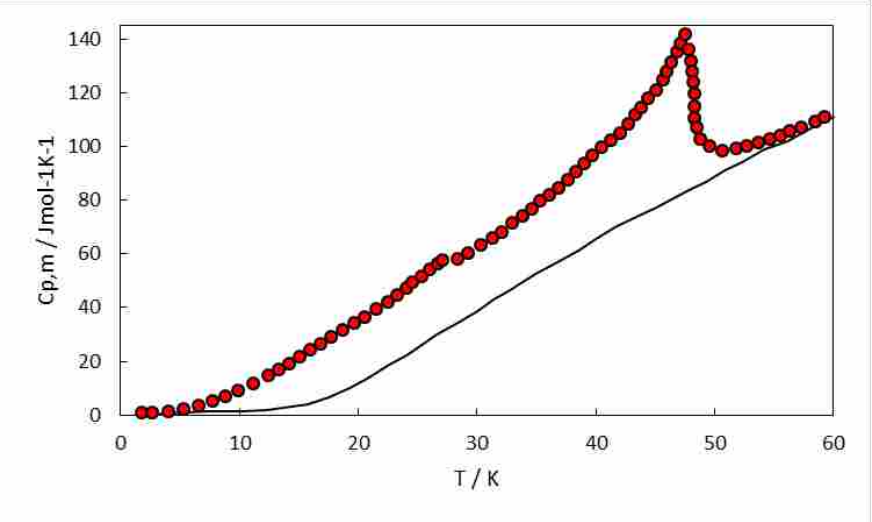

Figure 1-11: Heat capacity of $Fe_4(P_2O_7)_3$ around the magnetic transition. The line shows the lattice heat capacity (from Shi et al.[21])

When spins align parallel to each other from the random paramagnetic state, this is called ferromagnetism, and the transition temperature is the Curie temperature T_C.[5] A ferromagnet has a

net magnetic moment and is commonly observed in bar magnets. When the spins align anti-parallel to each other, this is call antiferromagnetism, and the transition temperature is referred to as the Néel temperature T_N.[5] Antiferromagnets have no net magnetic moment since the spins all cancel each other out. Another special form of magnetism can occur in which the spins align antiparallel, but the spins pointing in one direction have a weaker moment than the spins aligned in the opposite direction. Materials with this property are called ferrimagnets and behave similarly to ferromagnets in that they also have a net magenetic moment.[5] Figure 1-12 shows the electron spin orientations of all these common types of magnetism.[22]

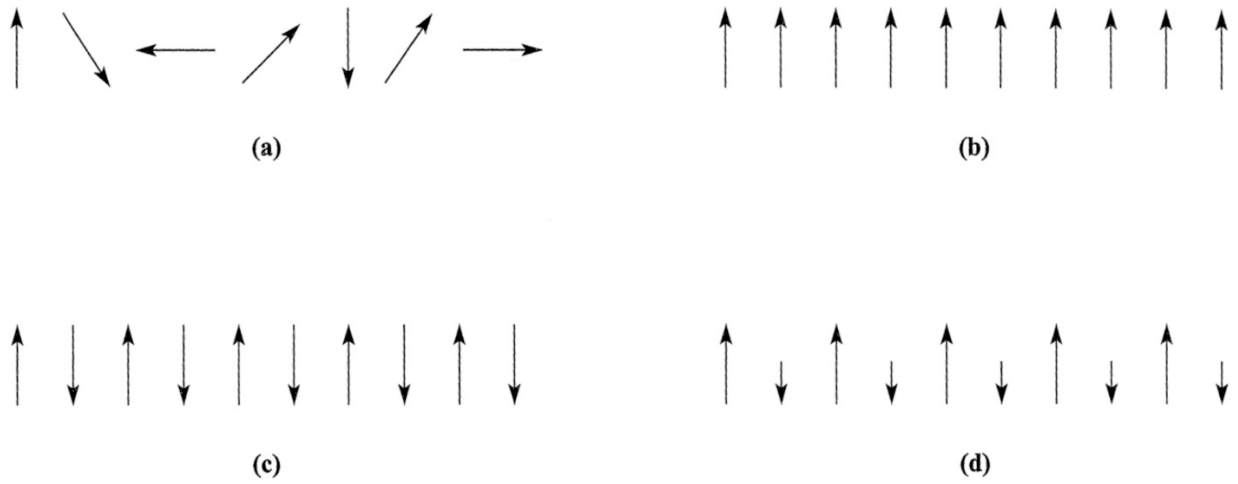

Figure 1-12: Spin Orientation of Several Types of Common Magnetism. a) Paramagnetism, b) Ferromagnetism, c) Antiferromagnetism, d) Ferrimagnetism (from Housecroft and Sharpe[22])

Several uncommon forms of magnetism are significant to this text, specifically chapter 7. One such form of magnetism that will be discussed in chapter 7 is the helical magnetism observed in CuO.[23-24] Figure 1-13 shows several complex magnetic ordering systems that deviate from the traditional types of magnetism shown in Figure 1-12.[4]

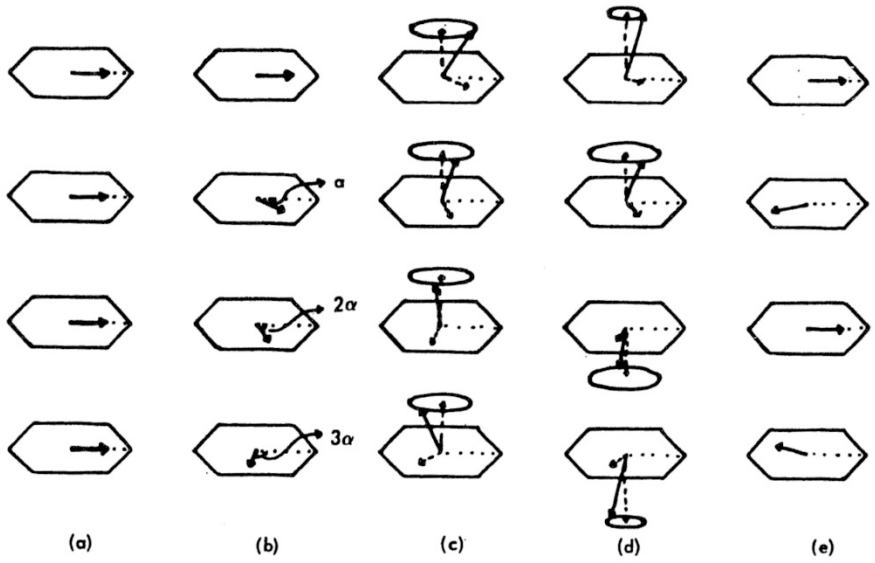

Figure 1-13: Unconventional Forms of Magnetism Including a) Collinear Ferromagnetism, b) Helicoidal Antiferromagnetism, c) Helicoidal Ferromagnetism, d) Cycloidal Antiferromagnetism, e) Transverse Oscillatory Antiparallel Ordering (from Gopal[4])

Magnetic states (similar to phonon or vibrational states) exist and also have a DOS or dispersion relation. In regards to magnetic states, however, the concept of waves is not as straightforward as it is for vibrations. A perfectly ordered ferromagnetic or antiferromagnet will have all spins aligned without exception. This unique state only occurs at 0 K as any thermal agitation of the lattice could be enough to disrupt the spin alignment at some point in the lattice by exciting an electron spin to a higher energy state. The distribution of the excited spins can be Fourier-analyzed into a set of waves called magnons.[4]

The spins of each electron can be classically thought of as precessing around some common axis. At perfect order (0 K), all spins will precess in phase, but when a magnon/spin wave is excited, the electron spins no longer precess in phase. The frequencies of these different

phases and the number of electron spins with those frequencies produces the dispersion relation or DOS. For ferromagnets (and ferrimagnets), the dispersion relation takes the form:[4-5, 25]

$$\omega_q = \alpha_f \frac{2Jsa^2}{\hbar} q^2 \tag{1-11}$$

and for antiferromagnetics, it takes the form:[4-5, 25]

$$\omega_q = \alpha_a \frac{2J'sa^2}{\hbar} q \tag{1-12}$$

where α_f and α_a are constants dependent on the crystal structure, J and J' are the magnitude of the ferromagnetic and antiferromagnetic exchange constants, respectively, $\hbar$ is Plank's constant, and q is the wavevector. It is noted that the vibrational dispersion relation (at low frequencies) has the same dependence on q as the antiferromagnet ($\omega \propto q$).[3-5, 25]

The heat capacity of these magnetic contributions can be derived using first-principle equations as was done with the vibrational heat capacity. McQuarrie[3] shows that when a system of wavelike quasi-particles (such as phonons and magnons) has a dispersion relation $\omega = Ak^n$, the heat capacity is proportional to $T^{3/n}$ at low temperatures. Neglecting the details of the derivations, the low-temperature heat capacity contribution from ferromagnetism (and ferrimagnetism) becomes:[4]

$$C_{FM} = c_f Nk \left(\frac{kT}{2Js}\right)^{3/2} \tag{1-13}$$

and of antiferromagnetic contributions becomes:[4]

$$C_{AFM} = c_a Nk \left(\frac{kT}{2J's}\right)^{3} \tag{1-14}$$

where c_f and c_a are constants dependent on the crystal structure. Although the heat capacity of the antiferromagnetic dependence on temperature is the same as that of vibrations at low temperatures (T^3), these magnetic contributions can still be identified in heat capacity data since

the magnitude of the magnetic contribution is usually about twenty times larger than the vibrational contribution (see Figure 1-11 above).[4]

These heat capacities are generally only valid at low temperatures and therefore low frequencies. At higher temperatures approaching the transition to the disordered paramagnetic state, modeling is much more ambiguous. Several models have been proposed, but these are generally only valid for the most simple of cases since the transition from a mostly ordered state to a mostly disordered state often involves a singularity where the heat capacity becomes infinite.[15]

One model that has been quite successful at representing a transition in the heat capacity data is the Schottky anomaly.[4] This transition is quite different from the order-disorder transitions associated with conventional magnetism. It is typically observed with magnetic properties, though many other non-magnetic systems also exhibit Schottky anomalies.[7, 17, 26-30] Figure 1-14 shows a simple Schottky heat capacity anomaly.[4]

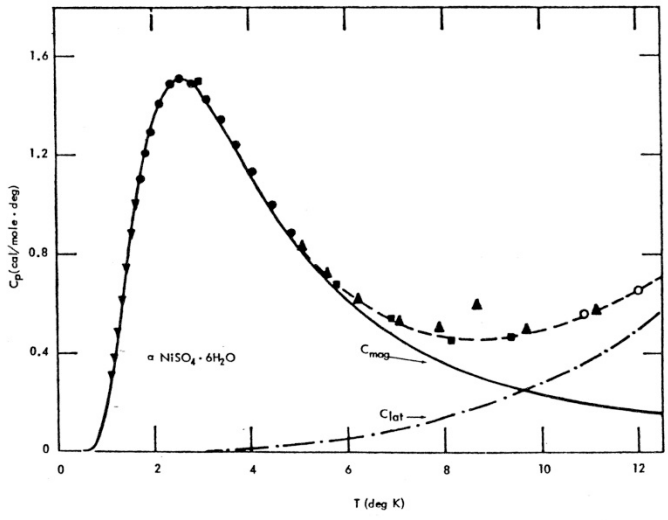

Figure 1-14: Schottky Heat Capacity Anomaly in α-$NiSO_4 \cdot 6H_2O$ (from Gopal[4])

Schottky anomalies are indicative of multi-level systems. In terms of magnetization and electron spins, the Schottky heat capacity arises from a transition of an electron from one spin state to another. Through simple Boltzmann statistics and the probabilities of an electron occupying a given state, one can derive an expression for energy and therefore heat capacity for this two (or more) level system:[4]

$$C_{Sch} = Nk\left(\frac{\delta}{T}\right)^2 \frac{g_0}{g_1} \frac{e^{\delta/T}}{\left(1 + \frac{g_0}{g_1} e^{\delta/T}\right)^2} \tag{1-15}$$

where δ is the energy separation of the two states with units of K ($\delta = \Delta E/k$), and g_0 and g_1 are the degeneracies of the ground and first excited states. This function is valuable for determining the separation of the multiple states as well as the number of particles participating in this effect as will be discussed in great detail in chapter 4.[7]

One other magnetic heat capacity feature relevant to this dissertation is anisotropy. Anisotropy in magnetism occurs when spins align "easier" along one direction of the crystal than another. An anisotropy energy directs the magnetic alignment along a particular direction as can be seen in Figure 1-15.[5] The energies of magnetization along the different axes are offset from each other producing an energy gap. This energy gap in the magnetization is manifest in the heat capacity with the formula for anisotropic ferromagnetism:[31]

$$C_{fsw} = \Lambda_{fsw} T^{3/2} e^{-\delta/T} \tag{1-16}$$

and for anisotropic antiferromagnetism:[32]

$$C_{asw} = \Lambda_{asw} T^3 e^{-\delta/T} \tag{1-17}$$

where Λ_{fsw} and Λ_{asw} are constants proportional to the molar volume and spin-wave stiffness constant, and δ is the spin-wave gap in units of K. In chapter 3, equations similar to these will be

derived from a model in which the vibrational DOS has a gap at low energies, and the value of the heat capacity modeling will be presented.[9]

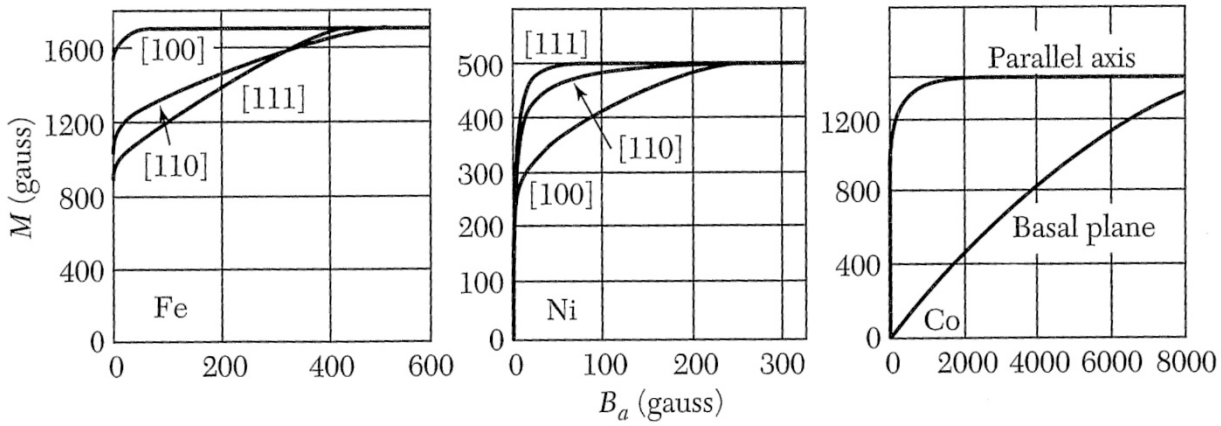

Figure 1-15: Magnetization Along Different Axes for Fe, Ni, and Co Showing Anisotropy.

Aside from the basic models introduced here, there are many other models that are more applicable under various circumstances.[6, 33-38] The purpose of this dissertation is to introduce two new models that describe some underlying physical properties of important materials (chapters 3 and 4). The remainder of the dissertation will apply these models to real systems of current interest and introduce many new scientific features derived from the heat capacity analyses. These new models as well as the traditional models will be shown to provide substantial information, especially for systems with nanoscale features.

1.2 Materials

Since these models will be applied to several materials, it is useful to briefly introduce the materials that will be discussed herein and identify the properties that are relevant to this work.

All of these material systems include nanoparticles, but comparison is often made between the nanoparticles and their bulk analogues.

1.2.1 Spinels

Metal oxides with the spinel structure are important in many areas of research and technology, with applications in magnetism, semiconductors, electrochemistry, geology, metallurgy, catalysis, fuel cells, water splitting, and others.[39-46] Not only are these materials significant in terms of technology, but the underlying physical phenomena intrinsic to these materials tend to be unusual and often lead to new discoveries of basic science.[47]

The common occurrence of spinels and their thermodynamic stability are related to the large number of valences that the cations can accommodate. Normal spinels of the 2-3 charge type, such as Co_3O_4 and Mn_3O_4, have the formula $A^{2+}(B^{3+})_2O_4$ where the A^{2+} cations occupy tetrahedral sites, and the B^{3+} cations occupy octahedral sites. Inverse 2-3 spinels, such as Fe_3O_4, fill the tetrahedral sites with B^{3+} cations, and the octahedral sites are occupied, usually approximately randomly, by the remaining B^{3+} and A^{2+} cations.

Co_3O_4 is a cubic normal spinel with Co^{2+} ions on tetrahedral sites and Co^{3+} ions on octahedral sites and exhibits Type-A or Type-II antiferromagnetism below its Néel temperature T_N of 30 K for bulk Co_3O_4.[42, 48-52] Mn_3O_4 is a tetragonal normal spinel with Mn^{2+} ions on the tetrahedral sites and Mn^{3+} ions on the octahedral sites but transforms to a cubic structure above about 1445 K.[53-55] It is ferrimagnetic below its Curie temperature T_C of about 43 K.[44-45, 54-57] Fe_3O_4 is a cubic inverse spinel having tetrahedral sites occupied by Fe^{3+} and octahedral sites that are approximately randomly occupied by the remaining Fe^{3+} and Fe^{2+}. It is ferrimagnetic up to a T_C of about 860 K,[58-59] but it also has a Verwey transition in which it converts from an insulator

to a metal below about 118 K (depending on oxygen stoichiometry).[58-60] The transition temperatures in these spinels are known to be related to particle size and typically decrease as particle size decreases.[42, 44, 47-48, 61-64]

Because of the different structures and cation site occupancies of these pure spinels, the solid solutions of these materials are strongly dependent on the cation distributions and site preferences.[65] These materials gradually shift from a cubic normal spinel to a cubic inverse spinel for the Co-Fe solid solutions and from a tetragonal normal spinel to a cubic inverse spinel for the Mn-Fe system. The mixing behavior of these materials has been the focus of many investigations;[39, 50, 53, 56-57, 65-72] however, a better understanding of the mixing in these spinels, especially in nanocrystalline species, can be acquired through the use of heat capacity measurements and modeling. This investigation targets the bulk and nanophase spinels Co_3O_4, Mn_3O_4, Fe_3O_4, and their solid solutions, with a focus on the effect of structural differences on entropies of mixing as determined by our new heat capacity measurements as well as work of others.[64, 73-81]

1.2.2 Al doped TiO_2 Nanoparticles

TiO_2 nanoparticles are widely used in industry as catalysts, catalyst supports, components of solar cells, and even household products.[82-87] Dopants are often incorporated into the nanoparticles to improve their structural and thermal stability, catalytic activity and selectivity, photoresponse, and other desirable chemical and physical properties.[88-93] Aluminum is a common dopant added to TiO_2 nanoparticles to control the thermal stability, surface area, and porosity of the nanostructure; however, the role the Al dopant has in stabilizing the structure is

unclear, as is often the case with doped materials. Understanding the role that the Al dopant has on TiO_2 nanoparticles is necessary to produce particles with optimized properties.

Many investigations using conventional methods have failed to provide a detailed understanding of the role that the Al has in stabilizing TiO_2 nanoparticles. Heat capacity is useful for identifying and quantifying concentrations of impurities and the average properties of a material;[4] therefore, using sophisticated models to treat the low-temperature ($T < 10$ K) heat capacity data one can determine structural information and the location of the dopant in Al doped TiO_2 nanoparticles.[7, 94] This chapter will use heat capacity measurements and models corroborated with traditional techniques to show that the Al dopant neither enters the Ti sites in the TiO_2 lattice nor binds to the surface (as has been proposed). It will be shown that the dopant forms a hybrid TiO_2-Al_2O_3 microstructure with short-range order.

1.2.3 CuO

Cupric oxide, CuO (tenorite), has been extensively investigated due to its significance in fundamental science as well as technological applications. Its structural and magnetic properties are unique,[95-97] and it is closely related to high-temperature superconducting cuprates such as $YBa_2Cu_3O_{7-x}$.[98] In terms of applications, it has use in catalysis,[99] photovoltaics,[100-102] batteries,[103] and possibly spintronic devices.[104-106] The high-temperature multiferroic behavior of CuO could also be used in sensors, memory devices, and magnetoelectric devices.[107]

The structure and magnetic properties of CuO are unique for a 3*d* transition-metal monoxide,[104, 108-110] and its Cu–O–Cu chains running along the [101] and $[10\bar{1}]$ directions make it relevant to cuprate superconductor research.[23-24, 98, 104, 111] CuO has multiple regions of different magnetic properties as shown by various measurements.[112-113] Heat capacity measurements show two distinct magnetic transitions at about 213 and 230 K.[96-98, 105, 111, 114-123] Magnetic

susceptibility data show a broad maximum at about 540 K, a minimum at about 150 K, and a subtle change in slope around 230 K.[95, 97-98, 104-106, 117, 122, 124-127] Neutron experiments have provided more details about the magnetic character of CuO in the various temperature regions and have shown that a helical incommensurate phase exists from 213-230 K.[23-24, 128-129]

Above the Néel temperature T_{N2} of 230 K, antiferromagnetism persists – in a 1D form – through the very large superexchange interactions (35-73 meV) along the $[10\bar{1}]$ direction.[23-24, 96-98, 125, 130-131] Multiferroic behavior, which is the coexistence of magnetism and ferroelectricity, has recently been discovered in the 213-230 K temperature range, which is significantly higher in temperature than most other materials.[104] This high temperature of multiferroicity in CuO has spurred many recent investigations involving practical applications as well as basic science related to cuprate superconductors and other similar materials.[104-106, 112-113]

All of the physical properties mentioned above (heat capacity, magnetization, etc.) have been extensively investigated for bulk CuO, but few studies have focused on these physical properties of CuO nanoparticles.[124-126, 132-134] Chapter 7 will present an investigation on the magnetic and structural properties of CuO nanoparticles and use heat capacity synergistically with other techniques show that structural features common to nanoparticles are responsible for extending the magnetic and ferroelectric temperature ranges to room temperature.

REFERENCES

1. Kulkarni, M. S., A Selective Review of the Quantification of Defect Dynamics in Growing Czochralski Silicon Crystals. *Industrial & engineering chemistry research* **2005**, *44*, 6246-6263.

2. Braga, A.; Moreira, S.; Zampieri, P.; Bacchin, J.; Mei, P., New Processes for the Production of Solar-Grade Polycrystalline Silicon: A Review. *Solar energy materials and solar cells* **2008**, *92*, 418-424.

3. McQuarrie, D., Statistical Mechanics. *University Science, Sausalito, USA* **2000**, 641.

4. Gopal, E. S. R., *Specific Heats at Low Temperatures*; Plenum Press New York, 1966; Vol. 227.

5. Kittel, C.; McEuen, P.; McEuen, P., *Introduction to Solid State Physics*; Wiley New York, 1976; Vol. 8.

6. Phillips, N. E., Low-Temperature Heat Capacity of Metals. *Critical Reviews in Solid State and Material Sciences* **1971**, *2*, 467-553.

7. Schliesser, J. M.; Woodfield, B. F., Lattice Vacancies Responsible for the Linear Dependence of the Low-Temperature Heat Capacity of Insulating Materials. *Physical Review B* **2015**, *91*, 024109.

8. Planck, M., Ueber Das Gesetz Der Energieverteilung Im Normalspectrum. *Annalen der physik* **1901**, *309*, 553-563.

9. Schliesser, J.; Woodfield, B., Development of a Debye Heat Capacity Model for Vibrational Modes with a Gap in the Density of States. *Journal of physics. Condensed matter: an Institute of Physics journal* **2015**, *27*, 285402-285402.

10. Fisher, R.; Gordon, J.; Reklis, S.; Wright, D.; Emerson, J.; Woodfield, B.; McCarron III, E.; Phillips, N., Magnetic-Field Dependence of the Low-Temperature Specific Heat of Some High-Tc Copper-Oxide Superconductors Evidence for an H12t Contribution in the Mixed State. *Physica C: Superconductivity* **1995**, *252*, 237-263.

11. Yildirim, H.; Kara, A.; Rahman, T. S., Structural, Vibrational and Thermodynamic Properties of Agncu34− N Nanoparticles. *Journal of Physics: Condensed Matter* **2009**, *21*, 084220.

12. Anderson, O. L., Thermoelastic Properties of Mgsio3 Perovskite Using the Debye Approach. *American Mineralogist* **1998**, *83*, 23-35.

13. Oganov, A. R.; Brodholt, J. P.; David Price, G., Comparative Study of Quasiharmonic Lattice Dynamics, Molecular Dynamics and Debye Model Applied to Mgsio3 Perovskite. *Physics of the Earth and Planetary Interiors* **2000**, *122*, 277-288.

14. Wei, Z.; Yang, J.; Bi, K.; Chen, Y., Mode Dependent Lattice Thermal Conductivity of Single Layer Graphene. *Journal of Applied Physics* **2014**, *116*, 153503.

15. Levine, I. N., *Physical Chemistry*; McGraw-Hill, 2008.

16. Fisher, R.; Gordon, J.; Phillips, N., Specific Heat of the High-Tc Oxide Superconductors. *Journal of Superconductivity* **1988**, *1*, 231-294.

17. Anderson, P. W.; Halperin, B.; Varma, C. M., Anomalous Low-Temperature Thermal Properties of Glasses and Spin Glasses. *Philosophical Magazine* **1972**, *25*, 1-9.

18. Phillips, N. E.; Emerson, J. P.; Fisher, R. A.; Gordon, J. E.; Woodfield, B. F.; Wright, D. A., Is There an Intrinsic Linear Term in the Specific Heat of Yba2cu3o7? *Physica C: Superconductivity* **1994**, *235–240, Part 3*, 1737-1738.

19. Coey, J. M. D.; Von Molnar, S.; Torressen, A., Low-Temperature Specific Heat of Bi2sr2cacu2o8: Comparison with Some Other Layered Oxides. *Journal of the Less Common Metals* **1989**, *151*, 191-194.

20. Heisenberg, W., Zur Theorie Des Ferromagnetismus. *Zeitschrift für Physik* **1928**, *49*, 619-636.

21. Shi, Q.; Zhang, L.; Schlesinger, M. E.; Boerio-Goates, J.; Woodfield, B. F., Low Temperature Heat Capacity Study of Fe3po7 and Fe4(P2o7)3. *The Journal of Chemical Thermodynamics* **2013**, *62*, 86-91.

22. Housecroft, C. E.; Sharpe, A. G., *Inorganic Chemistry*; Pearson, 2012.

23. Yang, B.; Tranquada, J.; Shirane, G., Neutron Scattering Studies of the Magnetic Structure of Cupric Oxide. *Physical Review B* **1988**, *38*, 174.

24. Yang, B. X.; Thurston, T. R.; Tranquada, J. M.; Shirane, G., Magnetic Neutron Scattering Study of Single-Crystal Cupric Oxide. *Physical Review B* **1989**, *39*, 4343-4349.

25. Kittel, C., *Quantum Theory of Solids*; Wiley, 1963.

26. Boerio-Goates, J.; Smith, S. J.; Liu, S.; Lang, B. E.; Li, G.; Woodfield, B. F.; Navrotsky, A., Characterization of Surface Defect Sites on Bulk and Nanophase Anatase and Rutile Tio2 by Low-Temperature Specific Heat. *The Journal of Physical Chemistry C* **2013**, *117*, 4544-4550.

27. Golding, B.; Birge, N.; Haemmerle, W.; Cava, R.; Rietman, E., Tunneling Systems in Superconducting Yba_{2} Cu_{3} O_{7}. *Physical Review B* **1987**, *36*, 5606-5608.

28. Chakraverty, B.; Sienko, M.; Bonnerot, J., Low-Temperature Specific Heat and Magnetic Susceptibility of Nonmetallic Vanadium Bronzes. *Physical Review B* **1978**, *17*, 3781.

29. Xu, J.; Tang, J.; Sato, K.; Tanabe, Y.; Miyasaka, H.; Yamashita, M.; Heguri, S.; Tanigaki, K., Low-Temperature Heat Capacity of Sr 8 Ga 16 Ge 30 and Ba 8 Ga 16 Ge 30: Tunneling States and Electron-Phonon Interaction in Clathrates. *Physical Review B* **2010**, *82*, 085206.

30. McWhan, D.; Varma, C.; Hsu, F.; Remeika, J., Low-Temperature Heat Capacity of Alkali-Metal and Silver B-Aluminas. *Physical Review B* **1977**, *15*, 553.

31. Fisher, R. A.; Bouquet, F.; Phillips, N. E.; Franck, J. P.; Zhang, G.; Gordon, J. E.; Marcenat, C., Electron, Spin-Wave, Hyperfine, and Phonon Contributions to the Low-Temperature Specific Heat of La0.65ca0.35mno3:Effects of Magnetic Fields and 16o/18o Exchange. *Physical Review B* **2001**, *64*, 134425.

32. Majzlan, J.; Navrotsky, A.; Woodfield, B. F.; Lang, B. E.; Boerio-Goates, J.; Fisher, R. A., Phonon, Spin-Wave, and Defect Contributions to the Low-Temperature Specific Heat of A-Feooh. *Journal of Low Temperature Physics* **2003**, *130*, 69-76.

33. Benedict, L. X.; Louie, S. G.; Cohen, M. L., Heat Capacity of Carbon Nanotubes. *Solid State Communications* **1996**, *100*, 177-180.

34. Lien, W. H.; Phillips, N. E., Heat Capacity of Small Particles of Mgo between 1.5° and 4° K. *The Journal of Chemical Physics* **1958**, *29*, 1415-1416.

35. Kelley, K. K.; King, E. G., *Entropies of the Elements and Inorganic Compounds*; US Government Printing Office, 1961; Vol. 592.

36. Ramirez, A. P.; Kowach, G. R., Large Low Temperature Specific Heat in the Negative Thermal Expansion Compound Zrw2o8. *Physical Review Letters* **1998**, *80*, 4903-4906.

37. Boerio-Goates, J.; Stevens, R.; Lang, B.; Woodfield, B. F., Heat Capacity Calorimetry. *Journal of Thermal Analysis and Calorimetry* **2002**, *69*, 773-783.

38. Tarasov, V.; Yunitskii, G., Theory of Heat Capacity of Chain and Layer Structures. *Zh. fiz. khim* **1950**, *24*, 111-128.

39. O'Neill, H. S. C.; Navrotsky, A., Cation Distributions and Thermodynamic Properties of Binary Spinel Solid Solutions. *American Mineralogist* **1984**, *69*, 733-753.

40. Xu, B.; Bhawe, Y.; Davis, M. E., Spinel Metal Oxide-Alkali Carbonate-Based, Low-Temperature Thermochemical Cycles for Water Splitting and Co2 Reduction. *Chemistry of Materials* **2013**, *25*, 1564-1571.

41. Raveau, B.; Seikh, M. M., Electronic and Magnetic Properties of Cobaltites with a 3d "Triangular Lattice". In *Cobalt Oxides: From Crystal Chemistry to Physics*, Wiley-VCH Verlag GmbH & Co. KGaA: 2012; pp 211-247.

42. Hill, A. H.; Harrison, A.; Ritter, C.; Yue, W.; Zhou, W., Neutron Powder Diffraction and Magnetic Studies of Mesoporous Co3o4. *Journal of Magnetism and Magnetic Materials* **2011**, *323*, 226-231.

43. Grundy, A. N.; Hallstedt, B.; Gauckler, L. J., Assessment of the Mn-O System. *Journal of phase equilibria* **2003**, *24*, 21-39.

44. Regmi, R.; Tackett, R.; Lawes, G., Suppression of Low-Temperature Magnetic States in Mn3o4 Nanoparticles. *Journal of Magnetism and Magnetic Materials* **2009**, *321*, 2296-2299.

45. Tackett, R.; Lawes, G.; Melot, B. C.; Grossman, M.; Toberer, E. S.; Seshadri, R., Magnetodielectric Coupling in Mn3o4. *Physical Review B* **2007**, *76*, 024409.

46. Navrotsky, A.; Ma, C.; Lilova, K.; Birkner, N., Nanophase Transition Metal Oxides Show Large Thermodynamically Driven Shifts in Oxidation-Reduction Equilibria. *Science* **2010**, *330*, 199-201.

47. Bisht, V.; Rajeev, K., Non-Equilibrium Effects in the Magnetic Behavior of Co3o4 Nanoparticles. *Solid State Communications* **2011**, *151*, 1275-1279.

48. Dutta, P.; Seehra, M.; Thota, S.; Kumar, J., A Comparative Study of the Magnetic Properties of Bulk and Nanocrystalline Co3o4. *Journal of Physics: Condensed Matter* **2008**, *20*, 015218.

49. Khriplovich, L.; Kholopov, E.; Paukov, I., Heat Capacity and Thermodynamic Properties of Co3o4 from 5 to 307 K Low-Temperature Transition. *The Journal of Chemical Thermodynamics* **1982**, *14*, 207-217.

50. Tristan, N.; Zestrea, V.; Behr, G.; Klingeler, R.; Büchner, B.; von Nidda, H. K.; Loidl, A.; Tsurkan, V., Spin Frustration and Magnetic Exchange in Cobalt Aluminum Oxide Spinels. *Physical Review B* **2008**, *77*, 094412.

51. Woodfield, B. F.; Shapiro, J. L.; Stevens, R.; Boerio-Goates, J.; Wilson, M. L., Critical Phenomena at the Antiferromagnetic Transition in Mno. *Physical Review B* **1999**, *60*, 7335.

52. Woodfield, B. F.; Wilson, M. L.; Byers, J. M., Low-Temperature Specific Heat of La1−Xsrxmno3+Δ. *Physical review letters* **1997**, *78*, 3201.

53. Guillemet-Fritsch, S.; Navrotsky, A.; Tailhades, P.; Coradin, H.; Wang, M., Thermochemistry of Iron Manganese Oxide Spinels. *Journal of Solid State Chemistry* **2005**, *178*, 106-113.

54. Robie, R. A.; Hemingway, B. S., Low-Temperature Molar Heat Capacities and Entropies of Mno2(Pyrolusite), Mn3o4(Hausmanite), and Mn2o3(Bixbyite). *The Journal of Chemical Thermodynamics* **1985**, *17*, 165-181.

55. Chhor, K.; Bocquet, J.; Pommier, C.; Chardon, B., Heat Capacity and Thermodynamic Behaviour of Mn3o4 and Znmn2o4 at Low Temperatures. *The Journal of Chemical Thermodynamics* **1986**, *18*, 89-99.

56. Kjellqvist, L.; Selleby, M., Thermodynamic Assessment of the Fe-Mn-O System. *Journal of phase equilibria and diffusion* **2010**, *31*, 113-134.

57. Naito, K.; Inaba, H.; Yagi, H., Heat Capacity Measurements of Mnxfe3−Xo4. *Journal of Solid State Chemistry* **1981**, *36*, 28-35.

58. Levy, D.; Giustetto, R.; Hoser, A., Structure of Magnetite (Fe3o4) above the Curie Temperature: A Cation Ordering Study. *Physics and Chemistry of Minerals* **2012**, *39*, 169-176.

59. Klotz, S.; Steinle-Neumann, G.; Strässle, T.; Philippe, J.; Hansen, T.; Wenzel, M. J., Magnetism and the Verwey Transition in ${\Mathrm{Fe}}_{3}{\Mathrm{O}}_{4}$ under Pressure. *Physical Review B* **2008**, *77*, 012411.

60. Verwey, E.; Haayman, P., Electronic Conductivity and Transition Point of Magnetite ("Fe 3 O 4"). *Physica* **1941**, *8*, 979-987.

61. Ambrose, T.; Chien, C., Finite-Size Effects and Uncompensated Magnetization in Thin Antiferromagnetic Coo Layers. *Physical review letters* **1996**, *76*, 1743.

62. He, L.; Chen, C.; Wang, N.; Zhou, W.; Guo, L., Finite Size Effect on Néel Temperature with Co3o4 Nanoparticles. *arXiv preprint arXiv:0705.4344* **2007**.

63. Kumzerov, Y. A.; Kartenko, N.; Parfen'eva, L.; Smirnov, I.; Sysoeva, A.; Misiorek, H.; Jezowski, A., Determination of the Néel Temperature from Measurements of the Thermal Conductivity of the Co3o4 Antiferromagnet Nanostructured in Porous Glass Channels. *Physics of the Solid State* **2012**, *54*, 1066-1069.

64. Snow, C. L.; Shi, Q.; Boerio-Goates, J.; Woodfield, B. F., Heat Capacity Studies of Nanocrystalline Magnetite (Fe3o4). *The Journal of Physical Chemistry C* **2010**, *114*, 21100-21108.

65. Sahu, S. K.; Huang, B.; Lilova, K.; Woodfield, B. F.; Navrotsky, A., Thermodynamics of Fe3o4–Co3o4 and Fe3o4–Mn3o4 Spinel Solid Solutions at the Bulk and Nanoscale. *Physical Chemistry Chemical Physics* **2015**.

66. Eschenfelder, A. H., Ionic Valences in Manganese-Iron Spinels. *Journal of Applied Physics* **1958**, *29*, 378-380.

67. Lavina, B.; Salviulo, G.; Della Giusta, A., Cation Distribution and Structure Modelling of Spinel Solid Solutions. *Physics and Chemistry of Minerals* **2002**, *29*, 10-18.

68. Navrotsky, A., Thermodynamics of A3o4-B3o4 Spinel Solid Solutions. *Journal of Inorganic and Nuclear Chemistry* **1969**, *31*, 59-72.

69. Navrotsky, A.; Kleppa, O., The Thermodynamics of Cation Distributions in Simple Spinels. *Journal of Inorganic and Nuclear Chemistry* **1967**, *29*, 2701-2714.

70. Navrotsky, A.; Kleppa, O., Thermodynamics of Formation of Simple Spinels. *Journal of Inorganic and Nuclear Chemistry* **1968**, *30*, 479-498.

71. O'Neill, H. S. C.; Navrotsky, A., Simple Spinels; Crystallographic Parameters, Cation Radii, Lattice Energies, and Cation Distribution. *American Mineralogist* **1983**, *68*, 181-194.

72. Brabers, V.; Dekker, P., Infrared Spectra and Cation Distributions of Manganese Ferrites. *physica status solidi (b)* **1968**, *29*, K73-K76.

73. Fritsch, S.; Navrotsky, A., Thermodynamic Properties of Manganese Oxides. *Journal of the American Ceramic Society* **1996**, *79*, 1761-1768.

74. King, E., Heat Capacities at Low Temperatures and Entropies at 298.15° K. Of Nickelous Oxide, Cobaltous Oxide and Cobalt Spinel. *Journal of the American Chemical Society* **1957**, *79*, 2399-2400.

75. Millar, R. W., The Specific Heats at Low Temperatures of Manganous Oxide, Manganous-Manganic Oxide and Manganese Dioxide. *Journal of the American Chemical Society* **1928**, *50*, 1875-1883.

76. Millar, R. W., The Heat Capacities at Low Temperatures of "Ferrous Oxide," Magnetite, and Cuprous and Cupric Oxides. *Journal of the American Chemical Society* **1929**, *51*, 215-222.

77. Caruntu, D.; Caruntu, G.; O'Connor, C. J., Magnetic Properties of Variable-Sized Fe3o4 Nanoparticles Synthesized from Non-Aqueous Homogeneous Solutions of Polyols. *Journal of Physics D: Applied Physics* **2007**, *40*, 5801.

78. Jacob, K.; Kumar, A.; Rajitha, G.; Waseda, Y., Thermodynamic Data for Mn3o4, Mn2o3 and Mno2. *High Temperature Materials and Processes* **2011**, *30*, 459-472.

79. Westrum, E. F.; Grønvold, F., Magnetite (Fe3o4) Heat Capacity and Thermodynamic Properties from 5 to 350 K, Low-Temperature Transition. *The Journal of Chemical Thermodynamics* **1969**, *1*, 543-557.

80. Tan, H.; Turner, S.; Yücelen, E.; Verbeeck, J.; Van Tendeloo, G., 2d Atomic Mapping of Oxidation States in Transition Metal Oxides by Scanning Transmission Electron Microscopy and Electron Energy-Loss Spectroscopy. *Physical Review Letters* **2011**, *107*, 107602.

81. Saal, J. E.; Wang, Y.; Shang, S.; Liu, Z.-K., Thermodynamic Properties of Co3o4 and Sr6co5o15 from First-Principles. *Inorganic chemistry* **2010**, *49*, 10291-10298.

82. Fox, M. A.; Dulay, M. T., Heterogeneous Photocatalysis. *Chemical reviews* **1993**, *93*, 341-357.

83. Fujishima, A.; Rao, T. N., Interfacial Photochemistry: Fundamentals and Applications. *Pure and applied chemistry* **1998**, *70*, 2177-2188.

84. Hoffmann, M. R.; Martin, S. T.; Choi, W.; Bahnemann, D. W., Environmental Applications of Semiconductor Photocatalysis. *Chemical reviews* **1995**, *95*, 69-96.

85. Anpo, M.; Aikawa, N.; Kubokawa, Y., Photocatalytic Hydrogenation of Alkynes and Alkenes with Water over Titanium Dioxide. Platinum Loading Effect on the Primary Processes. *The Journal of Physical Chemistry* **1984**, *88*, 3998-4000.

86. Ohtani, B.; Ueda, Y.; Nishimoto, S.; Kagiya, T.; Hachisuka, H., Photocatalytic Oxidative Decomposition of Fluoroalkenes by Titanium Dioxide. *J. Chem. Soc* **1990**, 1955-90.

87. Mor, G. K.; Shankar, K.; Paulose, M.; Varghese, O. K.; Grimes, C. A., Use of Highly-Ordered Tio2 Nanotube Arrays in Dye-Sensitized Solar Cells. *Nano letters* **2006**, *6*, 215-218.

88. Bartholomew, C. H.; Farrauto, R. J., *Fundamentals of Industrial Catalytic Processes*; John Wiley & Sons, 2011.

89. Enache, C. S.; Schoonman, J.; Van Krol, R., The Photoresponse of Iron-and Carbon-Doped Tio2 (Anatase) Photoelectrodes. *Journal of electroceramics* **2004**, *13*, 177-182.

90. Janousch, M.; Meijer, G. I.; Staub, U.; Delley, B.; Karg, S. F.; Andreasson, B. P., Role of Oxygen Vacancies in Cr-Doped Srtio3 for Resistance-Change Memory. *Advanced Materials* **2007**, *19*, 2232-2235.

91. Wang, Z. L.; Yin, J. S.; Jiang, Y. D., Eels Analysis of Cation Valence States and Oxygen Vacancies in Magnetic Oxides. *Micron* **2000**, *31*, 571-580.

92. Wu, Q.; Zheng, Q.; van de Krol, R., Creating Oxygen Vacancies as a Novel Strategy to Form Tetrahedrally Coordinated Ti4+ in Fe/Tio2 Nanoparticles. *The Journal of Physical Chemistry C* **2012**, *116*, 7219-7226.

93. Santra, P. K.; Kamat, P. V., Mn-Doped Quantum Dot Sensitized Solar Cells: A Strategy to Boost Efficiency over 5%. *Journal of the American Chemical Society* **2012**, *134*, 2508-2511.

94. Schliesser, J. M.; Woodfield, B. F., Development of a Debye Heat Capacity Model for Vibrational Modes with a Gap in the Density of States. *Journal of Physics: Condensed Matter* **2015 (accepted)**.

95. O'Keeffe, M.; Stone, F., The Magnetic Susceptibility of Cupric Oxide. *Journal of Physics and Chemistry of Solids* **1962**, *23*, 261-266.

96. Loram, J.; Mirza, K.; Joyce, C.; Osborne, A., Specific-Heat Evidence for Quasi-1d Magnetic Order in Cuo. *EPL (Europhysics Letters)* **1989**, *8*, 263.

97. Seehra, M. S.; Feng, Z.; Gopalakrishnan, R., Magnetic Phase Transitions in Cupric Oxide. *Journal of Physics C: Solid State Physics* **1988**, *21*, L1051.

98. Junod, A.; Eckert, D.; Triscone, G.; Müller, J.; Reichardt, W., A Study of the Magnetic Transitions in Cuo: Specific Heat (1-330 K), Magnetic Susceptibility and Phonon Density of States. *Journal of Physics: Condensed Matter* **1989**, *1*, 8021.

99. Zhou, K.; Wang, R.; Xu, B.; Li, Y., Synthesis, Characterization and Catalytic Properties of Cuo Nanocrystals with Various Shapes. *Nanotechnology* **2006**, *17*, 3939.

100. Chauhan, D.; Satsangi, V.; Dass, S.; Shrivastav, R., Preparation and Characterization of Nanostructured Cuo Thin Films for Photoelectrochemical Splitting of Water. *Bulletin of Materials Science* **2006**, *29*, 709.

101. Bao, Q.; Li, C. M.; Liao, L.; Yang, H.; Wang, W.; Ke, C.; Song, Q.; Bao, H.; Yu, T.; Loh, K. P., Electrical Transport and Photovoltaic Effects of Core–Shell Cuo/C60 Nanowire Heterostructure. *Nanotechnology* **2009**, *20*, 065203.

102. Wadia, C.; Alivisatos, A. P.; Kammen, D. M., Materials Availability Expands the Opportunity for Large-Scale Photovoltaics Deployment. *Environmental Science & Technology* **2009**, *43*, 2072-2077.

103. Gao, X.; Bao, J.; Pan, G.; Zhu, H.; Huang, P.; Wu, F.; Song, D., Preparation and Electrochemical Performance of Polycrystalline and Single Crystalline Cuo Nanorods as Anode Materials for Li Ion Battery. *The Journal of Physical Chemistry B* **2004**, *108*, 5547-5551.

104. Kimura, T.; Sekio, Y.; Nakamura, H.; Siegrist, T.; Ramirez, A., Cupric Oxide as an Induced-Multiferroic with High-Tc. *Nature materials* **2008**, *7*, 291-294.

105. Wang, F.; Zou, T.; Liu, Y.; Yan, L.-Q.; Sun, Y., Persistent Multiferroicity without Magnetoelectric Effects in Cuo. *Journal of Applied Physics* **2011**, *110*, 054106.

106. Babkevich, P.; Poole, A.; Johnson, R. D.; Roessli, B.; Prabhakaran, D.; Boothroyd, A. T., Electric Field Control of Chiral Magnetic Domains in the High-Temperature Multiferroic Cuo. *Physical Review B* **2012**, *85*, 134428.

107. Ortega, N.; Kumar, A.; Scott, J.; Katiyar, R. S., Multifunctional Magnetoelectric Materials for Device Applications. *Journal of Physics: Condensed Matter* **2015**, *27*, 504002.

108. Åsbrink, S.; Norrby, L.-J., A Refinement of the Crystal Structure of Copper (Ii) Oxide with a Discussion of Some Exceptional Esd's. *Acta Crystallographica Section B: Structural Crystallography and Crystal Chemistry* **1970**, *26*, 8-15.

109. Brese, N.; O'Keeffe, M.; Ramakrishna, B.; Von Dreele, R., Low-Temperature Structures of Cuo and Ago and Their Relationships to Those of Mgo and Pdo. *Journal of Solid State Chemistry* **1990**, *89*, 184-190.

110. Wu, W.; Hiraoka, N.; Huang, D.; Huang, S.; Tsuei, K.; van Veenendaal, M.; van den Brink, J.; Sekio, Y.; Kimura, T., Effective Orbital Symmetry of Cuo: Examination by Nonresonant Inelastic X-Ray Scattering. *Physical Review B* **2013**, *88*, 205129.

111. Gmelin, E., Cupric Oxide-Cuo: Its Structural, Electrical, Thermal and Magnetic Properties. *Indian Journal of Pure and Applied Physics* **1992**, *30*, 596-608.

112. Villarreal, R.; Quirion, G.; Plumer, M.; Poirier, M.; Usui, T.; Kimura, T., Magnetic Phase Diagram of Cuo Via High-Resolution Ultrasonic Velocity Measurements. *Physical review letters* **2012**, *109*, 167206.

113. Rebello, A.; Winter, Z. C. M.; Viall, S.; Neumeier, J. J., Multiple Phase Transitions in Cuo Observed with Thermal Expansion. *Physical Review B* **2013**, *88*, 094420.

114. Millar, R. W., The Heat Capacities at Low Temperatures of "Ferrous Oxide," Magnetite and Cuprous and Cupric Oxides. *Journal of the American Chemical Society* **1929**, *51*, 215-222.

115. Hu, J.-H.; Johnston, H. L., Low Temperature Heat Capacities of Inorganic Solids. Xvi. Heat Capacity of Cupric Oxide from 15 to 300 K. 1. *Journal of the American Chemical Society* **1953**, *75*, 2471-2473.

116. Kellogg, H. H., Thermodynamic Properties of the Oxides of Copper and Nickel. *Journal of Chemical & Engineering Data* **1969**, *14*, 41-44.

117. Junod, A.; Eckert, D.; Triscone, G.; Muller, J.; Reichardt, W., Specific Heat (1–330k), Magnetic Susceptibility (5–250k) and Phonon Dos of Cuo: A Study of the Magnetic Transitions. *Physica C: Superconductivity* **1989**, *162*, 478-479.

118. Gmelin, E.; Köbler, U.; Brill, W.; Chattopadhyay, T.; Sastry, S., Magnetic Specific Heat and Susceptibility of Cupric Oxide (Cuo) Single Crystals. *Bulletin of Materials Science* **1991**, *14*, 117-123.

119. Ota, S.; Gmelin, E., Magnetic Phase Transitions and Specific Heat of Single Crystalline Cupric Oxide. *Journal of Thermal Analysis and Calorimetry* **1992**, *38*, 635-640.

120. Ota, S. B.; Gmelin, E., Incommensurate Antiferromagnetism in Copper(Ii) Oxide: Specific-Heat Study in a Magnetic Field. *Physical Review B* **1992**, *46*, 11632-11635.

121. Wang, B.-X.; Zhou, L.-P.; Peng, X.-F., Surface and Size Effects on the Specific Heat Capacity of Nanoparticles. *International journal of thermophysics* **2006**, *27*, 139-151.

122. Borzi, R.; Stewart, S.; Punte, G.; Mercader, R.; Zysler, R.; Tovar, M., History-Dependent Magnetic Properties in Pure and Zn-Doped Cupric Oxide. *Solid state communications* **2001**, *117*, 311-314.

123. Mekata, M.; Yaguchi, N.; Takagi, T.; Sugino, T.; Mitsuda, S.; Yoshizawa, H.; Hosoito, N.; Shinjo, T., Successive Magnetic Ordering in Cufeo2–a New Type of Partially Disordered Phase in a Triangular Lattice Antiferromagnet–. *Journal of the Physical Society of Japan* **1993**, *62*, 4474-4487.

124. Rehman, S.; Mumtaz, A.; Hasanain, S. K., Size Effects on the Magnetic and Optical Properties of Cuo Nanoparticles. *J Nanopart Res* **2011**, *13*, 2497-2507.

125. Punnoose, A.; Magnone, H.; Seehra, M.; Bonevich, J., Bulk to Nanoscale Magnetism and Exchange Bias in Cuo Nanoparticles. *Physical Review B* **2001**, *64*, 174420.

126. Bisht, V.; Rajeev, K.; Banerjee, S., Anomalous Magnetic Behavior of Cuo Nanoparticles. *Solid State Communications* **2010**, *150*, 884-887.

127. Bizette, H.; Tsaï, B., Susceptibilite Magnetique De L'oxyde Cuivrique Cuo. *Comptes Rendus Hebomadaires des Seances de L Academie des Sciences* **1955**, *241*, 182-188.

128. Forsyth, J. B.; Brown, P. J.; Wanklyn, B. M., Magnetism in Cupric Oxide. *Journal of Physics C: Solid State Physics* **1988**, *21*, 2917.

129. Ain, M.; Menelle, A.; Wanklyn, B.; Bertaut, E., Magnetic Structure of Cuo by Neutron Diffraction with Polarization Analysis. *Journal of Physics: Condensed Matter* **1992**, *4*, 5327.

130. Shimizu, T.; Matsumoto, T.; Goto, A.; Yoshimura, K.; Kosuge, K., Magnetic Dimensionality of the Antiferromagnet Cuo. *Journal of the Physical Society of Japan* **2003**, *72*, 2165-2168.

131. Koo, H. J.; Whangbo, M. H., Magnetic Superstructures of Cupric Oxide Cuo as Ordered Arrangements of One-Dimensional Antiferromagnetic Chains. *Inorganic Chemistry* **2003**, *42*, 1187-1192.

132. Viano, A.; Mishra, S. R.; Lloyd, R.; Losby, J.; Gheyi, T., Thermal Effects on Esr Signal Evolution in Nano and Bulk Cuo Powder. *Journal of Non-Crystalline Solids* **2003**, *325*, 16-21.

133. Charnaya, E.; Lee, M.; Tien, C.; Pak, V.; Formus, D.; Pirozerskii, A.; Nedbai, A.; Ubyivovk, E.; Baryshnikov, S.; Chang, L., Magnetic and Dielectric Studies of Multiferroic Cuo

Nanoparticles Confined to Porous Glass. *Journal of Magnetism and Magnetic Materials* **2012**, *324*, 2921-2925.

134. Dar, M. A.; Kim, Y. S.; Kim, W. B.; Sohn, J. M.; Shin, H. S., Structural and Magnetic Properties of Cuo Nanoneedles Synthesized by Hydrothermal Method. *Applied Surface Science* **2008**, *254*, 7477-7481.

2 METHODS

2.1 Introduction

The focus of this dissertation is to present several solid-state models that describe the energetics of various physical features found in nanoparticle samples. To extend the modeling from simple theory, measurements of the different physical properties related to the models have been performed. The relationship between theoretical models and measured properties is a significant portion of this dissertation; therefore, the techniques used for studying the physical and structural properties of the materials will be briefly reviewed here.

This work uses heat capacity measurements, X-ray diffraction (XRD), transmission electron microscopy (TEM), electron energy-loss spectroscopy (EELS), thermogravimetric analysis (TGA), and magnetization measurements to analyze physical and structural properties. Heat capacities provide an indirect measure of the vibrational, electronic, and magnetic energies to test the models. XRD and TEM were used to study the crystal structure, size, phase purity, and morphology. EELS provided information on the bonding, oxidation states, coordination numbers, and local geometries. TGA was used to provide stoichiometries of surface adsorbed water as well as metal to oxygen stoichiometries in some metal oxides. Magnetization measurements were used to determine susceptibility as a function of temperature of the magnetic phases in CuO nanoparticles. This chapter gives an overview of these techniques, but several

references are given that provide significantly more details on the mechanics and applications of each technique.

2.2 Heat Capacities

Four general techniques exist for measuring heat capacity data: adiabatic or semi-adiabatic pulse, continuous heating, AC, and relaxation. Each of these techniques has its own unique advantages and disadvantages. The adiabatic techniques are generally the most accurate, but large amounts of sample are required, which tends to make measurement times very long. The continuous heat technique is quite accurate and is good for measurements in which the heat capacity does not change much with temperature (typically high temperatures), but this technique also requires large amounts of sample. The advantage and disadvantages of the AC method are essentially opposite to those of the previous two methods in that much smaller samples can be used, but the data are not very accurate. Relaxation methods are perhaps the most versatile or all-around applicable. They can accommodate small amounts of sample, have good accuracy, and reasonable precision, but relaxation methods are typically poor for analyzing pronounced features in the heat capacity data such as first-order transitions.[1-2]

2.2.1 Physical Properties Measurement System (PPMS)

All of the heat capacity measurements performed for this dissertation were carried out on a Quantum Design Physical Propertied Measurement System (PPMS) which uses the relaxation technique.[3-5] The basic principles of operation are similar to the other heat capacity techniques in that a known amount of heat is added to or removed from the sample, and the change in temperature is measured. The PPMS adds a known amount of heat by applying a constant power

for a specified time, and the sample is then allowed to cool for the same amount of time. The resultant data is then fit to a function that produces the heat capacity at constant pressure C_p:[5-6]

$$C_p = \frac{-K_w(T - T_b) + P(t)}{dT/dt} \tag{2-1}$$

where K_w is the thermal conductance of the supporting wires, T is the sample temperature, T_b is the (reference) temperature of the puck frame, $P(t)$ is the power applied by the heater, and t is time. The heater and thermometer are attached to the platform that holds the sample, which is thermally connected with Apiezon grease, as shown in Figure 2-1.

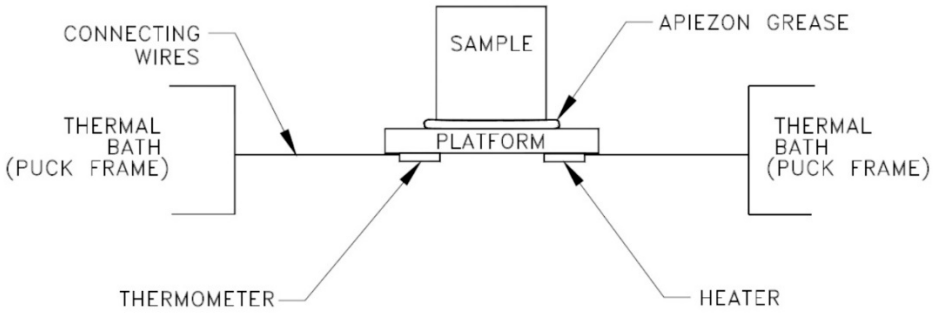

Figure 2-1: Sample Platform of PPMS Showing the Heater and Thermometer in Relation to the Sample (from PPMS manual[3]).

The PPMS itself consists of a large dewar for holding the cryogens and a sample probe that houses the superconducting magnet, the electronics, and the temperature control devices. A simple diagram of the main PPMS components is shown in Figure 2-2. Figure 2-3 shows the various components of the sample probe.

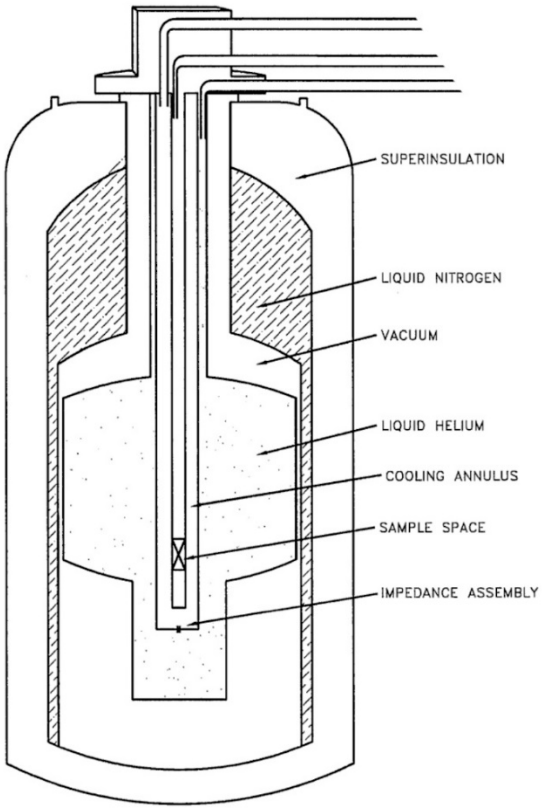

Figure 2-2: Simplified Schematic of the PPMS (from PPMS manual[4])

2.2.2 Data Analysis

Collecting a single heat capacity data point at a single temperature consists of a measurement that takes from a few seconds at low temperatures to an hour or more at high temperatures. Power (heat) and temperature data are collected at each temperature specified by the user between about 1.8-400 K. Figure 2-4 shows a typical relaxation curve that is fit to Eq. 2-1 (or some variation of Eq. 2-1) to produce a single heat capacity point.

Typically the amount of physical features that can be observed in a sample increases (as temperature decreases) with orders of magnitude of temperature (i.e. 1-10 K contains different data from 10-100 K, which contains different information from 100-1000 K). Because of this,

the density of data points is typically higher at low temperatures and decreases as temperature increases. Figure 2-5 shows the data of a typical heat capacity measurement.

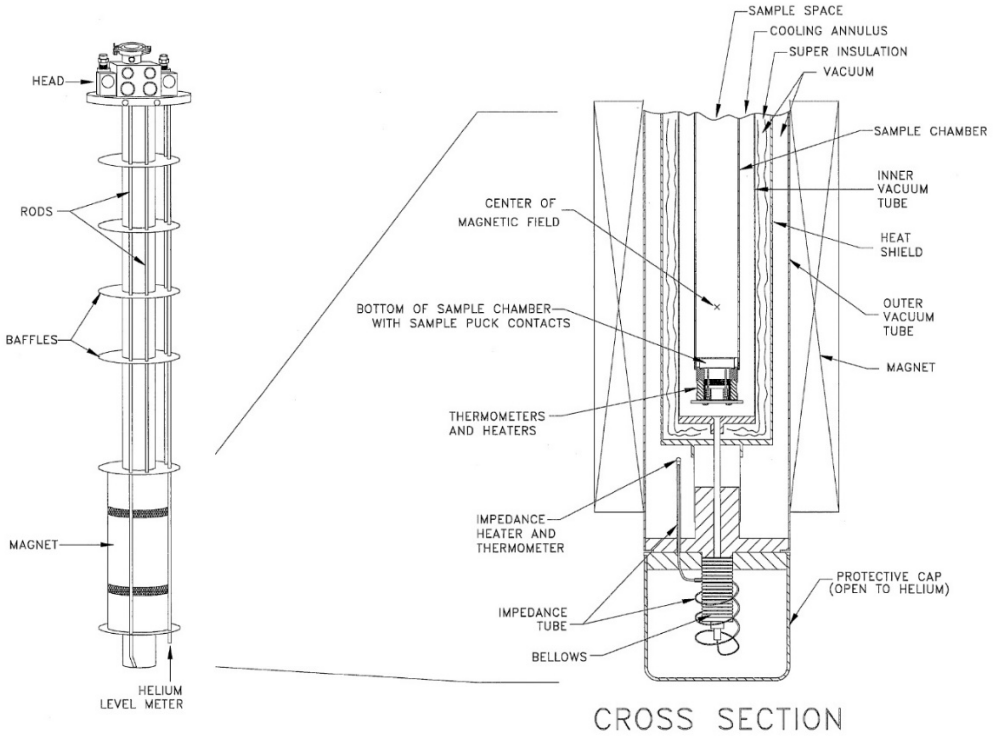

Figure 2-3: PPMS Sample Probe (from PPMS manual[4])

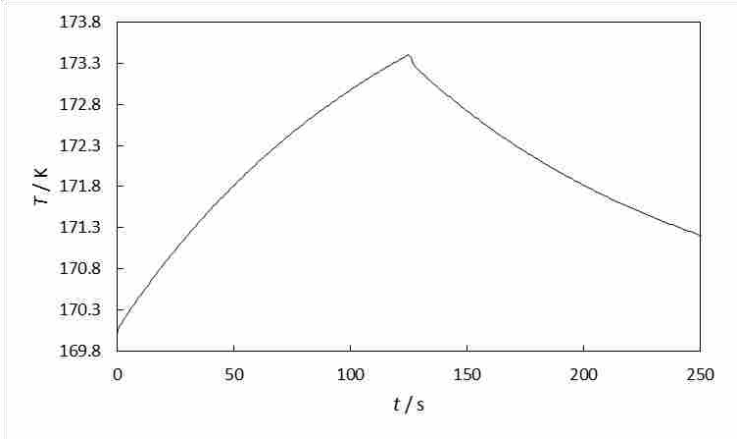

Figure 2-4: Relaxation curve for a typical heat capacity measurement

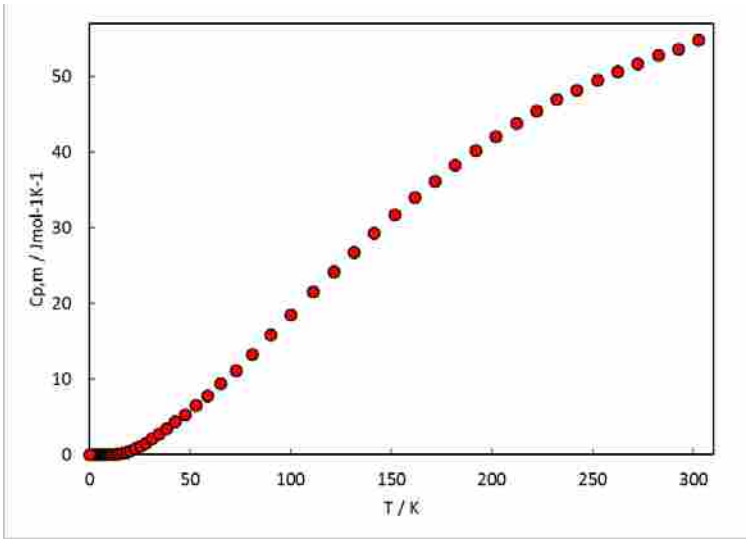

Figure 2-5: Heat Capacity of a Bulk Rutile TiO_2 Standard Collected on a PPMS

Because the heat capacity data collected on a PPMS span three orders of magnitude, typical data contain roughly three different temperature regions that each contain different information.[2] High-temperature data (higher than about 30 or 50 K) typically contain only information on vibrational properties in the absence of phase transitions. Low-temperature data (generally below 10 or 15 K) contain information on all the measureable heat capacity features a sample has such as vibrational, electronic, magnetic, superconducting, etc. The physical features in the mid-temperature data between these two extremes are usually too complicated to glean any useful information as has been discussed in chapter 1.

The general analysis of heat capacity data involves fitting a specific temperature range of data to functions.[7-9] To get the most information from the heat capacity data, these functions should be based on theoretical models such as has been discussed in chapter 1 and will be discussed in greater detail throughout the remainder of this dissertation; however, simple polynomial functions can be used to analyze heat capacity data. Fitting the mid-temperature region with polynomials has been done throughout this dissertation.

Because the low-temperature region can have many different contributions to the heat capacity, there are many possible functions that can possibly model the data. The specifics of each function will not be discussed in this portion of the dissertation but will be reserved for the subsequent chapters. The basic theory behind fitting low-temperature data, however, will be beneficial to the reader. Typical samples will have multiple low-temperature heat capacity contributions and as such will require data to be fit with a linear combination of the functions that describe each contribution. Because the number of possible fitting functions is $O(10^1)$, the number of possible combinations of such functions is $O(10^3)$; therefore, to avoid the need to sift through so many different fits, having some preliminary knowledge about the features that might be found in the sample is helpful in identifying what functions and combinations of functions to use. This problem can also be simplified with the use of modern programming and data analysis techniques, so data can quickly be fit to many combinations of functions, and bad fits can be identified and discarded.

Fitting high-temperature data is generally less arbitrary and more straightforward since vibrations are usually the only feature in this temperature range;[10] however, many transitions occur in this approximate region as will be seen in the chapters that will follow.[11] Analyzing data with a transition can be done in several ways, but a common basic principle is subtracting the lattice contribution from the total to give just the heat capacity of the transition. Perhaps the easiest way to do this is to fit the data around the transition to the traditional functions and just extrapolate that data into the transition region. This vibrational/lattice heat capacity can then be subtracted from the total heat capacity to produce the heat capacity of the transition. Another way to determine the lattice heat capacity is to find (or collect) heat capacity data of a similar sample (structure and properties) that does not have a transition and scale that heat capacity data

by the differences in mass.[2] The last common method is to measure or calculate the vibrational DOS of the sample and determine the lattice heat capacity from that. Because the bare transition data are often too sophisticated for modeling, they are typically fit with a cubic spline function.

With the various functions and their temperature ranges of validity, thermodynamic data such as entropies and enthalpies can then be determined using common thermodynamic definitions:[2, 12]

$$S(T) = \int_0^T \frac{C_v}{T} dT \tag{2-2}$$

and

$$H(T) = \int_0^T C_p dT \tag{2-3}$$

These functions give the absolute entropy and enthalpy from the heat capacity data.[13] Absolute entropies are the values found in textbooks and tables, but enthalpies are usually not published as absolute values but rather as relative values. As such, enthalpies derived from heat capacities have limited use compared to the easily determined *relative* enthalpies of formation.

2.3 X-ray Diffraction

X-ray diffraction (XRD) is a valuable technique for the study of materials for many reasons. It is a relatively fast, simple, and nondestructive technique that can be used to determine crystal structure, lattice parameters, particle size (and morphology to some degree), phase, and phase composition (including the degree of amorphicity).

To produce the X-rays impinging on a sample, high-energy electrons are collided with a metal to eject core-level electrons from the atomic nuclei. Electrons that occupy higher energy levels in the ionized metal atoms then drop down to the vacant core level and release X-ray

photons in the process. The energies/frequencies of these X-rays are dependent on the metal. Copper is a typical metal and produces K_α (a 2p electron drops into the vacant 1s state) X-rays with a wavelength of 1.5418 Å. The X-rays are typically filtered with a monochromator, pass through various optics to reach the sample, and the diffracted X-rays are then collected and analyzed.

The information gained from XRD comes from the diffraction of the X-rays in the material being investigated. When monochromatic X-rays interact with a crystal lattice, they are diffracted at all angles, but because diffracted photons will destructively or constructively interfere at angles that correspond to the angles and distances between the atoms, peaks at angles characteristic of each sample appear in a diffraction pattern as seen in Figure 2-6 below. It is noted that Figure 2-6 shows the diffraction profile of a powder sample (all samples in this work were powders), but a single crystal produces a three dimensional plot of intensity with two spacial axes.

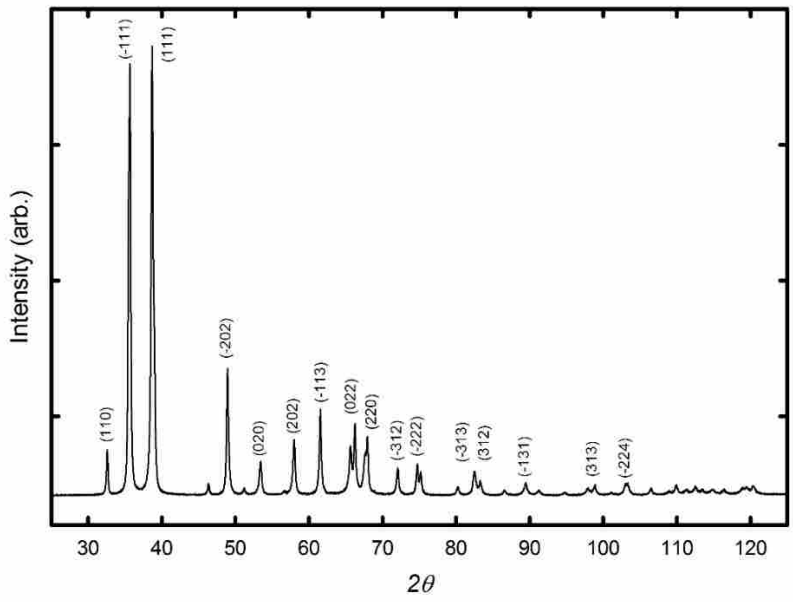

Figure 2-6: Powder X-ray Diffraction Pattern of CuO Nanoparticles

The diffraction pattern is unique for each crystalline structure. A crystal consists of repeating groups of atoms called a unit cell; thus, the unit cell that typically consist of a few atoms can describe the entire crystal that is made up of $O(10^{20})$ atoms by translation of that unit cell in 3 dimensions. Figure 2-7 shows the translation of a body-centered cubic unit cell, which is one of the 14 possible Bravais lattices. The unit cell can have any of these general shapes in which the axes have different lengths and the corners have different angles. These lengths and angles (called lattice parameters) are dependent on the atomic nature and bonding of the component atoms; therefore, diffraction patterns are typically unique for every material, though similar materials can have similar diffraction patterns.

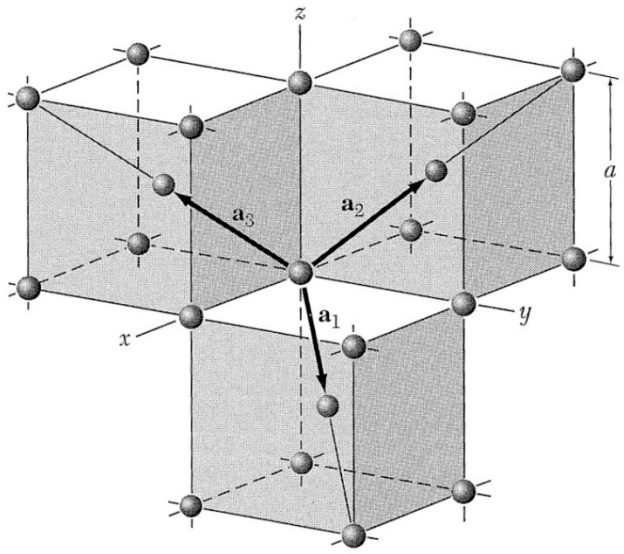

Figure 2-7: Unit Cell Translation Vectors of the Body Centered Cubic Lattice. (from Kittel[14])

It is instructive to note the conventions for discussing directions and orientations in a crystal lattice. In a 3D lattice, there are three axes and three angles. The simplest structure is the cubic structure that has all axes equal and all angles equal, $a = b = c$ and $\alpha = \beta = \gamma = 90°$ (hence

the name “cubic”). The direction within a crystal is defined by the vector that points from the origin of the three intersecting axes towards the atom of interest [*a*,*b*,*c*]. For example, the [1,1,1] direction is the vector that cuts through the center of the cube to point at the corner opposite of the origin. The plane of atoms normal to this vector can be described by the reciprocal of these values and is denoted as (*h*,*k*.*l*) (note the distinction between the brackets for direction and parentheses for the plane normal to that direction). Figure 2-8 shows several examples of such planes called Miller indices.

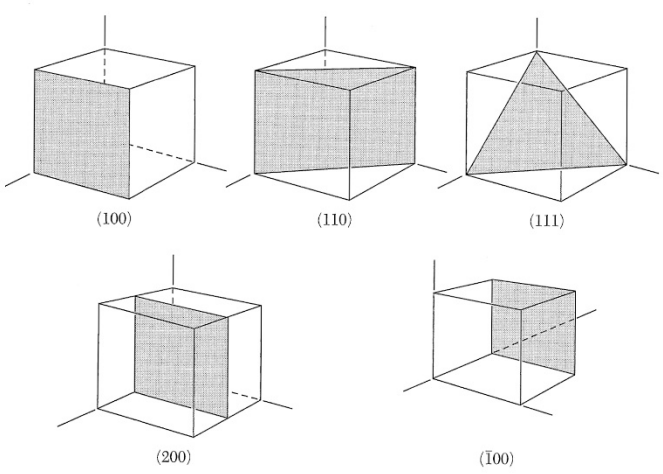

Figure 2-8: Miller Indices of Significant Planes in a Cubic Crystal. (from Kittel[14])

X-rays can interact with each of the atoms whether on the corners, faces, edges, or body-center. When the diffracted X-rays constructively interfere, a diffraction peak is observed. The constructive interference occurs under the Bragg condition:

$$n\lambda = 2d\ sin(\theta) \tag{2-4}$$

where n is an integer, λ is the wavelength of the impinging light, d is the spacing between lattice planes, and θ is the angle formed between the light and the surface. Figure 2-9 shows the

geometry of the Bragg condition. Basically, for constructive interference to occur, the length of BA_2 plus A_2C must equal an integer number of wavelengths of the impinging radiation. Figure 2-10 shows how diffraction occurs at various angles using the concept of Huygen wavelets. The diffracted peak in XRD is measured as a large intensity at the angles that satisfy the Bragg condition for the crystal structure of the material.

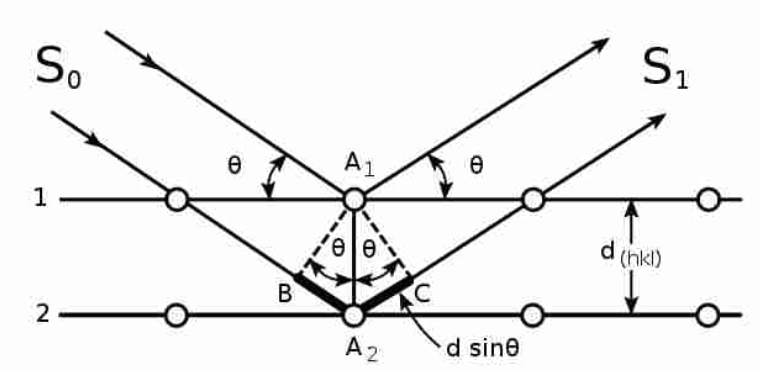

Figure 2-9: Bragg Diffraction from a Simple Lattice

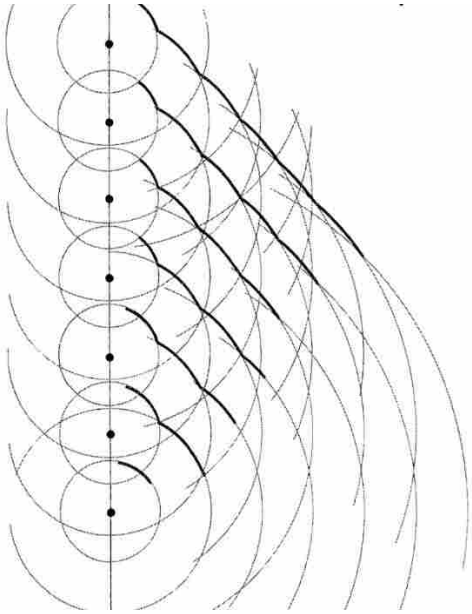

Figure 2-10: Sets of Huygen Wavelets Emitted from a Line of Coherent Point Sources. (from Hecht[15])

The most basic analysis of XRD data is for phase identification using the peak positions compared to those of a standard reference material of the same phase and composition. Extracting other information requires more sophisticated analysis. One of the less rigorous analyses is profile fitting. This procedure separately fits each peak in the data set to a sum of various statistical functions (Gaussian, Lorentzian, and Cagliotti). The width of the peak (when corrected for instrument broadening) gives information on the particle size and micro-strain. The positions of the peaks can give *d*-spacing, but this method is not very accurate. The most accurate method for determining all of these properties as well as the other properties mentioned above is through a Rietveld refinement. This process involves calculating the position and intensity of all diffraction peaks from the known crystal structure. The crystal structure and various other parameters are then slightly altered to make the theoretical diffraction pattern match the actual diffraction pattern. Although often tedious, Rietveld refinement significantly expands the usefulness of XRD and the amount of quantitative information that can be procured from it.

2.4 Transmission Electron Microscopy

The many imaging and analytical techniques afforded with transmission electron microscopy (TEM) are another invaluable technique for understanding and investigating solids.[16] Because electrons in a TEM have much smaller wavelengths than visible light, the spatial resolution of an image on the TEM can be less than an Angstrom, or diffraction patterns can be collected from sub-Angstrom regions of sample; whereas, the resolution of an optical microscope is limited to a few hundred nanometers. This makes TEM essential for imaging nanomaterials or any features with a nano scale.

The basic features of a TEM are the electron beam source, electromagnetic lenses, the sample stage, and something to collect and interpret the emergent electrons such as a CCD camera. Figure 2-11 shows the basic schematic of a modern TEM. Because the strength of the various lenses is adjustable, the beam can be focused in different ways to produce different images, specifically images of diffracted electrons and actual images of the sample.

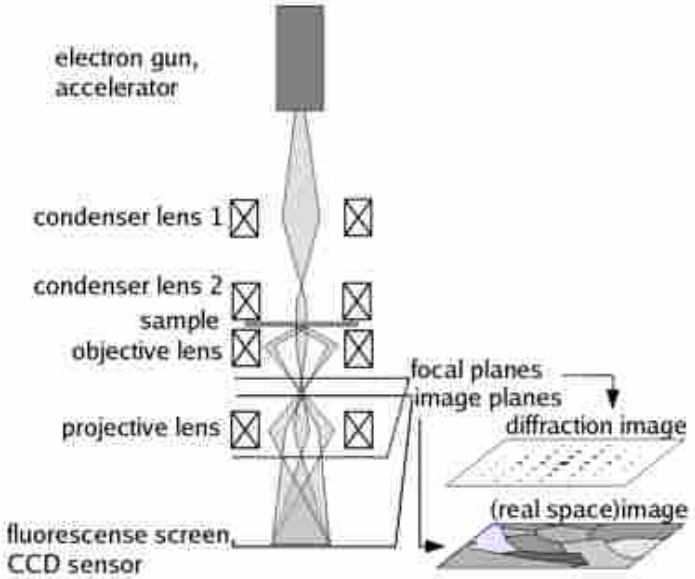

Figure 2-11: Schematic of a TEM

Electron diffraction occurs as electrons interact with the sample just as X-rays diffract from the sample lattice. Various modes of diffraction can be employed to produce different images on a TEM. Figure 2-12 shows that the difference between diffraction and imaging mode on the TEM is just a matter of where in the column the beam is focused. As the figure shows, imaging the sample actually requires the beam to be defocused on the screen.

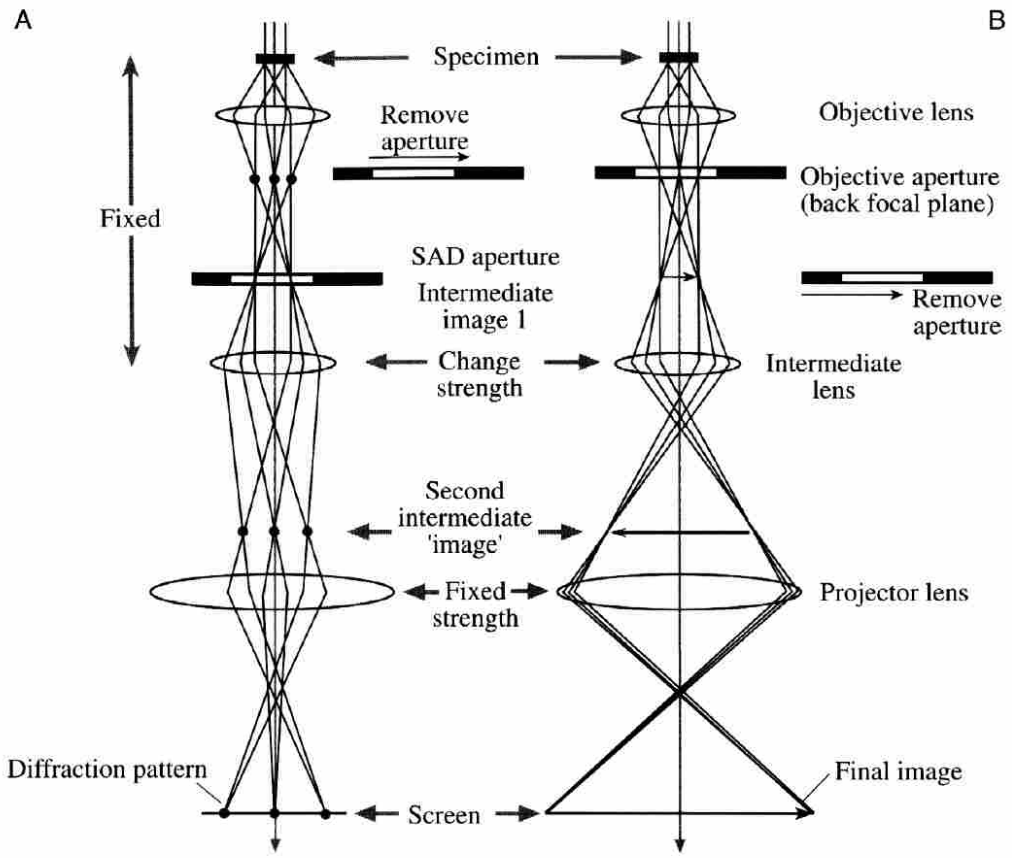

Figure 2-12: The Two Basic Forms of TEM Experiments: a) Diffraction, b) Imaging (from Williams and Carter[16])

Forming basic images on the TEM is often called parallel beam mode since the beam is not convergent when it passes through the sample; however, the beam can also be focused onto the sample, rastered across a selected area of sample, and the diffracted beam used to form an image. This latter method is called scanning TEM (STEM) and is capable of forming images with higher resolution than typical parallel beam images.

Diffraction patterns similar to those collected on an XRD can also be collected. Figure 2-13 shows the diffraction patter of a single crystal of Si. Powder samples have similar features, but because each crystallite is oriented randomly, rings are formed instead of spots. The unique

strength of diffraction on the TEM is not necessarily the diffraction pattern itself but that an image can be taken of a single diffracting beam. Dark field imaging utilizes this feature and can produce images of grains with a single orientation to show the randomness of the orientations. Hollow-cone dark field imaging can show all crystallites that diffract at a specified angle, which is useful for identifying phase impurities and amorphous material and then removing them from the images.

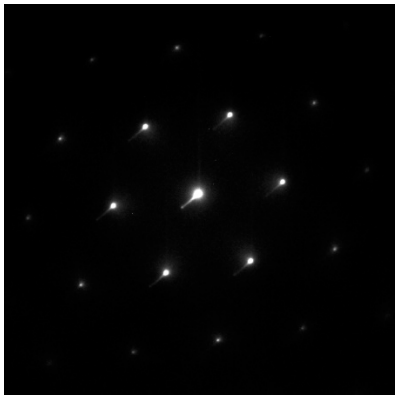

Figure 2-13: Diffraction Pattern of Single Crystal Si Along the [111] Direction.

There are many other ways that electrons can interact with a sample. Figure 2-14 shows the possible interactions, though the intensity of each varies significantly which can limit their use. These interactions can be summarized into three types of interactions: no interaction, elastic (no energy change of electrons), and inelastic (electrons lose energy to sample). Most imaging and diffraction techniques are performed with the elastically scattered electrons to produce mass contrast, bright field, dark field, hollow-cone dark field, high-resolution images, STEM, and various forms of diffraction patterns. The analytical techniques, such as X-ray energy dispersive spectroscopy (XEDS) and electron energy-loss spectroscopy (EELS), use the inelastically

scattered electrons and require more equipment to separate photons and electrons with different energies.

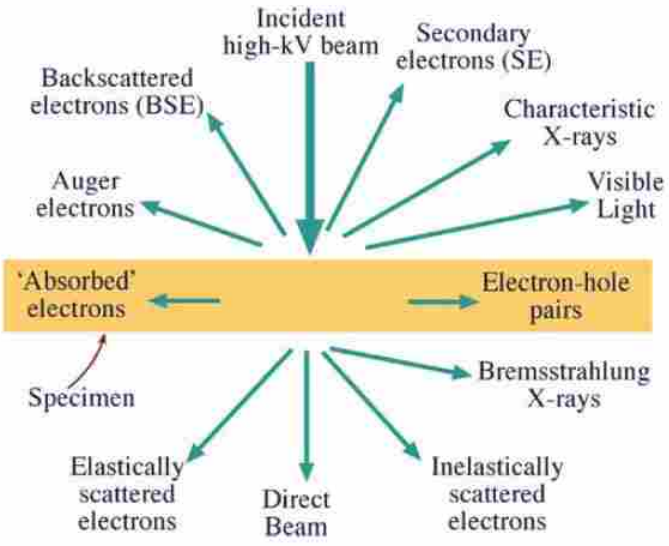

Figure 2-14: Types of Electron-Sample Interactions (from Williams and Carter[16])

2.5 Electron Energy Loss Spectroscopy

Although most electron energy-loss spectroscopy is performed inside a TEM, it is significantly unique from most other TEM methods to be a technique of its own. The basic principle behind EELS is collecting and analyzing the inelastically scattered electrons that have lost energy to the sample in some way and will therefore have a lower energy than that of the elastically scattered electrons (which are by far the most abundant).[17-18] Thus, EELS can be viewed as a measure of the unoccupied DOS since it measures transitions from the ground state to excited, unoccupied states. The various energy regions of EELS provide information on which specific energy-loss processes occur. Figure 2-15 shows the EELS spectrum of NiO and includes all regions of interest.

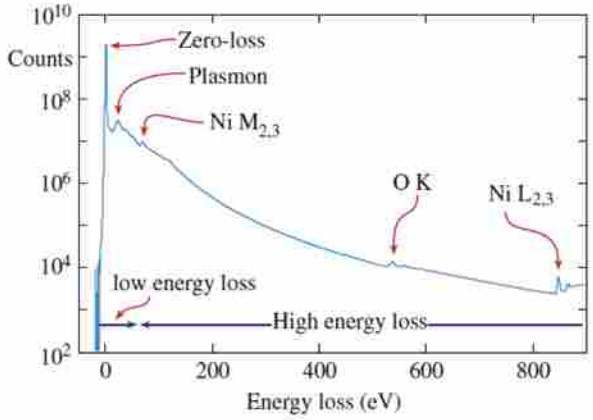

Figure 2-15: EELS Spectrum of NiO from Energy-loss Values of about 0 eV to about 900 eV (from Williams and Carter[16])

Elemental analysis, or chemical fingerprinting, is perhaps the easiest and most common EELS method. This method is similar to just obtaining phase information from XRD data, but instead of information on phases, elemental analysis give information on chemical composition. This is done by comparing the peaks observed in the acquired data to peaks of standard reference materials specific to each element.[18-19] Spectral comparison is often sufficient to identify the type of elements present in a sample.[20-27] Other information such as oxidation state and coordination number can also be obtained by comparing one's acquired spectrum to spectra of known samples of different oxidation state or coordination, though such data is not always available, in which case, a more detailed understanding of the causes for peak shapes is required to interpret such features and properties.

In general, there are two regions in an EELS spectrum that arise from different features of a sample's electronic character: low-loss and high-loss. The low-loss region is typically taken as all data below about 50 eV. This region includes the zero-loss peak (ZLP), which is the most intense feature since it contains all the electrons that did not undergo inelastic interactions.

Slightly above the ZLP (about 5-30 eV) is a very broad peak called the plasmon peak.[28-32] Plasmons occur when an electron from the beam interacts with the electrons in the conduction or valence band of the material and causes an excitation or vibration of the entire electron cloud around the solid structure. Most plasmons occur within the bulk of the material and represent three dimensional waves, while surface plasmons only occur on the surface of a material like ripples of water on the surface of a pond making them quite prevalent in nanoparticles.[16, 33] The low-energy loss peaks (also called edges) around 2-20 eV are the result of interband and intraband transitions. The low-loss data also contains information on dielectric constants and band gaps since these involve valence electrons which require much less energy to remove than core electrons.[18, 34-36]

The energy-loss region above about 50 eV contains information on core-level excitations and ionizations. Most elemental analysis uses this region of data, but, as mentioned above, much more information can be obtained from an understanding of the peak shapes. Two methods deal with interpreting peak shapes to provide useful information: energy-loss near-edge structure (ELNES) and extended energy-loss fine structure (EXELFS), which are analogous to the X-ray techniques X-ray absorption near-edge structure (XANES) and extended X-ray absorption fine structure (EXAFS), respectively. Figure 2-16 shows a peak that exhibits the features found in ELNES and EXELFS.

These methods are perhaps the most complicated methods of EELS because they involve rigorous calculations; however, they don't require the comparison to other spectra and the resultant information is very valuable. From these two techniques, information on how atoms are bonded, the coordination of those specific atoms, and their density of states can be generated. One can also determine an atom's radial distribution function, observe the anisotropy of chemical bonds, and create maps and images of all of these features.[16] Few other methods exist

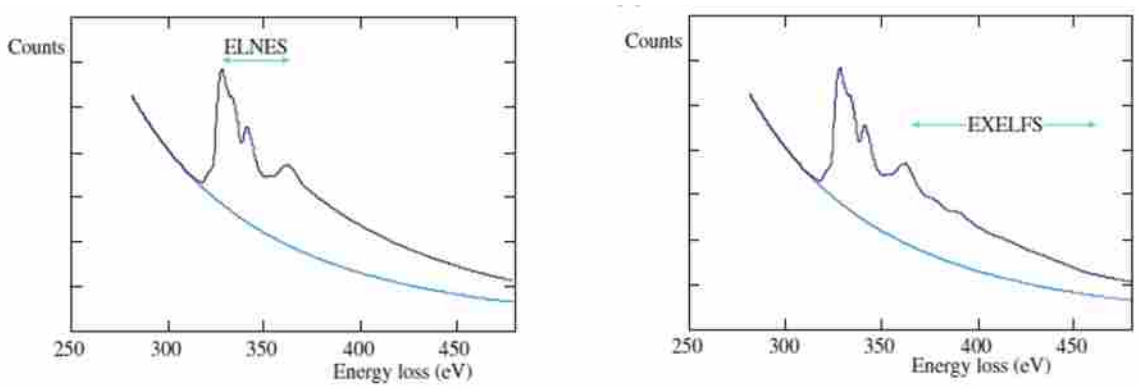

Figure 2-16: EELS Spectrum Showing ELNES (left) and EXELFS (right) Features of an Ionization Edge (from Williams and Carter[16]).

for obtaining this information, and they usually require expensive instrumentation and high energy electron, neutron, or x-ray beams. Although the quantum physics required to thoroughly understand these methods is beyond the scope of this work, a basic introduction will be valuable for understanding the analysis of such data presented in chapter 6.

Basically, the energy of an ionized electron in excess of the ionization energy is modeled as a wave. If the wave has a small energy (a few eV) then it undergoes plural, elastic scattering from the surrounding atoms. As the excess energy is increased the wave interacts with atoms farther from the ionized atom. These interactions are seen as small intensity variations in an ionization edge (see Figure 2-16). These variations represent an empty density of states which can be compared to standards or used for calculations. The calculations involve carefully removing the background signal, Fourier transforms, and inverse Fourier transforms to produce a radial probability distribution. Such calculations have provided many researchers with incredibly detailed information about bonding and coordination.[37-52].

2.6 Thermogravimetric Analysis

Thermal analysis in general is the study of how various material properties change with temperature and is typically used to provide information on enthalpy, heat capacity, mass change, coefficient of heat expansion, solid-state reactions, thermal degradation, and phase transitions.[53] Thermogravimetric analysis (TGA), which is usually coupled with differential thermal analysis (DTA), is performed in a furnace that has a purge gas flowing over the sample (usually in an inert cup). The mass of the sample is constantly measured to give the TGA signal, and thermocouples measure the temperature difference between the sample and a reference to give the DTA signal.

TGA is a very basic method in that it simply measures mass; however, mass changes that occur as temperature changes, such as decomposition or desorption of an adsorbed or absorbed gas, can be indicative of various properties of a material. These changes in mass indicate a change in composition of the material. TGA has been used in this work mostly for identifying the amount of surface adsorbed water on nanoparticles, though metal-oxide stoichiometry was also determined using a temperature programed reduction (TPR) in hydrogen gas for various samples.

DTA is somewhat more sophisticated, though it is still a basic method. In DTA experiments, the sample and an inert reference undergo identical thermal cycles (typically concomitantly). The instrument measures their temperature difference (determined by the voltage on the thermocouples), and the difference provides information on any process that would cause the sample to change temperature faster than the reference such as adsorption (exothermic), desorption (endothermic), crystallization (exothermic), melting (endothermic), or

phase transitions (endo- or exothermic). DTA can also provide heat capacities with the correct experimental setup as in differential scanning calorimetry (DSC).

2.7 VSM

Magnetization can be measured on the PPMS using the vibrating sample magnetometry (VSM) option.[4] This method uses a large motor that the sample is attached to and hangs from. The sample hangs in the center of a wire coil that is placed within the superconducting magnet field. The motor vibrates the sample, and the oscillating field of the sample induces an electrical response in the coil that is converted into a magnetic moment.[14, 54] In the PPMS, the magnetic moment can be measured as a function of temperature from 2-400 K or as a function of external field from 0-9 T.

2.8 Summary

These methods all provide a significant understanding of the chemical, physical, and structural properties of the materials that will be presented herein. Although many other techniques exist that could potentially provide more specific information to each technical problem, these techniques have been found to be generally applicable and valuable for material characterization.

REFERENCES

1. Woodfield, B. F. Specific-Heat of High-Temperature Superconductors: Apparatus and Measurements. University of California at Berkeley, 1995.

2. Gopal, E. S. R., *Specific Heats at Low Temperatures*; Plenum Press New York, 1966; Vol. 227.

3. Quantum Design, P., Ppms Heat Capacity Option User's Manual. *Quantum Design* **2004**.

4. Quantum Design, P., Hardware and Options Manual. *Quantum Design* **2004**.

5. Lashley, J.; Hundley, M.; Migliori, A.; Sarrao, J.; Pagliuso, P.; Darling, T.; Jaime, M.; Cooley, J.; Hults, W.; Morales, L., Critical Examination of Heat Capacity Measurements Made on a Quantum Design Physical Property Measurement System. *Cryogenics* **2003**, *43*, 369-378.

6. Hwang, J. S.; Lin, K. J.; Tien, C., Measurement of Heat Capacity by Fitting the Whole Temperature Response of a Heat-Pulse Calorimeter. *Review of Scientific Instruments* **1997**, *68*, 94-101.

7. Schliesser, J.; Woodfield, B., Development of a Debye Heat Capacity Model for Vibrational Modes with a Gap in the Density of States. *Journal of physics. Condensed matter: an Institute of Physics journal* **2015**, *27*, 285402-285402.

8. Schliesser, J. M.; Woodfield, B. F., Lattice Vacancies Responsible for the Linear Dependence of the Low-Temperature Heat Capacity of Insulating Materials. *Physical Review B* **2015**, *91*, 024109.

9. Snow, C. L.; Shi, Q.; Boerio-Goates, J.; Woodfield, B. F., Heat Capacity Studies of Nanocrystalline Magnetite (Fe3o4). *The Journal of Physical Chemistry C* **2010**, *114*, 21100-21108.

10. Kelley, K. K.; King, E. G., *Entropies of the Elements and Inorganic Compounds*; US Government Printing Office, 1961; Vol. 592.

11. Schliesser, J. M.; Huang, B.; Sahu, S. K.; Navrotsky, A.; Woodfield, B. F., Experimental Heat Capacities, Excess Entropies, and Magnetic Properties of Bulk and Nano Fe3o4-Co3o4 and Fe3o4-Mn3o4 Spinel Solid Solutions. *Journal of Physical Chemistry C* **2016**.

12. Levine, I. N., *Physical Chemistry*; McGraw-Hill, 2008.

13. McQuarrie, D., Statistical Mechanics. *University Science, Sausalito, USA* **2000**, 641.

14. Kittel, C.; McEuen, P.; McEuen, P., *Introduction to Solid State Physics*; Wiley New York, 1976; Vol. 8.

15. Hecht, E., Optics Fourth Edition,(2003). and.

16. Williams, D. B.; Carter, C. B., *The Transmission Electron Microscope*; Springer, 1996.

17. Egerton, R. F., Electron Energy-Loss Spectroscopy in the Tem. *Reports on Progress in Physics* **2009**, *72*, 016502.

18. Egerton, R. F., *Electron Energy-Loss Spectroscopy in the Electron Microscope*; Springer, 2011.

19. Ahn, C.; Krivanek, O., *Eels Atlas*; Gatan, 1983.

20. Botton, G.; Gupta, J.; Landheer, D.; McCaffrey, J.; Sproule, G.; Graham, M., Electron Energy Loss Spectroscopy of Interfacial Layer Formation in Gdo Films Deposited Directly on Si (001). *Journal of Applied Physics* **2002**, *91*, 2921.

21. Bertoni, G.; Beyers, E.; Verbeeck, J.; Mertens, M.; Cool, P.; Vansant, E. F.; Van Tendeloo, G., Quantification of Crystalline and Amorphous Content in Porous Samples from Electron Energy Loss Spectroscopy. *Ultramicroscopy* **2006**, *106*, 630-635.

22. Egerton, R. F., K-Shell Ionization Cross-Sections for Use in Microanalysis. *Ultramicroscopy* **1979**, *4*, 169-179.

23. Egerton, R. F., Oscillator-Strength Parameterization of Inner-Shell Cross Sections. *Ultramicroscopy* **1993**, *50*, 13-28.

24. Hofer, F.; Golob, P.; Brunegger, A., Eels Quantification of the Elements Sr to W by Means of M45 Edges. *Ultramicroscopy* **1988**, *25*, 81-84.

25. Rez, P., Electron Ionization Cross Sections for Atomic Subshells. *Microscopy and Microanalysis* **2003**, *9*, 42-53.

26. Taftø, J.; Krivanek, O. L., Site-Specific Valence Determination by Electron Energy-Loss Spectroscopy. *Physical Review Letters* **1982**, *48*, 560-563.

27. Tan, H.; Turner, S.; Yücelen, E.; Verbeeck, J.; Van Tendeloo, G., 2d Atomic Mapping of Oxidation States in Transition Metal Oxides by Scanning Transmission Electron Microscopy and Electron Energy-Loss Spectroscopy. *Physical Review Letters* **2011**, *107*, 107602.

28. Batson, P. E., Surface Plasmon Coupling in Clusters of Small Spheres. *Physical Review Letters* **1982**, *49*, 936-940.

29. Ding, Y.; Wang, Z. L., Electron Energy-Loss Spectroscopy Study of Zno Nanobelts. *Journal of electron microscopy* **2005**, *54*, 287-291.

30. Hunt, J. A.; Disko, M. M.; Behal, S. K.; Leapman, R. D., Electron Energy-Loss Chemical Imaging of Polymer Phases. *Ultramicroscopy* **1995**, *58*, 55-64.

31. Muller, D. A.; Silcox, J., Delocalization in Inelastic Scattering. *Ultramicroscopy* **1995**, *59*, 195-213.

32. Oleshko, V. P.; Howe, J. M., In Situ Determination and Imaging of Physical Properties of Metastable and Equilibrium Precipitates Using Valence Electron Energy-Loss Spectroscopy and Energy-Filtering Transmission Electron Microscopy. *Journal of Applied Physics* **2007**, *101*, 054308-054308-5.

33. Williams, D. B.; Edington, J. W., High Resolution Microanalysis in Materials Science Using Electron Energy Loss Measurements. *Journal of Microscopy* **1976**, *108*, 113-145.

34. Erni, R.; Browning, N. D., The Impact of Surface and Retardation Losses on Valence Electron Energy-Loss Spectroscopy. *Ultramicroscopy* **2008**, *108*, 84-99.

35. Kimoto, K.; Kothleitner, G.; Grogger, W.; Matsui, Y.; Hofer, F., Advantages of a Monochromator for Bandgap Measurements Using Electron Energy-Loss Spectroscopy. *Micron* **2005**, *36*, 185-189.

36. García de Abajo, F. J.; Kociak, M., Probing the Photonic Local Density of States with Electron Energy Loss Spectroscopy. *Physical Review Letters* **2008**, *100*, 106804.

37. Batson, P. E., Carbon 1s near-Edge-Absorption Fine Structure in Graphite. *Physical Review B* **1993**, *48*, 2608-2610.

38. Batson, P. E., Silicon L2, 3 near-Edge Fine Structure in Confined Volumes. *Ultramicroscopy* **1993**, *50*, 1-12.

39. Botton, G. A., A New Approach to Study Bonding Anisotropy with Eels. *Journal of Electron Spectroscopy and Related Phenomena* **2005**, *143*, 129-137.

40. Bruley, J.; Williams, D. B.; Cuomo, J. J.; Pappas, D. P., Quantitative near-Edge Structure Analysis of Diamond-Like Carbon in the Electron Microscope Using a Two-Window Method. *Journal of Microscopy* **1995**, *180*, 22-32.

41. Brydson, R.; Sauer, H.; Engel, W.; Thomass, J. M.; Zeitler, E.; Kosugi, N.; Kuroda, H., Electron Energy Loss and X-Ray Absorption Spectroscopy of Rutile and Anatase: A Test of Structural Sensitivity. *Journal of Physics: Condensed Matter* **1989**, *1*, 797.

42. Grunes, L. A.; Leapman, R. D.; Wilker, C. N.; Hoffmann, R.; Kunz, A. B., Oxygen K near-Edge Fine Structure: An Electron-Energy-Loss Investigation with Comparisons to New Theory for Selected 3d Transition-Metal Oxides. *Physical Review B* **1982**, *25*, 7157-7173.

43. Kurata, H.; Lefèvre, E.; Colliex, C.; Brydson, R., Electron-Energy-Loss near-Edge Structures in the Oxygen K-Edge Spectra of Transition-Metal Oxides. *Physical Review B* **1993**, *47*, 13763-13768.

44. Mitterbauer, C.; Kothleitner, G.; Grogger, W.; Zandbergen, H.; Freitag, B.; Tiemeijer, P.; Hofer, F., Electron Energy-Loss near-Edge Structures of 3d Transition Metal Oxides Recorded at High-Energy Resolution. *Ultramicroscopy* **2003**, *96*, 469-480.

45. Wang, Z. L.; Yin, J. S.; Mo, W. D.; Zhang, Z. J., In-Situ Analysis of Valence Conversion in Transition Metal Oxides Using Electron Energy-Loss Spectroscopy. *The Journal of Physical Chemistry B* **1997**, *101*, 6793-6798.

46. Keast, V. J.; Bruley, J.; Rez, P.; Maclaren, J. M.; Williams, D. B., Chemistry and Bonding Changes Associated with the Segregation of Bi to Grain Boundaries in Cu. *Acta Materialia* **1998**, *46*, 481-490.

47. Kurata, H.; Colliex, C., Electron-Energy-Loss Core-Edge Structures in Manganese Oxides. *Physical Review B* **1993**, *48*, 2102-2108.

48. Leapman, R. D.; Kocsis, E.; Zhang, G.; Talbot, T. L.; Laquerriere, P., Three-Dimensional Distributions of Elements in Biological Samples by Energy-Filtered Electron Tomography. *Ultramicroscopy* **2004**, *100*, 115-125.

49. McComb, D. W.; Craven, A. J.; Hamilton, D. A.; MacKenzie, M., Probing Local Coordination Environments in High-K Materials for Gate Stack Applications. *Applied Physics Letters* **2004**, *84*, 4523-4525.

50. Muller, D. A.; Subramanian, S.; Batson, P. E.; Silcox, J.; Sass, S. L., Structure, Chemistry and Bonding at Grain Boundaries in Ni3al—I. The Role of Boron in Ductilizing Grain Boundaries. *Acta Materialia* **1996**, *44*, 1637-1645.

51. Ostanin, S.; Craven, A. J.; McComb, D. W.; Vlachos, D.; Alavi, A.; Paxton, A. T.; Finnis, M. W., Electron Energy-Loss near-Edge Shape as a Probe to Investigate the Stabilization of Yttria-Stabilized Zirconia. *Physical Review B* **2002**, *65*, 224109.

52. Sikora, T.; Hug, G.; Jaouen, M.; Rehr, J. J., Multiple-Scattering Exafs and Exelfs of Titanium Aluminum Alloys. *Physical Review B* **2000**, *62*, 1723-1732.

53. Gabbott, P., *Principles and Applications of Thermal Analysis*; John Wiley & Sons, 2008.

54. Housecroft, C. E.; Sharpe, A. G., *Inorganic Chemistry*; Pearson, 2012.

3 DEVELOPMENT OF A DEBYE HEAT CAPACITY MODEL FOR VIBRATIONAL MODES WITH A GAP IN THE DENSITY OF STATES

3.1 Introduction

Heat capacity measurements can provide valuable information about the various energetic contributions of a material. Many theories model these contributions by simplifying the energy levels of the system to a mean energy through statistical methods and then converting the simplified energy into a heat capacity.[1-2] Heat capacity data can then be fit with these theoretical heat capacity functions to extract valuable information about each energetic contribution of a system.

Typical contributions to the heat capacity of solids include vibrational, electronic, magnetic, superconducting, and even energy states associated with lattice vacancies.[1-5] The vibrational contribution dominates the heat capacity at all but low temperatures (below about 10 or 15 K) where the other contributions become observable. These contributions can be determined by fitting the low-temperature heat capacity data to many different combinations of these theoretical functions and selecting the best fit, but determining the fit that most correctly models the data and underlying energy contributions is not trivial.

The best fit is determined by its physical meaningfulness, the percent root mean squared deviation (%RMS), and a deviation plot. To be physically meaningful, the fit must be a sum of functions or terms that correspond to the physical properties of the system (e.g. the fit of a

nonmagnetic material should not contain a magnetic function), and the parameters should have a reasonable magnitude and be positive (with a few exceptions in the harmonic lattice expansion). The %RMS gives a gross approximation to the quality of the fit especially when comparing different fits of the same data. Generally, the best fit has the lowest %RMS, but fits of low precision data sets may have a deceptively low %RMS if a function is fitting the noise. The deviation plot overcomes this problem by showing how each data point deviates from the fit. Data points will deviate randomly from a good fit but systematically from a bad fit. Each of these aspects should be considered when determining the best fit of heat capacity data and, therefore, the underlying contributions.

We have measured the heat capacities of over thirty samples that should only have vibrational contributions but do not fit well with conventional vibrational heat capacity models. Each of these materials either have AO_4 tetrahedra or long chains, and their heat capacities exhibit a "boson peak", which is observed as a broad peak in the data plotted as C/T^3 versus ln T and is related to excess low-energy modes. The low-temperature data of these samples could not be reasonably fit using conventional models; therefore, we introduce a new model for the vibrational heat capacity of materials that have excess low-energy modes that also have a gap in the density of states (DOS). Fits to these data show significant improvement in both quality and meaningfulness when using this model. To provide a context for our model, we introduce several of the conventional models, but complete reviews of these theories are available elsewhere.[1-4]

3.1.1 Vibrational Heat Capacity

The largest contribution to the heat capacity of a solid generally comes from atomic and molecular vibrations, which are represented by the equation:[2]

$$C_V = k\int_0^{\infty} \frac{(h\nu/kT)^2 e^{-h\nu/kT} g(\nu) d\nu}{(1-e^{-h\nu/kT})^2} \tag{3-1}$$

where k is Boltzmann's constant, h is Planck's constant, ν is the frequency of oscillation, T is temperature, and $g(\nu)$ represents the vibrational DOS. For Eq. 3-1 to have a form that can be compared directly to heat capacity data, $g(\nu)$ must be known, but rather than determining the entire set of individual frequencies exactly, $g(\nu)$ can be generalized and simplified through various models that still yield heat capacity functions that agree reasonably well with experimental data.

Einstein modeled the atoms in a solid as independent harmonic oscillators vibrating at the same frequency ν_E thereby modeling the DOS as a delta function (shown in Figure 3-1). Using the delta function as $g(\nu)$ in Eq. 3-1 results in the Einstein heat capacity:[2]

$$C_E = 3Nk\left(\frac{\theta_E}{T}\right)^2 \frac{e^{\theta_E/T}}{(e^{\theta_E/T}-1)^2} \tag{3-2}$$

where N is the number of atoms, and the Einstein temperature is defined as $\theta_E = h\nu_E/k$. This simple DOS model sometimes provides adequate correlation with experimental heat capacity measurements at high temperatures but fails at low temperatures where it approximates to[1]

$$C_E(T \ll \theta_E) = 3Nk\left(\frac{\theta_E}{T}\right)^2 e^{-\theta_E/T} \tag{3-3}$$

Although this model often fails, it has been useful for modeling optical modes,[1] and dispersion in acoustic modes,[6] while others have used a sum of multiple Einstein functions to model heat capacity data well.[7]

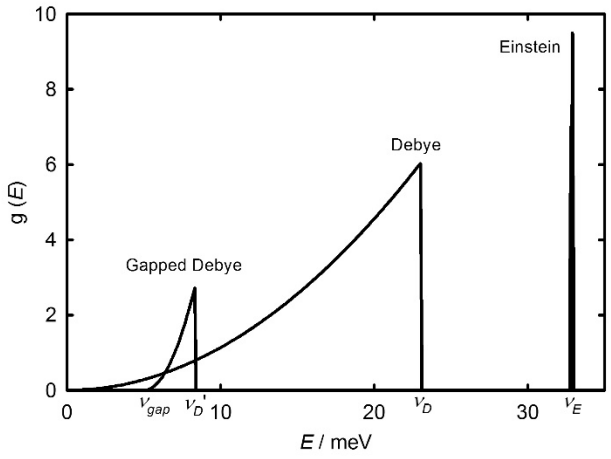

Figure 3-1: Generic DOS Models Showing Debye, Einstein, and Gapped Debye (Subject of this Chapter) Models. The various characteristic energies are also shown.

Debye modeled the vibrations in a solid as normal mode vibrations of a continuous elastic body, which works well for long wavelength vibrations that do not depend on the detailed atomic character of the solid. For a three dimensional solid, this results in a DOS that is quadratic with v up to a cutoff frequency v_D related to the total number of normal modes $3N$ (see Figure 3-1). The Debye heat capacity that results when $g(v) \propto v^2$ has the form[2]

$$C_D = 9Nk\left(\frac{T}{\theta_D}\right)^3 \int_0^{\theta_D/T} \frac{x^4 e^x}{(e^x - 1)^2} dx \tag{3-4}$$

where the Debye temperature $\theta_D = hv_D/k$, and $x = hv/kT$. At low temperatures ($T \ll \theta_D$) this approximates to[1]

$$C_D(T \ll \theta_D) = \frac{12\pi^4}{5} Nk\left(\frac{T}{\theta_D}\right)^3 \tag{3-5}$$

Debye's model was the first major step in relating a theoretical heat capacity to experimental data at low temperatures where the heat capacities of many materials were known to have a T^3 dependence.

Although Debye's model fits the experimental heat capacity data of many materials well, it fails for many other materials. These materials have been found to have either a gap in the DOS (non-zero onset of the modes), many modes with frequencies higher than the Debye frequency v_D, or a DOS that does not have a v^2 dependence at low frequencies.[8-9]

The harmonic lattice dynamic theory is useful for materials that do not have a v^2 dependence at low frequencies.[4, 10-16] This theory is similar to the Debye model but includes terms that are an expansion in v^2, specifically, $g(v) = b_2v^2 + b_4v^4 + b_6v^6 + \cdots$. The extra terms produce a low temperature heat capacity expansion of the form:[4]

$$C_{HL} = A_3T^3 + A_5T^5 + A_7T^7 + \cdots \tag{3-6}$$

where

$$A_{2n+1} = \pi k \left(\frac{k}{h}\right)^{2n+1} B_{2n}b_{2n} \tag{3-7}$$

in which B_{2n} are the Bernoulli numbers and the b_{2n} terms are related to the normal mode density and can be approximated. For the first term in Eq. 3-6, b_2 has the form[4]

$$b_2 = \frac{9N}{8\pi^3}\left(\frac{h}{k\theta_D}\right)^3 \tag{3-8}$$

which, when inserted into Eq. 3-7, yields the low-temperature Debye coefficients (see Eq. 3-5). Because the Bernoulli numbers within the coefficients A_5 and A_9 in Eq. 3-6 are negative, the T^5 and T^9 terms should be negative, though the heat capacity fits of some metals have been reported to have positive T^5 terms.[4]

The terms beyond T^3 in Eq. 3-6 model the deviations from a Debye crystal in the form of phonon dispersion; whereas, Debye's model attempts to handle such deviations by imposing a variable Debye temperature.[1-2] The extra terms also extend the temperature range over which a

fit is valid. For data fit below 10 K, only the T^3 and T^5 terms should be necessary, but a T^7 is acceptable when θ_D is small. Although heat capacity data is often fit to Eq. 3-6 better than the Debye model, the extra information provided about phonon dispersion is "rather severely limited".[4] The review by Phillips[4] gives an excellent derivation of these equations and compares the various lattice heat capacity models in more detail.

These theories form the foundation for modeling vibrational heat capacity data, but they have been adapted to better model heat capacity data through methods such as applying the Debye model to one and two dimensions,[1, 17-18] which at low temperatures ($T \ll \theta_D$) have the expressions (following the derivation of McQuarrie[2])

$$C_V(1D) = \pi^2 Nk \frac{T}{\theta_D} \tag{3-9}$$

and

$$C_V(2D) = 36\zeta(3)Nk \left(\frac{T}{\theta_D}\right)^2 \tag{3-10}$$

where ζ represents the Riemann zeta function. For the 1D system, $g(v)$ is a constant value up to the cutoff energy v_D, which is proportional to θ_D, and for the 2D system, $g(v)$ is linear up to the cutoff energy. Also, using a sum of Einstein and Debye functions is a common alteration that has been applied to better analyze data that has low-energy modes.[19-24]

3.1.2 Low-energy Modes and Gaps in the DOS

Low-energy modes are caused by phonon scattering from regions of short-range order in the crystal structure and result in the "boson peak".[25] Boson peaks have been observed most notably in glasses,[26-29] but they have also been observed in other materials such as the polymer poly(methyl methacrylate) (PMMA),[30] the semiconductor α-Se, B_2O_3, As_2S_3,[31] and the metallic

glass PdZr.[32-33] Boson peaks also appear in the heat capacity data of biological compounds,[34] zeolites,[21, 35] and even some negative thermal expansion (NTE) materials.[21] Figure 3-2 shows the boson peaks of many more materials. The boson peaks in glasses, zeolites, and these NTE materials are believed to arise from coordinated vibrations of AO_4 tetrahedra deemed "rigid unit modes" (RUMs).[21, 36-43] Related investigations have shown that these low-energy modes have peak maxima around 5 meV (58 K) that are dependent on the size of the domain.[26, 44-45]

The energy bands of these modes typically have a gap in the vibrational DOS due to the finite size of the contributing feature.[46] Jura *et al.*[47] noted such a low frequency cutoff or gap in the DOS of 10 nm cube particles. Burton *et al.*[48] performed calculations that also suggest the vibrational modes of small particles have a non-zero energy onset. Saviot *et al.*[44] found a gap in the phonon DOS from 0 to 2 meV (23 K) in TiO_2 nanoparticles using inelastic neutron scattering (INS), which they attribute to the size of the 5 nm crystallites. Many others have also observed a gap in the DOS because of small particle size.[45, 49-51]

Not surprisingly, because of the unconventional nature of these vibrations, conventional models have failed to properly analyze heat capacity data of these materials; however, a model specific to these gapped vibrational modes has never been established. Equations having an exponential dependence on temperature ($B_{gap}T^n e^{-\delta/T}$ - with many possible values of n related to the particular system) have been derived for magnetic and superconducting systems that have a gap in the DOS,[52-60] and we extend those theories to derive low-temperature heat capacity equations for one, two, and three dimensions of a gapped vibrational DOS. Our derived equations provide insight on the short-range, phonon scattering domains in crystals that create boson peaks in the DOS and heat capacity. We have applied these equations to the low temperature heat capacity data fitting of the samples shown in Figure 3-2 and observe marked

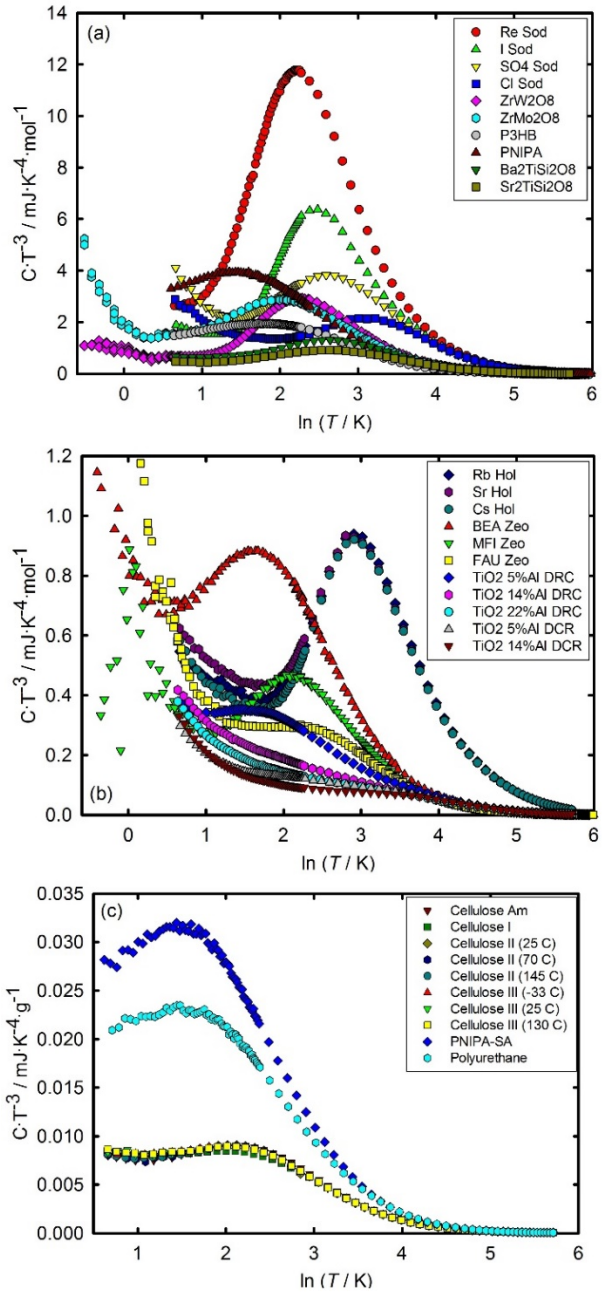

Figure 3-2: Heat Capacity Data of Several Samples Plotted as C/T^3 versus ln T Showing "Boson" Peaks or Excess Low-energy Modes.

improvement in both quality and physical meaningfulness of the fits relative to fits without these terms. The fitting parameters of several samples have also been inverted into DOS, which are comparable to measured DOS data published in the literature.

3.2 Derivation of Gapped Heat Capacities

The derivation of a gapped Debye function at low temperatures is similar to the derivation without the gap, but we now assume $g(\nu) \propto (\nu - \nu_{gap})^2$ where ν_{gap} is the offset from zero; therefore, $g(\nu)$ takes the form (similar to McQuarrie[2])

$$g(\nu)d\nu = \begin{cases} 0, & \nu < \nu_{gap} \; or \; \nu > \nu_D' \\ \dfrac{12\pi V}{{v_o}^3}(\nu - \nu_{gap})^2 d\nu, & \nu_{gap} < \nu < \nu_D' \end{cases} \tag{3-11}$$

where V is the volume, v_o is the average velocity of the two transverse waves and one longitudinal wave, and ν_D' is the high-end cutoff (where the prime indicates the cutoff of the gapped DOS as opposed to the conventional DOS cutoff ν_D). The conventional derivation accounts for all $3N$ vibrational modes in the integral of $g(\nu)d\nu$, but the phonons in a band with a gapped DOS do not account for all of these modes; therefore, we will constrain the integral of the gapped $g(\nu)d\nu$ to equal F, and the remaining modes integrate to a value G such that $F + G = 3N$. This yields the integral

$$\int_0^\infty g(\nu)d\nu = \int_{\nu_{gap}}^{\nu_D'} \frac{12\pi V}{{v_o}^3}(\nu - \nu_{gap})^2 d\nu = \frac{4\pi V}{{v_o}^3}\left({\nu_D'}^3 - 3{\nu_D'}^2\nu_{gap} + 3\nu_D'{\nu_{gap}}^2 - {\nu_{gap}}^3\right) = F$$

We can now eliminate the volume and velocity terms to get $g(\nu)d\nu$ in terms of the frequencies and F by solving for ${v_o}^3$ and substituting this into Eq. 3-11 producing the equation

$$g(\nu)d\nu = \begin{cases} 0, & \nu_{gap} > \nu > \nu_D' \\ \dfrac{3F(\nu - \nu_{gap})^2 d\nu}{\left({\nu_D'}^3 - 3{\nu_D'}^2\nu_{gap} + 3\nu_D'{\nu_{gap}}^2 - {\nu_{gap}}^3\right)}, & \nu_{gap} < \nu < \nu_D' \end{cases} \tag{3-12}$$

This can now be inserted into Eq. 3-1, which yields, with the substitution $x = h\nu/kT$,

$$C_V = \frac{3Fk}{\left({x_D'}^3 - 3{x_D'}^2 x_{gap} + 3x_D'{x_{gap}}^2 - {x_{gap}}^3\right)} \int_{x_{gap}}^{x_D'} \frac{x^2 e^x}{(e^x - 1)^2}(x - x_{gap})^2 dx \tag{3-13}$$

This integral can be evaluated in closed form for low temperatures, where x_D' can be assumed to approach infinity ($x_D' = hv_D'/kT \approx \infty$), and if we assume x_{gap} is approximately zero. With these assumptions, the integral in Eq. 3-13 evaluates to

$$\frac{4\pi^4}{15} - 2x_{gap}6\zeta(3) + {x_{gap}}^2\frac{\pi^2}{3}$$

By factoring out $4\pi^4/15$ this becomes

$$\frac{4\pi^4}{15}\left[1 - \frac{90\zeta(3)}{\pi^4}\left(\frac{x_{gap}}{2}\right) + \frac{5}{\pi^2}\left(\frac{x_{gap}}{2}\right)^2\right]$$

Because $90\zeta(3)/\pi^4 \approx 1$ and $5/\pi^2 \approx 1/2$, we can use the expansion

$$e^{-x} = 1 - x + \frac{x^2}{2} - \cdots$$

and the integral of the heat capacity expression becomes

$$\frac{4\pi^4}{15}e^{-\frac{x_{gap}}{2}}$$

Plugging this back into Eq. 3-13 while making the substitutions $x_{gap} = \delta/T$ and $x_D' = \theta_D'/T$ produces the heat capacity equation

$$C_V = \frac{4\pi^4 Fk}{5\left[1 - 3\left(\frac{\delta}{\theta_D'}\right) + 3\left(\frac{\delta}{\theta_D'}\right)^2 - \left(\frac{\delta}{\theta_D'}\right)^3\right]}\left(\frac{T}{\theta_D'}\right)^3 e^{-\frac{\delta}{2T}} \tag{3-14}$$

In line with the previous assumption that v_{gap} or δ is small ($\delta \ll \theta_D'$) this becomes

$$C_V(3D) = \frac{4\pi^4 Fk}{5}\left(\frac{T}{\theta_D'}\right)^3 e^{-\frac{\delta}{2T}} \tag{3-15}$$

By setting $\delta = 0$ and $F = 3N$, the original Debye equation for low temperatures (see Eq. 3-5) is produced.

This derivation is of a three dimensional Debye equation with a gap in the DOS, but the one and two dimensional derivations are similar, resulting in the equations:

$$C_V(1D) = \frac{\pi^2}{3} Fk \left(\frac{T}{\theta'_D}\right) e^{-\frac{\delta}{2T}} \tag{3-16}$$

and

$$C_V(2D) = 12Fk\zeta(3) \left(\frac{T}{\theta'_D}\right)^2 e^{-\frac{\delta}{2T}} \tag{3-17}$$

These also produce the conventional Debye heat capacity equations at low temperatures when $\delta = 0$ and $F = 3N$ (see Eqs. 3-9 and 3-10). These three equations (Eqs. 3-15 to 3-17) can be generalized to the *n* dimensional expression:

$$C_V(nD) = 2 \times 6^{n-1} \zeta(n+1) Fk \left(\frac{T}{\theta'_D}\right)^n e^{-\frac{\delta}{2T}} \tag{3-18}$$

We note that we have also applied a gapped DOS to the harmonic lattice dynamic theory. The derivation is essentially the same as the gapped Debye derivation but results in the expansion $A_3 T^3 e^{-\delta/T} + A_5 T^5 e^{-\delta/T} + \cdots$. Fits with these extra gapped terms, however, were found to be cumbersome and did not show any significant improvement in quality versus fits with just a gapped T^3 as in Eq. 3-15.

These equations for gapped vibrational DOS (Eqs. 3-15 to 3-17) resemble the equations derived for the gapped DOS associated with superconducting and magnetic materials in terms of temperature dependence, but here we have explicitly derived the equations with all parameters defined in terms of constants and physically meaningful variables that can be directly related to the vibrational DOS. Thus, we have made it possible to invert heat capacity data into a meaningful vibrational DOS, but we note that inverting heat capacity data into a DOS is much less quantitative than directly measuring the DOS; nevertheless, heat capacity data can be inverted into a DOS with some degree of accuracy.[61-62]

3.3 Comparison to Measured Heat Capacity Data

The low-temperature heat capacity data ($T < 10\ K$) of all samples listed in Table 3-1 were fit to two basic functions: one having only conventional contributions and the other having conventional contributions and any necessary gapped terms (Eqs. 3-15 to 3-17). These functions have the general expression

$$C_{fit} = \gamma T + A_3 T^3 + A_5 T^5 + A_7 T^7 + A_9 T^9 + B_{gap} T^n e^{-\frac{\delta}{2T}} \tag{3-19}$$

where the γ term represents lattice vacancies,[5] the A_3 through A_9 terms represent the harmonic lattice expansion,[4] and the B_{gap} term represent the bands of excess low-energy modes that have a gap. The dimensionality, given by n, was determined by fitting data to Eq. 3-19 using all three

Table 3-1: %RMS of Low-temperature Heat Capacity Fits Comparing Fits with and without a Gapped Term

material	%RMS w/ gapped term	%RMS w/o gapped term	material	%RMS w/ gapped term	%RMS w/o gapped term
sodalites			*zeolites*		
$Na_8Al_6Si_6O_{24}(ReO_4)_2$	0.419	4.59[a,b]	BEA	2.72	4.49[a]
$Na_8Al_6Si_6O_{24}I_{1.64}$	1.19	1.94[a,b]	FAU	6.62[c]	6.42[b]
$Na_8Al_6Si_6O_{24}(SO_4)$	0.791	0.812[a]	MFI	20.8	38.0[b]
$Na_8Al_6Si_6O_{24}Cl_{1.92}$	1.54	1.61[a]	*Al doped TiO_2*		
hollandites			5 % DRC	0.329	0.771[a,b]
$BaCs_{0.21}Ti_{5.5}Al_{2.5}O_{16}$	1.13	1.42	14 % DRC	0.471	0.509[b]
$BaRb_{0.22}Ti_{5.5}Al_{2.5}O_{16}$	1.26	1.87	22 % DRC	0.440	0.496[b]
$BaSr_{0.10}Ti_{5.5}Al_{2.5}O_{16}$	0.708	1.01	5 % DCR	0.646	0.714[a,b]
fresnoites			14 % DCR	0.477	0.505[a,b]
$Sr_2TiSi_2O_8$	0.676	0.780[a]	*polymers*		
$Ba_2TiSi_2O_8$	0.809	1.23[a,b]	Cellulose	0.504	0.536[a,b]
NTE			P3HB	0.592	1.67[a,b]
$ZrMo_2O_8$	5.48[c]	7.72[a,b]	PNIPA	0.638	2.36[a,b]
ZrW_2O_8	10.9	9.51[a,b]	PNIPA-SA	1.04	1.87[a,b]
			PU	1.24	1.45[a,b]

[a]harmonic lattice parameters have incorrect sign
[b]number of harmonic lattice parameters is unreasonable
[c]two gapped terms used

dimensions and selecting the fit that had the lowest %RMS and the most random deviation. B_{gap} is zero for the conventional fits but nonzero for the fits with the gapped term. As mentioned in section I, the T^9 harmonic lattice term is not valid for fits below 10 K, but we include it in the conventional fits in order to have the same number of terms as the fits with the gapped term. Even with the excessive terms, the conventional fits are worse than the fits that have a reasonable number of expansion terms but include the gapped term. Table 3-1 compares the %RMS of the fits both with and without the gapped term, but we will discuss the fitting details of a few representative samples.

3.3.1 1-D Gapped Phonons

Several of the samples with boson peaks are polymers that behave as 1D chains. In our recent work on cellulose, we found that a gapped $T^{3/2}$ term substantially improved the low temperature heat capacity fitting.[63] We have revisited this data and have found a 1D gapped term (see Eq. 3-16) to be more meaningful and produce a better fit. Table 3-1 gives the %RMS for amorphous cellulose, but the other cellulose samples had similar improvement in fit quality with the 1D gapped term. Other polymers that we have investigated have also shown a substantial improvement in fit quality and plausibility by adding the 1D gapped term: poly(3-hydroxybutyrate) (P3HB),[23] poly(N-isopropylacrylamide) (PNIPA),[24] PNIPA with poly(sodium acrylate) (PNIPA-SA), and polyurethane (PU) (see Table 3-1).

Stephens *et al.*[30] also observed boson peaks in the heat capacity data of several polymers and suggested three possible causes – the most probable being attributed to 1D motion along the polymer backbone between entanglement points. Vibrations along the polymer backbone would likely have low-energies because the backbone chain is quite large relative to typical molecules allowing for longer wavelength modes; furthermore, a nonzero onset of these modes is

understandable since the length of the vibrating backbone is small relative to typical bulk crystals that obey the Debye model.

Table 3-2: Fit Parameters and %RMS of Select Samples Fit with and without a Gapped Parameter (units are $J \cdot mol^{-1} \cdot K^{-x}$)

	Re sodalite – 1D		$Ti_{0.95}Al_{0.05}O_{1.975}$ – 2D		MFI zeolite – 3D	
γ			$5.6E10^{-4}$	$2.2E10^{-4}$	$5.8E10^{-4}$	$3.1E10^{-5}$
A_3	$2.7E10^{-3}$	$1.3E10^{-3}$	$1.9E10^{-4}$	$3.0E10^{-4}$	$1.4E10^{-4}$	$3.5E10^{-4}$
A_5	$-2.3E10^{-5}$	$2.6E10^{-4}$	$-1.6E10^{-6}$	$3.1E10^{-6}$	$-4.0E10^{-6}$	$-5.5E10^{-6}$
A_7		$-9.8E10^{-7}$	$5.3E10^{-9}$	$-7.3E10^{-8}$		$2.5E10^{-7}$
A_9		$-6.8E10^{-9}$		$4.0E10^{-10}$		$-2.0E10^{-9}$
B_{gap}	9.7		$4.0E10^{-3}$		$1.5E10^{-3}$	
δ_n	43		15		15.571	
%RMS	0.42	4.6	0.33	0.77	21	38

As part of another investigation, we have measured the heat capacities of several sodalite samples containing ReO_4^-, I^-, Cl^-, and SO_4^{2-} ions that exhibit pronounced boson peaks. The data fitting of these materials greatly benefited by the addition of a 1D gapped term. Table 3-2 gives the fit parameters and %RMS of the ReO_4^- sodalite fits. The %RMS of the fit with the gapped term is an order of magnitude smaller than the fit without the gapped term. The signs of several parameters of the fit without the gapped term are inverted from what they should be (see Table 3-2), and the deviation plot of the conventional fit shows strong systematic error (see Figure 3-3). Even when adding more terms to the harmonic lattice expansion, the quality of the conventional fit did not improve significantly; therefore, the fit with the gapped term is best with regards to the meaningfulness of the terms, %RMS, and the lack of a systematic deviation of the fit.

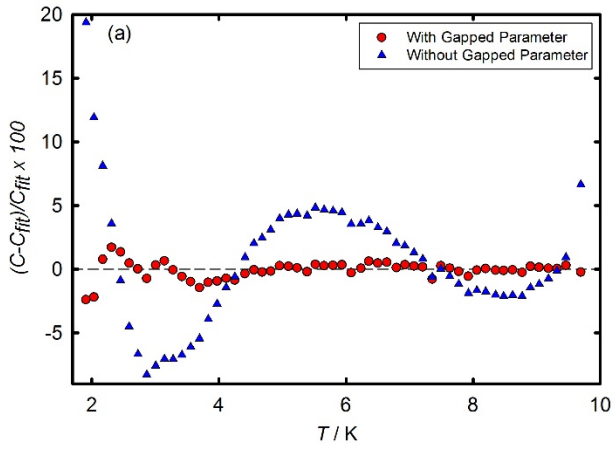

Figure 3-3: Deviation Plots of $Na_8Al_6Si_6O_{24}(ReO_4)_2$ (Re-sodalite) Comparing Fit Quality between Fits with (red circles) and without (blue triangles) a Gapped Term in the Low-temperature Heat Capacity Fitting.

These samples are very similar to zeolites in that they are composed of SiO_4 and AlO_4 tetrahedra that form cages;[64] therefore, it is not unreasonable to expect these compounds to have excess low-energy modes caused by the concerted motion of rigid tetrahedra (RUMs) as observed in zeolites.[41] Because sodalites form small cages, having diameters on the order of a few nanometers, vibrations of these domains will have a relatively small minimum wavelength causing a gap in the DOS. The origin of the 1D vibrational character is unknown, but we postulate that the ring and wireframe-like structure of the connected tetrahedra creates pseudo-linear vibrations.

3.3.2 2-D Gapped Phonons

We have recently investigated eight samples of Al doped TiO_2 to determine the location of the Al^{3+} dopant ions from the low-temperature heat capacities, electron energy-loss spectroscopy (EELS), and X-ray diffraction (XRD).[65-66] We have shown that these dopant ions

enter the TiO_2 lattice and form small domains of short-range order that resemble a $TiAlO_x$ glass-like structure.

The five samples with the lowest concentrations of Al^{3+} dopant (5-22 mol% Al) required 2D gapped terms (see Eq. 3-17) to fit the low-temperature heat capacity data; whereas, the pure TiO_2 and TiO_2 doped with 50 mol% Al did not need the gapped terms. The %RMS and fitting parameters of fits with and without the gapped term are given in Table 3-2 for the sample with 5 mol% Al prepared with the dry-rinse-calcine (DRC) method. Justification for fitting the data of these samples with the gapped term versus conventional fits is similar to the other samples discussed thus far. The %RMS is significantly lower with the gapped term, the deviation is random (see Figure 3-4), and the terms are physically meaningful.

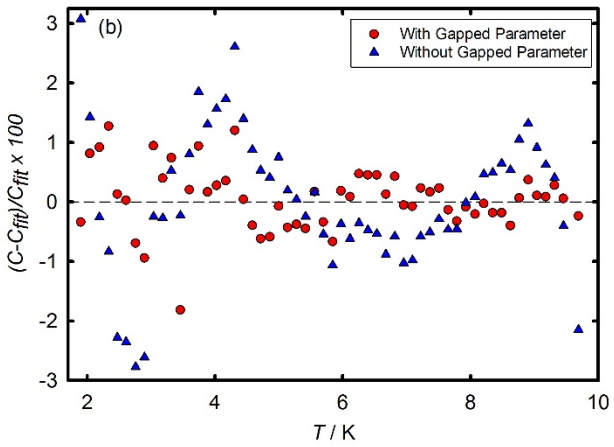

Figure 3-4: Deviation Plots of TiO_2 Doped with 5 mol% Al Using DRC Method Comparing Fit Quality between fits with (red circles) and without (blue triangles) a Gapped Term in the Low-temperature Heat Capacity Fitting.

The small regions of the $TiAlO_x$ structure form in the TiO_2 lattice during crystal growth. We speculate that the synthesis begins with the formation of small TiO_2 clusters having on the order of a hundred atoms. Clusters that form near regions having a high concentration of Al^{3+}

(related to the solvent deficient synthesis that creates a slightly inhomogeneous environment on the nanoscale[67-68]) react with the Al^{3+}, which forms thin island-like structures. The TiO_2 structure continues to grow and eventually grows over the Al islands, similar to how a tree grows over a sign nailed to its trunk, creating highly disordered 2D regions of $TiAlO_x$ within the TiO_2 lattice. These particles retain the TiO_2-like structure as observed with EELS and XRD but have these small glass-like domains that are responsible for the excess low-energy modes similar to RUMs observed in glasses. The gap in the DOS exists in the particles with low concentrations of dopant because the $TiAlO_x$ domains are small; whereas, at higher dopant concentrations these domains become sufficiently large that their vibrations can be treated as traditional Debye modes. (See ref. 66 for more details.)

3.3.3 3-D Gapped Phonons

The other samples with boson peaks shown in Figure 3-2 required a 3D gapped term to fit the data well. Although our original publication of the fresnoites $Ba_2TiSi_2O_8$ and $Sr_2TiSi_2O_8$ used a gapped $T^{3/2}$ term (ferromagnetic),[69] we have found that a gapped T^3 term (see Eq. 3-15) models the data better and is more meaningful since these materials are known to have TiO_4 tetrahedra.[70] The heat capacity fitting of Rb hollandite benefits from a gapped T^3 term as well; however, the Sr and Cs hollandites appear to have slightly better fits with the 1D gapped *T* term, though the difference between the 3D gapped T^3 and 1D gapped *T* fits is very small for these samples.

We have also revisited the heat capacity data published by Boerio-Goates *et al.*[21] of the negative thermal expansion (NTE) materials ZrW_2O_8 and $ZrMo_2O_8$ and the zeolites BEA, MFI, and FAU using gapped terms rather than the five Debye and Einstein functions originally used to fit each data set. The quality of our fits are comparable to those published in terms of modeling

the heat capacity data; however, we will show that our fits are more meaningful with regards to the derived DOS. We note that the FAU zeolite and $ZrMo_2O_8$ fits required two gapped T^3 parameters which are related to separate contributions. To illustrate the quality of our fits we present the MFI fitting results. The %RMS of the fit with the gapped term is about half that of the fit without the gapped term even when using lattice terms up to T^9 (see Table 3-2). The deviation plot (Figure 3-5) shows that the fit with the gapped terms is random at all temperatures above 2 K; whereas, the conventional fit is systematic at all temperatures.

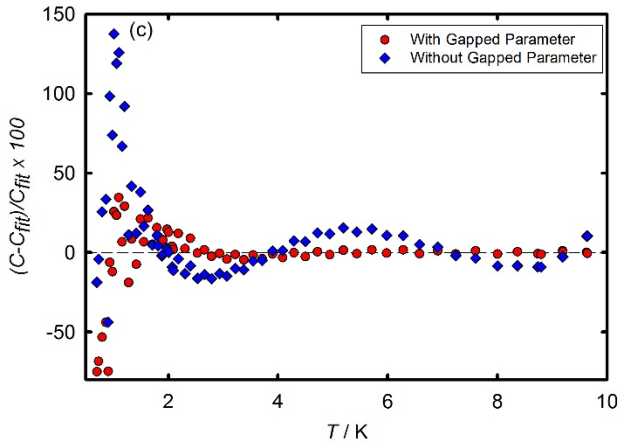

Figure 3-5: Deviation Plots of Zeolite MFI Comparing Fit Quality between fits with (red circles) and without (blue triangles) a Gapped Term in the Low-temperature Heat Capacity Fitting.

The fits of the other zeolites and NTE samples improve similarly by adding the gapped term, but we note that the %RMS of FAU and ZrW_2O_8 are slightly better for the conventional fits (see Table 3-1). We believe this is because the conventional fit is fitting the noise below 1 K as a result of the unrealistically large number of lattice expansion terms. The deviation plots of these samples show that the gapped fits are less systematic than the conventional fits, and the T^5

term of the ZrW_2O_8 conventional fit is positive and therefore not physical; therefore, the fits of these samples using the gapped term are still better than conventional fits.

Low frequency modes in these NTE materials and zeolites have been related to tetrahedra and RUMs.[21, 35, 71-75] and because these span the volume of the crystal, it is reasonable that the gapped term is three-dimensional. The FAU zeolite is composed of tetrahedra that make secondary building units (primarily α-cages and β-cages), and the different characteristics of these units give rise to different vibrational bands.[35] We believe these distinct bands create the need for two gapped terms.

We note that fitting the heat capacity data of complex materials such as these is much easier when more is known about the materials. By knowing that many of these samples have tetrahedra, we could deduce the presence of low-energy modes; likewise, we knew that FAU and $ZrMo_2O_8$ have more than one excess, low-energy contribution to the DOS from the work of Greaves *et al.*[35] and Mittal *et al.*[73]

3.4 Derived DOS Compared to Measured DOS

Because the fitting parameters have been derived in terms of values related to the DOS, we can further verify the validity of these fits by converting the parameters into a DOS that can be compared to the measured DOS. Recall that δ in Eqs. 3-15 to 3-17 is proportional to the low-energy gap in the DOS ν_{gap}, while θ_D' is related to the energy cutoff ν_D' (see Eq. 3-12). Because the fitting coefficient that contains θ_D' also contains F, and F is not necessarily known, we approximated F either from the number of tetrahedra or simply from the value that results in a realistic DOS. Table 3-3 gives the values of F used as well as the derived DOS parameters ν_{gap} and ν_D' of all samples in Table 3-1. We also note that several of the values of δ given in Table 3-

3 are somewhat larger than permissible by our assumption that δ is small, but we consider these values to be qualitatively acceptable, nonetheless.

Table 3-3: DOS Parameters Derived from Low-temperature Heat Capacity Fitting Variables (units are meV)

Sample	G	F	F'	ν_D	$\nu_{gap,1}$	$\nu'_{D,1}$	$\nu_{gap,2}$	$\nu'_{D,2}$
$Na_8Al_6Si_6O_{24}(ReO_4)_2$	80	20		27.19	3.705	7.902		
$Na_8Al_6Si_6O_{24}I_{1.64}$	65	35		31.86	5.473	8.737		
$Na_8Al_6Si_6O_{24}(SO_4)$	90	10		35.03	5.124	8.742		
$Na_8Al_6Si_6O_{24}Cl_{1.92}$	90	10		40.54	8.503	12.80		
$BaCs_{0.21}Ti_{5.5}Al_{2.5}O_{16}$	67	33		39.89	8.606	12.67		
$BaRb_{0.22}Ti_{5.5}Al_{2.5}O_{16}$	67	33		36.11	4.710	10.39		
$BaSr_{0.10}Ti_{5.5}Al_{2.5}O_{16}$	67	33		36.64	8.760	12.24		
$Sr_2TiSi_2O_8$	90	10		33.52	1.999	8.704		
$Ba_2TiSi_2O_8$	90	10		28.19	2.904	7.295		
TiO_2 5 % Al DRC	95	5		30.77	1.326	12.68		
TiO_2 14 % Al DRC	95	5		27.50	4.566	6.636		
TiO_2 22 % Al DRC	95	5		30.30	4.767	6.621		
TiO_2 5 % Al DCR	95	5		33.29	3.582	6.631		
TiO_2 14 % Al DCR	95	5		37.85	3.139	13.88		
P3HB	99	1		22.08	1.994	6.455		
PNIPA	99	1		19.54	1.777	6.041		
PNIPA-SA	99	1		19.58	2.099	5.520		
PU	99	1		21.06	2.528	5.861		
Cellulose	98.5	1.5		28.75	3.470	6.488		
BEA	90	10		23.64	0.2221	7.368		
MFI	90	10		28.76	1.342	6.271		
FAU	82	8	10	23.54	1.293	9.335	3.992	5.481
$ZrMo_2O_8$	50	10	40	43.83	0.5654	6.420	1.696	17.72
ZrW_2O_8	85	15		22.92	2.034	3.917		

The DOS data of several of the materials discussed herein have been measured with INS. Muller *et al.*[76] showed that cellulose has low-energy modes that are nearly a constant with energy such as would be expected for 1D phonons. The energies of the excess modes derived from our

gapped fit of the amorphous cellulose data (Table 3-3) correspond to the energies in the measured DOS.

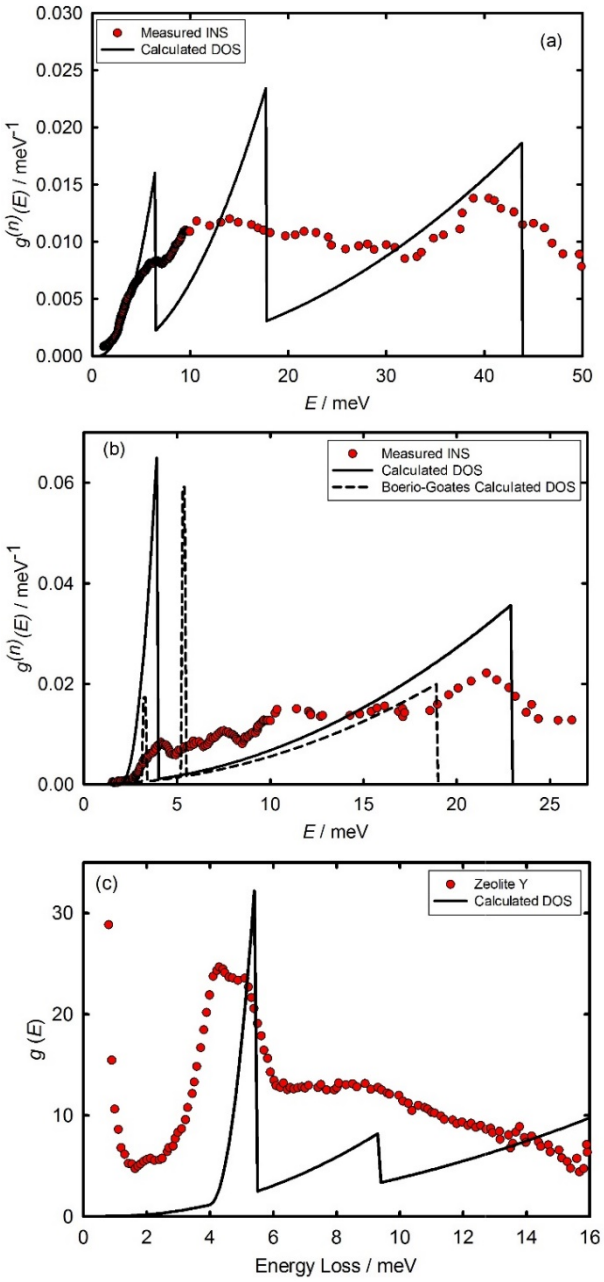

Figure 3-6: Measured DOS Data (red circles) of a) $ZrMo_2O_8$,[73] b) ZrW_2O_8,[74-75] and c) FAU zeolite[35] Compared to the DOS Derived from the Low-temperature Heat Capacity Fitting

The DOS of $ZrMo_2O_8$ and ZrW_2O_8 have been measured by Mittal *et al.*[73-75] Figures 3-6a and 3-6b show their data as well the DOS derived from our heat capacity data fitting. As can be seen, the derived DOS grossly simplifies the actual DOS, but many of the most prominent features are identifiable. For example, the magnitude of the derived low energy peak in the ZrW_2O_8 data (Figure 3-6b) is rather large compared to the actual data, but the peak maximum corresponds to the peak from the INS data. Also included in Figure 3-6b is the DOS derived from the fitting method of Boerio-Goates *et al.*,[21] which models the heat capacity data well, but the derived DOS does not appear to match any of the features of the actual DOS.

Greaves *et al.* [35] measured the DOS of zeolite Y, $Na_{56}Al_{56}Si_{136}O_{384}$, which has the same structure as FAU but with Al^{3+} and Na^{+} ions replacing some of the Si^{4+} ions. For the DOS of FAU to be comparable to the DOS of zeolite Y, it was scaled from SiO_2 to $Na_{56}Al_{56}Si_{136}O_{384}$ using a factor of 192 (number of equivalent SiO_2 in $Na_{56}Al_{56}Si_{136}O_{384}$). Figure 3-6c shows the measured data with our derived DOS showing that our DOS is qualitatively similar to the measured DOS despite having a slightly different composition.

3.5 Conclusions

We have derived gapped heat capacity functions in one, two, and three dimensions from DOS with a non-zero onset of vibrational modes and have shown that adding these functions to the low-temperature heat capacity data fitting greatly improves fit quality for samples that have excess low-energy modes. From the fitting parameters, we have derived meaningful DOS that are comparable to the measured DOS of several materials. This study provides a physically meaningful method for analyzing low-temperature heat capacity data of materials that have an excess of low-energy modes with a gap in the DOS that also yields a crude approximation of the DOS.

REFERENCES

1. Gopal, E. S. R., *Specific Heats at Low Temperatures*; Plenum Press New York, 1966; Vol. 227.

2. McQuarrie, D., Statistical Mechanics, 2000. *University Science, Sausalito, USA*.

3. Kittel, C.; McEuen, P.; McEuen, P., *Introduction to Solid State Physics*; Wiley New York, 1976; Vol. 8.

4. Phillips, N. E., Low-Temperature Heat Capacity of Metals. *Critical Reviews in Solid State and Material Sciences* **1971**, *2*, 467-553.

5. Schliesser, J. M.; Woodfield, B. F., Lattice Vacancies Responsible for the Linear Dependence of the Low-Temperature Heat Capacity of Insulating Materials. *Physical Review B* **2015**, *91*, 024109.

6. Fisher, R.; Gordon, J.; Reklis, S.; Wright, D.; Emerson, J.; Woodfield, B.; McCarron III, E.; Phillips, N., Magnetic-Field Dependence of the Low-Temperature Specific Heat of Some High-Tc Copper-Oxide Superconductors Evidence for an H12t Contribution in the Mixed State. *Physica C: Superconductivity* **1995**, *252*, 237-263.

7. McWhan, D.; Varma, C.; Hsu, F.; Remeika, J., Low-Temperature Heat Capacity of Alkali-Metal and Silver B-Aluminas. *Physical Review B* **1977**, *15*, 553.

8. Anderson, O. L., Thermoelastic Properties of Mgsio3 Perovskite Using the Debye Approach. *American Mineralogist* **1998**, *83*, 23-35.

9. Oganov, A. R.; Brodholt, J. P.; David Price, G., Comparative Study of Quasiharmonic Lattice Dynamics, Molecular Dynamics and Debye Model Applied to Mgsio3 Perovskite. *Physics of the Earth and Planetary Interiors* **2000**, *122*, 277-288.

10. Fisher, R.; Gordon, J.; Phillips, N., Specific Heat of the High-Tc Oxide Superconductors. *Journal of Superconductivity* **1988**, *1*, 231-294.

11. Born, M.; Huang, K., *Dynamical Theory of Crystal Lattices Oxford Classic Texts in the Physical Sciences*; Clarendon Press, Oxford, 1988.

12. Leibfried, G.; Flügge, S., Encyclopedia of Physics. *Crystal Physics I (2nd ed.) Springer, Berlin* **1955**, 104.

13. Blackman, M.; Flügge, S., Encyclopedia of Physics, Vol. *VIISpringer, Berlin* **1955**, 325.

14. de Launay, J.; Seitz, F.; Turnbull, D., Solid State Physics. *Ed. F. Seitz and D. Turnbull, Academic Press, New York* **1956**, *2*, 219.

15. Maradudin, A. A.; Montroll, E. W.; Weiss, G. H.; Ipatova, I., *Theory of Lattice Dynamics in the Harmonic Approximation*; Academic press New York, 1963; Vol. 12.

16. Joshi, S.; Rajagopal, A.; Seitz, F.; Turnbull, D.; Ehrenreich, H., Solid State Physics, Vol. 22Academic Press, New York: 1968.

17. Benedict, L. X.; Louie, S. G.; Cohen, M. L., Heat Capacity of Carbon Nanotubes. *Solid State Communications* **1996**, *100*, 177-180.

18. Lien, W. H.; Phillips, N. E., Heat Capacity of Small Particles of Mgo between 1.5° and 4° K. *The Journal of Chemical Physics* **1958**, *29*, 1415-1416.

19. Kelley, K. K.; King, E. G., *Entropies of the Elements and Inorganic Compounds*; US Government Printing Office, 1961; Vol. 592.

20. Ramirez, A. P.; Kowach, G. R., Large Low Temperature Specific Heat in the Negative Thermal Expansion Compound Zrw2o8. *Physical Review Letters* **1998**, *80*, 4903-4906.

21. Boerio-Goates, J.; Stevens, R.; Lang, B.; Woodfield, B. F., Heat Capacity Calorimetry. *Journal of Thermal Analysis and Calorimetry* **2002**, *69*, 773-783.

22. Tarasov, V.; Yunitskii, G., Theory of Heat Capacity of Chain and Layer Structures. *Zh. fiz. khim* **1950**, *24*, 111-128.

23. Czerniecka, A.; Magoń, A.; Schliesser, J.; Woodfield, B.; Pyda, M., Heat Capacity of Poly (3-Hydroxybutyrate). *The Journal of Chemical Thermodynamics* **2014**, *73*, 76-84.

24. Czerniecka-Kubicka, A.; Zarzyka, I.; Schliesser, J.; Woodfield, B.; Pyda, M., Vibrational Heat Capacity of Poly (N-Isopropylacrylamide). *Polymer* **accepted**.

25. Elliott, S., A Unified Model for the Low-Energy Vibrational Behaviour of Amorphous Solids. *EPL (Europhysics Letters)* **1992**, *19*, 201.

26. Uchino, T.; Yoko, T., Localized Low-Frequency Dynamics in Sio Glass. *The Journal of chemical physics* **1998**, *108*, 8130.

27. Flubacher, P.; Leadbetter, A.; Morrison, J.; Stoicheff, B., The Low-Temperature Heat Capacity and the Raman and Brillouin Spectra of Vitreous Silica. *Journal of Physics and Chemistry of Solids* **1959**, *12*, 53-65.

28. Gil, L.; Ramos, M.; Bringer, A.; Buchenau, U., Low-Temperature Specific Heat and Thermal Conductivity of Glasses. *Physical review letters* **1993**, *70*, 182.

29. Nakamura, M.; Arai, M.; Inamura, Y.; Otomo, T.; Bennington, S. M., Effect of Low-Energy Dynamics on Anomalous Vibrational Amplitudes in Vitreous Silica. *Physical Review B* **2002**, *66*, 024203.

30. Stephens, R.; Cieloszyk, G.; Salinger, G., Thermal Conductivity and Specific Heat of Non-Crystalline Solids: Polystyrene and Polymethyl Methacrylate. *Physics Letters A* **1972**, *38*, 215-217.

31. Stephens, R. B., Intrinsic Low-Temperature Thermal Properties of Glasses. *Physical Review B* **1976**, *13*, 852.

32. Hunklinger, S.; Raychaudhuri, A., *Thermal and Elastic Anomalies in Glasses at Low Temperatures*; Amsterdam: Elsevier, 1986; Vol. 9.

33. Graebner, J. E.; Golding, B.; Schutz, R.; Hsu, F.; Chen, H., Low-Temperature Properties of a Superconducting Disordered Metal. *Physical Review Letters* **1977**, *39*, 1480.

34. Rakvin, B.; Maltar-Strmečki, N.; Ramsey, C. M.; Dalal, N. S., Heat Capacity and Electron Spin Echo Evidence for Low Frequency Vibrational Modes and Lattice Disorder in L-Alanine at Cryogenic Temperatures. *The Journal of chemical physics* **2004**, *120*, 6665.

35. Greaves, G. N.; Meneau, F.; Majérus, O.; Jones, D. G.; Taylor, J., Identifying Vibrations That Destabilize Crystals and Characterize the Glassy State. *Science* **2005**, *308*, 1299-1302.

36. Buchenau, U.; Nücker, N.; Dianoux, A., Neutron Scattering Study of the Low-Frequency Vibrations in Vitreous Silica. *Physical Review Letters* **1984**, *53*, 2316.

37. Buchenau, U.; Prager, M.; Nücker, N.; Dianoux, A. J.; Ahmad, N.; Phillips, W. A., Low-Frequency Modes in Vitreous Silica. *Physical Review B* **1986**, *34*, 5665-5673.

38. Buchenau, U.; Zhou, H. M.; Nucker, N.; Gilroy, K. S.; Phillips, W. A., Structural Relaxation in Vitreous Silica. *Physical Review Letters* **1988**, *60*, 1318-1321.

39. Courtens, E.; Foret, M.; Hehlen, B.; Vacher, R., The Vibrational Modes of Glasses. *Solid State Communications* **2001**, *117*, 187-200.

40. Dove, M. T.; Harris, M. J.; Hannon, A. C.; Parker, J. M.; Swainson, I. P.; Gambhir, M., Floppy Modes in Crystalline and Amorphous Silicates. *Physical Review Letters* **1997**, *78*, 1070-1073.

41. Dove, M.; Hammonds, K.; Harris, M.; Heine, V.; Keen, D.; Pryde, A.; Trachenko, K.; Warren, M., Amorphous Silica from the Rigid Unit Mode Approach. *Mineralogical Magazine* **2000**, *64*, 377-388.

42. Boerio-Goates, J.; Stevens, R.; Hom, B. K.; Woodfield, B. F.; Piccione, P. M.; Davis, M. E.; Navrotsky, A., Heat Capacities, Third-Law Entropies and Thermodynamic Functions of Sio2 Molecular Sieves from T = 0 K to 400 K. *The Journal of Chemical Thermodynamics* **2002**, *34*, 205-227.

43. Hammonds, K. D.; Heine, V.; Dove, M. T., Rigid-Unit Modes and the Quantitative Determination of the Flexibility Possessed by Zeolite Frameworks. *The Journal of Physical Chemistry B* **1998**, *102*, 1759-1767.

44. Saviot, L.; Netting, C. H.; Murray, D. B.; Rols, S.; Mermet, A.; Papa, A.-L.; Pighini, C.; Aymes, D.; Millot, N., Inelastic Neutron Scattering Due to Acoustic Vibrations Confined in Nanoparticles: Theory and Experiment. *Physical Review B* **2008**, *78*, 245426.

45. Duval, E.; Boukenter, A.; Champagnon, B., Vibration Eigenmodes and Size of Microcrystallites in Glass: Observation by Very-Low-Frequency Raman Scattering. *Physical Review Letters* **1986**, *56*, 2052-2055.

46. Shirane, G.; Axe, J. D.; Harada, J.; Linz, A., Inelastic Neutron Scattering from Single-Domain Batio3. *Physical Review B* **1970**, *2*, 3651-3657.

47. Jura, G.; Pitzer, K. S., The Specific Heat of Small Particles at Low Temperatures. *Journal of the American Chemical Society* **1952**, *74*, 6030-6032.

48. Burton, J., Configuration, Energy, and Heat Capacity of Small Spherical Clusters of Atoms. *The Journal of chemical physics* **1970**, *52*, 345.

49. Nishiguchi, N.; Sakuma, T., Vibrational Spectrum and Specific Heat of Fine Particles. *Solid State Communications* **1981**, *38*, 1073-1077.

50. Wang, B.-X.; Zhou, L.-P.; Peng, X.-F., Surface and Size Effects on the Specific Heat Capacity of Nanoparticles. *International journal of thermophysics* **2006**, *27*, 139-151.

51. Wyart, M.; Nagel, S. R.; Witten, T. A., Geometric Origin of Excess Low-Frequency Vibrational Modes in Weakly Connected Amorphous Solids. *EPL (Europhysics Letters)* **2005**, *72*, 486.

52. Kresin, V.; Parkhomenko, V., Thermodyanamic Properties of Superconductors with Strong Coupling. *Fizika Tverdogo Tela* **1974**, *16*, 3363-3370.

53. Junod, A.; Jarlborg, T.; Muller, J., Heat-Capacity Analysis of a Large Number of a 15-Type Compounds. *Physical Review B* **1983**, *27*, 1568.

54. Bouquet, F.; Wang, Y.; Fisher, R.; Hinks, D.; Jorgensen, J.; Junod, A.; Phillips, N., Phenomenological Two-Gap Model for the Specific Heat of Mgb2. *EPL (Europhysics Letters)* **2001**, *56*, 856.

55. Hutchings, M. T.; Samuelsen, E. J., Measurement of Spin-Wave Dispersion in Nio by Inelastic Neutron Scattering and Its Relation to Magnetic Properties. *Physical Review B* **1972**, *6*, 3447-3461.

56. Niira, K., Temperature Dependence of the Magnetization of Dysprosium Metal. *Physical Review* **1960**, *117*, 129.

57. Fisher, R. A.; Bouquet, F.; Phillips, N. E.; Franck, J. P.; Zhang, G.; Gordon, J. E.; Marcenat, C., Electron, Spin-Wave, Hyperfine, and Phonon Contributions to the Low-Temperature Specific Heat of La0.65ca0.35mno3:Effects of Magnetic Fields and 16o/18o Exchange. *Physical Review B* **2001**, *64*, 134425.

58. Majzlan, J.; Navrotsky, A.; Woodfield, B. F.; Lang, B. E.; Boerio-Goates, J.; Fisher, R. A., Phonon, Spin-Wave, and Defect Contributions to the Low-Temperature Specific Heat of A-Feooh. *Journal of Low Temperature Physics* **2003**, *130*, 69-76.

59. Snow, C. L.; Shi, Q.; Boerio-Goates, J.; Woodfield, B. F., Heat Capacity Studies of Nanocrystalline Magnetite (Fe3o4). *The Journal of Physical Chemistry C* **2010**, *114*, 21100-21108.

60. Hu, B.; McCandless, G. T.; Garlea, V. O.; Stadler, S.; Xiong, Y.; Chan, J. Y.; Plummer, E. W.; Jin, R., Structure-Property Coupling in Sr3(Ru1−Xmnx)2o7. *Physical Review B* **2011**, *84*, 174411.

61. Junod, A.; Bichsel, D.; Muller, J., Modification of Acoustic Phonon-Spectrum as Fucntion of Electron State Density in A15-Type Superconductors. *Helvetica Physica Acta* **1979**, *52*, 580-596.

62. Chambers, R. G., The Inversion of Specific Heat Curves. *Proceedings of the Physical Society* **1961**, *78*, 941.

63. Goldberg, R. N.; Schliesser, J.; Mittal, A.; Decker, S. R.; Santos, A. F. L.; Freitas, V. L.; Urbas, A.; Lang, B. E.; Heiss, C.; da Silva, M. D. R., A Thermodynamic Investigation of the Cellulose Allomorphs: Cellulose (Am), Cellulose Iβ (Cr), Cellulose Ii (Cr), and Cellulose Iii (Cr). *The Journal of Chemical Thermodynamics* **2015**, *81*, 184-226.

64. Hassan, I.; Grundy, H., The Crystal Structures of Sodalite-Group Minerals. *Acta Crystallographica Section B: Structural Science* **1984**, *40*, 6-13.

65. Olsen, R. E.; Alam, T. M.; Bartholomew, C. H.; Enfield, D. B.; Schliesser, J. M.; Woodfield, B. F., Structure Analysis of Al-Modified Tio2 Nanocatalyst Supports. *Journal of Physical Chemistry C* **2014**, *118*, 9176-9186.

66. Schliesser, J. M.; Olsen, R. E.; Enfield, D. B.; Woodfield, B. F., Determining the Location and Role of Al in Al-Modified Tio2 Nanoparticles Using Low-Temperature Heat Capacity, Electron Energy-Loss Spectroscopy, and X-Ray Diffraction. **submitted**.

67. Olsen, R. E.; Bartholomew, C. H.; Huang, B.; Simmons, C.; Woodfield, B. F., Synthesis and Characterization of Pure and Stabilized Mesoporous Anatase Titanias. *Microporous and Mesoporous Materials* **2014**, *184*, 7-14.

68. Woodfield, B. F.; Liu, S.; Boerio-Goates, J.; Liu, Q.; Smith, S. J., Preparation of Uniform Nanoparticles of Ultra-High Purity Metal Oxides, Mixed Metal Oxides, Metals, and Metal Alloys. Google Patents: 2012.

69. Shi, Q.; Park, T.-J.; Schliesser, J.; Navrotsky, A.; Woodfield, B. F., Low Temperature Heat Capacity Study of Ba2tisi2o8 and Sr2tisi2o8. *The Journal of Chemical Thermodynamics* **2014**, *72*, 77-84.

70. Höche, T.; Neumann, W.; Esmaeilzadeh, S.; Uecker, R.; Lentzen, M.; Rüssel, C., The Crystal Structure of Sr2tisi2o8. *Journal of Solid State Chemistry* **2002**, *166*, 15-23.

71. Pryde, A. K.; Hammonds, K. D.; Dove, M. T.; Heine, V.; Gale, J. D.; Warren, M. C., Origin of the Negative Thermal Expansion in And. *Journal of Physics: Condensed Matter* **1996**, *8*, 10973.

72. Pryde, A. K.; Hammonds, K. D.; Dove, M. T.; Heine, V.; Gale, J. D.; Warren, M. C., Rigid Unit Modes and the Negative Thermal Expansion in Zrw2o8. *Phase Transitions* **1997**, *61*, 141-153.

73. Mittal, R.; Chaplot, S. L.; Schober, H.; Kolesnikov, A. I.; Loong, C. K.; Lind, C.; Wilkinson, A. P., Negative Thermal Expansion in Cubic Zrmo2o8: Inelastic Neutron Scattering and Lattice Dynamical Studies. *Physical Review B* **2004**, *70*, 214303.

74. Mittal, R.; Chaplot, S. L., Phonon Density of States and Thermodynamic Properties in Cubic and Orthorhombic Phases of Zrw2o8. *Solid State Communications* **2000**, *115*, 319-322.

75. Mittal, R.; Chaplot, S. L.; Schober, H.; Mary, T. A., Origin of Negative Thermal Expansion in Cubic Zrw2o8 Revealed by High Pressure Inelastic Neutron Scattering. *Physical Review Letters* **2001**, *86*, 4692-4695.

76. Müller, M.; Czihak, C.; Schober, H.; Nishiyama, Y.; Vogl, G., All Disordered Regions of Native Cellulose Show Common Low-Frequency Dynamics. *Macromolecules* **2000**, *33*, 1834-1840.

4 LATTICE VACANCIES RESPONSIBLE FOR THE LINEAR DEPENDENCE ON THE LOW-TEMPERATURE HEAT CAPACITY OF INSULATING MATERIALS

4.1 Introduction

4.1.1 Linear Heat Capacity at Low Temperatures

Traditionally, the linear dependence on temperature of the low temperature ($T < 15$ K) heat capacity has been associated with conduction electrons in metals,[1-2] but a linear term, γT, has been found in many non-metallic materials as well.[3-5] The linear dependence of these materials has been an area of great interest and has resulted in a number of theories having broad and often inconsistent origins.

In metals, the linear dependence arises from electrons that populate energy levels above the Fermi level at any finite temperature.[1-2] High temperature ceramic superconductors have been found to show a linear dependence in the heat capacity. This could easily be misinterpreted as arising from conduction electrons similar to those in metals, but because the conductivity arises from Cooper pairs,[6] which behave as bosons rather than fermions, new theories were needed to explain the linear dependence.

Many theories suggested the linear dependence was intrinsic to superconductivity,[4, 7-10] while others have attributed the linear term to a tunneling-system related to oxygen,[11] impurity

phases such as $BaCuO_2$ in $YBa_2Cu_3O_7$ (YBCO),[12] or twin boundaries and oxygen vacancies.[13-15] The arguments of those against an intrinsic linear term are that linear terms are inconsistent from sample to sample and depend strongly on sample quality;[4, 10] furthermore, some superconductors that become insulators at certain stiochiometries retain a similar linear term in the heat capacity even as insulators.[16-17]

Several studies have attempted to identify the origins of the linear terms in insulating materials resulting in theories as diverse as the samples. Table 4-1 lists the linear terms of several insulating materials as determined from a combination of adiabatic,[18-25] semi-adiabatic pulse,[19-23, 26-30] isothermal,[21, 26] and relaxation calorimetry methods,[5, 18, 21, 27, 31-43] and Figure 4-1 graphically shows a sampling of these linear terms relative to each other. The linear term in $BaCuO_2$ has been attributed to magnetic degrees of freedom[23] but has also been disregarded simply because it is an insulator.[44] Nanocrystalline magnetite (Fe_3O_4) and hematite (Fe_2O_3) have linear terms that have been attributed to superparamagnetism.[19, 31] The linear terms in several vanadium bronzes have been attributed to singlet bipolarons.[24] In several insulating layered oxides, the linear terms are attributed to a localized density of states associated with lattice vacancies.[5] Many investigations of insulators with linear terms adopt some form of this latter explanation since lattice vacancies are inherent to all materials to some degree; however, the only derivation of a linear heat capacity from lattice vacancies treats the vacancies the same as a free-electron gas where vacancies “move practically freely through a crystal”, which is wholly unsupported in the original manuscript.[45]

In glasses, the linear dependence on the low temperature heat capacity has been attributed to particles trapped in defect sites that create a particle-in-a-box system,[46-47] but a more common theory is based on a system of tunneling states.[3, 48-49] This theory assumes that there are two

Table 4-1: Linear Terms from Fits to the Low-temperature (T < 15 K) Heat Capacity Data (units are mJ·mol^{-1}·K^{-2})

Sample	γ	Sample	γ	Sample	γ
CuO[18]	0.022	γ-Al_2O_3 (n)[41]	1.3542	$Sr_2TiSi_2O_8$[40]	0.0803
CuO (n)*	0.489	γ-Al_2O_3 (n)[41]	1.3905	$BaCuO_2$[23]	10.6
ZnO (n)[38]	0.103	γ-Al_2O_3 (n)[41]	1.22	$BaCuO_2$[23]	12.4
Co/ZnO[38]	31.64	γ-Al_2O_3 (n)[41]	1.3912	$BaCuO_{2.14}$[23]	5.7
Co/ZnO (n)[38]	21.635	SnO_2[37]	0.172	$Li_{1.2}Ti_{1.8}O_4$[16]	3.6
$GeCo_2O_4$[21]	0.33	SnO_2 (n)[37]	0.401	$Na_{0.25}V_2O_5$[24]	11.3
CoO[20]	0.4	HfO_2[39]	0.0793	$Na_{0.28}V_2O_5$[24]	9.42
CoO[38]	0.1856	γ-FeOOH[27]	0.0927	$Na_{0.33}V_2O_5$[24]	9.85
CoO (n)[20]	6.0	γ-FeOOH[27]	0.3526	$Na_{0.40}V_2O_5$[24]	5.73
Co_3O_4*	2.138	β-FeOOH[27]	0.1449	$K_{0.20}V_2O_5$[24]	15.2
Co_3O_4 (n)*	8.46	2-line FeOOH[32]	0.1551	$Cu_{0.40}V_2O_5$[24]	60.1
Co_3O_4 (n)*	14.111	α-FeOOH[26]	0.23	$Cu_{0.55}V_2O_5$[24]	32.5
TiO_2 rut[22]	0.0993	α-Fe_2O_3[33]	0.0362	$Cu_{0.60}V_2O_5$[24]	26.4
TiO_2 ana[22]	0.1099	α-Fe_2O_3[33]	0.0224	$Ag_{0.33}V_2O_5$[24]	8.05
TiO_2 rut (n)[29]	0.508	α-Fe_2O_3 (n)[31]	1.0235	$La_{1.98}Ba_{0.02}CuO_4$[17]	0.5
TiO_2 rut (n)[29]	0.564	Fe_3O_4 (n)[19]	3.4619	$La_{0.7}Ca_{0.3}MnO_3$[25]	5.2
TiO_2 rut (n)[29]	0.4994	$FePO_4$[36]	13.211	$La_{0.7}Ba_{0.3}MnO_3$[25]	6.1
TiO_2 ana (n)[30]	0.5941	Fe_3PO_7[35]	16.32	$La_{0.7}Sr_{0.3}MnO_3$[25]	6.0
TiO_2 ana (n)[30]	0.6564	$Fe_3(P_2O_7)_2$[36]	26.613	$Y_{0.7}Sr_{0.3}MnO_3$[25]	8.1
TiO_2 ana (n)[30]	0.6877	$Fe_4(P_2O_7)_3$[35]	73.69	α-D-xylose[43]	0.4902
$Ti_{0.78}Al_{0.22}O_2$ (n)[42]	0.8118	$Fe_2P_2O_7$[34]	83.61	Muskovite[5]	25.5
$Ti_{0.5}Al_{0.5}O_2$ (n)[42]	1.101	SiO_2[28]	0.066		

*linear terms and data to be published elsewhere.
(n) indicates nanoparticles

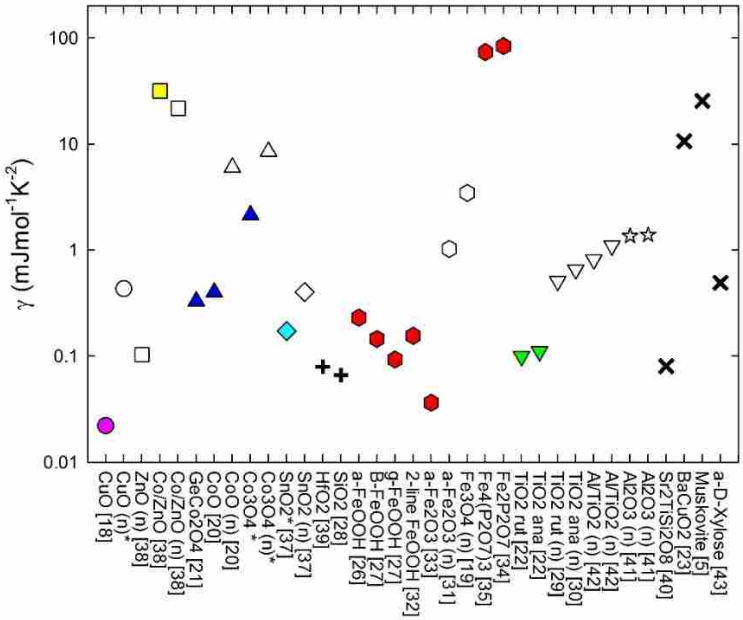

Figure 4-1: Selected Linear Terms, γ, from Low-temperature Heat Capacity Fits. Hollow symbols represent the nanophase of the material; solid symbols represent bulk.

equilibrium orientations that atoms or groups of atoms can have. The two energy minima associated with each of these orientations are separated by an energy barrier that must be overcome by phonon-assisted tunneling in order for the atoms to shift from one orientation to the other. The separation in energy between the two minima is different for every group of atoms because of local strains and the local configuration of the atoms around the group. Each of these two-level systems (TLS) for which the tunneling barrier is not too large results in a Schottky anomaly in the low temperature heat capacity[1]

$$C_{Sch} = n_{Sch}(\theta)k\left(\frac{\theta}{T}\right)^2 \frac{e^{\theta/T}}{\left(1+e^{\theta/T}\right)^2} \tag{4-1}$$

where θ is the energy separation of the two states with units of K ($\theta = \Delta E/k$), $n_{Sch}(\theta)$ is the moles of anomalies per mole of material for a given separation θ, and k is the Boltzmann constant. Because the number and energies of these tunneling systems is random, the distribution $n_{Sch}(\theta)$ can be assumed to be a constant value $n(0)$, which makes the sum of all Schottky anomalies approximated by the integral[3]

$$C_{lin}(T) = \int_0^\infty n_{Sch}(\theta)k\left(\frac{\theta}{T}\right)^2 \frac{e^{\theta/T}}{\left(1+e^{\theta/T}\right)^2} d\theta \approx \frac{\pi^2}{6}k^2 n(0)T \tag{4-2}$$

where $n(0)$ is the number of contributing TLSs per mole of sample per unit energy. As seen in Eq. 4-2 the heat capacity contribution from these TLSs is linear with temperature.

The original manuscript by Anderson, Halperin, and Varma[3] outlining this theory provides no support for the use of a TLS believed to produce a Schottky anomaly or justification for a random distribution of energies produced by the TLSs. Several others have recognized this and have attempted to provide evidence for these properties while others have modified the

model to make the TLS and distribution more meaningful.[11, 24, 50-51] A major flaw in this theory is this lack of understanding the source and distribution of the TLSs.

To understand the distribution one must first understand the heat capacity that is produced by it. The linear heat capacity in metals exists up to high temperatures (O(1000 K)) but is generally undetectable due to the much larger contribution from phonons at temperatures any higher than about 15 K; however, the linear term in insulating materials does not extend up to high temperatures, and the extent to which the linear term is nonzero/non-negligible has been investigated by several groups. Anderson *et al* claimed that the linear term of glasses must exist up to about 10 K before vanishing.[3] Investigations of $BaCuO_2$ have shown that this contribution to the heat capacity remains linear until about 30 K where it begins to decrease until becoming negligible around 40 to 50 K.[23, 44] Others investigating the heat capacity of $Fe_2P_2O_7$ claim that the linear term begins to decrease between 15 – 20 K.[34] McWhan's study of several doped Al_2O_3 compounds shows linearity until about 25 K above which the slope (γ) quickly decreases to zero.[51] Data of TiO_2 from Sandin show an excess heat capacity that increases approximately linearly until about 15 K then quickly drops to zero by about 20 K.[52] Therefore, we will consider the shape of this excess heat capacity to be linear up to about 15 K at which point, it decreases until becoming negligible around 50 K.

The broad range of insulating materials that have a linear heat capacity and the relatively similar cutoff temperature of these linear terms suggests that there exists a common underlying factor in all of these materials that produces the linear dependence in the low temperature heat capacity.

4.1.2 Lattice Vacancies

Lattice vacancies appear in all materials to some degree. At thermal equilibrium the concentration of vacancies can be estimated using the Boltzmann factor (for $n_{vac} \ll N$):[2]

$$n_{vac}/N \cong \exp(-E_v/kT) \tag{4-3}$$

where n_{vac}/N is the ratio of the number of lattice vacancies n_{vac} to the number of atoms N, E_v is the energy required to remove an atom from the lattice site inside the crystal and place it on the surface, k is Boltzmann's constant, and T is the temperature of the crystal or the temperature at which the crystal was calcined if it was suddenly cooled (thereby freezing in vacancies). For a typical E_v (about 1 eV) and calcination temperature (about 1000 K), Eq. 4-3 yields a concentration of lattice vacancies on the order of 10^{-5} moles of vacancies per mole of atoms.

Lattice vacancies are generally determined using redox titrations or thermogravimetric analysis (TGA),[53-59] but for nanomaterials and materials with very few vacancies, less conventional methods are required such as EXAFS,[60-61] XANES,[61] other X-ray techniques,[53, 61] Raman spectroscopy,[60-61] high resolution TEM,[61] EELS,[62] XEDS,[63] STEM,[64] neutron diffraction,[53, 59] and a plethora of esoteric techniques.[65-73] Each of these methods is limited by experimental error, resolution, or applicability that constrain what samples can be tested and the amount of useful information that can be obtained (hence the large number of specialized techniques). The detection limit for most of these techniques is around parts per thousand or $n_{vac}/N \approx 10^{-3}$, making these techniques only suitable for highly nonstoichiometric samples. Table 4-2 lists lattice vacancy concentrations of a wide range of materials as measured from these techniques.[57-62, 64-74]

When a lattice vacancy is present in a crystal, the atomic structure around the vacancy takes on one of two possible conformations: dimer or puckered.[74-77] Each of these conformations

Table 4-2: Lattice Vacancy Concentrations for Several Materials (units are moles of vacancy per mole of formula unit)

Sample	n_{vac}	Sample	n_{vac}
C doped TiO_2[65]	1.12×10^{-3}	CeO_2 (5 nm)[60]	6.01×10^{-3}
C doped TiO_2[65]	0.0176	CeO_2 (10 nm)[60]	2.4×10^{-3}
TiO_2 as prepared[65]	9.41×10^{-4}	CeO_2 (10 nm)[66]	2.0×10^{-3}
TiO_2 oxidized[65]	2.01×10^{-5}	CeO_2 (15 nm)[68]	2.4×10^{-4}
Fe doped TiO_2[61]	6.27×10^{-3}	CeO_2 (20 nm)[60]	1.2×10^{-4}
Cr doped $SrTiO_3$[67]	6.6×10^{-4}	CeO_2 (30 nm)[60]	2.4×10^{-5}
$LaSrCoO_x$[64]	0.25	CeO_2 (65 nm)[60]	1.2×10^{-5}
$Sr_2MgMoO_{(6-\delta)}$[58]	0.05	Fe_3O_4[73]	4.9×10^{-3}
$Ba_{0.5}Sr_{0.5}Co_{0.8}Fe_{0.2}O_{(3-\delta)}$[59]	0.661	Fe_3O_4 (10 nm)[70]	0.036
$Ba_{0.5}Sr_{0.5}Co_{0.8}Fe_{0.2}O_{(3-\delta)}$[59]	0.807	Fe_3O_4 (n)*	0.1250
$Ce_{0.9}Gd_{0.1}O_{1.95}$[69]	0.13	CuO[71]	6.2×10^{-4}
$La_{0.67}Ca_{0.33}MnO_{(3-y)}$[62]	0.065	CuO[57]	9.8×10^{-4}
$MgO \cdot 3.5Al_2O_3$[72]	0.072	CuO (n)*	0.0109
Co_3O_4*	9.5×10^{-3}	Cu_2O[57]	7.3×10^{-4}
Co_3O_4 (n)*	0.1230	SiO_2[74]	$\sim 3 \times 10^{-4}$
CoO (n)*	0.1639	Al_2O_3 (n)*	4.7×10^{-3}

*this study

has an energy minimum separated by an energy barrier. These two energy levels would result in a Schottky anomaly in the low temperature heat capacity (Eq. 4-1) with an energy separation θ equal to the difference between the two levels. Surface configurations, which are somewhat similar to vacancies due to their similar coordinations and strain, have been shown to have similar two-level systems that produce Schottky anomalies.[78-81]

The energies of the dimer and puckered configurations of amorphous SiO_2 have been investigated by Boero *et al* using first principles calculations approximating the two levels to be separated by an energy difference of about 0.25 eV.[75] Skuja reviewed several articles on spectroscopic methods used to investigate energies associated with vacancies and showed that a spectrum of energy levels up to 0.1 eV arises from vacancies in a typical solid.[82] Rigid unit modes of SiO_4 tetrahedra have two-level systems similar to lattice vacancies and have a range of

possible energies up to around 500 GHz or about 2 meV.[83] Di Valentin *et al.* investigated tunneling related to rotations of surface atoms and found tunneling barriers between about 10 and 20 meV.[79] Gryaznov *et al.* discovered lattice vacancy energy levels with energies around 20 meV different from the lattice.[84] Smith investigated librational frequencies covering the range of 30 peV to 33.5 meV.[80] Strong librational frequencies around oxygen vacancies in perovskites have been found to have energies of about 90 – 120 cm^{-1} (11 – 15 meV), and a broad spectrum of peaks below 90 cm^{-1} have been attributed to thermally induced disorder, which essentially consists of lattice vacancies as Eq. 4-3 shows.[85] From all these investigations, we conclude that energies associated with lattice vacancies have a broad distribution of possible states, likely caused by differences in the lattice surrounding each vacancy, and have an average maximum of about 20 meV.

From the information presented above, it can be seen that a single lattice vacancy results in a two-level system that is capable of producing a Schottky anomaly in the low temperature heat capacity. Multiple vacancies have a random distribution of energy differences that would yield a distribution of Schottky anomalies. The cutoff of the energies from the TLSs would also produce a cutoff (albeit gradual) in the sum of the Schottky anomalies produced from the vacancies. We will show how the energies associated with TLSs are responsible for the linear term and its cutoff temperature and matches what has been observed experimentally.

4.2 Theory and Correlations

4.2.1 Distributions

We first consider the distribution of energies associated with the TLSs from vacancies that determine $n_{Sch}(\theta)$ in Eq. 4-2. The distribution $n_{Sch}(\theta)$ used for Eq. 4-2 assumes that n_{Sch} is a

single value for all values of θ up to infinity, but we will examine several other possible and more meaningful distributions that correspond to the experimental data outlined above and that could produce a linear (or pseudo-linear) heat capacity with an appropriate ending temperature. All of the following distributions have been tailored so that $n_{Sch}(\theta)$ is negligible by about 150 K (or 13 meV). These distributions use θ with units of K rather than meV to be applicable to the Schottky heat capacity as given in Eq. 4-1. We note here that 1 meV = 11.6 K.

Figure 4-2 shows several hypothetical distributions of $n_{Sch}(\theta)$. A simple Gaussian distribution with θ_{max} centered at 30 K and a standard deviation of 40 K is shown in Figure 4-2a. In this distribution, n_{Sch} at θ = 30 K corresponds to the average energy produced by vacancies that is more probable than the others perhaps due to the homogeneous nature inside the bulk of the material. The other energies arise because of the vacancies' proximity to grain boundaries, other vacancies, or the surface, which are generally less common than a homogeneous environment. This type of distribution might be suitable for large grain, crystalline materials.

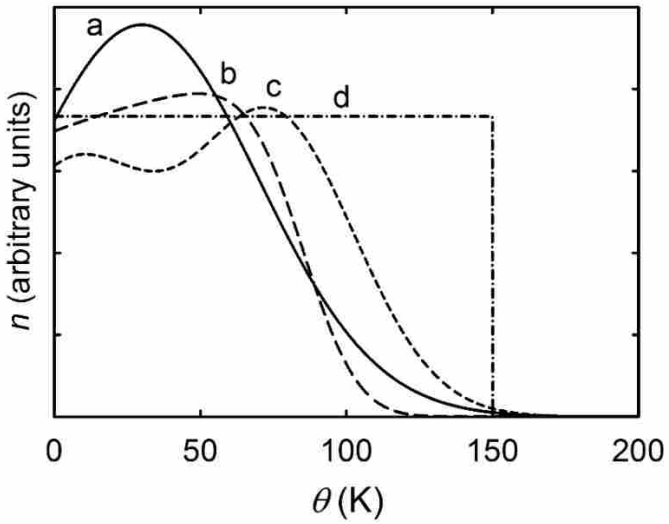

Figure 4-2: Possible Distributions of Energy Gaps, $n_{Sch}(\theta)$, of Lattice Vacancies. a) Gaussian (solid line), b) Skewed Gaussian (long dash line), c) Two Gaussians Summed (short dash line), d) Step (dash-dot-dash line).

A left skewed Gaussian that has an average θ = 85 K is shown in Figure 4-2b. The average here would again represent the vacancies in a homogeneous environment likely within the bulk of the material, but the skew would arise from a large concentration of vacancies near some similar inhomogeneous structure such as the surface. This distribution would likely apply to nanomaterials with a high surface to bulk ratio or materials with a high degree of disorder such as amorphous solids.

Figure 4-2c shows the sum of two Gaussian distributions that are centered at 5 K and 75 K with standard deviations of 28 K. These Gaussians would be similar to the one discussed for Figure 4-2a, but here we suppose the low energy Gaussian arises from vacancies near or on the surface where there is less strain, and the high energy Gaussian arises from the vacancies in the bulk of the material. This distribution may be more meaningful than the others because the center position, height, and width of each Gaussian can be varied as long as the sum has the same general shape. This allows for a different distribution for every sample that has a linear heat capacity and could therefore apply to any type of material.

A step distribution with a cutoff of θ = 150 K (based on the experimental data outlined above) is shown in Figure 4-2d. This distribution is very similar to the constant value distribution used in Eq. 4-2 and assumes that the energies associated with the lattice vacancies are completely random and only exist below a particular energy, treating vacancies on the surface, in the bulk, and near defects or grain boundaries the same. The only variable factor in this distribution is the cutoff energy, which Anderson *et al* postulated to be related to the glass transition temperature on the order of 1000 K. Although this distribution simplifies calculations, it is unlikely that vacancies' energies will be completely random because bulk and surface energetics are so

different,[86] and a meaningful distribution must not ignore surface energies since many of the materials with linear terms are nanoparticles (see Table 4-1).

4.2.2 Resultant Heat Capacity

When these distributions are used in Eq. 4-2, the resultant heat capacity as determined by numerical integration is approximately linear up to about 15 K and then gradually drops towards zero. Figure 4-3 shows the heat capacity curves (as C/T versus T in which a linear heat capacity will appear as a constant) that result from the distributions of Figure 4-2. The Gaussian distribution yields a heat capacity that deviates the most from linearity (up to about 15 %) as can be seen in Figure 4-3a. The heat capacity derived from the skewed Gaussian distribution, seen in Figure 4-3b, results in a heat capacity with less than a 5 % deviation from linearity below 15 K. The distribution created by summing two Gaussian results in a heat capacity that deviates from linearity by less than 0.8 % (see Figure 4-3c), and the step distribution results in a heat capacity that deviates from linearity by about 0.05 % below 10 K but increases to 0.3 % by 15 K (see Figure 4-3d). For temperatures much less than the cutoff temperature, the step distribution produces the same linear heat capacity result of Eq. 4-2. All of these distributions resemble the energies typically produced from lattice vacancies and result in a heat capacity function that resembles what has been observed in many insulating materials, but the sum of two Gaussian distributions appears to be the most meaningful and has a high degree of linearity.

The distributions discussed above are just a few of the possible distributions that result in a linear heat capacity similar to what has been reported in the literature.[3, 23, 34, 44, 51-52] The actual distributions likely vary from the distributions presented here, but these distributions demonstrate the general shape that $n_{Sch}(\theta)$ must have. Low temperature heat capacity data can have an uncertainty of about 2 %, and fits can have an uncertainty on the order of 1 %; therefore, the

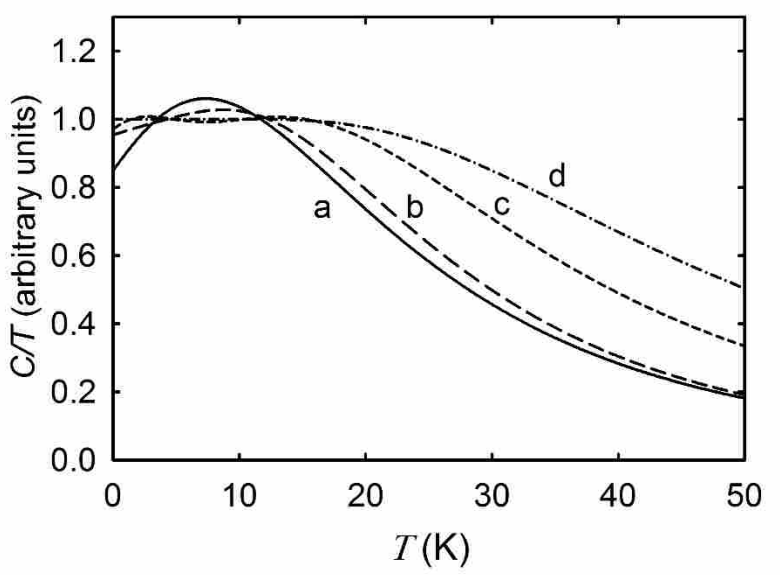

Figure 4-3: Heat Capacities Generated from the Distribution of Figure 4-2. a) Gaussian, b) Skewed Gaussian, c) Two Gaussians Summed, and d) Step. Plots are of *C*/*T*; therefore, a linear heat capacity will be a constant in these plots.

nonlinearity of these derived heat capacities would likely be buried in the error of the data or fit. These results show that lattice vacancies do indeed produce a linear (or pseudo-linear) contribution to the low temperature heat capacity.

4.2.3 Quantification of Vacancies from γ

Because each Schottky anomaly is a result of a lattice vacancy, the sum of all Schottky anomalies will give a measure of the total number of vacancies n_{vac} in a given sample. Finding n_{vac} is simply done by integrating the distribution $n_{Sch}(\theta)$ over all θ. The height or normalization of the distribution will be manifest in the slope or linear term γ of the resultant heat capacity. We have calculated linear terms from typical vacancy concentrations of $n_{vac} = 10^{-5}$ to 1 vacancies per formula unit (see Table 4-2). Each distribution (see Figure 4-2) was normalized to these values, and the linear term was determined by averaging the resultant heat capacity divided by

temperature (*C/T*) from 0.5-15 K. These values were then used to determine constants of proportionality for each distribution by fitting to a line with zero intercept. The proportionalities are in the form $\gamma_{calc} = c \times n_{vac}$, and values of c were found to be 157, 151, 115, and 91 $mJ \cdot mol^{-1} \cdot K^{-2}$ for the Gaussian, skewed Gaussian, two-Gaussian, and step distributions, respectively. These calculations have an estimated uncertainty of about 6 % based on the heat capacity data, the fit, and the distribution's linearity, but with better data and fits an uncertainty of about 2% would be reasonable.

4.2.4 Comparison to Experimental Data

To test the results of this model against actual data, we have measured the linear terms and vacancy concentrations of Co_3O_4, Co_3O_4 (n), CoO (n), Fe_3O_4 (n), CuO (n), and Al_2O_3 (n) which are part of separate, ongoing projects in our laboratory. The samples were found to have no chemical or phase impurities, and all characterization and thermodynamic data will be reported elsewhere.

The low temperature heat capacities of Fe_3O_4 (n), CoO (n), and Al_2O_3 (n) and the experimental details have been published previously.[19-20, 41] The other samples' heat capacities were measured on a Quantum Design Physical Properties Measurement System (PPMS) from 1.8 – 300 K following the method of Shi *et al.*[87] Approximately 30 mg of each sample were mixed with copper stips (Alpha Aesar mass fraction purity 0.9995) to provide better thermal contact and put into copper cups that were pressed into pellets. Addenda measurements were performed that measured the heat capacity of the calorimeter and the grease used to attach the sample. After each addenda measurement, the sample was attached to the PPMS puck, and the heat capacity was measured. The system automatically corrects for the heat capacities of the

calorimeter and grease, and the heat capacity of the copper was corrected for using data from Stevens and Boerio-Goates.[88] Data measured on the PPMS using this method have an estimated uncertainty of ± 0.02·C_p° for 2 < T/K < 10 and ± 0.01·C_p° for 10 < T/K < 300.[87] The data below 10 K were fit to a theoretical function of the form

$$C(T) = \sum_{i=3,5,7} B_i T^i + \gamma T \tag{4-4}$$

where the summation term represents the contribution from lattice vibrations, and the linear term is related to lattice vacancies. The fits having the same number of lattice terms but no linear contribution resulted in %RMS values of 7.16, 18.1, and 13.2 for Co_3O_4, Co_3O_4 (n), and CuO (n), respectively, whereas the fits including the linear term resulted in %RMS values of 0.82, 1.80, and 1.18. The values of γ obtained from the fits were 2.138, 14.111, and 0.489 mJ·mol^{-1}·K^{-2} for Co_3O_4, Co_3O_4 (n), and CuO (n), respectively (see Table 4-1), and the approximated uncertainty in these values is 2.5 % based on the heat capacity data and the fitting error.

The vacancy concentrations of Co_3O_4, Co_3O_4 (n), CoO (n), and Fe_3O_4 (n) were measured using a thermogravimetric reduction technique. Approximately 20 mg of each sample were placed in Pt crucibles which were inserted into a Mettler Toledo TGA/DSC 1 equipped with an automated GC 200 gas controller. To remove any surface-bound water the samples were heated to 400 °C in He and cooled back to room temperature. The reduction gas was 10 % H_2 in He with a flow rate of 100 mL·min^{-1}, and the samples were heated at a rate of 3 °C·min^{-1} to 900 °C. Reduction occurred abruptly at about 300 °C for the cobalt oxides and at about 400 for the iron oxide and resulted in mass losses of 26.5310 %, 25.9726 %, 18.50 %, and 28.50 % corresponding to stoichiometries of $Co_3O_{3.9905}$, $Co_3O_{3.8770}$ (n), $CoO_{0.8361}$ (n), and $Fe_{2.8750}O_4$ (n) respectively, yielding vacancy concentrations of n_{vac} = 0.0095, 0.1230, 0.1639, and 0.1250. The approximated uncertainty of these values is 15 %.

The vacancy concentration of CuO (n) was determined by performing Rietveld refinement on powder X-ray diffraction (XRD) data collected at 100 K. CuO powder was packed into a polyimide capillary with an inner diameter of 0.012 mm, and XRD data were collected in transmission mode using a MACH3 four circle single crystal diffractometer coupled to a Bruker Apex II CCD detector with a Bruker-Nonius FR591 rotating anode X-ray source producing Cu K_α radiation (λ = 1.5418 Å). Data were collected between 2° – 133° 2θ by performing a series of 8 overlapping phi 360 scans. The Bruker XRD^2 program was used to merge the images and integrate the intensity of the diffraction rings. Rietveld refinement was performed using the PANalytical Highscore Plus software. The details of the analysis will be published elsewhere, but from the refinement, copper atoms were found to be slightly deficient yielding $Cu_{0.9891}O$ or n_{vac} = 0.0109 having an approximate uncertainty of 10 %.

The vacancy concentration of Al_2O_3 (n) was determined using Eq. 4-3 and the value of E_v (0.18 eV) from Tanaka *et al*.[89] Although the Al_2O_3 (n) samples used to determine γ were calcined at 973 K, we can assume that $T \approx 300$ K because the samples were cooled slowly to room temperature after calcination but were cooled quickly from room temperature to perform heat capacity measurements.[41] Using these values in Eq. 4-3 and accounting for the five atoms per formula unit gives an n_{vac} of 0.0047 moles of vacancies per mole of Al_2O_3 (n). The estimated uncertainty of n_{vac} determined using this method is 50 %.

All these values of γ and n_{vac} are plotted in Figure 4-4 along with the proportionalities derived herein. The plot shows how γ increases as n_{vac} increases. The error bars represent the uncertainties discussed above for each value of n_{vac}, and the uncertainty in γ of 2.5 % is smaller than the size of the symbols. The deviations of the ratio of the actual values of γ and n_{vac} ($c = \gamma/n_{vac}$) from our calculations are 40 % (using the Gaussian distribution) for Al_2O_3, 30 % (using

the Gaussian distribution) for Co_3O_4, 100 % (using the step distribution) for CuO (n), 6.3 % (using 2-Gaussian distributions) for Co_3O_4 (n), 230 % (using the step distribution) for Fe_3O_4 (n), 150 % (using the step distribution) for CoO (n).

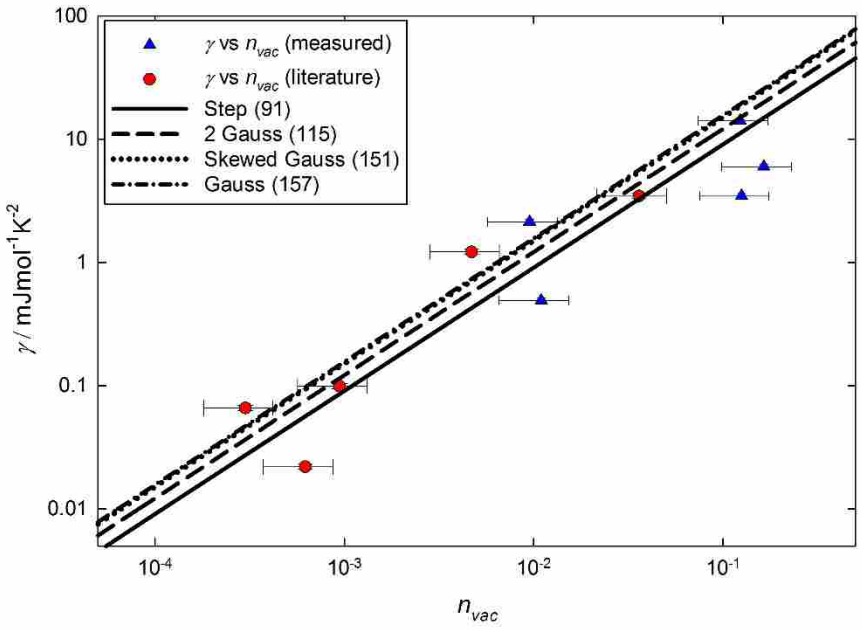

Figure 4-4: γ vs n_{vac} of Several Samples. From left to right: Al_2O_3 (n), Co_3O_4, CuO (n), Co_3O_4 (n), Fe_3O_4 (n), and CoO (n). Also shown are the lines derived from the four distributions of Schottky anomalies with the slopes (units of $mJ \cdot mol^{-1} \cdot K^{-2}$) shown in parenthesis in the legend.

The experimental values of γ and n_{vac} differ from our theoretical values by at most a factor of two or three and as little as a few percent. When all the uncertainties are taken into account, these calculations show qualitative agreement as well as quantitative agreement providing further evidence that the linear term of insulating materials does indeed stem from lattice vacancies. As further evidence supporting our claims, we note that the differences between the measured and calculated values of γ from n_{vac} are similar despite the method used to determine n_{vac}.

4.2.5 Trends in γ and n_{vac}

As a final note, we recognize several trends emphasizing our conclusions. All values of γ found in Table 4-1 lie between 0.01 $mJ \cdot mol^{-1} \cdot K^{-2}$ and 100 $mJ \cdot mol^{-1} \cdot K^{-2}$, and values of n_{vac} in Table 4-2 lie between 10^{-5} and 1, which is the same range of values we would expect when applying our calculations to γ. Values of γ for nano phase TiO_2, CoO, Co_3O_4, α-Fe_2O_3, CuO, SnO_2, and ZnO are all larger than the bulk phase values of γ. Values of n_{vac} from Table 4-2 also increase as particle size decreases for CeO_2 and Fe_3O_4. The Co doped ZnO and Al doped TiO_2 systems have γ much greater than what would be expected for a simple CoO/ZnO or Al_2O_3/TiO_2 mixture, and values of n_{vac} for TiO_2 are also larger when dopants are present. Mitchell has also shown that the concentration of defects increases with increasing dopant concentrations.[72]

4.3 Conclusion

We have shown that the linear term, which is often necessary to fit the low temperature heat capacity data for nonmetallic materials, is related to the number of lattice vacancies. We have created several distributions of $n_{Sch}(\theta)$ that have similar energy cutoffs to experimental data from the literature and are physically meaningful. The vacancy energies associated with these distributions are assumed to result in small Schottky anomalies due to a puckering of the lattice. These distributions have been shown to produce a linear heat capacity similar to what has been observed for these kinds of materials. We have measured values of γ and n_{vac} of several samples and compared those to our theoretical values. These values show qualitative and quantitative agreement with our model, and linear terms and lattice vacancy concentrations have been shown to have many similar trends providing further evidence for our arguments. This manuscript provides meaningful evidence supporting the claim that the linear term in insulating materials results from lattice vacancies.

REFERENCES

1. Gopal, E. S. R., *Specific Heats at Low Temperatures*; Plenum Press New York, 1966; Vol. 227.

2. Kittel, C.; McEuen, P., *Introduction to Solid State Physics*; Wiley New York, 1996; Vol. 7.

3. Anderson, P. W.; Halperin, B.; Varma, C. M., Anomalous Low-Temperature Thermal Properties of Glasses and Spin Glasses. *Philosophical Magazine* **1972**, *25*, 1-9.

4. Phillips, N. E.; Emerson, J. P.; Fisher, R. A.; Gordon, J. E.; Woodfield, B. F.; Wright, D. A., Is There an Intrinsic Linear Term in the Specific Heat of Yba2cu3o7? *Physica C: Superconductivity* **1994**, *235–240, Part 3*, 1737-1738.

5. Coey, J. M. D.; Von Molnar, S.; Torressen, A., Low-Temperature Specific Heat of Bi2sr2cacu2o8: Comparison with Some Other Layered Oxides. *Journal of the Less Common Metals* **1989**, *151*, 191-194.

6. Bardeen, J.; Cooper, L. N.; Schrieffer, J. R., Theory of Superconductivity. *Physical Review* **1957**, *108*, 1175.

7. Fisher, R.; Gordon, J.; Phillips, N., Specific Heat of the High-T C Oxide Superconductors. *Journal of Superconductivity* **1988**, *1*, 231-294.

8. Phillips, N. E.; Fisher, R.; Gordon, J.; Kim, S.; Stacy, A.; Crawford, M.; McCarron III, E., Specific Heat of Yba_ {2} Cu_ {3} O_ {7}: Origin of the" Linear" Term and Volume Fraction of Superconductivity. *Physical review letters* **1990**, *65*, 357.

9. Wright, D.; Emerson, J.; Woodfield, B.; Gordon, J.; Fisher, R.; Phillips, N., Low-Temperature Specific Heat of Yba_ {2} Cu_ {3} O_ {7-Δ}, 0≤ Δ≤ 0.2: Evidence for D-Wave Pairing. *Physical review letters* **1999**, *82*, 1550.

10. Phillips, N. E.; Emerson, J. P.; Fisher, R. A.; Gordon, J. E.; Woodfield, B. F.; Wright, D. A., Specific Heat of Yba2cu3o7. *Journal of Superconductivity* **1994**, *7*, 251-255.

11. Golding, B.; Birge, N.; Haemmerle, W.; Cava, R.; Rietman, E., Tunneling Systems in Superconducting Yba_{2} Cu_{3} O_{7}. *Physical Review B* **1987**, *36*, 5606-5608.

12. Eckert, D.; Junod, A.; Bezinge, A.; Graf, T.; Muller, J., Low-Temperature Specific Heat of Yba2cu3o7, Yba2cu3o6, Y2bacuo5, Yba3cu2o7, Bacuo2, and Cuo. *Journal of Low Temperature Physics* **1988**, *73*, 241-254.

13. Moler, K. A.; Sisson, D. L.; Urbach, J. S.; Beasley, M. R.; Kapitulnik, A.; Baar, D. J.; Liang, R.; Hardy, W. N., Specific Heat of Yba 2 Cu 3 O 7-Δ. *Physical Review B* **1997**, *55*, 3954.

14. Emerson, J.; Wright, D.; Woodfield, B.; Reklis, S.; Gordon, J.; Fisher, R.; Phillips, N., Dependence of the Low-Temperature Specific Heat of Yba2cu3o7− Δ on Δ and Magnetic Field: The H1/2t Term for H≠ 0; Absence of Evidence for a T2 Term for H= 0. *Journal of Low Temperature Physics* **1996**, *105*, 897-902.

15. Emerson, J.; Wright, D.; Woodfield, B.; Gordon, J.; Fisher, R.; Phillips, N., Specific Heat of Yba_ {2} Cu_ {3} O_ {7-Δ}, 0≤ Δ≤ 0.2: Concentrations of Paramagnetic Centers and Values of Other Parameters as Functions of Δ. *Physical review letters* **1999**, *82*, 1546.

16. McCallum, R.; Johnston, D.; Luengo, C.; Maple, M., Superconducting and Normal State Properties of Li1+ X Ti2− X O4 Spinel Compounds. Ii. Low-Temperature Heat Capacity. *Journal of Low Temperature Physics* **1976**, *25*, 177-193.

17. Kumagai, K.; Nakamichi, Y.; Watanabe, I.; Nakamura, Y.; Nakajima, H.; Wada, N.; Lederer, P., Linear Temperature Term of Heat Capacity in Insulating and Superconducting La-Ba-Cu-O Systems. *Physical review letters* **1988**, *60*, 724.

18. Junod, A.; Eckert, D.; Triscone, G.; Müller, J.; Reichardt, W., A Study of the Magnetic Transitions in Cuo: Specific Heat (1-330 K), Magnetic Susceptibility and Phonon Density of States. *Journal of Physics: Condensed Matter* **1989**, *1*, 8021.

19. Snow, C. L.; Shi, Q.; Boerio-Goates, J.; Woodfield, B. F., Heat Capacity Studies of Nanocrystalline Magnetite (Fe3o4). *The Journal of Physical Chemistry C* **2010**, *114*, 21100-21108.

20. Wang, L.; Vu, K.; Navrotsky, A.; Stevens, R.; Woodfield, B. F.; Boerio-Goates, J., Calorimetric Study: Surface Energetics and the Magnetic Transition in Nanocrystalline Coo. *Chemistry of materials* **2004**, *16*, 5394-5400.

21. Lashley, J.; Stevens, R.; Crawford, M.; Boerio-Goates, J.; Woodfield, B.; Qiu, Y.; Lynn, J.; Goddard, P.; Fisher, R., Specific Heat and Magnetic Susceptibility of the Spinels Geni_ {2} O_ {4} and Geco_ {2} O_ {4}. *Physical Review B* **2008**, *78*, 104406.

22. Smith, S. J.; Stevens, R.; Liu, S.; Li, G.; Navrotsky, A.; Boerio-Goates, J.; Woodfield, B. F., Heat Capacities and Thermodynamic Functions of Tio2 Anatase and Rutile: Analysis of Phase Stability. *American Mineralogist* **2009**, *94*, 236-243.

23. Fisher, R. A.; Wright, D. A.; Emerson, J. P.; Woodfield, B. F.; Phillips, N. E.; Wang, Z. R.; Johnston, D. C., Low-Temperature Specific Heat of Bacuo_{2} and Bacuo_{2.14} in Magnetic Fields to 7 T. *Physical Review B* **2000**, *61*, 538-548.

24. Chakraverty, B.; Sienko, M.; Bonnerot, J., Low-Temperature Specific Heat and Magnetic Susceptibility of Nonmetallic Vanadium Bronzes. *Physical Review B* **1978**, *17*, 3781.

25. Coey, J. M. D.; Viret, M.; Ranno, L.; Ounadjela, K., Electron Localization in Mixed-Valence Manganites. *Physical review letters* **1995**, *75*, 3910.

26. Majzlan, J.; Navrotsky, A.; Woodfield, B. F.; Lang, B. E.; Boerio-Goates, J.; Fisher, R. A., Phonon, Spin-Wave, and Defect Contributions to the Low-Temperature Specific Heat of A-Feooh. *Journal of Low Temperature Physics* **2003**, *130*, 69-76.

27. Snow, C. L.; Smith, S. J.; Lang, B. E.; Shi, Q.; Boerio-Goates, J.; Woodfield, B. F.; Navrotsky, A., Heat Capacity Studies of the Iron Oxyhydroxides Akaganéite (B-Feooh) and Lepidocrocite (Γ-Feooh). *The Journal of Chemical Thermodynamics* **2011**, *43*, 190-199.

28. Stephens, R., Low-Temperature Specific Heat and Thermal Conductivity of Noncrystalline Dielectric Solids. *Physical Review B* **1973**, *8*, 2896.

29. Schliesser, J. M.; Smith, S. J.; Li, G.; Li, L.; Walker, T. F.; Parry, T.; Boerio-Goates, J.; Woodfield, B. F., Heat Capacity and Thermodynamic Functions of Nano-Tio2 Rutile in Relation to Bulk-Tio2 Rutile. *The Journal of Chemical Thermodynamics* **2014**.

30. Schliesser, J. M.; Smith, S. J.; Li, G.; Li, L.; Walker, T. F.; Perry, T.; Boerio-Goates, J.; Woodfield, B. F., Heat Capacity and Thermodynamic Functions of Nano-Tio< Sub> 2</Sub> Anatase in Relation to Bulk-Tio< Sub> 2</Sub> Anatase. *The Journal of Chemical Thermodynamics* **2014**.

31. Snow, C. L.; Lee, C. R.; Shi, Q.; Boerio-Goates, J.; Woodfield, B. F., Size-Dependence of the Heat Capacity and Thermodynamic Properties of Hematite (A-Fe< Sub> 2</Sub> O< Sub> 3</Sub>). *The Journal of Chemical Thermodynamics* **2010**, *42*, 1142-1151.

32. Snow, C.; Lilova, K.; Radha, A.; Shi, Q.; Smith, S.; Navrotsky, A.; Boerio-Goates, J.; Woodfield, B., Heat Capacity and Thermodynamics of a Synthetic Two-Line Ferrihydrite, Feooh< Sup>.</Sup> 0.027 H< Sub> 2</Sub> O. *The Journal of Chemical Thermodynamics* **2013**, *58*, 307-314.

33. Snow, C. L.; Shi, Q.; Boerio-Goates, J.; Woodfield, B. F., Heat Capacity, Third-Law Entropy, and Low-Temperature Physical Behavior of Bulk Hematite (A-Fe< Sub> 2</Sub> O< Sub> 3</Sub>). *The Journal of Chemical Thermodynamics* **2010**, *42*, 1136-1141.

34. Shi, Q.; Zhang, L.; Schlesinger, M. E.; Boerio-Goates, J.; Woodfield, B. F., Low Temperature Heat Capacity Study of Fe(Po3)3 and Fe2p2o7. *The Journal of Chemical Thermodynamics* **2013**, *61*, 51-57.

35. Shi, Q.; Zhang, L.; Schlesinger, M. E.; Boerio-Goates, J.; Woodfield, B. F., Low Temperature Heat Capacity Study of Fe< Sub> 3</Sub> Po< Sub> 7</Sub> and Fe< Sub> 4</Sub>(P< Sub> 2</Sub> O< Sub> 7</Sub>)< Sub> 3</Sub>. *The Journal of Chemical Thermodynamics* **2013**, *62*, 86-91.

36. Shi, Q.; Zhang, L.; Schlesinger, M. E.; Boerio-Goates, J.; Woodfield, B. F., Low Temperature Heat Capacity Study of Fepo< Sub> 4</Sub> and Fe< Sub> 3</Sub>(P< Sub> 2</Sub> O< Sub> 7</Sub>)< Sub> 2</Sub>. *The Journal of Chemical Thermodynamics* **2013**, *62*, 35-42.

37. Shi, Q.; Boerio-Goates, J.; Woodfield, K.; Rytting, M.; Pulsipher, K.; Spencer, E. C.; Ross, N. L.; Navrotsky, A.; Woodfield, B. F., Heat Capacity Studies of Surface Water Confined on Cassiterite (Sno2) Nanoparticles. *The Journal of Physical Chemistry C* **2012**, *116*, 3910-3917.

38. Ma, C.; Shi, Q.; Woodfield, B. F.; Navrotsky, A., Low Temperature Heat Capacity of Bulk and Nanophase Zno and Zn< Sub> 1-X</Sub> Co< Sub> X</Sub> O Wurtzite Phases. *The Journal of Chemical Thermodynamics* **2013**, *60*, 191-196.

39. Zhou, W.; Shi, Q.; Woodfield, B. F.; Navrotsky, A., Heat Capacity of Hafnia at Low Temperature. *The Journal of Chemical Thermodynamics* **2011**, *43*, 970-973.

40. Shi, Q.; Park, T.-J.; Schliesser, J.; Navrotsky, A.; Woodfield, B. F., Low Temperature Heat Capacity Study of Ba< Sub> 2</Sub> Tisi< Sub> 2</Sub> O< Sub> 8</Sub> and Sr< Sub> 2</Sub> Tisi< Sub> 2</Sub> O< Sub> 8</Sub>. *The Journal of Chemical Thermodynamics* **2014**, *72*, 77-84.

41. Spencer, E. C.; Huang, B.; Parker, S. F.; Kolesnikov, A. I.; Ross, N. L.; Woodfield, B. F., The Thermodynamic Properties of Hydrated Γ-Al2o3 Nanoparticles. *The Journal of chemical physics* **2013**, *139*, 244705.

42. Olsen, R. E.; Alam, T. M.; Bartholomew, C. H.; Enfield, D. B.; Schliesser, J.; Woodfield, B. F., Structure Analysis of Al-Modified Tio2 Nano Catalyst Supports. *The Journal of Physical Chemistry C* **2014**, *118*, 9176-9186.

43. Ribeiro da Silva, M. A.; Ribeiro da Silva, M. D.; Lobo Ferreira, A. I.; Shi, Q.; Woodfield, B. F.; Goldberg, R. N., Thermochemistry of A-D-Xylose (Cr). *The Journal of Chemical Thermodynamics* **2012**.

44. Genoud, J.-Y.; Mirmelstein, A.; Triscone, G.; Junod, A.; Muller, J., Phase Stability and Low-Temperature Specific Heat up to 14 T of Bacuo_ {X} as a Function of Oxygen Stoichiometry. *Physical Review B* **1995**, *52*, 12833.

45. Andreev, A.; Lifshits, I., Quantum Theory of Defects in Crystals. *ZHUR EKSPER TEORET FIZIKI* **1969**, *56*, 2057-2068.

46. Rosenstock, H. B., Anomalous Specific Heat of Glasses: Its Temperature Dependence. *Journal of Non-Crystalline Solids* **1972**, *7*, 123-126.

47. Fisher, R. A., Anomalous Heat Capacity of Vitreous Silica: Effect of Interstitial 4he. *Journal of Non-Crystalline Solids* **1980**, *41*, 251-256.

48. Phillips, W., Tunneling States in Amorphous Solids. *Journal of Low Temperature Physics* **1972**, *7*, 351-360.

49. Phillips, W., Two-Level States in Glasses. *Reports on Progress in Physics* **1987**, *50*, 1657.

50. Xu, J.; Tang, J.; Sato, K.; Tanabe, Y.; Miyasaka, H.; Yamashita, M.; Heguri, S.; Tanigaki, K., Low-Temperature Heat Capacity of Sr 8 Ga 16 Ge 30 and Ba 8 Ga 16 Ge 30:

Tunneling States and Electron-Phonon Interaction in Clathrates. *Physical Review B* **2010**, *82*, 085206.

51. McWhan, D.; Varma, C.; Hsu, F.; Remeika, J., Low-Temperature Heat Capacity of Alkali-Metal and Silver B-Aluminas. *Physical Review B* **1977**, *15*, 553.

52. Sandin, T.; Keesom, P., Specific Heat and Paramagnetic Susceptibility of Stoichiometric and Reduced Rutile (Ti O 2) from 0.3 to 20 K. *Physical Review* **1969**, *177*, 1370.

53. Wang, Z. L.; Yin, J. S.; Jiang, Y. D., Eels Analysis of Cation Valence States and Oxygen Vacancies in Magnetic Oxides. *Micron* **2000**, *31*, 571-580.

54. Liu, L.; Lee, T.; Qiu, L.; Yang, Y.; Jacobson, A., A Thermogravimetric Study of the Phase Diagram of Strontium Cobalt Iron Oxide, Srco< Sub> 0.8</Sub> Fe< Sub> 0.2</Sub> O< Sub> 3− Δ</Sub>. *Materials research bulletin* **1996**, *31*, 29-35.

55. Mizusaki, J.; Mima, Y.; Yamauchi, S.; Fueki, K.; Tagawa, H., Nonstoichiometry of the Perovskite-Type Oxides La< Sub> 1− X</Sub> Sr< Sub> X</Sub> Coo< Sub> 3− Δ</Sub>. *Journal of solid state chemistry* **1989**, *80*, 102-111.

56. Lankhorst, M. H.; Bouwmeester, H.; Verweij, H., High-Temperature Coulometric Titration of La< Sub> 1− X</Sub> Sr< Sub> X</Sub> Coo< Sub> 3− Δ</Sub>: Evidence for the Effect of Electronic Band Structure on Nonstoichiometry Behavior. *Journal of solid state chemistry* **1997**, *133*, 555-567.

57. Tretyakov, Y. D.; Komarov, V.; Prosvirnina, N.; Kutsenok, I., Nonstoichiometry and Defect Structures in Copper Oxides and Ferrites. *Journal of solid state chemistry* **1972**, *5*, 157-167.

58. Matsuda, Y.; Karppinen, M.; Yamazaki, Y.; Yamauchi, H., Oxygen-Vacancy Concentration in< I> a</I>< Sub> 2</Sub> Mgmoo< Sub> 6−</Sub>< I> Δ</I> Double-Perovskite Oxides. *Journal of Solid State Chemistry* **2009**, *182*, 1713-1716.

59. McIntosh, S.; Vente, J. F.; Haije, W. G.; Blank, D. H. A.; Bouwmeester, H. J. M., Oxygen Stoichiometry and Chemical Expansion of Ba0.5sr0.5co0.8fe0.2o3-Δ Measured by in Situ Neutron Diffraction. *Chemistry of Materials* **2006**, *18*, 2187-2193.

60. Kosacki, I.; Suzuki, T.; Anderson, H. U.; Colomban, P., Raman Scattering and Lattice Defects in Nanocrystalline Ceo2 Thin Films. *Solid State Ionics* **2002**, *149*, 99-105.

61. Wu, Q.; Zheng, Q.; van de Krol, R., Creating Oxygen Vacancies as a Novel Strategy to Form Tetrahedrally Coordinated Ti4+ in Fe/Tio2 Nanoparticles. *The Journal of Physical Chemistry C* **2012**, *116*, 7219-7226.

62. Wang, Z. L.; Yin, J.; Jiang, Y.; Zhang, J., Studies of Mn Valence Conversion and Oxygen Vacancies in Lacamno Using Electron Energy-Loss Spectroscopy. *Applied physics letters* **1997**, *70*, 3362.

63. Mayer, T.; Elam, J.; George, S.; Kotula, P.; Goeke, R., Atomic-Layer Deposition of Wear-Resistant Coatings for Microelectromechanical Devices. *Applied Physics Letters* **2003**, *82*, 2883-2885.

64. Kim, Y.-M.; He, J.; Biegalski, M. D.; Ambaye, H.; Lauter, V.; Christen, H. M.; Pantelides, S. T.; Pennycook, S. J.; Kalinin, S. V.; Borisevich, A. Y., Probing Oxygen Vacancy Concentration and Homogeneity in Solid-Oxide Fuel-Cell Cathode Materials on the Subunit-Cell Level. *Nature Materials* **2012**, *11*, 888-894.

65. Enache, C. S.; Schoonman, J.; Van Krol, R., The Photoresponse of Iron-and Carbon-Doped Tio2 (Anatase) Photoelectrodes. *Journal of electroceramics* **2004**, *13*, 177-182.

66. Chiang, Y.; Lavik, E.; Kosacki, I.; Tuller, H.; Ying, J., Nonstoichiometry and Electrical Conductivity of Nanocrystalline Ceo {2-X}. *Journal of Electroceramics* **1997**, *1*, 7-14.

67. Janousch, M.; Meijer, G. I.; Staub, U.; Delley, B.; Karg, S. F.; Andreasson, B. P., Role of Oxygen Vacancies in Cr-Doped Srtio3 for Resistance-Change Memory. *Advanced Materials* **2007**, *19*, 2232-2235.

68. Hwang, J.-H.; Mason, T. O., Defect Chemistry and Transport Properties of Nanocrystalline Cerium Oxide. *Zeitschrift für Physikalische Chemie* **1998**, *207*, 21-38.

69. Duncan, K. L.; Wang, Y.; Bishop, S. R.; Ebrahimi, F.; Wachsman, E. D., Role of Point Defects in the Physical Properties of Fluorite Oxides. *Journal of the American Ceramic Society* **2006**, *89*, 3162-3166.

70. Schedin, F.; Hill, E.; Van der Laan, G.; Thornton, G., Magnetic Properties of Stoichiometric and Nonstoichiometric Ultrathin Fe3o4 (111) Films on Al2o3 (0001). *Journal of applied physics* **2004**, *96*, 1165-1169.

71. O'Keeffe, M.; Moore, W. J., Thermodynamics of the Formation and Migration of Defects in Cuprous Oxide. *The Journal of Chemical Physics* **1962**, *36*, 3009-3013.

72. Mitchell, T. E., Dislocations and Mechanical Properties of Mgo-Al2o3 Spinel Single Crystals. *Journal of the American Ceramic Society* **1999**, *82*, 3305-3316.

73. Koenitzer, J.; Keesom, P.; Honig, J., Heat Capacity of Magnetite in the Range 0.3 to 10 K. *Physical Review B* **1989**, *39*, 6231.

74. Mysovsky, A. S.; Sushko, P. V.; Mukhopadhyay, S.; Edwards, A. H.; Shluger, A. L., Calibration of Embedded-Cluster Method for Defect Studies in Amorphous Silica. *Physical Review B* **2004**, *69*, 085202.

75. Boero, M.; Pasquarello, A.; Sarnthein, J.; Car, R., Structure and Hyperfine Parameters of E 1′ Centers in A-Quartz and in Vitreous Sio 2. *Physical review letters* **1997**, *78*, 887.

76. Van de Walle, C. G.; Blöchl, P., First-Principles Calculations of Hyperfine Parameters. *Physical Review B* **1993**, *47*, 4244.

77. Blöchl, P. E., First-Principles Calculations of Defects in Oxygen-Deficient Silica Exposed to Hydrogen. *Physical Review B* **2000**, *62*, 6158.

78. Boerio-Goates, J.; Smith, S. J.; Liu, S.; Lang, B. E.; Li, G.; Woodfield, B. F.; Navrotsky, A., Characterization of Surface Defect Sites on Bulk and Nanophase Anatase and Rutile Tio2 by Low-Temperature Specific Heat. *The Journal of Physical Chemistry C* **2013**, *117*, 4544-4550.

79. Di Valentin, C.; Tilocca, A.; Selloni, A.; Beck, T.; Klust, A.; Batzill, M.; Losovyj, Y.; Diebold, U., Adsorption of Water on Reconstructed Rutile Tio2 (011)-(2× 1): Ti O Double Bonds and Surface Reactivity. *Journal of the American Chemical Society* **2005**, *127*, 9895-9903.

80. Smith, D., Hindered Rotation of the Ammonium Ion in the Solid State. *Chemical reviews* **1994**, *94*, 1567-1584.

81. Li, J. C. M.; Pitzer, K. S., Energy Levels and Thermodynamic Functions for Molecules with Internal Rotation. Iv. Extended Tables for Molecules with Small Moments of Inertia. *The Journal of Physical Chemistry* **1956**, *60*, 466-474.

82. Skuja, L., Optically Active Oxygen-Deficiency-Related Centers in Amorphous Silicon Dioxide. *Journal of Non-Crystalline Solids* **1998**, *239*, 16-48.

83. Buchenau, U.; Nücker, N.; Dianoux, A., Neutron Scattering Study of the Low-Frequency Vibrations in Vitreous Silica. *Physical Review Letters* **1984**, *53*, 2316.

84. Gryaznov, D.; Blokhin, E.; Sorokine, A.; Kotomin, E. A.; Evarestov, R. A.; Bussmann-Holder, A.; Maier, J., A Comparative Ab Initio Thermodynamic Study of Oxygen Vacancies in Zno and Srtio3: Emphasis on Phonon Contribution. *The Journal of Physical Chemistry C* **2013**, *117*, 13776-13784.

85. Colomban, P.; Romain, F.; Neiman, A.; Animitsa, I., Double Perovskites with Oxygen Structural Vacancies: Raman Spectra, Conductivity and Water Uptake. *Solid State Ionics* **2001**, *145*, 339-347.

86. Huang, B.; Schliesser, J.; Olsen, R. E.; J Smith, S.; F Woodfield, B., Synthesis and Thermodynamics of Porous Metal Oxide Nanomaterials. *Current Inorganic Chemistry* **2014**, *4*, 40-53.

87. Shi, Q.; Boerio-Goates, J.; Woodfield, B. F., An Improved Technique for Accurate Heat Capacity Measurements on Powdered Samples Using a Commercial Relaxation Calorimeter. *The Journal of Chemical Thermodynamics* **2011**, *43*, 1263-1269.

88. Stevens, R.; Boerio-Goates, J., Heat Capacity of Copper on the Its-90 Temperature Scale Using Adiabatic Calorimetry. *The Journal of Chemical Thermodynamics* **2004**, *36*, 857-863.

89. Tanaka, I.; Oba, F.; Tatsumi, K.; Kunisu, M.; Nakano, M.; Adachi, H., Theoretical Formation Energy of Oxygen-Vacancies in Oxides. *Materials Transactions* **2002**, *43*, 1426-1429.

5 EXPERIMENTAL HEAT CAPACITIES, EXCESS ENTROPIES, AND MAGNETIC PROPERTIES OF BULK AND NANO FE3O4-CO3O4 AND FE3O4-MN3O4 SPINEL SOLID SOLUTIONS

5.1 Introduction

Metal oxides with the spinel structure are important in many areas of research and technology, with applications in magnetism, semiconductors, electrochemistry, geology, metallurgy, catalysis, fuel cells, water splitting, and others.[1-8] Not only are these materials significant in terms of technology, but the intrinsic, underlying physical features of these materials tend to be unusual and often lead to new discoveries in basic science.[9]

The common occurrence and thermodynamic stability of spinels are related to the large variety of cations with different valences that can be accommodated. Normal spinels of the 2-3 charge type, such as Co_3O_4 and Mn_3O_4, have the formula $A^{2+}(B^{3+})_2O_4$ where the A^{2+} cations occupy tetrahedral sites, and the B^{3+} cations occupy octahedral sites. Inverse 2-3 spinels, such as Fe_3O_4, fill the tetrahedral sites with B^{3+} cations, and the octahedral sites are occupied (usually approximately randomly) by the remaining B^{3+} and A^{2+} cations. This investigation targets the spinels Co_3O_4, Mn_3O_4, Fe_3O_4, and their solid solutions, with a focus on the effect of structural differences on entropies of mixing as determined by our new heat capacity measurements as well as the work of others.[10-19]

5.1.1 Magnetic Properties

Co_3O_4, as a cubic normal spinel, has Co^{2+} ions on tetrahedral sites and Co^{3+} ions on octahedral sites. The tetrahedrally coordinated Co^{2+} cations have seven electrons in the high-spin $e_g^4 t_{2g}^3$ configuration, and the octahedrally coordinated Co^{3+} cations are diamagnetic due to the six electrons having a t_{2g}^6 low-spin configuration.[3] The magnetic character of Co_3O_4 arises from super-exchange interactions between the Co^{2+} ions through either A–O–A or A–O–B–O–A interactions.[3, 20] Planes of ferromagnetically ordered spins stack such that the spins align antiparallel from plane to plane giving rise to what is called Type-A or Type-II antiferromagnetism.[21-22] The temperature at which the spins transition from the ordered antiferromagnetic state to the disordered paramagnetic state (known as the Néel temperature T_N) is generally agreed to be 30 K for bulk Co_3O_4,[4, 20, 23-24] though it has been reported to be as high as 40 K.[20, 25] T_N is known to be related to particle size,[26] and has been reported to adopt values as low as 15 K for 4 nm Co_3O_4 particles.[4, 9, 20, 27-28]

Mn_3O_4 is a tetragonal normal spinel that transforms to a cubic structure above about 1445 K.[29-30] The tetrahedral Mn^{2+} ions have five electrons in an $e_g^2 t_{2g}^3$ high-spin configuration, and the octahedral Mn^{3+} ions have four electrons in a Jahn-Teller distorted $t_{2g}^3 e_g^1$ high-spin configuration resulting in a total of nine unpaired spins.[31] Because both the Mn^{2+} and Mn^{3+} ions have unpaired spins, the magnetic character of Mn_3O_4 has several unique features. The paramagnetic material becomes ferrimagnetic below its Curie temperature T_C (analogous to T_N) of about 43 K[6-7, 30-33] but exists in a magnetically incommensurate phase from 33 to 39 K.[6-7, 31] Mn_3O_4 nanoparticles, however, do not exhibit the incommensurate phase, and similar to Co_3O_4, nanoparticles of Mn_3O_4 have a lower T_C due to size effects.[6]

Fe_3O_4 is a cubic inverse spinel having tetrahedral sites occupied by Fe^{3+} and octahedral sites that are approximately randomly occupied by the remaining Fe^{3+} and Fe^{2+}. It is ferrimagnetic up to a T_C of about 860 K,[34-35] but it also has a Verwey transition in which it converts from an insulator to a metal below about 118 K (depending on oxygen stoichiometry).[34-36] The ferrimagnetism arises from antiferromagnetic coupling between tetrahedral Fe^{3+} ions having an $e_g^2 t_{2g}^3$configuration with octahedral Fe^{3+} ions having a $t_{2g}^3 e_g^2$ configuration, while the octahedral Fe^{2+} ions are diamagnetic with a t_{2g}^6 configuration.[34]

5.1.2 Solid Solutions

Given that these materials differ in structure and cation site and valence preference, the solid solutions (1-*x*)Fe_3O_4-*x*Co_3O_4 and (1-*x*)Fe_3O_4-*x*Mn_3O_4 have interesting features analogous to those of high-entropy alloys, such as NiFeCrCo, in which antiferromagnetic Cr atoms must disperse throughout the matrix of ferromagnetic Ni, Fe, and Co atoms and thus create a "high-entropy" state.[37] In spinels, cation distributions vary with temperature and composition. Co^{3+} and Mn^{3+} strongly prefer octahedral sites, while the site preference of Fe^{3+} and the divalent ions is weaker;[38] furthermore, these solid solutions gradually shift from a cubic normal spinel to a cubic inverse spinel for the Co-Fe solid solutions and from a tetragonal normal spinel to a cubic inverse spinel for the Mn-Fe system. The mixing behavior of these spinels has been the focus of many investigations; nevertheless, detailed understanding of the energies and entropies of mixing and their microscopic sources, especially in nanocrystalline systems, is still needed.

The present investigation focuses on the excess entropy of mixing, which must be distinguished from the residual or "configurational" (used interchangeably herein) entropy of mixing. The former reflects changes in vibrational, magnetic, and electronic behavior, while the

latter arises from the positional disorder of cations on a given set of sites (in this case the octahedral and tetrahedral sublattices in the spinel structure).

The excess (non-configurational) entropies can be derived from heat capacity data. The deviations of the solid solution heat capacities from a linear combination of the end-member heat capacities result in an excess entropy.[39-41] Excess entropies of mixing have been observed in polymers,[42-44] alloys,[45-47] minerals,[48-58] and nanoparticles.[59] Despite the significance and occurrence of these mixing effects, much of the literature ignores their presence, primarily because of the lack of accurate heat capacity data for the solid solutions.

The present investigation follows a companion study on these same materials in which the enthalpies of mixing were measured by high-temperature oxide melt solution calorimetry, configurational entropies of mixing were calculated from models of cation and valence distributions, and the results were corroborated with Gibbs energy data found in the literature.[38] The companion study treated excess entropies of mixing as negligible and found that enthalpies of mixing are independent of particle size for a solid solution having roughly constant surface area.

This study uses newly measured heat capacity data, which are not influenced by configurational entropies, to determine the excess entropy of mixing for the bulk and nano spinel solid solutions $(1-x)Fe_3O_4$-xCo_3O_4 and $(1-x)Fe_3O_4$-xMn_3O_4. We show that the excess entropy of mixing is positive and can be comparable to the configurational entropy of mixing and that it differs for bulk and nanophase materials. We interpret the excess entropies of mixing in terms of vibrational and magnetic behavior. Our findings are supported by analyses of the magnetic transitions obtained from the heat capacity data.

5.2 Experimental Methods

5.2.1 Synthesis and Characterization

Solid solutions of (1-*x*)Fe_3O_4–*x*M_3O_4 (M: Co, or Mn) where *x* = 0.2, 0.33, 0.5, 0.67, 0.8, and 1.0 were synthesized via a chemical co-precipitation method. Stoichiometric amounts of $Co(NO_3)_2 \cdot 6H_2O$ or $MnCl_2 \cdot 4H_2O$ were dissolved in distilled water with $Fe(NO_3)_3 \cdot 9H_2O$ and stirred for 10 min to prepare a transparent, aqueous stock solution of pH 0.5. The precipitating agent, 0.5 M NaOH, was added dropwise to the stock solution while stirring until a pH of 12 was reached. The solution was then heated (while stirring) at 100 °C for 2 h followed by heating at 150 °C for 1 h. The resulting black gel was washed with distilled water several times, dried at 110 °C overnight, and then calcined at 250 °C for 2 h. Nanocrystalline Co_3O_4 and Mn_3O_4 were prepared by the solvent deficient method developed by Woodfield *et al*.[60] All of the bulk phase samples were prepared by calcining the corresponding nanocrystalline phase in a vacuum furnace at elevated temperatures for 24 h. The samples were the same as used for our prior studies of heats of formation.[38]

Powder X-ray diffraction (XRD) patterns were recorded using a Panalytical X'Pert Pro X-ray diffractometer using a Cu Kα radiation source (λ = 0.15418 nm). Data were recorded from 2θ = 10-90° at a scanning rate of $0.01° \cdot s^{-1}$.

The amounts of surface-bound water on the samples were determined by thermogravimetric analysis (TGA) using a Netzsch STA-409 PC. Prior to the TGA measurements, the samples were dried in a vacuum oven (*p* = 16.2 kPa) at 373 K for about 6 h to remove all loosely bound water that might have adsorbed from the atmosphere and that would otherwise be removed during heat capacity measurements under high vacuum. TGA measurements were carried out in a platinum crucible heated from 293 K to 1173 K (1373 K for

bulk Mn-Fe samples) in a helium atmosphere at 5 $K \cdot min^{-1}$. A buoyancy correction was made by measuring an empty platinum crucible under the same conditions and subtracting this from the measured data. Measurements were repeated twice and show good reproducibility, and the water contents were determined from the average of the resulting TGA weight loss curves.

5.2.2 Heat Capacity Calorimetry

Heat capacities were measured from 1.9 to 300 K using a Quantum Design Physical Property Measurement System (PPMS), which uses a thermal relaxation technique. The samples were dried at 373 K *in vacuo* for several hours and subsequently stored in an argon atmosphere to prevent re-adsorption of water from the atmosphere. In the argon atmosphere, 10-14 mg of each sample were mixed with high purity (mass fraction 0.9995) copper strips (to provide better thermal conductivity) and put into copper cups that were pressed into disks approximately 3 mm in diameter and 1 mm in height following the method of Shi *et al*.[61] Addenda measurements were performed before each measurement that determined the heat capacity of the calorimeter and the Apiezon N grease used to attach the sample. After each addenda measurement, the sample was attached to the PPMS puck, and the heat capacity was measured. The system automatically corrects for the heat capacities of the calorimeter and grease, and the heat capacity of the copper contribution was subtracted using data from Stevens and Boerio-Goates.[62] Data measured on the PPMS using this method have an estimated uncertainty of $\pm 0.02 \cdot C_p^\circ$ for $2 < T/K < 10$ and $\pm 0.01 \cdot C_p^\circ$ for $10 < T/K < 300$.[61] Details of the measured samples are given in Table 5-1 below.

Table 5-1: Properties of Samples for Heat Capacity Measurements in the PPMS (water content in moles; mass in mg)

	Formula	Water Content	Sample Mass	Copper Mass
bulk	$Co_{0.6}Fe_{2.4}O_4$	–	27.07	23.88
	$CoFe_2O_4$	–	30.48	24.30
	$Co_{1.5}Fe_{1.5}O_4$	–	26.91	25.05
	Co_2FeO_4	–	32.58	23.84
	$Co_{2.4}Fe_{0.6}O_4$	–	21.21	21.79
	Co_3O_4	–	29.52	22.30
nano	$Co_{0.6}Fe_{2.4}O_4$	1.512	17.41	22.85
	$CoFe_2O_4$	0.973	16.39	20.06
	$Co_{1.5}Fe_{1.5}O_4$	1.460	16.26	19.67
	Co_2FeO_4	1.056	12.01	22.05
	$Co_{2.4}Fe_{0.6}O_4$	0.479	13.36	24.26
	Co_3O_4	0.530	15.08	23.05
bulk	$MnFe_2O_4$	–	23.86	22.21
	Mn_3O_4	–	12.61	18.98
nano	$Mn_{0.6}Fe_{2.4}O_4$	1.134	13.23	21.27
	$MnFe_2O_4$	0.892	15.51	22.05
	$Mn_{1.5}Fe_{1.5}O_4$	0.674	17.37	20.74
	Mn_2FeO_4	0.516	18.36	21.42
	$Mn_{2.4}Fe_{0.6}O_4$	0.887	9.11	20.35
	Mn_3O_4	0.480	15.54	20.87

5.3 Results/Discussion

5.3.1 Characterization

The XRD data for all samples are shown in Figure 5-1 below. These data show that all samples are highly crystalline and phase pure. The progression of lattice parameters is apparent as the peaks gradually shift to higher 2θ values as Fe_3O_4 concentration increases. The gradual shift from the tetragonal phase of Mn_3O_4 towards the cubic Fe_3O_4 phase can also be seen.

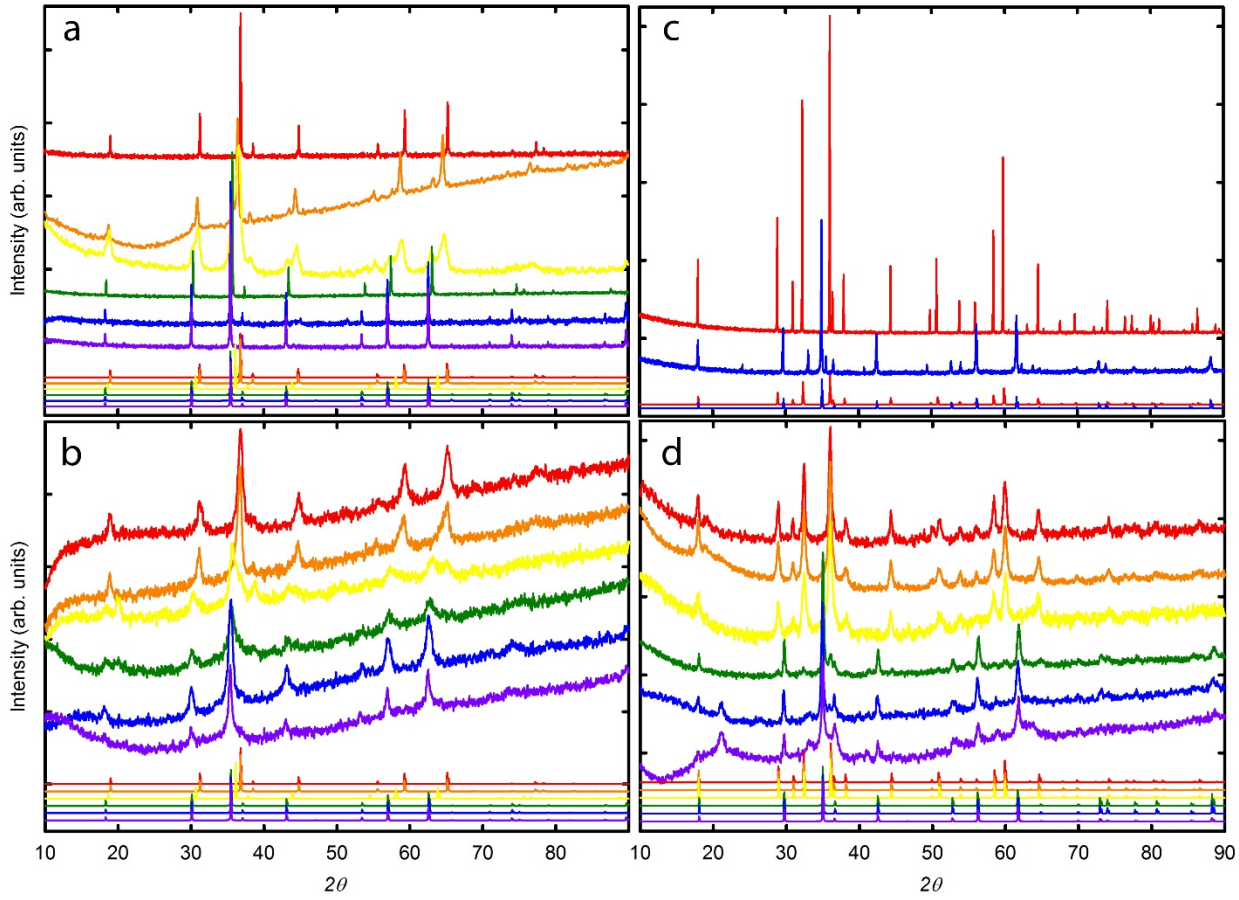

Figure 5-1: XRD Data of All Samples Showing Phase Purity and Progression of Peaks as Cation Concentrations Change. Data have been scaled and offset for clarity. red – M_3O_4; orange – $M_{2.4}Fe_{0.6}O_4$; yellow – M_2FeO_4; green – $M_{1.5}Fe_{1.5}O_4$; blue – MFe_2O_4; purple – $M_{0.6}Fe_{2.4}O_4$ (M: Co or Mn). Bottom lines in each graph represent the XRD patterns of standard materials. a) bulk Co-Fe, b) nano Co-Fe, c) bulk Mn-Fe, d) nano Mn-Fe.

The TGA-DSC data presented in Figure 5-2 show that the bulk Co-Fe spinels are reduced by about 1050 K, and the nano Co-Fe spinels reduce at about 850 K for $x < 0.67$ and at about 1050 K for $x > 0.67$. Bulk Mn_3O_4 did not reduce even by 1350 K, but bulk $MnFe_2O_4$ appears to begin reduction around 850 K. The nano Mn-Fe samples show no obvious step-like reduction in the TGA curves, but the DSC curves for $x < 0.5$ show exothermic peaks at about 850 K. The water content of all bulk samples was taken to be negligible, and the water contents of the

nanocrystalline samples (given in Table 5-1) were taken at the inflection points before reduction at about 750 K.

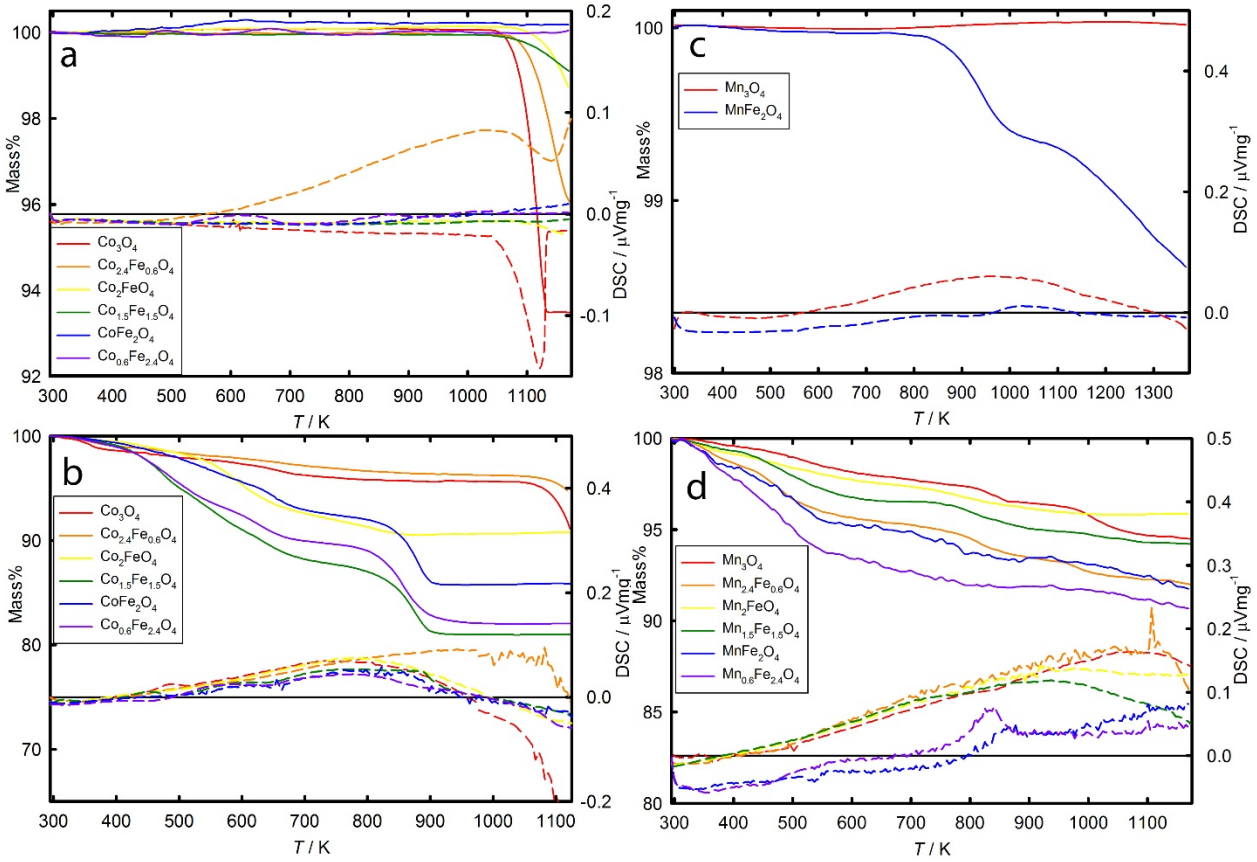

Figure 5-2: TGA-DSC Data of All Samples Showing Mass Loss Due to Water Desorption and Reduction. Only one run of each sample is shown for clarity. The left axis gives the percent mass and is represented with solid lines. The right axis gives the DSC data and is represented with dashed lines. The solid black line corresponds to 0 μV·mg^{-1} for the DSC axis. red – M_3O_4; orange – $M_{2.4}Fe_{0.6}O_4$; yellow – M_2FeO_4; green – $M_{1.5}Fe_{1.5}O_4$; blue – MFe_2O_4; purple – $M_{0.6}Fe_{2.4}O_4$ (M: Co or Mn). a) bulk Co-Fe, b) nano Co-Fe, c) bulk Mn-Fe, d) nano Mn-Fe.

5.3.2 Heat Capacity General Analysis

The measured heat capacity data are shown in Figure 5-3.

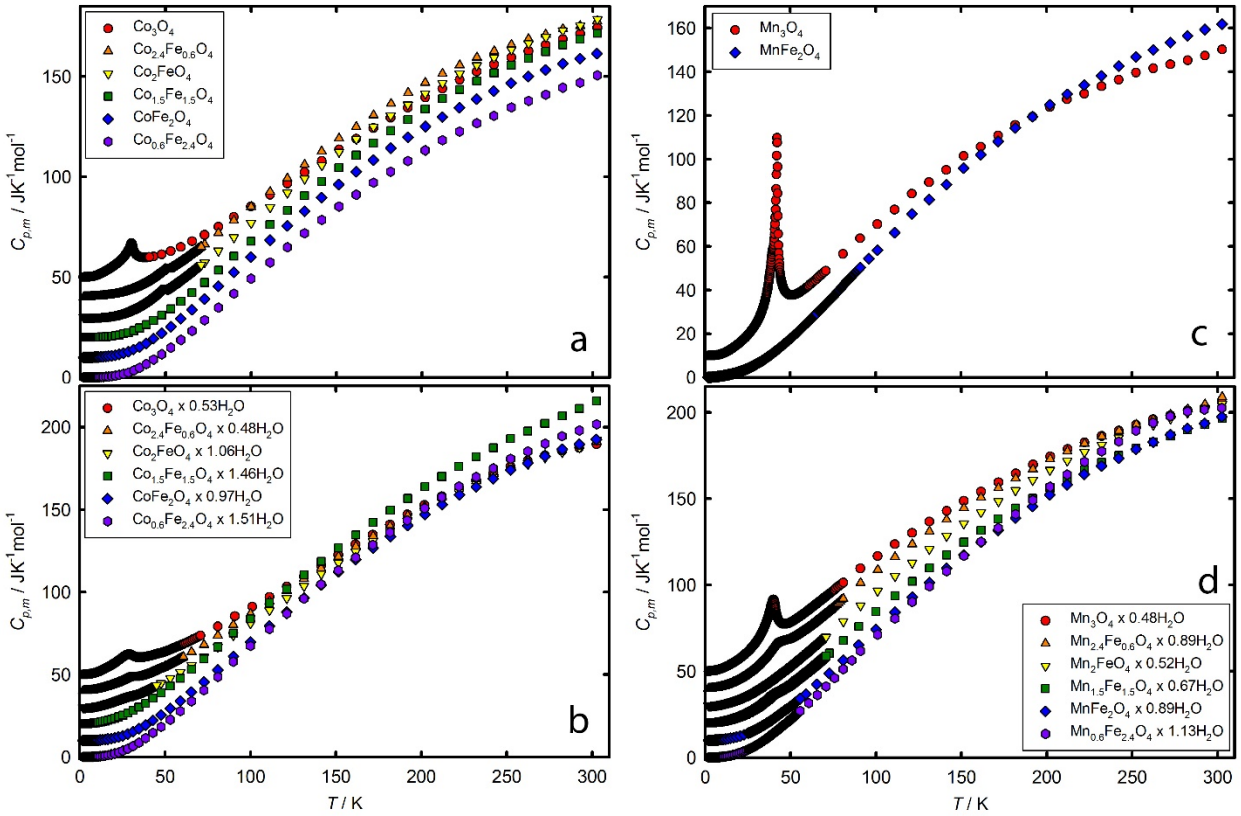

Figure 5-3: Raw Heat Capacity Data of All Spinel Samples. red circles – M_3O_4; orange triangles – $M_{2.4}Fe_{0.6}O_4$; yellow inverted triangles – M_2FeO_4; green squares – $M_{1.5}Fe_{1.5}O_4$; blue diamonds – MFe_2O_4; purple hexagons – $M_{0.6}Fe_{2.4}O_4$ (M: Co or Mn). a) bulk Co-Fe, b) nano Co-Fe, c) bulk Mn-Fe, d) nano Mn-Fe. The data have been offset for clarity.

5.3.2.1 Water Correction

Heat capacity data of the nanoparticle samples were corrected for water contributions by subtracting the heat capacity of water using various water models. Figure 5-4 shows several of the various models that have been developed and published in the literature.[63-68] These data were smoothed by fitting to a sum of Debye and Einstein functions (also shown in Figure 5-4).[65-66]

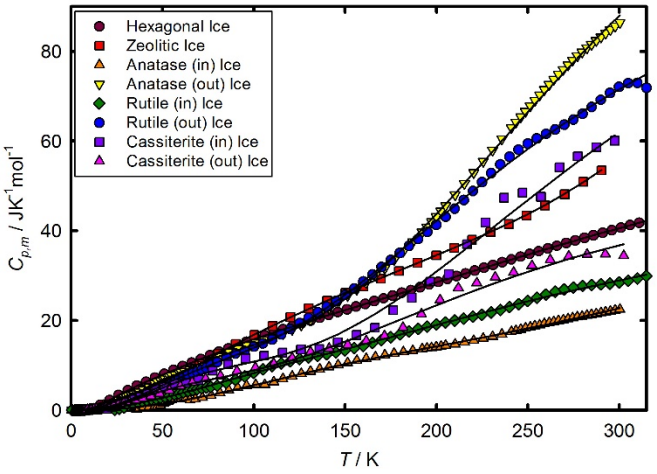

Figure 5-4: Water Models Used for Subtracting Water from Spinel Nanoparticles. Smooth fits to the data are also shown. maroon circles – hexagonal ice;[67] red squares – zeolitic ice;[68] orange triangles – TiO_2 anatase (inner) ice;[66-67] yellow inverted triangles – TiO_2 anatase (outer) ice;[66-67] green diamonds – TiO_2 rutile (inner) ice;[65, 67] blue circles – TiO_2 rutile (outer) ice;[65, 67] purple squares – SnO_2 cassiterite (inner) ice;[63] magenta triangles – SnO_2 cassiterite (outer) ice.[63]

Surface-bound water affects the stabilization of nanoparticles and nanoporous materials.[8, 63-75] Treating the surface water on metal oxides as hexagonal ice has proven to be a poor model because its heat capacity remains relatively large at low temperatures; thus, when the spinel data were corrected for water using the hexagonal ice model, the resultant anhydrous spinel heat capacity data became negative. Instead, we chose to use the model of inner-bound layers of water on TiO_2 anatase nanoparticles.[66-67] This is a reasonable choice for this investigation because the spinel samples have been dried under vacuum, which would remove any loosely-bound outer water and leave only inner layer water that is strongly bound to the surface. Using surface water data of TiO_2 anatase is also a reasonable choice since the surface enthalpy of TiO_2 anatase (0.74 J·m^{-2})[76] is very similar to the surface enthalpies of these samples (0.62-0.83 J·m^{-2})[38] and the surface energy is highly correlated to the adsorbed water thermodynamics.[70]

All calculations involving nanoparticle data use the water corrected data shown in Figure 5-5 below. The heat capacity data of nano Fe_3O_4 used in this investigation were adapted from Snow *et al.*[17] by correcting their data for water using this same model.

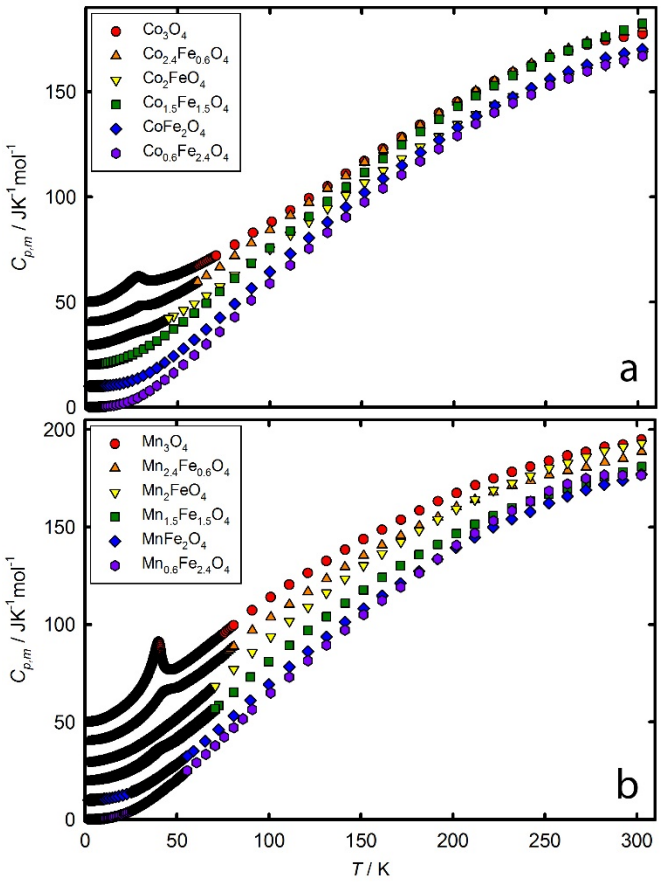

Figure 5-5: Heat Capacity Data of Nanoparticle Samples after Water Correction. red circles – M_3O_4; orange triangles – $M_{2.4}Fe_{0.6}O_4$; yellow inverted triangles – M_2FeO_4; green squares – $M_{1.5}Fe_{1.5}O_4$; blue diamonds – MFe_2O_4; purple hexagons – $M_{0.6}Fe_{2.4}O_4$ (M: Co or Mn). a) Co-Fe, b) Mn-Fe. The data have been offset for clarity.

5.3.2.2 Heat Capacity Data Fitting

The heat capacity data of all samples were fit to theoretical functions that provide information on the various contributions to the heat capacity. The best fits for each temperature range were determined from the percent root mean square deviation (% RMS) and a plot of the

deviation of each point from the fitting function. Fits that were physically meaningful (no negative heat capacities), had the lowest % RMS, and had random deviations were selected as the best fits.

The heat capacity data below 10 K were fit to the sum of theoretical functions:

$$C_{low\,T} = A_{nh}T^{-2} + \gamma T + B_{fm}T^{3/2} + B_3T^3 + B_5T^5 + B_7T^7 + B_9T^9 \quad (5\text{-}1)$$

$$+ B_{gap}T^n e^{-\delta/T} + n_{Sch}R\left(\frac{\theta}{T}\right)^2 \frac{e^{\theta/T}}{(1-e^{\theta/T})^2}$$

where the A_{nh} term represents contributions due to a nuclear hyperfine structure[77], the γ term represents the contribution from lattice vacancies or other defects,[78] the B_{fm} term represents ferro- or ferrimagnetic contributions, the B_3, B_5, B_7, and B_9 terms represent the harmonic-lattice expansion,[79] the "gapped" B_{gap} term represents magnetic contributions (the type of magnetism given by n) that have a gap δ in the density of states (DOS) due to anisotropy,[21-22, 80-81] and the n_{Sch} term represents a Schottky contribution arising from a two-level system with energy separation θ.[82] We note that the magnetic contribution in antiferromagnetic samples also has a T^3 dependence making it indistinguishable from the phonons. Fits had a maximum of six parameters; thus, not all parameters were necessary for all samples.

Data of samples that do not exhibit a magnetic transition in the mid temperature range (6 – 50 K) were fit with polynomials to provide sufficient overlap with the low temperature and high temperature fits and have the general form:

$$C_{mid\,T} = \sum_{n=0,1,2\ldots6} A_n T^n \quad (5\text{-}2)$$

Although these fits do not provide information on the underlying physical contributions, they are often necessary to fit data through inflection points.

The high temperature data (T > 30 K) were fit to a linear combination of Debye and Einstein functions that provides information on the lattice heat capacity:

$$C_{high\,T} = m \cdot D(\Theta_D/T) + n_1 \cdot E(\Theta_{E,1}/T) + n_2 \cdot E(\Theta_{E,2}/T) \quad (5\text{-}3)$$

where D(Θ_D / T), E($\Theta_{E,1}$ / T), and E($\Theta_{E,2}$ / T) are Debye and Einstein functions; m, n_1, n_2, Θ_D, $\Theta_{E,1}$, and $\Theta_{E,2}$ are all adjustable parameters; and (m + n_1 + n_2) should be approximately equal to the number of atoms in the formula unit.[83] Samples that had a transition in this region were fit at temperatures above the transitions, starting at about 70 K, with one Debye and one Einstein function, but the samples that had no transitions were fit above about 30 K with one Debye and *two* Einstein functions.

5.3.3 Transitions

The heat capacities of the magnetic transitions were determined by subtracting the lattice contribution from the total heat capacity and are shown in Figure 5-6. These data were fit with a cubic spline function that was used to generate enthalpies and entropies of the transitions. These values, as well as the Néel (antiferromagnetic ordering) and Curie (ferromagnetic ordering) temperatures, are given in Table 5-2.

The Néel temperature T_N of bulk Co_3O_4 is most commonly reported to be 29.9 K from a variety of measurements,[20, 23-24] which corresponds well with our values of T_N = 30.0 K. The higher T_N observed for bulk $Co_{2.4}Fe_{0.6}O_4$ and Co_2FeO_4 (about 50 K) is attributed to enhancement of the magnetic coupling with increasing Fe concentration as has been observed for Mn-Fe spinel solid solutions.[32] Tristan *et al.* observed frustration in $Co(Al_{1-x}Co_x)_2O_4$ spinels as the amount of Al^{3+} in octahedral sites increased.[24] The Al^{3+} ions hindered the antiferromagnetic coupling across the next-nearest-neighbor A–O–B–O–A exchange interaction and thus decreased T_N by about 10 K. Our results suggest that the Fe^{3+} ions in $Co_{2.4}Fe_{0.6}O_4$ and Co_2FeO_4 have the opposite effect on

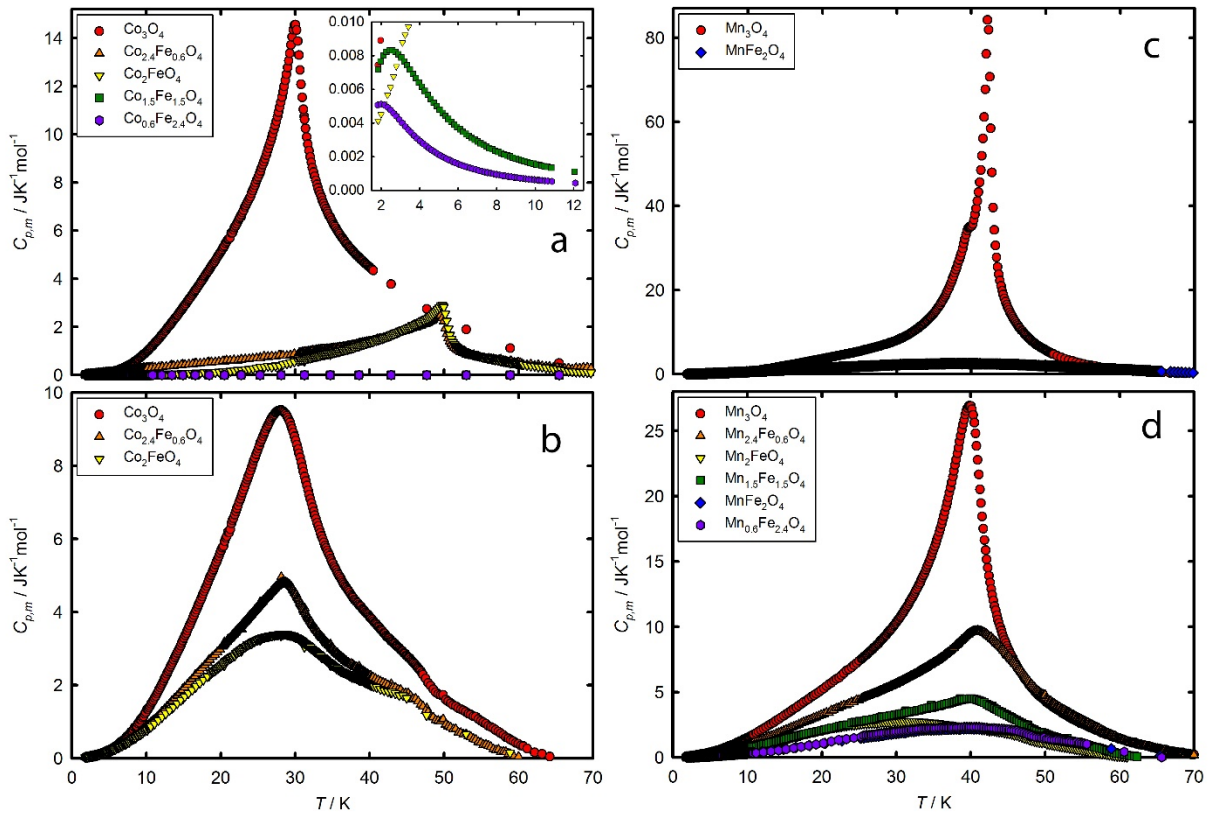

Figure 5-6: Heat Capacities of the Magnetic Transitions. red circles – M_3O_4; orange triangles – $M_{2.4}Fe_{0.6}O_4$; yellow inverted triangles – M_2FeO_4; green squares – $M_{1.5}Fe_{1.5}O_4$; blue diamonds – MFe_2O_4; purple hexagons – $M_{0.6}Fe_{2.4}O_4$ (M: Co or Mn). a) bulk Co-Fe, b) nano Co-Fe, c) bulk Mn-Fe, d) nano Mn-Fe.

the long-range antiferromagnetic ordering and increase the coupling across the A–O–B–O–A system and therefore increase T_N by about 20 K.

The significant decrease in T_N for $Co_{1.5}Fe_{1.5}O_4$ and $Co_{0.6}Fe_{2.4}O_4$ to 2.52 and 2.00 K from 30-50 K (as well as the absence of any transition for $CoFe_2O_4$) suggests that the Fe cations become detrimental to the coupling at larger concentrations and produce strong spin frustration to the point that a spin-glass state is achieved.[24] This reversal in effect of the Fe cations is likely related to the type and site of the mixing Fe cations. Because Fe_3O_4 is ferrimagnetic (as opposed

to the antiferromagnetic Co_3O_4), the coupling between the $Fe^{2+/3+}$ cations for $x < 0.67$ dominates and disrupts the Co^{2+}–Co^{2+} nearest-neighbor and next-nearest-neighbor interactions.

Table 5-2: Néel and Curie Temperatures, Entropies, and Enthalpies of the Magnetic Transitions

	Sample	$T_{N,C}$ / K	$\Delta_o^T S_{trans}^o$ / $J \cdot mol^{-1} \cdot K^{-1}$	$\Delta_o^T H_{trans}^o$ / $J \cdot mol^{-1}$
bulk	$Co_{0.6}Fe_{2.4}O_4$	2.00	0.008075	0.02062
	$Co_{1.5}Fe_{1.5}O_4$	2.52	0.01316	0.05615
	Co_2FeO_4	49.8	1.099	44.77
	$Co_{2.4}Fe_{0.6}O_4$	49.3	1.721	55.03
	Co_3O_4	30.0	8.828	245.8
nano	Co_2FeO_4	28.3	3.911	97.07
	$Co_{2.4}Fe_{0.6}O_4$	28.1	4.651	115.3
	Co_3O_4	28.1	8.390	214.3
bulk	$MnFe_2O_4$	38.0	3.294	100.1
	Mn_3O_4	42.2	15.49	557.7
nano	$Mn_{0.6}Fe_{2.4}O_4$	40.1	2.499	76.98
	$MnFe_2O_4$	39.4	2.491	75.75
	$Mn_{1.5}Fe_{1.5}O_4$	39.8	4.343	124.5
	Mn_2FeO_4	32.1	3.715	92.21
	$Mn_{2.4}Fe_{0.6}O_4$	40.9	8.064	254.2
	Mn_3O_4	39.9	13.78	426.0

Figure 5-6 shows that the nano Co-Fe spinels all have T_N near 28 K, the peaks are broader than their bulk counterparts, and a shoulder is observed at about 45 K. The decrease in T_N is commonly observed for nanoparticles in which the size of the particle begins to be comparable to the size of the magnetic domains.[4, 9, 20, 26-28] The broadening of the peaks is also common for nanomaterials and is likely caused by clusters of the parent Co_3O_4 and Fe_3O_4 phases being randomly distributed in the volume of the nanoparticles.[24] These properties suggest that the mixing of the magnetically active cations in the nanoparticles is not random. The shoulder at 45 K could arise from phase impurities, but the lack of evidence of such impurities in the XRD data

suggests this is not likely, at least at levels of more than 2-3 %,. We believe this shoulder arises from enhancement effects of the Fe cations in a small percentage of the magnetic domains causing an increase in the transition temperature as seen in the bulk $Co_{2.4}Fe_{0.6}O_4$ and Co_2FeO_4. This explanation would also suggest that the distribution of cations in each sublattice of the nanoparticle solid solutions is not random.

Bulk Mn_3O_4 has a sharp transition at 42.2 K due to ferrimagnetic ordering as is observed in the literature.[6-7, 30-33] The small shoulder at about 39 K has been related to an incommensurate magnetic transition, but the commensurate transition at about 33 K that has been reported in the literature is not observed.[6-7, 31] Bulk $MnFe_2O_4$, however, has a broad and weak transition at a slightly lower temperature, 38.0 K. Naito *et al.* have shown that bulk $MnFe_2O_4$ has a Curie temperature T_C of about 600 K;[33] therefore, we suspect that this small peak is an artifact arising from the lattice heat capacity subtraction.

The nano Mn-Fe samples all have a T_C of about 40 K except for the nano-Mn_2FeO_4 sample, which seems to have a T_C of 32.1 (this difference is possibly a result of errors in subtracting the water or lattice contributions). As with the nano Co-Fe samples, we attribute the slightly lower T_C to size.[4, 6, 9, 20, 26-28] The broadening of these peaks can also be attributed to randomly dispersed clusters of magnetic domains as seen in the nano Co-Fe spinels.[6, 24] As mentioned for the bulk Mn-Fe solid solutions, the transitions observed in our samples at about 40 K and for these compositions have not been observed in the literature.[32-33] The peaks in our nano Mn-Fe solid solutions at the same temperature (regardless of composition) might suggest Mn_3O_4 impurities, but the concentrations of these impurities would have to be significant and should therefore be visible in the XRD data where no such impurities are observed. We believe that these transitions are caused by clustering of the ions on an atomic scale thereby leaving domains

of Mn ions that have a similar magnetic structure to that of pure Mn_3O_4 but that have the physical structure of the Mn-Fe solid solutions. In other words, the coherence length of any such clustered domains is too small to give rise to distinct powder XRD peaks.

Based on the spin states of these materials (S = 3/5 for Co_3O_4 and S = 9/2 for Mn_3O_4) and assuming a completely ordered state below the transition temperature and a completely disordered state above the transition temperature, the excess entropies of transition of Co_3O_4 and Mn_3O_4 would be 11.5 and 19.1 $J \cdot mol^{-1} \cdot K^{-1}$, respectively.[23, 31] Our results are roughly 25 % lower than these theoretical values which could indicate some residual short-range order in the high-temperature phase. This discrepancy could also be partially caused by errors introduced when subtracting the lattice heat capacity.

Our entropy for bulk Co_3O_4 of 8.8 $J \cdot mol^{-1} \cdot K^{-1}$ at about 72 K (where the transition heat capacity becomes zero) is in good agreement with the entropy obtained by Khriplovich *et al.* of 9.2 $J \cdot mol^{-1} \cdot K^{-1}$,[23] and our value for bulk Mn_3O_4 of 15.5 $J \cdot mol^{-1} \cdot K^{-1}$ at 70 K is in fair agreement with that of Chhor *et al.*[31] (note that their published entropy of 11.5 $J \cdot mol^{-1} \cdot K^{-1}$ was taken at T_C rather than 70 K as in the present study; the entropy of our sample at T_C is 11.47 $J \cdot mol^{-1} \cdot K^{-1}$ which agrees well with the literature).

5.3.4 Standard Enthalpies, Entropies and Excess Entropies of Mixing

Thermodynamic data were calculated from the fits of the heat capacity data that have been corrected for water. The lattice enthalpies and entropies were determined from the low, mid, and high-temperature fits for samples without a transition and from the high temperature fits (Eq. 5-3) extrapolated to 0 K for samples that do have a transition. Figure 5-7 shows the standard molar entropies and enthalpies of all samples at 298.15 K as a function of $x_{M_3O_4}(M: Co, Mn)$.

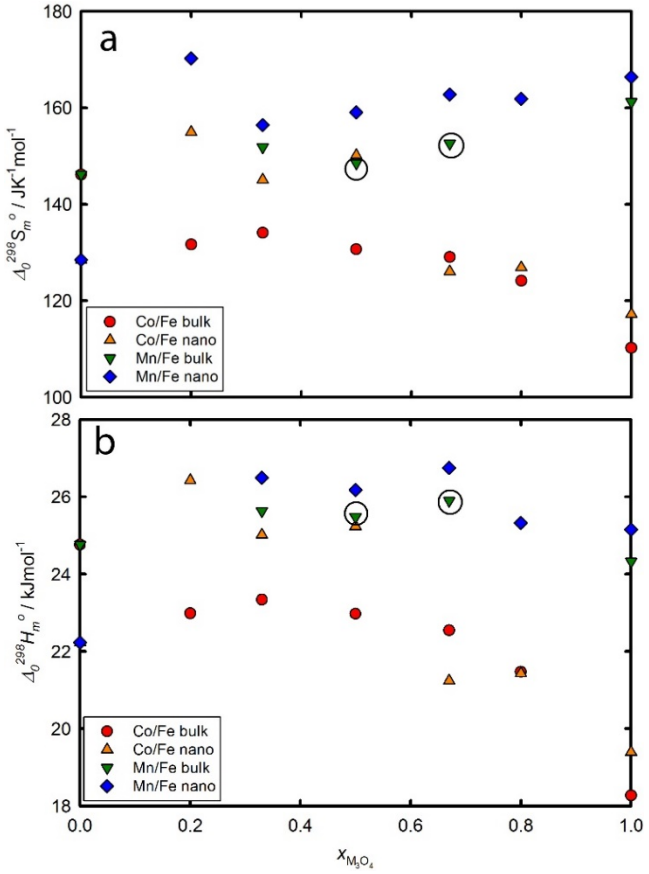

Figure 5-7: Standard Molar Entropies (a) and Enthalpies (b) at 298.15 K Determined from Water-corrected Heat Capacity Data. Circled points are from Naito et al.[33]

As previously mentioned, configurational entropies cannot be measured from heat capacity data and will therefore not be discussed in any detail herein. For details regarding this entropic contribution, the reader is referred to the work of Sahu *et al.*[38] , though some results will be repeated here graphically for comparison purposes. These values will be referred to herein as the configurational entropy of mixing $\Delta_{mix}S^{conf}$ and are included in Table 5-3.[84] It is important to remember that these configurational entropies of mixing are based on maximum configurational entropies at each composition resulting from random distributions on each sublattice of the ions calculated from the assumed cation and valence distributions.

The excess (non-configurational) entropies of mixing for all spinel solid solutions investigated herein have been determined as deviations of the solid solution entropies from a linear combination of the entropies of the two pure end-members as has been done in our companion study.[38] These values include both the vibrational and magnetic entropy contributions. Figure 5-8 and Table 5-3 show these values as well as $\Delta_{mix}S^{conf}$ and the total entropy of mixing $\Delta_{mix}S^{total}$ obtained by summing all contributions;

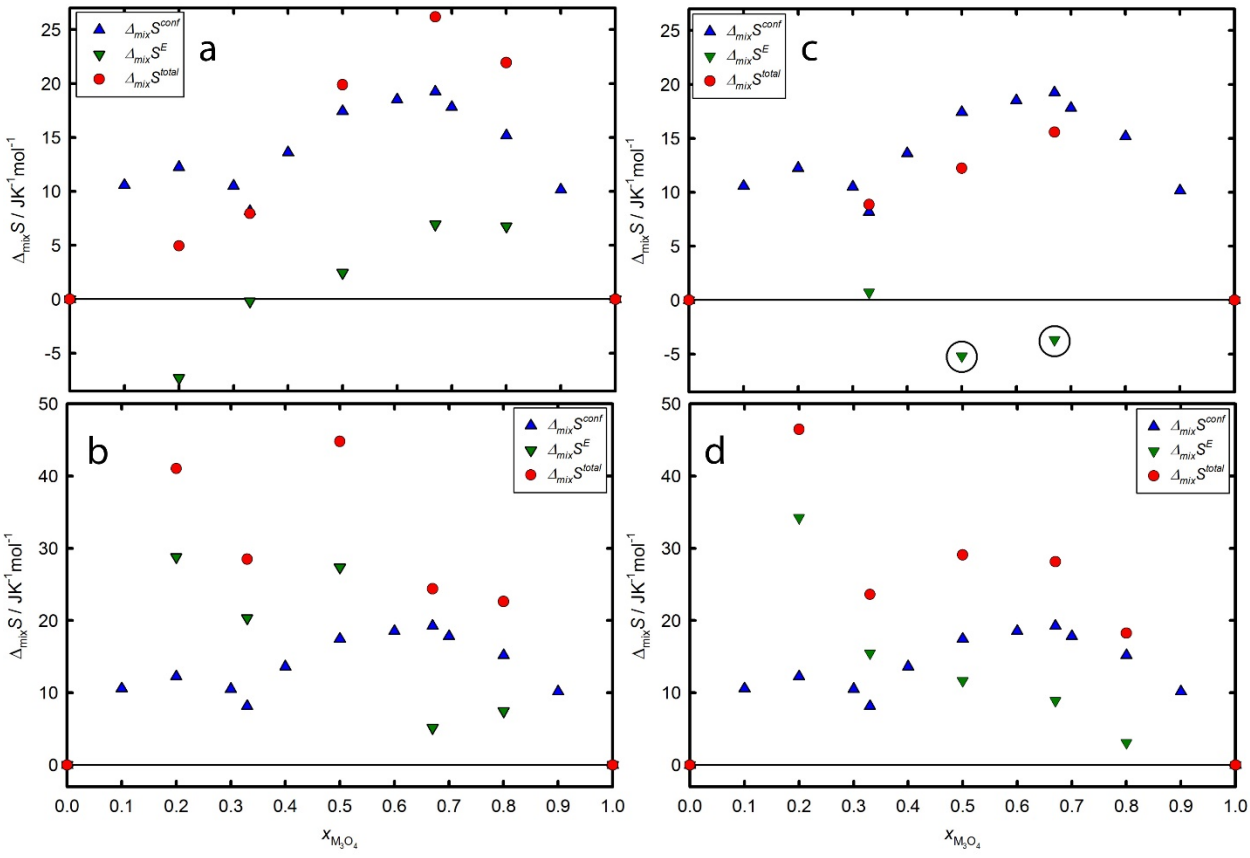

Figure 5-8: Excess Entropies of Mixing (green inverted triangles) of All Materials Investigated Herein as well as Configurational Entropies of Mixing (blue triangles) Obtained from Sahu *et al.*[38] and Total Entropies of Mixing (red circles) a) bulk Co-Fe, b) nano Co-Fe, c) bulk Mn-Fe (circled points were generated from the data of Naito *et al.*[33]), d) nano Mn-Fe.

Table 5-3: Excess Entropies of Mixing of (1-*x*)Fe_3O_4–*x*M_3O_4 (M: Co or Mn)

Sample	$x_{M_3O_4}$	$\Delta_{mix}S^E_{Co\ bulk}$	$\Delta_{mix}S^E_{Co\ nano}$	$\Delta_{mix}S^E_{Mn\ bulk}$	$\Delta_{mix}S^E_{Mn\ nano}$	$\Delta_{mix}S^{conf}$
Fe_3O_4	0	0	0	0	0	0
$M_{0.6}Fe_{2.4}O_4$	0.2	-7.306	28.79	–	34.21	12.25
MFe_2O_4	0.33	-0.2036	20.34	0.7128	15.45	8.153
$M_{1.5}Fe_{1.5}O_4$	0.5	2.453	27.36	-5.197[a]	11.66	17.43
M_2FeO_4	0.67	6.936	5.145	-3.668[a]	8.897	19.25
$M_{2.4}Fe_{0.6}O_4$	0.8	6.744	7.445	–	3.067	15.19
M_3O_4	1	0	0	0	0	0

[a]values obtained from data of Naito *et al.*[33]

As can be seen in Figure 5-8, the excess non-configurational entropies of mixing are all positive and can be significant when compared to the configurational entropies of mixing. The magnitudes of the excess entropies of mixing in the bulk Co-Fe spinel solid solutions are 60, 2.5, 14, 36 and 44 % of the corresponding configurational entropies of mixing for $x_{M_3O_4}$ = 0.2, 0.33, 0.5, 0.67, and 0.8, respectively. Similarly, the magnitudes of the $\Delta_{mix}S^E$ of the bulk Mn-Fe spinels correspond to 8.7, 30, and 19 % of $\Delta_{mix}S^{conf}$ for $x_{M_3O_4}$ = 0.33, 0.5, and 0.67, respectively. The excess entropies of mixing of the nanocrystalline samples are significantly greater than those of their bulk counterparts. For nano Co-Fe spinels they represent 235, 249, 157, 27, and 49 % of the configurational entropies for $x_{M_3O_4}$ = 0.2, 0.33, 0.5, 0.67, and 0.8, respectively, and for nano Mn-Fe spinels they represent 279, 189, 67, 46, and 20 of the configurational values for $x_{M_3O_4}$ = 0.2, 0.33, 0.5, 0.67, and 0.8, respectively. These values indicate that although the non-configurational mixing effects are present in both bulk and nano samples, they are much more pronounced in the nanoparticles.

These values of $\Delta_{mix}S^E$ indicate that changes in lattice and magnetic behavior on an atomic scale must be taken into account when considering the thermodynamics of mixing. Excess entropies have been attributed to short-range order, vibrational effects, and electron-

exchange interactions.[38, 44, 48, 50, 53, 56-57, 85-86] In a recent study on the mixing in Al-doped TiO_2 nanoparticles, we showed that short-range order effects and a glass-like state were correlated with an excess entropy of mixing;[59] however, short-range ordering typically causes negative excess configurational entropies, which would not be measured by heat capacities.

Excess entropies with similar magnitudes to those determined in the present investigation have been related to the added vibrational freedom a small ion might have on a particular site relative to a larger ion on the same site.[56] Although the ions in these spinels are all similar in size, they differ in charge (2+ and 3+), and this may affect the strength of metal-oxygen bonds and therefore the vibrational heat capacity. Figure 5-9 shows that the contribution from lattice vibrations dominate the excess non-configurational entropies of nanoparticle samples; whereas, the bulk samples have competing and even dominating magnetic contributions for several concentrations. We note that the excess entropy of mixing values for the nanoparticle systems have substantially more uncertainty than those of the bulk systems because of the water correction. The errors associated with this correction could produce an artificially large positive excess entropy.

These systems evolve from a cubic normal spinel to a cubic inverse spinel for the Co-Fe solid solutions and from a tetragonal normal spinel to a cubic inverse spinel for the Mn-Fe system. The structural change as a function of composition is correlated to the vibrational character. Mn_3O_4 has a characteristic Jahn-Teller distorted structure and the degree of long-range (crystallographic) distortion diminishes and eventually disappears as Fe or Co is substituted; however, local distortions around Mn^{3+} may persist into the cubic phase. All these factors may affect the vibrational density of states. The nanoparticles have larger excess entropies; therefore,

the vibrational disorder appears to be greater in nanoparticles. This result correlates well with investigations on the vibrational character of bulk and nano materials.[75]

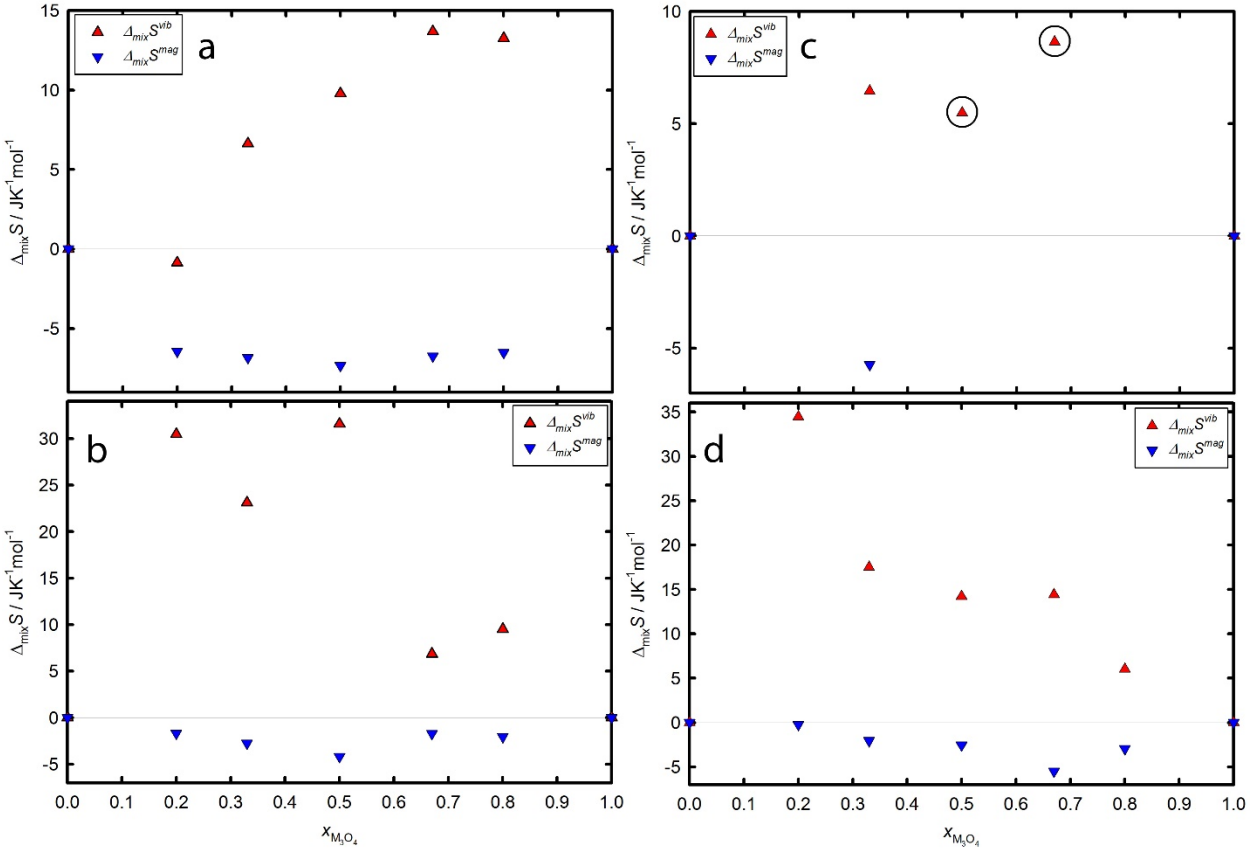

Figure 5-9: Vibrational $\Delta_{mix}S^{vib}$ (red triangles) and Magnetic $\Delta_{mix}S^{mag}$ (blue inverted triangles) Entropy of Mixing Contributions. a) bulk Co-Fe, b) nano Co-Fe, c) bulk Mn-Fe (circled points were generated from the data of Naito *et al.*[33]), d) nano Mn-Fe.

A final observation from the data in Figures 5-8 and 5-9 is the asymmetry of the excess entropies of mixing in the nanoparticle samples, which has been observed elsewhere.[86] The excess entropies greatly surpass the configurational entropies for higher Fe concentrations, while these values represent a much smaller percentage of the configurational entropies for low Fe concentrations. This gives rise to the conclusion that, along with a shift in structure, such as

tetragonal to cubic for Mn-Fe spinels, the contribution to the excess entropy from the redistribution of oxidation states is also significant and will affect bond lengths, cation distributions, and lattice vibrations.

5.4 Conclusions

The large, positive excess non-configurational entropies of mixing arise both from shifts in magnetic transitions and from lattice vibrational effects. The arguments related to magnetic behavior suggest some clustering into domains, particularly those that may resemble Mn_3O_4. Any such clustering will lead to nonrandom distributions of cations on each sublattice and thus diminish the configurational entropy from that of ideal mixing (maximum randomness) on each sublattice. Such clustering may be temperature dependent. Our previous work [38] used measured enthalpies of mixing at 298 K and configurational entropies calculated assuming maximum randomness on each sublattice for the proposed cation distribution to compare with free energies of mixing measured at or above 1000 K. The results, without using any non-configurational excess entropy terms, were reasonably concordant. The present heat capacity measurements suggest large non-configurational excess entropies of mixing at 298 K and may suggest smaller than random configurational entropies because of possible domain formation; however, additional phase transitions, decrease of clustering, and changes in vibrational properties between room temperature and the temperature of free energy measurements may well affect the heat capacities and entropies in that temperature range. In the absence of accurate heat capacity data between 298 and 1000-1300 K, it is premature to try to model the entropies of mixing at high temperature; nevertheless, the current work shows that differences in magnetic and vibrational properties across these complex solid solutions can lead to significant non-

configurational excess entropies of mixing, which may persist to higher temperature and must be considered and quantified.

REFERENCES

1. O'Neill, H. S. C.; Navrotsky, A., Cation Distributions and Thermodynamic Properties of Binary Spinel Solid Solutions. *American Mineralogist* **1984**, *69*, 733-753.

2. Xu, B.; Bhawe, Y.; Davis, M. E., Spinel Metal Oxide-Alkali Carbonate-Based, Low-Temperature Thermochemical Cycles for Water Splitting and Co2 Reduction. *Chemistry of Materials* **2013**, *25*, 1564-1571.

3. Raveau, B.; Seikh, M. M., Electronic and Magnetic Properties of Cobaltites with a 3d "Triangular Lattice". In *Cobalt Oxides: From Crystal Chemistry to Physics*, Wiley-VCH Verlag GmbH & Co. KGaA: 2012; pp 211-247.

4. Hill, A. H.; Harrison, A.; Ritter, C.; Yue, W.; Zhou, W., Neutron Powder Diffraction and Magnetic Studies of Mesoporous Co3o4. *Journal of Magnetism and Magnetic Materials* **2011**, *323*, 226-231.

5. Grundy, A. N.; Hallstedt, B.; Gauckler, L. J., Assessment of the Mn-O System. *Journal of phase equilibria* **2003**, *24*, 21-39.

6. Regmi, R.; Tackett, R.; Lawes, G., Suppression of Low-Temperature Magnetic States in Mn3o4 Nanoparticles. *Journal of Magnetism and Magnetic Materials* **2009**, *321*, 2296-2299.

7. Tackett, R.; Lawes, G.; Melot, B. C.; Grossman, M.; Toberer, E. S.; Seshadri, R., Magnetodielectric Coupling in Mn3o4. *Physical Review B* **2007**, *76*, 024409.

8. Navrotsky, A.; Ma, C.; Lilova, K.; Birkner, N., Nanophase Transition Metal Oxides Show Large Thermodynamically Driven Shifts in Oxidation-Reduction Equilibria. *Science* **2010**, *330*, 199-201.

9. Bisht, V.; Rajeev, K., Non-Equilibrium Effects in the Magnetic Behavior of Co3o4 Nanoparticles. *Solid State Communications* **2011**, *151*, 1275-1279.

10. Fritsch, S.; Navrotsky, A., Thermodynamic Properties of Manganese Oxides. *Journal of the American Ceramic Society* **1996**, *79*, 1761-1768.

11. King, E., Heat Capacities at Low Temperatures and Entropies at 298.15° K. Of Nickelous Oxide, Cobaltous Oxide and Cobalt Spinel. *Journal of the American Chemical Society* **1957**, *79*, 2399-2400.

12. Millar, R. W., The Specific Heats at Low Temperatures of Manganous Oxide, Manganous-Manganic Oxide and Manganese Dioxide. *Journal of the American Chemical Society* **1928**, *50*, 1875-1883.

13. Millar, R. W., The Heat Capacities at Low Temperatures of "Ferrous Oxide," Magnetite, and Cuprous and Cupric Oxides. *Journal of the American Chemical Society* **1929**, *51*, 215-222.

14. Caruntu, D.; Caruntu, G.; O'Connor, C. J., Magnetic Properties of Variable-Sized Fe3o4 Nanoparticles Synthesized from Non-Aqueous Homogeneous Solutions of Polyols. *Journal of Physics D: Applied Physics* **2007**, *40*, 5801.

15. Jacob, K.; Kumar, A.; Rajitha, G.; Waseda, Y., Thermodynamic Data for Mn3o4, Mn2o3 and Mno2. *High Temperature Materials and Processes* **2011**, *30*, 459-472.

16. Westrum, E. F.; Grønvold, F., Magnetite (Fe3o4) Heat Capacity and Thermodynamic Properties from 5 to 350 K, Low-Temperature Transition. *The Journal of Chemical Thermodynamics* **1969**, *1*, 543-557.

17. Snow, C. L.; Shi, Q.; Boerio-Goates, J.; Woodfield, B. F., Heat Capacity Studies of Nanocrystalline Magnetite (Fe3o4). *The Journal of Physical Chemistry C* **2010**, *114*, 21100-21108.

18. Tan, H.; Turner, S.; Yücelen, E.; Verbeeck, J.; Van Tendeloo, G., 2d Atomic Mapping of Oxidation States in Transition Metal Oxides by Scanning Transmission Electron Microscopy and Electron Energy-Loss Spectroscopy. *Physical Review Letters* **2011**, *107*, 107602.

19. Saal, J. E.; Wang, Y.; Shang, S.; Liu, Z.-K., Thermodynamic Properties of Co3o4 and Sr6co5o15 from First-Principles. *Inorganic chemistry* **2010**, *49*, 10291-10298.

20. Dutta, P.; Seehra, M.; Thota, S.; Kumar, J., A Comparative Study of the Magnetic Properties of Bulk and Nanocrystalline Co3o4. *Journal of Physics: Condensed Matter* **2008**, *20*, 015218.

21. Woodfield, B. F.; Shapiro, J. L.; Stevens, R.; Boerio-Goates, J.; Wilson, M. L., Critical Phenomena at the Antiferromagnetic Transition in Mno. *Physical Review B* **1999**, *60*, 7335.

22. Woodfield, B. F.; Wilson, M. L.; Byers, J. M., Low-Temperature Specific Heat of La 1− X Sr X Mno 3+ Δ. *Physical review letters* **1997**, *78*, 3201.

23. Khriplovich, L.; Kholopov, E.; Paukov, I., Heat Capacity and Thermodynamic Properties of Co3o4 from 5 to 307 K Low-Temperature Transition. *The Journal of Chemical Thermodynamics* **1982**, *14*, 207-217.

24. Tristan, N.; Zestrea, V.; Behr, G.; Klingeler, R.; Büchner, B.; von Nidda, H. K.; Loidl, A.; Tsurkan, V., Spin Frustration and Magnetic Exchange in Cobalt Aluminum Oxide Spinels. *Physical Review B* **2008**, *77*, 094412.

25. Roth, W., The Magnetic Structure of Co3o4. *Journal of Physics and Chemistry of Solids* **1964**, *25*, 1-10.

26. Ambrose, T.; Chien, C., Finite-Size Effects and Uncompensated Magnetization in Thin Antiferromagnetic Coo Layers. *Physical review letters* **1996**, *76*, 1743.

27. He, L.; Chen, C.; Wang, N.; Zhou, W.; Guo, L., Finite Size Effect on Néel Temperature with Co3o4 Nanoparticles. *arXiv preprint arXiv:0705.4344* **2007**.

28. Kumzerov, Y. A.; Kartenko, N.; Parfen'eva, L.; Smirnov, I.; Sysoeva, A.; Misiorek, H.; Jezowski, A., Determination of the Néel Temperature from Measurements of the Thermal Conductivity of the Co3o4 Antiferromagnet Nanostructured in Porous Glass Channels. *Physics of the Solid State* **2012**, *54*, 1066-1069.

29. Guillemet-Fritsch, S.; Navrotsky, A.; Tailhades, P.; Coradin, H.; Wang, M., Thermochemistry of Iron Manganese Oxide Spinels. *Journal of Solid State Chemistry* **2005**, *178*, 106-113.

30. Robie, R. A.; Hemingway, B. S., Low-Temperature Molar Heat Capacities and Entropies of Mno2(Pyrolusite), Mn3o4(Hausmanite), and Mn2o3(Bixbyite). *The Journal of Chemical Thermodynamics* **1985**, *17*, 165-181.

31. Chhor, K.; Bocquet, J.; Pommier, C.; Chardon, B., Heat Capacity and Thermodynamic Behaviour of Mn3o4 and Znmn2o4 at Low Temperatures. *The Journal of Chemical Thermodynamics* **1986**, *18*, 89-99.

32. Kjellqvist, L.; Selleby, M., Thermodynamic Assessment of the Fe-Mn-O System. *Journal of phase equilibria and diffusion* **2010**, *31*, 113-134.

33. Naito, K.; Inaba, H.; Yagi, H., Heat Capacity Measurements of Mnxfe3−Xo4. *Journal of Solid State Chemistry* **1981**, *36*, 28-35.

34. Levy, D.; Giustetto, R.; Hoser, A., Structure of Magnetite (Fe3o4) above the Curie Temperature: A Cation Ordering Study. *Physics and Chemistry of Minerals* **2012**, *39*, 169-176.

35. Klotz, S.; Steinle-Neumann, G.; Strässle, T.; Philippe, J.; Hansen, T.; Wenzel, M. J., Magnetism and the Verwey Transition in ${\Mathrm{Fe}}_{3}{\Mathrm{O}}_{4}$ under Pressure. *Physical Review B* **2008**, *77*, 012411.

36. Verwey, E.; Haayman, P., Electronic Conductivity and Transition Point of Magnetite ("Fe 3 O 4"). *Physica* **1941**, *8*, 979-987.

37. Niu, C.; Zaddach, A.; Oni, A.; Sang, X.; Hurt III, J.; LeBeau, J.; Koch, C.; Irving, D., Spin-Driven Ordering of Cr in the Equiatomic High Entropy Alloy Nifecrco. *Applied Physics Letters* **2015**, *106*, 161906.

38. Sahu, S. K.; Huang, B.; Lilova, K.; Woodfield, B. F.; Navrotsky, A., Thermodynamics of Fe3o4–Co3o4 and Fe3o4–Mn3o4 Spinel Solid Solutions at the Bulk and Nanoscale. *Physical Chemistry Chemical Physics* **2015**.

39. Gujrati, P. D.; Goldstein, M., Viscous Liquids and the Glass Transition. 9. Nonconfigurational Contributions to the Excess Entropy of Disordered Phases. *The Journal of Physical Chemistry* **1980**, *84*, 859-863.

40. Couchman, P.; Karasz, F., A Classical Thermodynamic Discussion of the Effect of Composition on Glass-Transition Temperatures. *Macromolecules* **1978**, *11*, 117-119.

41. Ganguly, J., Thermodynamic Modelling of Solid Solutions. *Solid Solutions in Silicate and Oxide Systems of Geological Importance. EMU Notes in Mineralogy* **2001**, *3*, 37.

42. Matsuoka, S., Free Volume, Excess Entropy and Mechanical Behavior of Polymeric Glasses. *Polymer Engineering & Science* **1981**, *21*, 907-921.

43. Shamblin, S. L.; Taylor, L. S.; Zografi, G., Mixing Behavior of Colyophilized Binary Systems. *Journal of pharmaceutical sciences* **1998**, *87*, 694-701.

44. Bates, F. S.; Fredrickson, G. H., Conformational Asymmetry and Polymer-Polymer Thermodynamics. *Macromolecules* **1994**, *27*, 1065-1067.

45. Benisek, A.; Dachs, E., A Relationship to Estimate the Excess Entropy of Mixing: Application in Silicate Solid Solutions and Binary Alloys. *Journal of Alloys and Compounds* **2012**, *527*, 127-131.

46. Witusiewicz, V. T.; Sommer, F., Estimation of the Excess Entropy of Mixing and the Excess Heat Capacity of Liquid Alloys. *Journal of Alloys and Compounds* **2000**, *312*, 228-237.

47. Sommer, F.; Singh, R. N.; Witusiewicz, V., On the Entropy of Mixing. *Journal of Alloys and Compounds* **2001**, *325*, 118-128.

48. Haselton, H. T.; Hovis, G. L.; Hemingway, B. S.; Robie, R. A., Calorimetric Investigation of the Excess Entropy of Mixing in Analbite-Sanidine Solid Solutions: Lack of Evidence for Na, K Short-Range Order and Implications for Two-Fbldspar Thermometry. *American Mineralogist* **1983**, *68*, 398-413.

49. Berman, R., Mixing Properties of Ca-Mg-Fe-Mn Garnets. *American Mineralogist* **1990**, *75*, 328-344.

50. Dachs, E.; Geiger, C. A.; von Seckendorff, V.; Grodzicki, M., A Low-Temperature Calorimetric Study of Synthetic (Forsterite+ Fayalite){(Mg 2 Sio 4+ Fe 2 Sio 4)} Solid Solutions: An Analysis of Vibrational, Magnetic, and Electronic Contributions to the Molar Heat Capacity and Entropy of Mixing. *The Journal of Chemical Thermodynamics* **2007**, *39*, 906-933.

51. Dachs, E.; Harlov, D.; Benisek, A., Excess Heat Capacity and Entropy of Mixing Along the Chlorapatite–Fluorapatite Binary Join. *Physics and Chemistry of Minerals* **2010**, *37*, 665-676.

52. Benisek, A.; Dachs, E.; Kroll, H., Excess Heat Capacity and Entropy of Mixing in High Structural State Plagioclase. *American Mineralogist* **2009**, *94*, 1153-1161.

53. Benisek, A.; Dachs, E.; Kroll, H., Excess Heat Capacity and Entropy of Mixing in the High-Structural State (K, Ca)-Feldspar Binary. *Physics and Chemistry of Minerals* **2010**, *37*, 209-218.

54. Bhattacharya, A.; Mohanty, L.; Maji, A.; Sen, S. K.; Raith, M., Non-Ideal Mixing in the Phlogopite-Annite Binary: Constraints from Experimental Data on Mg−Fe Partitioning and a Reformulation of the Biotite-Garnet Geothermometer. *Contributions to Mineralogy and Petrology* **1992**, *111*, 87-93.

55. Graham, C. M.; Navrotsky, A., Thermochemistry of the Tremolite-Edenite Amphiboles Using Fluorine Analogues, and Applications to Amphibole-Plagioclase-Quartz Equilibria. *Contributions to Mineralogy and Petrology* **1986**, *93*, 18-32.

56. Thompson, J.; Hovis, G. L., Entropy of Mixing in Sanidine. *American Mineralogist* **1979**, *64*, 57-65.

57. Thompson, J.; Waldbaum, D., Mixing Properties of Sandine Crystalline Solutions. 3. Calculations Based on 2-Phase Data. *American Mineralogist* **1969**, *54*, 811-&.

58. Holland, T.; Blundy, J., Non-Ideal Interactions in Calcic Amphiboles and Their Bearing on Amphibole-Plagioclase Thermometry. *Contributions to Mineralogy and Petrology* **1994**, *116*, 433-447.

59. Schliesser, J. M.; Olsen, R. E.; Enfield, D. B.; Woodfield, B. F., Determining the Location and Role of Al in Al-Modified Tio2 Nanoparticles Using Low-Temperature Heat Capacity, Electron Energy-Loss Spectroscopy, and X-Ray Diffraction. *The Journal of Physical Chemistry C* **2015**, *119*, 17867-17875.

60. Woodfield, B. F.; Liu, S.; Boerio-Goates, J.; Liu, Q.; Smith, S. J. Preparation of Uniform Nanoparticles of Ultra-High Purity Metal Oxides, Mixed Metal Oxides, Metals, and Metal Alloys. US 8,211,388 B2, Jul. 3, 2012.

61. Shi, Q.; Boerio-Goates, J.; Woodfield, B. F., An Improved Technique for Accurate Heat Capacity Measurements on Powdered Samples Using a Commercial Relaxation Calorimeter. *The Journal of Chemical Thermodynamics* **2011**, *43*, 1263-1269.

62. Stevens, R.; Boerio-Goates, J., Heat Capacity of Copper on the Its-90 Temperature Scale Using Adiabatic Calorimetry. *The Journal of Chemical Thermodynamics* **2004**, *36*, 857-863.

63. Shi, Q.; Boerio-Goates, J.; Woodfield, K.; Rytting, M.; Pulsipher, K.; Spencer, E. C.; Ross, N. L.; Navrotsky, A.; Woodfield, B. F., Heat Capacity Studies of Surface Water Confined on Cassiterite (Sno2) Nanoparticles. *The Journal of Physical Chemistry C* **2012**, *116*, 3910-3917.

64. Spencer, E. C.; Huang, B.; Parker, S. F.; Kolesnikov, A. I.; Ross, N. L.; Woodfield, B. F., The Thermodynamic Properties of Hydrated Γ-Al2o3 Nanoparticles. *The Journal of chemical physics* **2013**, *139*, 244705.

65. Schliesser, J. M.; Smith, S. J.; Li, G.; Li, L.; Walker, T. F.; Parry, T.; Boerio-Goates, J.; Woodfield, B. F., Heat Capacity and Thermodynamic Functions of Nano-Tio2 Rutile in Relation to Bulk-Tio2 Rutile. *The Journal of Chemical Thermodynamics* **2014**.

66. Schliesser, J. M.; Smith, S. J.; Li, G.; Li, L.; Walker, T. F.; Perry, T.; Boerio-Goates, J.; Woodfield, B. F., Heat Capacity and Thermodynamic Functions of Nano-Tio2 Anatase in Relation to Bulk-Tio2 Anatase. *The Journal of Chemical Thermodynamics* **2014**.

67. Boerio-Goates, J.; Li, G.; Li, L.; Walker, T. F.; Parry, T.; Woodfield, B. F., Surface Water and the Origin of the Positive Excess Specific Heat for 7 Nm Rutile and Anatase Nanoparticles. *Nano Letters* **2006**, *6*, 750-754.

68. Paukov, I.; Moroz, N.; Kovalevskaya, Y. A.; Belitsky, I., Low-Temperature Thermodynamic Properties of Disordered Zeolites of the Natrolite Group. *Physics and chemistry of minerals* **2002**, *29*, 300-306.

69. Navrotsky, A., Nanoscale Effects on Thermodynamics and Phase Equilibria in Oxide Systems. *ChemPhysChem* **2011**, *12*, 2207-2215.

70. Navrotsky, A., Energetics of Nanoparticle Oxides: Interplay between Surface Energy and Polymorphism. *Geochem. Trans* **2003**, *4*, 34-37.

71. Ross, N.; Spencer, E.; Parker, S.; Kolesnikov, A.; Boerio-Goates, J.; Woodfield, B.; Navrotsky, A. In *Influence of Adsorbed Water on Energetics of Cassiterite Nanoparticles*, Geochimica et Cosmochimica Acta, PERGAMON-ELSEVIER SCIENCE LTD THE BOULEVARD, LANGFORD LANE, KIDLINGTON, OXFORD OX5 1GB, ENGLAND: 2010; pp A884-A884.

72. Ross, N. L.; Spencer, E. C.; Levchenko, A. A.; Kolesnikov, A. I.; Abernathy, D. L.; Boerio-Goates, J.; Woodfield, B. F.; Navrotsky, A.; Li, G.; Wang, W. In *Dynamics of Water Confined on the Surface of Titania and Cassiterite Nanoparticles*, MRS Proceedings, Cambridge Univ Press: 2011; pp mrss11-1352-gg04-05.

73. Spencer, E. C.; Levchenko, A. A.; Ross, N. L.; Kolesnikov, A. I.; Boerio-Goates, J.; Woodfield, B. F.; Navrotsky, A.; Li, G., Inelastic Neutron Scattering Study of Confined Surface Water on Rutile Nanoparticles. *The Journal of Physical Chemistry A* **2009**, *113*, 2796-2800.

74. Spencer, E. C.; Ross, N. L.; Parker, S. F.; Kolesnikov, A. I.; Woodfield, B. F.; Woodfield, K.; Rytting, M.; Boerio-Goates, J.; Navrotksy, A., Influence of Particle Size and Water Coverage on the Thermodynamic Properties of Water Confined on the Surface of Sno2 Cassiterite Nanoparticles. *The Journal of Physical Chemistry C* **2011**, *115*, 21105-21112.

75. Huang, B.; Schliesser, J.; Olsen, R. E.; J Smith, S.; F Woodfield, B., Synthesis and Thermodynamics of Porous Metal Oxide Nanomaterials. *Current Inorganic Chemistry* **2014**, *4*, 40-53.

76. Levchenko, A. A.; Li, G.; Boerio-Goates, J.; Woodfield, B. F.; Navrotsky, A., Tio2 Stability Landscape: Polymorphism, Surface Energy, and Bound Water Energetics. *Chemistry of Materials* **2006**, *18*, 6324-6332.

77. Shapiro, J. L.; Woodfield, B. F.; Stevens, R.; Boerio-Goates, J.; Wilson, M. L., Molar Heat Capacity and Thermodynamic Functions of the Type Ii Antiferromagnet Mno. *The Journal of Chemical Thermodynamics* **1999**, *31*, 725-739.

78. Schliesser, J. M.; Woodfield, B. F., Lattice Vacancies Responsible for the Linear Dependence of the Low-Temperature Heat Capacity of Insulating Materials. *Physical Review B* **2015**, *91*, 024109.

79. Phillips, N. E., Low-Temperature Heat Capacity of Metals. *Critical Reviews in Solid State and Material Sciences* **1971**, *2*, 467-553.

80. Fisher, R. A.; Bouquet, F.; Phillips, N. E.; Franck, J. P.; Zhang, G.; Gordon, J. E.; Marcenat, C., Electron, Spin-Wave, Hyperfine, and Phonon Contributions to the Low-Temperature Specific Heat of La0.65ca0.35mno3:Effects of Magnetic Fields and 16o/18o Exchange. *Physical Review B* **2001**, *64*, 134425.

81. Schliesser, J.; Woodfield, B., Development of a Debye Heat Capacity Model for Vibrational Modes with a Gap in the Density of States. *Journal of physics. Condensed matter: an Institute of Physics journal* **2015**, *27*, 285402-285402.

82. Gopal, E. S. R., *Specific Heats at Low Temperatures*; Plenum Press New York, 1966; Vol. 227.

83. Kelley, K. K.; King, E. G., *Entropies of the Elements and Inorganic Compounds*; US Government Printing Office, 1961; Vol. 592.

84. Pitzer, K. S., Thermodynamics; 3rd Edition. *McGraw-Hill Book Co, New York* **1995**, 626.

85. Navrotsky, A., Thermodynamics of A3o4-B3o4 Spinel Solid Solutions. *Journal of Inorganic and Nuclear Chemistry* **1969**, *31*, 59-72.

86. Wood, B., Activity Measurements and Excess Entropy-Volume Relationships for Pyrope-Grossular Garnets. *The Journal of Geology* **1988**, 721-729.

6 DETERMINING THE LOCATION AND ROLE OF AL IN AL-MODIFIED TIO2 NANOPARTICLES USING LOW-TEMPERATURE HEAT CAPACITY, ELECTRON ENERGY-LOSS SPECTROSCOPY, AND X-RAY DIFFRACTION

6.1 Introduction

TiO_2 nanoparticles are widely used in industry as catalysts, catalyst supports, components of solar cells, and even household products[1-6]. Dopants are often incorporated to improve structural and thermal stability, catalytic activity and selectivity, photoresponse, and other desirable chemical and physical properties[7-12]. Al is a common dopant added to TiO_2 nanoparticles to control the thermal stability, surface area, and porosity of the nanostructure; however, the role the Al dopant has in stabilizing the structure is unclear, as is often the case with doped materials. Understanding the role that the Al dopant has on TiO_2 nanoparticles is necessary to produce particles with optimized properties.

A fundamental knowledge of dopant functionality requires that its location in the lattice be known. Although often difficult, determining the location of the dopant in a material has been made more feasible with several techniques such as sophisticated X-ray diffraction (XRD) and electron microscopy techniques. Unfortunately, these techniques often have poor detection limits which has led to contradictory conclusions using similar data. For example, the absence of separate aluminum oxide peaks in the XRD data of Al doped TiO_2 suggests that the Al dopant is

interstitially[13] or substitutionally[14-16] incorporated into the TiO_2 lattice, yet several investigations report that Al is found on the surface or between TiO_2 nanoparticles in an Al_2O_3 phase[17-19].

Heat capacity, a bulk measurement, is often quite useful for identifying and quantifying concentrations of impurities and the average properties of a material[20]. The heat capacity of a material is a measure of all the energy states (vibrational, electronic, magnetic, etc.) at a given temperature, and its dependence on temperature can be modeled with theoretical functions for each contribution[20-22]. We have recently shown that a linear dependence in the low-temperature ($T < 10$ K) heat capacity data for insulators can be directly proportional to lattice vacancy concentrations[23]. We have also shown that many samples that have short-range correlations such as AlO_x polyheda have excess low-energy modes with a gap in the density of states (DOS) that is also manifest in the low-temperature heat capacity data[24]. Entropy values can be derived from heat capacity data and can give information about mixing effects. These three characteristics can provide important structural information on Al doped TiO_2 nanoparticles.

We have recently investigated the structure of Al doped TiO_2 nanoparticles (focusing on 22 mol% Al doped TiO_2) using XRD, X-ray absorption near edge structure (XANES), extended X-ray absorption fine structure (EXAFS), transmission electron microscopy (TEM), ^{27}Al magic-angle spinning nuclear magnetic resonance (^{27}Al MAS-NMR), and N_2 sorption isotherms using the Brunauer-Emmett-Teller (BET) method[25]. The analysis also included a preliminary heat capacity investigation using the linear term of the low-temperature data fitting, which at that time was only believed to be related to lattice vacancies. We have since shown that the linear term is indeed directly proportional to lattice vacancy concentrations and have improved the heat capacity data analysis using our recently developed linear term[23] and gapped term[24] models.

This work supplements our previous work[25] by giving a more detailed and accurate analysis of the heat capacities of these Al doped TiO_2 nanoparticles. Specifically, our investigation provides greater insight on the location of the Al dopant having concentrations of 5-50 mol% Al, demonstrates a new method for determining the location of a dopant, and introduces a new use for low-temperature heat capacity analysis. The linear terms and gapped terms generated from the low-temperature heat capacity data and the entropies at 298.15 K indicate that the Al is located in the TiO_2 lattice and creates a more stable structure than pure TiO_2. Electron energy-loss spectroscopy (EELS) and XRD, using a better radiation source than previously used, were also performed to support the conclusions drawn from the heat capacity analysis.

6.2 Experimental

6.2.1 Sample Preparation

Ten samples of Al doped TiO_2 were prepared following a general solvent deficient method taking two different routes: dry-rinse-calcine (DRC) and dry-calcine-rinse (DCR), the details of which can be found elsewhere[25-27]. For the pure TiO_2, $TiCl_4$ was mixed with NH_4HCO_3, and for Al-modified TiO_2, $Al(NO_3)_3 \cdot 9H_2O$ was added to the mixture of $TiCl_4$ and NH_4HCO_3. Water was added to produce a slurry which was then dried in air at 100°C. DRC samples were then rinsed with distilled water and calcined at 400°C for three hours in air. DCR samples were first calcined under the same conditions and then rinsed. These two synthesis methods produce materials with quite different pore properties such as size and shape. Samples from each method consisted of pure TiO_2, 5 mol%, 14 mol%, 22 mol% and 50 mol% Al-modified TiO_2, where mol% indicates the percent of Al^{3+} ions relative to all metal cations.

6.2.2 Sample Characterization

The samples were previously characterized by powder XRD, XANES, EXAFS, TEM, ^{27}Al MAS-NMR, and N_2 sorption isotherms using the BET method[25]. XRD results of pure and 22 mol% Al indicate these samples have no detectable Al_2O_3 phase. Particles sizes determined from XRD range from 2-7 nm. XANES gives the Ti coordination of both pure TiO_2 samples and 22 mol% Al DCR to be 6-coordinate Ti, while 22 mol% Al DRC shows the presence of 5-coordinate Ti. The ^{27}Al NMR results reveal primarily 6-coordinate Al for both pure TiO_2 samples and a mixture of 6-, 5-, and 4-coordinate Al for both 22 mol% Al samples[25]. Water contents have been determined by thermogravimetric analysis (TGA) and range from 0.20-0.50 and 0.26-0.59 mol H_2O per mol TiO_2 for DCR and DRC, respectively. A summary of the pore properties of these materials is given in Table 6-1, and further details on the sample characterization can be found in our previously published papers on these Al-doped TiO_2 samples[25-26].

Table 6-1: Summary of the Pore Properties of All Samples Including Surface Area (SA), Pore Volume (PV), and Pore Diameter (PD)[25]

	mol% Al	formula	SA (m^2/g)	PV (cm^3/g)	PD (nm)
DCR	0	$TiO_2 \cdot 0.20H_2O$	124	0.30	7.8
	5	$Ti_{0.95}Al_{0.05}O_{1.975} \cdot 0.45H_2O$	138	0.25	3.8
	14	$Ti_{0.86}Al_{0.14}O_{1.93} \cdot 0.28H_2O$	172	0.35	7.4
	22	$Ti_{0.78}Al_{0.22}O_{1.89} \cdot 0.28H_2O$	184	0.34	6.3
	50	$Ti_{0.50}Al_{0.50}O_{1.75} \cdot 0.50H_2O$	307	0.37	4.3
DRC	0	$TiO_2 \cdot 0.26H_2O$	164	0.24	4.7
	5	$Ti_{0.95}Al_{0.05}O_{1.975} \cdot 0.57H_2O$	375	0.33	4.0
	14	$Ti_{0.86}Al_{0.14}O_{1.93} \cdot 0.59H_2O$	490	0.77	5.7
	22	$Ti_{0.78}Al_{0.22}O_{1.89} \cdot 0.49H_2O$	471	0.44	4.4
	50	$Ti_{0.50}Al_{0.50}O_{1.75} \cdot 0.44H_2O$	349	0.34	4.4

6.2.3 Heat Capacities

Heat capacities were measured from 1.9 to 300 K using a Quantum Design Physical Property Measurement System (PPMS), which uses a thermal relaxation technique. Prior to measurement, the powder samples were dried *in vacuo* at 100° C for about 6 hrs and stored in an argon atmosphere to prevent readsorption of water from the atmosphere. In the argon atmosphere, 10-14 mg of each sample were mixed with copper strips (Alpha Aesar mass fraction purity 0.9995) and put into copper cups that were pressed into disks approximately 3 mm in diameter and 1 mm in height following the method of Shi *et al*[28]. Addenda measurements were performed before each measurement that determined the heat capacity of the calorimeter and the Apiezon N grease used to attach the sample. After each addenda measurement, the sample was attached to the PPMS puck, and the heat capacity was measured. The system automatically corrects for the heat capacities of the calorimeter and grease, and the heat capacity of the copper contribution was corrected using data from Stevens and Boerio-Goates[29]. Data measured on the PPMS using this method have an estimated uncertainty of $\pm 0.02 \cdot C_p^\circ$ for $2 < T/\mathrm{K} < 10$ and $\pm 0.01 \cdot C_p^\circ$ for $10 < T/\mathrm{K} < 300$[28].

6.2.4 Electron Energy-Loss Spectroscopy

EELS was performed for pure and Al doped TiO_2 samples as well as an Al_2O_3 sample used as a reference[30]. Data were collected using a Tecnai F20 analytical S/TEM with an incident beam energy of 200 keV equipped with a Gatan parallel-collection spectrometer. Scanning TEM (STEM) and high-resolution TEM (HRTEM) images were taken of the sampling areas used to collect the EELS data. Figure 6-1a shows an HRTEM image of 50 mol% Al DCR (slightly out of focus to produce Fresnel contrast) in which diffraction fringes can be seen for several particles,

and Figure 6-1b shows a STEM image of 14 mol% Al DRC in which planes of atoms are distinguishable for several particles.

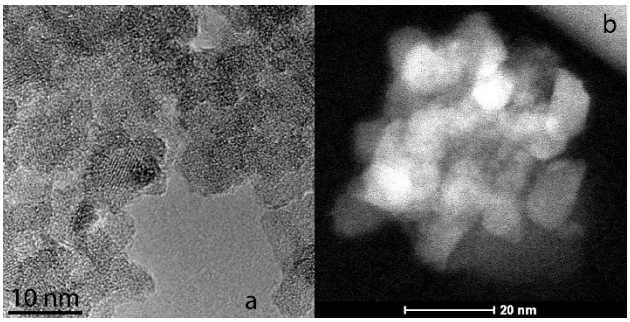

Figure 6-1: TEM Images Showing EELS Data Sampling Region of (a) 50 mol% Al TiO_2 DCR Nanoparticles (HRTEM) and (b) 14 mol% Al TiO_2 DRC Nanoparticles (STEM).

EELS data were collected in parallel imaging mode with several energy-loss ranges and over several regions of space. Resolution of the EELS spectrometer, as determined by the full width of the zero-loss peak (ZLP) at half maximum, was found to be about 0.8 eV. We note that the spectrometer experienced some issues that appear in the center of some of the spectra as an abrupt shift in the intensity, but this is merely an artifact and is not related to any peaks.

6.2.5 X-Ray Diffraction

Powder XRD data of all samples were collected at 100 K and in transmission mode using a MACH3 four circle single crystal diffractometer coupled to a Bruker Apex II CCD detector with a Bruker-Nonius FR591 rotating anode X-ray source producing Cu K_α radiation (λ = 1.5418 Å). The samples were prepared for the XRD measurements by packing the powders into polyimide capillaries with an inner diameter of 0.305 mm. Data were collected between 2° – 133° 2θ by performing a series of 8 overlapping phi 360 scans. The Bruker XRD^2 program was used to merge the images and integrate the intensity of the diffraction rings.

6.3 Results/Discussion

6.3.1 Heat Capacity Fitting Analysis

The experimental heat capacity data are shown graphically in Figure 6-2. The data were fit to functions that provide information on the contributions. The best fits for each temperature range are determined from the percent root mean square deviation (%RMS) and a plot of the deviation of each point from the fitting function. Fits that were physically meaningful (no negative contributions), had the lowest %RMS, and had random deviations were selected as the best fits.

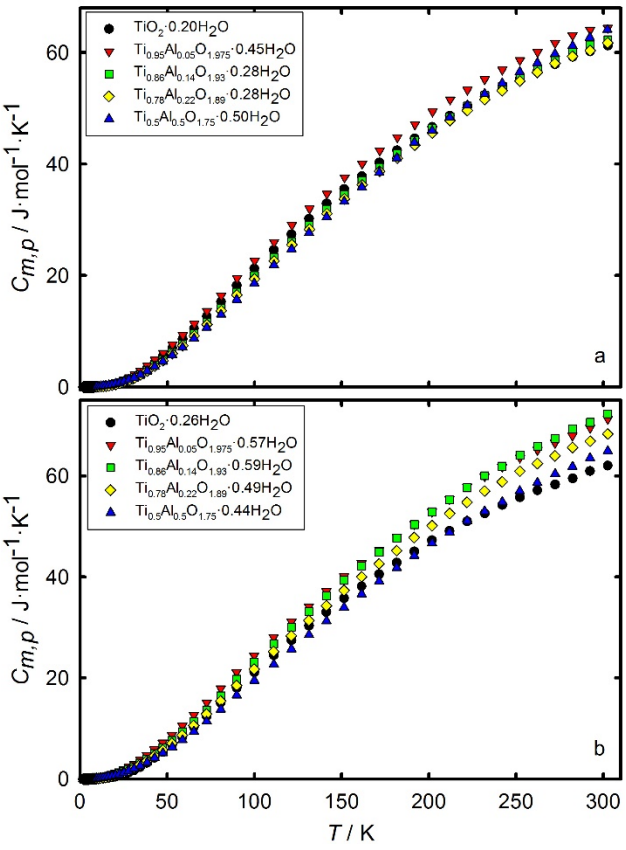

Figure 6-2: Molar Heat Capacity Data from 1.9-300 K Measured on a Quantum Design PPMS of Pure and Al Doped TiO_2 Nanoparticles. (a) DCR. (b) DRC.

High temperature data (T > 30 K) were fit to a sum of Debye and Einstein functions that provide information on the lattice heat capacity

$$C_{high\,T} = m \cdot D(\Theta_D/T) + n_1 \cdot E(\Theta_{E,1}/T) + n_2 \cdot E(\Theta_{E,2}/T) \quad (6\text{-}1)$$

where D(Θ_D / T), E($\Theta_{E,1}$ / T), and E($\Theta_{E,2}$ / T) are Debye and Einstein functions[22, 31]; m, n_1, n_2, Θ_D, $\Theta_{E,1}$, and $\Theta_{E,2}$ are all adjustable parameters; and ($m + n_1 + n_2$) should be approximately equal to the number of atoms in the formula unit[32]. Generally one Debye and one Einstein function are sufficient to fit high temperature data, but for these samples such a fit was only valid above about 100 K. To fit a larger range, the extra Einstein function was needed.

Data in the mid temperature range (from 6 – 50 K) were fit with polynomials to provide sufficient overlap with the low temperature and high temperature fits having the form:

$$C_{mid\,T} = \sum_{n=0,1,2\ldots6} A_n T^n \quad (6\text{-}2)$$

Although these fits do not provide information on the underlying physical contributions, they are often necessary to fit data through inflection points.

The heat capacity data below 10 K (shown in Figure 6-3 as C/T versus T) were fit to the sum of theoretical functions:

$$C_{low\,T} = \gamma T + B_3 T^3 + B_5 T^5 + B_7 T^7 + B_{gap} T^2 e^{-\delta/2T} \quad (6\text{-}3)$$

where the γ term represents the contribution from lattice vacancies[23], the B_3, B_5, and B_7 terms represent the harmonic-lattice expansion[33], and the "gapped" B_{gap} term represents phonon contributions from low-energy modes with a gap in the vibrational DOS [24]. The contributions related to vacancies and low energy modes can be used to identify where the Al dopant is located in the TiO_2.

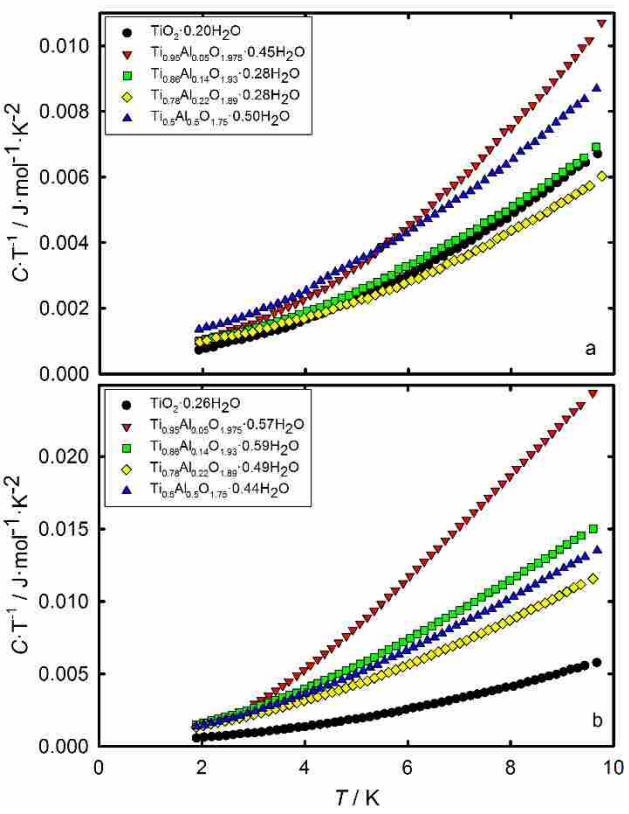

Figure 6-3: Low-temperature Heat Capacity Data from 1.9-10 K of Pure and Al Doped TiO_2 Nanoparticles Plotted as *C*/*T* versus *T*. (a) DCR. (b) DRC.

Fits having various combinations of the parameters given in Eq. 6-3 were used until the best combination of parameters was found as determined by the fit with a low %RMS and a random deviation. The fits of all samples were significantly better when the linear term was included. Only five samples showed improvement in the fit quality (lower %RMS and random deviation) when the gapped term was included: 5 mol% DCR, 5 mol% DRC, 14 mol% DCR, 14 mol% DRC, and 22 mol% DRC. We note that the linear terms were not affected by the addition of the gapped terms; therefore, the analysis of the linear terms remains valid for all fits whether the gapped term was used or not.

6.3.1.1 Analysis of Linear Terms

The linear term γ in the low-temperature heat capacity fitting is directly proportional to the concentration of lattice vacancies in insulators[23]; therefore, any trends in γ will be indicative of trends in vacancy concentrations. The linear terms of all samples are plotted as a function of mol% Al in Figure 6-4. Also included in Figure 6-4 are the linear terms that are expected for a mechanical mixture of TiO_2 and Al_2O_3. The value for pure TiO_2 is taken as the average of the two pure TiO_2 samples investigated here, and the value for Al_2O_3 is taken as the average of several γ-Al_2O_3 samples we have published elsewhere[30].

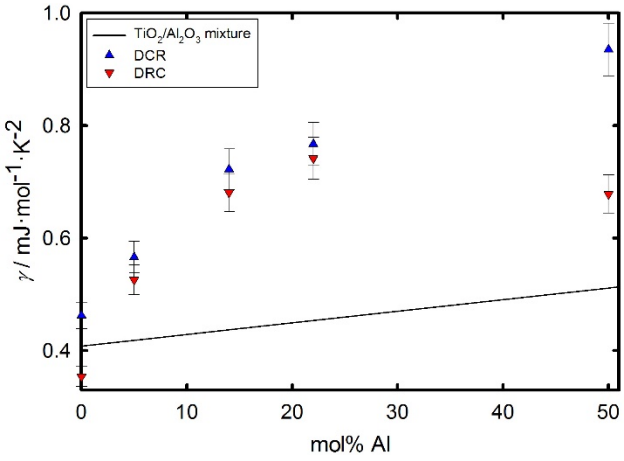

Figure 6-4: Linear Terms from Fits of the Low-temperature Heat Capacity Data of Pure and Al Doped TiO_2 Nanoparticles Plotted as a Function of mol% Al. The line represents values that would be expected for a mechanical mixture of TiO_2 and Al_2O_3 based on γ of pure TiO_2 and the average of several γ values of Al_2O_3 published elsewhere.[30] DCR are blue triangles; DRC are green inverted triangles.

As seen in Figure 6-4, the trends for both synthesis routes are very similar. Upon addition of 5 mol% Al, the linear term, and therefore the concentration of lattice vacancies, increases much more than what would be expected for a mechanical mixture. The increase from 5-14 mol% Al is not as large as the increase from 0-5 mol% Al but is still greater than the increase for

a mechanical mixture. The increase from 14-22 mol% Al is again larger than the mechanical mixture but lower than the increase from 5-14 mol% Al. The values of γ for the DCR samples from 22-50 mol% Al then increase with approximately the same slope as from 14-22 mol% Al, but the value of the 50 mol% Al DRC sample actually decreases from 22 mol% Al.

The significant increase in vacancy concentration with the addition of Al^{3+} indicates that separate phases of TiO_2 and Al_2O_3 are not being formed but that Al^{3+} must be affecting the TiO_2 lattice. We interpret this to suggest that Al^{3+} enters the TiO_2 lattice causing an increase in vacancies due to the charge difference between the Al^{3+} and Ti^{4+} ions. The increase from 0-14 mol% Al is approximately linear and reflects the increase in vacancy concentration below the saturation point. At lower concentrations, the Al^{3+} ions enter disperse sites in the TiO_2 lattice and behave similar to Ti^{4+}.

After the saturation point is passed, at about 14 mol% Al, γ increases linearly but with a different slope than before the saturation point. This saturation point is consistent with work on Fe^{3+} doped TiO_2 in which it was shown that TiO_2 accommodated as much as 10 mol% Fe^{3+} before the TiO_2 structure broke down[11]. The linear increase in γ from 14-50 mol% Al for the DCR samples suggests that a highly disordered $TiAlO_x$ phase forms in proportion to the amount of Al^{3+} dopant. The decrease in γ from 22-50 mol% Al for the DRC sample suggests that the lattice is becoming more ordered in this range, which could be indicative of the formation of Al_2O_3. Therefore, the disorder increases from 0-14 mol% Al due to charge mismatch between Al^{3+} and Ti^{4+} and continues to increase from 14-50 mol% Al (except for 50 mol% Al DRC which appears to form some Al_2O_3) but with less magnitude due to the formation of a highly disordered secondary phase.

These measured values of γ approximately correspond to vacancy concentrations between 2.3×10^{-3} (pure TiO_2 DRC) and 6.0×10^{-3} (50 mol% Al DCR) vacancies per formula unit[23], which are similar to values reported elsewhere (9.41×10^{-4} for pure TiO_2 [8], and 6.27×10^{-3} for Fe^{3+} doped TiO_2 [11]); therefore, vacancies increase by 3.7×10^{-3} upon the addition of 50 mol% Al for the DCR sample.

The dopant ions have been proposed to interact with TiO_2 by entering either the naturally occurring vacancies in TiO_2 referred to as interstitial sites[13] or by entering the Ti^{4+} sites though substitution[14-16]. If Al^{3+} enters the TiO_2 lattice in Ti^{4+} sites, oxygen vacancies will be created to compensate for the charge difference between Al^{3+} and Ti^{4+}; likewise, if Al^{3+} enters interstitial sites, Ti^{4+} vacancies or a combination of Ti^{4+} and O^{2-} vacancies will increase to compensate for the extra positive charge. In the former case, the substitution of two Al^{3+} ions for two Ti^{4+} ions will create a net charge of -2 that must be compensated for by removing an O^{2-} (making an Al:vacancy ratio of 2:1), but in the latter case, four Al^{3+} ion will create either three Ti^{4+} vacancies (4:3) or six TiO^{2+} vacancies (twelve total vacancies yielding the ratio 1:3); therefore, Al^{3+} entering interstitial sites will create more lattice vacancies than if they enter Ti^{4+} sites. The situation becomes further complicated if we no longer assume that Ti has only a +4 charge or if we consider the possibility that the dopant ions could enter both sites.

The smallest increase in lattice vacancies from these hypothetical values occurs for substitution, which creates one mole of O^{2-} vacancies for every two moles of Al^{3+} added. This is orders of magnitude larger than the actual increase in vacancies determined from the heat capacity data (3.7×10^{-3}) suggesting that most vacancies do not behave as defects that contribute to the heat capacity; therefore, the addition of Al dopant appears to create small regions of some

hybrid $TiAlO_x$ structure void of short-range defects but that lacks long-range order similar to a glass, which is confirmed with the other experiments discussed herein.

6.3.1.2 Analysis of Gapped Terms

The gapped terms derived from the low-temperature heat capacity data are related to excess low-energy modes with a gap in the DOS caused by short-range correlations typically associated with long-chain polymers or loosely bound polyhedra such as those found in glasses and zeolites[24]. The dimensionality of the physical feature causing the contribution is reflected in the exponent of *T* in the gapped term.

The presence of the gapped terms in the heat capacity fitting of the five samples mentioned above suggests that at low dopant concentrations, regions of short-range order are created within the TiO_2 lattice. At higher concentrations (22-50 mol% Al DCR and 50 mol% Al DRC), long-range order in the lattice is restored. This suggests that at low concentrations the dopant Al^{3+} ions enter the TiO_2 lattice and form very small regions of a $TiAlO_x$ structure having primarily TiO_2-like character, but as the dopant concentration increases beyond about 22 mol% Al, these regions become sufficiently large that short-range correlations that cause the gapped term no longer exist. These conclusions are similar to those of a recent investigation on the perovskite $Sr_3Ru_2O_7$ in which the magnetic long-range order was disrupted as Mn dopant was added[34].

The two-dimensional character of these gapped terms in the 5, 14, and 22 (DRC) mol% Al samples suggests that these regions of $TiAlO_x$ structure must be planar, but we know from other measurements that the Al^{3+} ions are not concentrated on the surface[25]. We believe that these 2D regions are created during particle growth as follows: very small TiO_2 clusters initially form; clusters near regions of concentrated Al^{3+} (a byproduct of the solvent-deficient synthesis[26-

[27]) react with the ions, which create small monolayer island-like structures; TiO_2 continues to grow, eventually growing over the Al monolayer as a tree grows over a wound or a sign nailed to its trunk; this creates a highly disordered $TiAlO_x$ region while retaining most of the bulk properties of TiO_2 as observed in these samples by the EELS and XRD experiments discussed herein and our other experiments reported elsewhere[25]. The absence of the gapped terms for samples with more dopant suggests that the $TiAlO_x$ features in these particles are more Al_2O_3-like such that their vibrations can be treated as traditional Debye modes.

6.3.2 Thermodynamic Results

The low, mid, and high temperature fitting functions were used to generate smooth heat capacity data $C_{m,p}^{\circ}$ and thermodynamic functions $\Delta_o^T S_m^{\circ}$ and $\Delta_0^T H_m^{\circ}$ at selected temperatures from 0 – 300 K. Water contributions were subtracted from the thermodynamic values at $T = 298.15$ K using thermodynamic data of water bound to the surface of TiO_2 nanoparticles as we have done previously[35-37].

The entropies are indicative of stability and could aid in understanding the structural and stabilization effects of the Al dopant. The entropy of mixing is particularly useful for determining the site of the Al because a solid solution is expected to have an excess entropy related to mixing on an atomic scale. This excess entropy of mixing is given as

$$\Delta S_{mix} = -R[X_a \ln(X_a) + X_b \ln(X_b)] \quad (6\text{-}4)$$

where R is the gas constant, X_a is the mole fraction of substance a, and X_b is the mole fraction of substance b[38-40]. The entropy of a mechanical mixture of two solid powders, such as TiO_2 and Al_2O_3, is just a weighted sum of the entropies of the respective pure substances, but the entropy of a solid solution will be the entropy of the mechanical mixture plus the entropy of mixing (Eq. 6-4). Because the metal cations do not enter O^{2-} anion sites, we can treat the constituents of Eq.

6-4 as TiO_2 and $AlO_{1.5}$ equivalents and assume that mixing occurs on an oxide scale rather than an atomic scale[39-40].

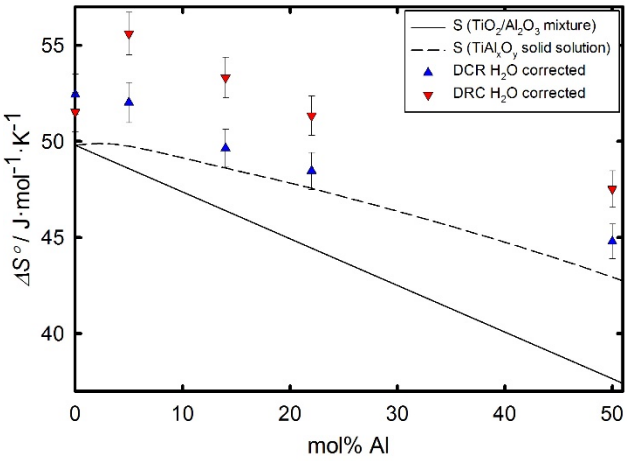

Figure 6-5: Entropies of All Samples after having been Corrected for Water-loss Using the Inner-water Model of ref. 37. Also shown are theoretical values of entropies expected for a mechanical mixture (solid line) and a solid solution (dashed line) of these compounds. DCR are blue triangles; DRC are green inverted triangles.

Figure 6-5 compares the entropies obtained from this investigation with those expected for mechanical mixtures and solid solutions of the cations in the forms TiO_2 and $AlO_{1.5}$. Entropy values of pure TiO_2 anatase and $AlO_{1.5}$ are taken as 49.8 $J \cdot mol^{-1}K^{-1}$ [41] and 25.5 $J \cdot mol^{-1}K^{-1}$ (half the value of Al_2O_3)[42], respectively. As can be seen, the entropy data of all samples more closely resemble those of the solid solutions, which include the entropy of mixing. The DRC data have slightly higher entropy values than the DCR counterparts, which we attribute to errors when correcting for water. We estimate the average uncertainty in these values to be about 5 %, but we note that the uncertainties of samples with either a large amount of water or Al dopant are greater. Therefore, entropies provide greater evidence that Al is entering the TiO_2 lattice to form a solid solution.

6.3.3 Electron Energy-Loss Spectroscopy Results

EELS data were collected over several regions of interest for these samples. Figures 6-6, 6-7, and 6-8 show the low-loss data (below 55 eV), the energy-loss near-edge structure (ELNES) data around the Al L edge (70 – 130 eV), and the ELNES data around the Ti L and O K edges (440 – 545 eV), respectively. Data around the Al K (about 1500 eV) edge were also acquired but are not shown since the signal to noise or signal to background ratios were usually too small to obtain any interpretable data. We also note that the Ti L_1 edge at about 565 eV (data also not shown) was only observed for pure TiO_2 suggesting a strong interaction with the Al.

6.3.3.1 Low-loss Region

The low-loss data (see Figure 6-6) contain the ZLP, the plasmon peak, transitions involving valence electrons, and even the Ti M edge at about 47 eV. The ZLP of each spectrum was used to calibrate the spectrum to correct energy losses. Low-loss peaks at about 6, 11, 25, 38, and 47 eV are common for TiO_2, while Al_2O_3 typically has only one low-loss peak at about 25 eV[43].

Figures 6-6a and 6-6b show low-loss data for all DCR and DRC samples, respectively, that have all been scaled and offset for clarity. Also shown are the data of pure Al_2O_3 as a reference[30]. Dashed vertical lines have been inserted into the figures to aid in showing the shift or disappearance of several peaks. These figures show that as the dopant concentration increases from 0 mol% Al (bottom spectrum) to pure Al_2O_3 (top spectrum), the Ti inter/intraband transitions at about 6, 12, and 38 eV become less pronounced. By 50 mol% Al the material appears to be more like Al_2O_3 than TiO_2, having only faint traces of these transitions. The peak at about 25 eV (likely caused by plasmons in both TiO_2 and Al_2O_3) in DCR samples also shows a distinct shift towards lower energies. Only the plasmon peak at 25 eV and the Ti M peak remain

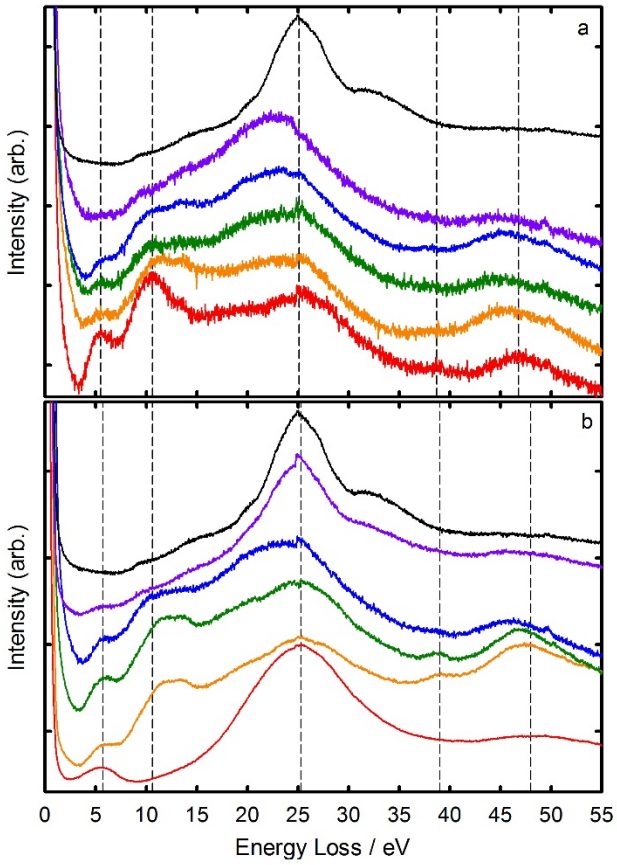

Figure 6-6: EELS Low-loss Data (below 55 eV) of All Samples as well as Data of an Al_2O_3 Standard Showing Progression of Peaks as Al Concentration Increases. Curves represent, starting from the bottom, TiO_2 (red), $Ti_{0.95}Al_{0.05}O_{1.975}$ (orange), $Ti_{0.86}Al_{0.14}O_{1.93}$ (green), $Ti_{0.78}Al_{0.22}O_{1.89}$ (blue), $Ti_{0.5}Al_{0.5}O_{1.75}$ (purple), and Al_2O_3 (black). Data have been scaled and offset for clarity. (a) DCR and (b) DRC.

by 50 mol% Al, but the Ti M peak is very different from that of pure TiO_2 as can be seen by the shift of this peak towards lower energies.

These changes suggest that the dopant is changing the electronic and structural character of the TiO_2 nanoparticles as would be expected for a solid solution. A mixture of TiO_2 and Al_2O_3 phases would not show any disappearance or shifts in peaks but rather a sum of all TiO_2 and Al_2O_3 peaks having the same energies as their parent materials. Because these particles have an average diameter of about 5 nm, approximately one third of the atoms are on the surface.

Forming a TiO_2/Al_2O_3 core/shell structure for such small particles could induce the shifts in the electronic structure discussed herein, but these surface effects would not likely have such a substantial impact on electronic structure of the remaining two-thirds of the atoms.

6.3.3.2 ELNES Analysis of the Al L Edge

The Al $L_{2,3}$ and L_1 ELNES edges arise from electronic transitions involving core electrons and are centered at about 80, 95, and 120 eV[43-45]. Figure 6-7 shows the data collected around these edges. The Al L edge positions and shapes of the Al_2O_3 standard correspond well with literature data published elsewhere[43-45]. At low dopant concentrations, Al is not observed (see Figure 6-7) suggesting that it is very disperse as would be expected for a solid solution of 5-14 mol% Al in TiO_2. In both 22 mol% Al samples and 50 mol% Al DCR, Al is observed as broad peaks quite different from the Al L edge of pure Al_2O_3 but somewhat similar to highly disordered Al at interfaces[44-45]. In 50 mol% Al DRC, the Al L edge appears very similar to that of Al_2O_3 suggesting that the atomic character immediately surrounding the Al atoms appears Al_2O_3-like.

6.3.3.3 ELNES Analysis of the Ti L and O K Edges

The Ti $L_{2,3}$ and O K ELNES edges are centered at about 460 and 535 eV, respectively[43, 46]. The shape and position of these edges is indicative of the density of unoccupied electronic states immediately surrounding the atom undergoing the transition; therefore, the same type of atom usually produces very different edge shapes and onsets for different materials (such as the O K edge in TiO_2 versus Al_2O_3). The Ti $L_{2,3}$ edge is typically observed as four narrow peaks known as “white lines”, while the O K edge of TiO_2 is seen as a doublet peak at about 530 eV followed by a broad and low intensity peak centered at about 540 eV (see the bottom spectra in

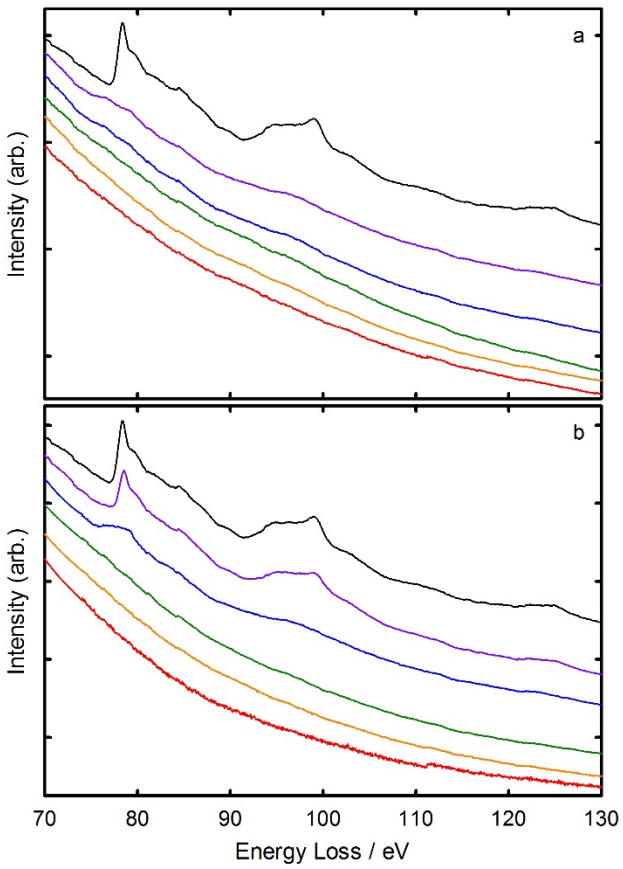

Figure 6-7: EELS Data around the Al L Edge (70-130 eV) of All Samples as well as Data of an Al_2O_3 Standard Showing Progression of Peaks as Al Concentration Increases. Curves represent, starting from the bottom, TiO_2 (red), $Ti_{0.95}Al_{0.05}O_{1.975}$ (orange), $Ti_{0.86}Al_{0.14}O_{1.93}$ (green), $Ti_{0.78}Al_{0.22}O_{1.89}$ (blue), $Ti_{0.5}Al_{0.5}O_{1.75}$ (purple), and Al_2O_3 (black). Data have been scaled and offset for clarity. (a) DCR and (b) DRC

Figure 6-8). The O K edge of Al_2O_3 abruptly increases to a high intensity at about 535 eV and abruptly decreases back down to the baseline at about 545 eV (see the top spectra in Figure 6-8).

Figures 6-8a and 6-8b show the Ti $L_{2,3}$ and O K edges of all DCR and DRC samples, respectively, that have all been scaled and offset for clarity. As can be seen in the figures, the Ti $L_{2,3}$ edge has only two discernable peaks for all samples even though the spectrometer has sufficient resolution to distinguish all four peaks; therefore, the peak broadening that merges the four peaks into two must be related to the samples. Figure 6-8 shows how the O K edge shifts

from having primarily TiO_2 character to having mostly Al_2O_3 character. As mentioned above, a mixture of TiO_2 and Al_2O_3 phases would have a sum of both types of peaks, but here we see a shift in the electronic structure surrounding O towards a more Al_2O_3-like environment. This suggests that at low concentrations the Al dopant enters the TiO_2 lattice without having much of an effect on the TiO_2 electronic character, but as the dopant concentration increases it significantly alters the TiO_2 such that the sort-range electronic character of O more closely resembles Al_2O_3. Further evidence for this is the ratio of the Ti $L_{2,3}$ and TiO_2-like O K edges. As the Al concentration increases, this ratio becomes much greater as a result of Ti being surrounded by Al_2O_3-like O atoms. The broadening of the Ti $L_{2,3}$ edge also suggests a change in the electronic energy levels of the Ti as would be expected for a change in environment. We note that Ti^{3+} would appear as a shoulder on the high-energy tail of the Ti $L_{2,3}$ edge, but the lack of any significant intensity in this region likely shows that these samples contain primarily Ti^{4+}.

6.3.4 X-Ray Diffraction Results

Figure 6-9 shows the XRD data of all samples including reference data of TiO_2 anatase and γ-Al_2O_3 standards[47-48]. Figure 6-9a shows how DCR samples retain a primarily TiO_2-like lattice at all concentrations of Al dopant. The only changes that occur to these spectra as dopant is added is that the peak to background ratio becomes smaller, and the peaks become broader to the point of merging even. The 50 mol% Al sample shows very subtle increases in intensity above the background at about 45° and 67°, which correspond to the two most prominent peaks in γ-Al_2O_3. Figure 6-9b shows that DRC samples are also primarily TiO_2-like at all concentrations of Al, but the peak to background ratio is significantly lower for these samples. The peaks are also much broader such that by 50 mol% Al several peaks are no longer distinguishable from the background. Slight increases in intensity are also observed in 50 mol%

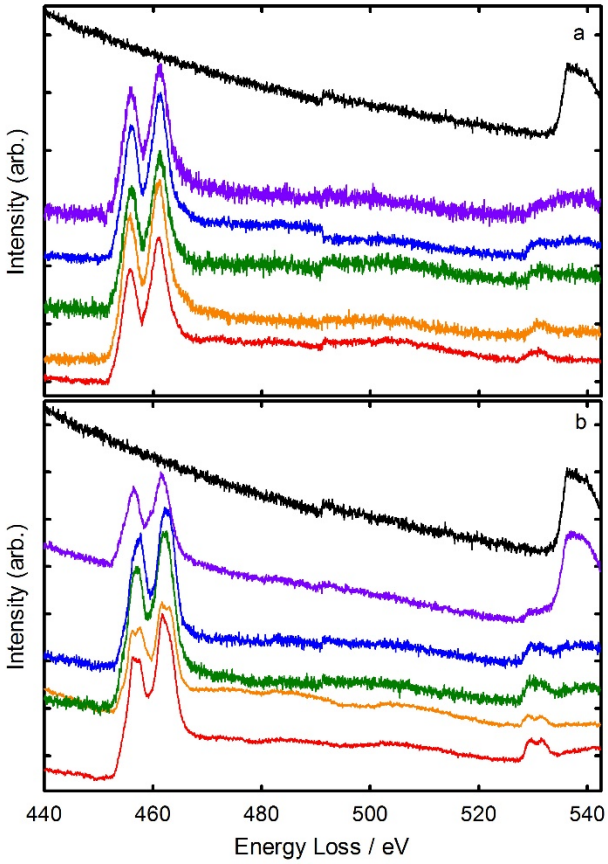

Figure 6-8: EELS Data around the Ti $L_{2,3}$ and O K Edges (440-545 eV) of All Samples as well as Data of an Al_2O_3 Standard Showing Progression of Peaks as Al Concentration Increases. Curves represent, starting from the bottom, TiO_2 (red), $Ti_{0.95}Al_{0.05}O_{1.975}$ (orange), $Ti_{0.86}Al_{0.14}O_{1.93}$ (green), $Ti_{0.78}Al_{0.22}O_{1.89}$ (blue), $Ti_{0.5}Al_{0.5}O_{1.75}$ (purple), and Al_2O_3 (black). Data have been scaled and offset for clarity. (a) DCR and (b) DRC

Al DRC at about 45° and 67°. A Rietveld refinement would be useful to identify the presence any γ-Al_2O_3 contribution, but the breadth of the peaks and high background at higher dopant concentrations makes such an analysis unfeasible.

These results suggest that the long-range ordering of these particles remains primarily TiO_2-like for both synthesis routes and at all concentrations. The absence of any defined γ-Al_2O_3 peaks suggests that Al enters the TiO_2 lattice and does not form any significant amount of γ-Al_2O_3 particles large enough to diffract X-rays. The increase in the background intensity and the

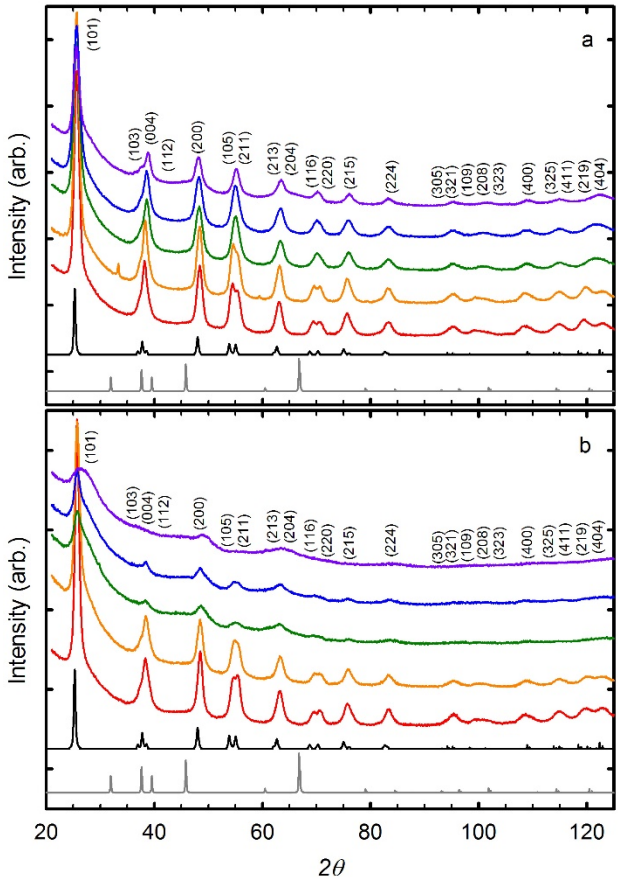

Figure 6-9: XRD Data of All Samples from 2θ = 20°-125° as well as Data of TiO_2 Anatase and γ-Al_2O_3 Standards Showing Progression of Peaks as Al Concentration Increases. Curves represent, starting from the bottom, γ-Al_2O_3 standard (grey), TiO_2 anatase standard (black), pure TiO_2 (red), $Ti_{0.95}Al_{0.05}O_{1.975}$ (orange), $Ti_{0.86}Al_{0.14}O_{1.93}$ (green), $Ti_{0.78}Al_{0.22}O_{1.89}$ (blue), and $Ti_{0.5}Al_{0.5}O_{1.75}$ (purple). Data have been offset for clarity. (a) DCR and (b) DRC

broadening of all peaks as Al concentration increases indicates that the materials are losing long range order as a result of the lattice gradually shifting from TiO_2-like to Al_2O_3-like. The DRC samples appear to lose the long range order quite readily (by 14 mol% Al); whereas, the DCR samples retain their long range order to a much greater extent.

6.4 Conclusions

Vacancy concentrations determined from the linear terms of the low-temperature heat capacity fitting suggest that the Al dopant enters the TiO_2 lattice and creates excess O^{2-} vacancies due to charge differences between Al^{3+} and Ti^{4+}. The 2D gapped terms found in the low-temperature heat capacity data fitting have been attributed to planar regions of a highly disordered $TiAlO_x$ structure within the TiO_2 lattice that cause glass-like short-range order while lacking any long-range structure. A theory on the origins of these 2D features has been presented suggesting that these features are created within the TiO_2 nanoparticles during particle growth. The excess entropies attributed to entropy of mixing also suggest the Al is entering the TiO_2 lattice. EELS data show that the short-range character of the atoms gradually shifts from TiO_2-like to Al_2O_3-like as seen by several changes in the Al, Ti, and O electronic structures as the concentration of Al dopant increases. The XRD analysis shows that the long-range order of all particles remains primarily TiO_2-like, though at higher dopant concentrations, the particles become significantly more amorphous. We believe that this increase in amorphicity is caused by the short-range reordering of the lattice towards an Al_2O_3-like structure around regions of $TiAlO_x$ while maintaining a long range TiO_2-like character. These experiments combined with our previous knowledge[25] show that the Al dopant forms a highly defective short-range structure within the TiO_2 lattice that appears more Al_2O_3-like at higher dopant concentrations.

Our previous investigation, focused primarily on 22 mol% Al doped TiO_2, reported that these small particles were more stable when doped with Al because the Al either forms a shell on the TiO_2 particles or incorporates Al into the TiO_2 lattice. We emphasized differences in the particles based on the synthesis route, and these differences also appear in the present investigation. The gapped term analysis suggests that the character of the DRC samples begins to

deviate from that of the DCR samples at 22 mol% Al; the linear term analysis and the EELS data suggest that the 50 mol% Al DRC and DCR samples are substantially different, specifically, the DRC sample appears to have more Al_2O_3-like short-range character. XRD data show that DRC samples are affected much more by the addition of Al, which causes the samples to become highly amorphous, while DCR samples become only slightly more amorphous. From the current results, we postulate that the reversal of the calcine and rinse steps does not affect the location or function of the dopant but significantly affects the grain growth of these doped particles observed most notably in the XRD results.

The conclusions from our previous work about the exact position and role of the dopant were rather nebulous as they were drawn, to a great extent, from our preliminary heat capacity interpretations, but we can now state with greater certainty that Al enters the TiO_2 lattice for all samples. The role that the dopant has on stabilizing the particles could be related to the lack of long-range order created by Al entering the TiO_2 lattice and forming a hybrid TiO_2/Al_2O_3 lattice especially at higher concentrations of Al. This investigation using the linear and gapped terms of low-temperature heat capacity fits to provide insight on dopant sites has never been performed previously, and the results are similar to those obtained from the more conventional methods presented herein.

REFERENCES

1. Fox, M. A.; Dulay, M. T., Heterogeneous Photocatalysis. *Chemical reviews* **1993**, *93*, 341-357.

2. Fujishima, A.; Rao, T. N., Interfacial Photochemistry: Fundamentals and Applications. *Pure and applied chemistry* **1998**, *70*, 2177-2188.

3. Hoffmann, M. R.; Martin, S. T.; Choi, W.; Bahnemann, D. W., Environmental Applications of Semiconductor Photocatalysis. *Chemical reviews* **1995**, *95*, 69-96.

4. Anpo, M.; Aikawa, N.; Kubokawa, Y., Photocatalytic Hydrogenation of Alkynes and Alkenes with Water over Titanium Dioxide. Platinum Loading Effect on the Primary Processes. *The Journal of Physical Chemistry* **1984**, *88*, 3998-4000.

5. Ohtani, B.; Ueda, Y.; Nishimoto, S.; Kagiya, T.; Hachisuka, H., Photocatalytic Oxidative Decomposition of Fluoroalkenes by Titanium Dioxide. *J. Chem. Soc* **1990**, 1955-90.

6. Mor, G. K.; Shankar, K.; Paulose, M.; Varghese, O. K.; Grimes, C. A., Use of Highly-Ordered Tio2 Nanotube Arrays in Dye-Sensitized Solar Cells. *Nano letters* **2006**, *6*, 215-218.

7. Bartholomew, C. H.; Farrauto, R. J., *Fundamentals of Industrial Catalytic Processes*; John Wiley & Sons, 2011.

8. Enache, C. S.; Schoonman, J.; Van Krol, R., The Photoresponse of Iron-and Carbon-Doped Tio2 (Anatase) Photoelectrodes. *Journal of electroceramics* **2004**, *13*, 177-182.

9. Janousch, M.; Meijer, G. I.; Staub, U.; Delley, B.; Karg, S. F.; Andreasson, B. P., Role of Oxygen Vacancies in Cr-Doped Srtio3 for Resistance-Change Memory. *Advanced Materials* **2007**, *19*, 2232-2235.

10. Wang, Z. L.; Yin, J. S.; Jiang, Y. D., Eels Analysis of Cation Valence States and Oxygen Vacancies in Magnetic Oxides. *Micron* **2000**, *31*, 571-580.

11. Wu, Q.; Zheng, Q.; van de Krol, R., Creating Oxygen Vacancies as a Novel Strategy to Form Tetrahedrally Coordinated Ti4+ in Fe/Tio2 Nanoparticles. *The Journal of Physical Chemistry C* **2012**, *116*, 7219-7226.

12. Santra, P. K.; Kamat, P. V., Mn-Doped Quantum Dot Sensitized Solar Cells: A Strategy to Boost Efficiency over 5%. *Journal of the American Chemical Society* **2012**, *134*, 2508-2511.

13. Lee, J. E.; Oh, S.-M.; Park, D.-W., Synthesis of Nano-Sized Al Doped Tio2 Powders Using Thermal Plasma. *Thin Solid Films* **2004**, *457*, 230-234.

14. Tsai, C.-Y.; Hsi, H.-C.; Bai, H.; Fan, K.-S.; Sun, H.-D., Single-Step Synthesis of Al-Doped Tio2 Nanoparticles Using Non-Transferred Thermal Plasma Torch. *Japanese Journal of Applied Physics* **2012**, *51*, 01AL01.

15. Stebbins, J. F.; Farnan, I.; Klabunde, U., Aluminum in Rutile [Tio2]: Characterization by Single-Crystal and Magic-Angle-Spinning Nuclear Magnetic Resonance. *Journal of the American Ceramic Society* **1989**, *72*, 2198-2200.

16. Wang, L.-Y.; Sun, Y.-P.; Xu, B.-S., Comparison Study on the Size and Phase Control of Nanocrystalline Tio2 in Three Ti–Si Oxide Structures. *Journal of Materials Science* **2008**, *43*, 1979-1986.

17. Liao, L.; Ingram, C. W., Mesoporous I-Ag Codoped Titania and Alumina Modified Titania Catalysts: Synthesis, Characterization and Photocatalytic Properties. *Applied Catalysis A: General* **2012**, *433*, 18-25.

18. Smitha, V. S.; Baiju, K. V.; Perumal, P.; Ghosh, S.; Warrier, K. G., Hydrophobic, Photoactive Titania–Alumina Nanocrystallites and Coatings by an Aqueous Sol–Gel Process. *European Journal of Inorganic Chemistry* **2012**, *2012*, 226-233.

19. Zhou, Z.; Zeng, T.; Cheng, Z.; Yuan, W., Preparation and Characterization of Titania−Alumina Mixed Oxides with Hierarchically Macro-/Mesoporous Structures. *Industrial & Engineering Chemistry Research* **2010**, *50*, 883-890.

20. Gopal, E. S. R., *Specific Heats at Low Temperatures*; Plenum Press New York, 1966; Vol. 227.

21. Kittel, C.; McEuen, P., *Introduction to Solid State Physics*; Wiley New York, 1996; Vol. 7.

22. McQuarrie, D., Statistical Mechanics, 2000. *University Science, Sausalito, USA*.

23. Schliesser, J. M.; Woodfield, B. F., Lattice Vacancies Responsible for the Linear Dependence of the Low-Temperature Heat Capacity of Insulating Materials. *Physical Review B* **2015**, *91*, 024109.

24. Schliesser, J. M.; Woodfield, B. F., Development of a Debye Heat Capacity Model for Vibrational Modes with a Gap in the Density of States. *Journal of Physics: Condensed Matter* **2015**, *27*, 285402.

25. Olsen, R. E.; Alam, T. M.; Bartholomew, C. H.; Enfield, D. B.; Schliesser, J. M.; Woodfield, B. F., Structure Analysis of Al-Modified Tio2 Nano Catalyst Supports. *The Journal of Physical Chemistry C* **2014**, *118*, 9176-9186.

26. Olsen, R. E.; Bartholomew, C. H.; Huang, B.; Simmons, C.; Woodfield, B. F., Synthesis and Characterization of Pure and Stabilized Mesoporous Anatase Titanias. *Microporous and Mesoporous Materials* **2014**, *184*, 7-14.

27. Woodfield, B. F.; Liu, S.; Boerio-Goates, J.; Liu, Q.; Smith, S. J., Preparation of Uniform Nanoparticles of Ultra-High Purity Metal Oxides, Mixed Metal Oxides, Metals, and Metal Alloys. Google Patents: 2012.

28. Shi, Q.; Boerio-Goates, J.; Woodfield, B. F., An Improved Technique for Accurate Heat Capacity Measurements on Powdered Samples Using a Commercial Relaxation Calorimeter. *The Journal of Chemical Thermodynamics* **2011**, *43*, 1263-1269.

29. Stevens, R.; Boerio-Goates, J., Heat Capacity of Copper on the Its-90 Temperature Scale Using Adiabatic Calorimetry. *The Journal of Chemical Thermodynamics* **2004**, *36*, 857-863.

30. Spencer, E. C.; Huang, B.; Parker, S. F.; Kolesnikov, A. I.; Ross, N. L.; Woodfield, B. F., The Thermodynamic Properties of Hydrated Γ-Al2o3 Nanoparticles. *The Journal of chemical physics* **2013**, *139*, 244705.

31. Kittel, C.; McEuen, P.; McEuen, P., *Introduction to Solid State Physics*; Wiley New York, 1976; Vol. 8.

32. Kelley, K. K.; King, E. G., *Entropies of the Elements and Inorganic Compounds*; US Government Printing Office, 1961; Vol. 592.

33. Phillips, N. E., Low-Temperature Heat Capacity of Metals. *Critical Reviews in Solid State and Material Sciences* **1971**, *2*, 467-553.

34. Hu, B.; McCandless, G. T.; Garlea, V. O.; Stadler, S.; Xiong, Y.; Chan, J. Y.; Plummer, E. W.; Jin, R., Structure-Property Coupling in Sr3(Ru1−Xmnx)2o7. *Physical Review B* **2011**, *84*, 174411.

35. Schliesser, J. M.; Smith, S. J.; Li, G.; Li, L.; Walker, T. F.; Parry, T.; Boerio-Goates, J.; Woodfield, B. F., Heat Capacity and Thermodynamic Functions of Nano-Tio2 Rutile in Relation to Bulk-Tio2 Rutile. *The Journal of Chemical Thermodynamics* **2014**.

36. Schliesser, J. M.; Smith, S. J.; Li, G.; Li, L.; Walker, T. F.; Perry, T.; Boerio-Goates, J.; Woodfield, B. F., Heat Capacity and Thermodynamic Functions of Nano-Tio2 Anatase in Relation to Bulk-Tio2 Anatase. *The Journal of Chemical Thermodynamics* **2014**.

37. Boerio-Goates, J.; Li, G.; Li, L.; Walker, T. F.; Parry, T.; Woodfield, B. F., Surface Water and the Origin of the Positive Excess Specific Heat for 7 Nm Rutile and Anatase Nanoparticles. *Nano Letters* **2006**, *6*, 750-754.

38. Levine, I. N., *Physical Chemistry*; McGraw-Hill, 2008.

39. O'Neill, H. S. C.; Navrotsky, A., Cation Distributions and Thermodynamic Properties of Binary Spinel Solid Solutions. *American Mineralogist* **1984**, *69*, 733-753.

40. O'Neill, H. S. C.; Navrotsky, A., Simple Spinels; Crystallographic Parameters, Cation Radii, Lattice Energies, and Cation Distribution. *American Mineralogist* **1983**, *68*, 181-194.

41. Smith, S. J.; Stevens, R.; Liu, S.; Li, G.; Navrotsky, A.; Boerio-Goates, J.; Woodfield, B. F., Heat Capacities and Thermodynamic Functions of Tio2 Anatase and Rutile: Analysis of Phase Stability. *American Mineralogist* **2009**, *94*, 236-243.

42. Haynes, W. M., *Crc Handbook of Chemistry and Physics*; CRC press, 2013.

43. Ahn, C.; Krivanek, O., *Eels Atlas*; Gatan, 1983.

44. Scheu, C.; Dehm, G.; Müllejans, H.; Brydson, R.; Rühle, M., Electron Energy-Loss near-Edge Structure of Metal-Alumina Interfaces. *Microscopy Microanalysis Microstructures* **1995**, *6*, 19-31.

45. Scheu, C.; Dehm, G.; Rühle, M.; Brydson, R., Electron-Energy-Loss Spectroscopy Studies of Cu-A-Al2o3 Interfaces Grown by Molecular Beam Epitaxy. *Philosophical Magazine A* **1998**, *78*, 439-465.

46. Grunes, L. A.; Leapman, R. D.; Wilker, C. N.; Hoffmann, R.; Kunz, A. B., Oxygen K near-Edge Fine Structure: An Electron-Energy-Loss Investigation with Comparisons to New Theory for Selected 3d Transition-Metal Oxides. *Physical Review B* **1982**, *25*, 7157-7173.

47. Howard, C.; Sabine, T.; Dickson, F., Structural and Thermal Parameters for Rutile and Anatase. *Acta Crystallographica Section B: Structural Science* **1991**, *47*, 462-468.

48. Smrčok, Ľ.; Langer, V.; Křesťan, J., Γ-Alumina: A Single-Crystal X-Ray Diffraction Study. *Acta Crystallographica Section C: Crystal Structure Communications* **2006**, *62*, 83-84.

7 EXTENDED TEMPERATURE REGIONS OF MULTIFERROICITY IN NANOSCALE CUO

7.1 Introduction

Cupric oxide, CuO (tenorite), has been extensively studied due to its significance in basic science as well as technological applications. CuO has unique structural and magnetic properties,[1-3] and it is closely related to high-temperature superconducting cuprates such as $YBa_2Cu_3O_{7-x}$.[4] In terms of applications, it has use in catalysis,[5] photovoltaics,[6-8] batteries,[9] and potential uses in spintronic devices.[10-12]

CuO is unique for a 3*d* transition-metal monoxide having a C2/c monoclinic structure instead of the rocksalt structure common to the other 3*d* transition-metal oxides.[13-14] The Cu atom is surrounded by four O atoms in a square planar configuration which can be viewed as edge shared ribbon chains of CuO_2 or as two zigzag Cu–O chains running along the [101] and $[10\bar{1}]$ directions (see Figure 7-1).[10, 15] These chains are what make CuO important in cuprate superconductor research since the cuprate superconductors also have CuO_2 chains.[4, 10, 16-18]

The magnetic behavior of CuO is also unique relative to the other 3*d* transition-metal monoxides which all behave as 3D antiferromagnets; whereas, CuO exhibits various forms of magnetism within different temperature ranges..[19-20] Heat capacity measurements on bulk CuO performed by many groups[2-4, 18, 21-28] show two distinct magnetic transitions at about 213 and 230 K. The peak at 213 K has been attributed to a transition from a 3D commensurate

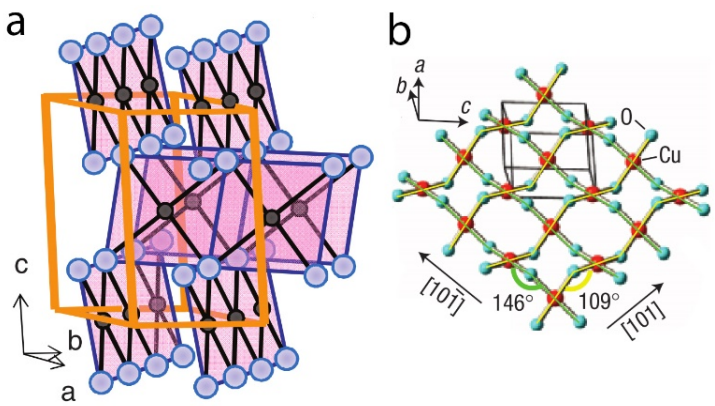

Figure 7-1: Structure of CuO Showing a) Edge-shared Ribbon Chains of CuO_2 (from Wu et al.[15] with permission) and b) Zigzag Chains along the [101] (yellow lines) and $[10\bar{1}]$ (green lines) Directions (from Kimura *et al.*[10] with permission).

antiferromagnetic state below 213 K (AF1) to a 3D incommensurate state above 213 K (AF2). The peak at 230 K has been attributed to a transition from the AF2 state to a 1D antiferromagnetic state above 230 K. Heat capacity measurements have not previously been performed on nanoscale CuO.

Magnetic susceptibility data of bulk[1, 3-4, 10-12, 24, 29-30] and nanoscale[31-33] CuO are similar to each other and show neither a cusp at the temperatures of the transitions observed in heat capacity data nor typical Curry-Weiss behavior; instead, a broad maximum at about 540 K and a minimum at about 150 K are observed. The only evidence of any transitions in the range of 213-230 K from susceptibility data is a subtle change in slope.[3-4, 10, 33]

Neutron experiments have provided more details about the magnetic character of bulk CuO in the various temperature regions and show that the incommensurate AF2 state occurs because of competing ferromagnetic and antiferromagnetic interactions.[11, 16-17, 29, 34-36] Figure 7-2 shows the orientation of the spins in the commensurate AF1 and incommensurate AF2 states.[10] The direction of the easy axis is along *b*,[19, 36] and the strongest antiferromagnetic ordering occurs

along the $[10\bar{1}]$ chains because of the large Cu–O–Cu angle (146°).[16-17] Superexchange interactions along the other directions are very weak (either ferromagnetically or antiferromagnetically) due to the smaller bond angles (less than 109°).[17, 37] In the AF1 state the spins align parallel to *b* with a wave propagation vector of $\mathbf{q}_{cm}$ = (0.5,0,-0.5), and in the AF2 state, the wave propagation vector is $\mathbf{q}_{icm}$ = (0.506,0,-0.483) having a helical spin structure such that the Cu^{2+} moments nearly circle in a plane.[12] To the best of our knowledge, no neutron experiments have investigated the magnetic character of nanoscale CuO.

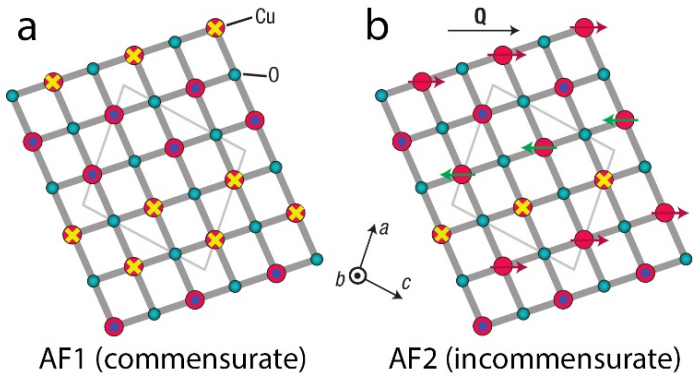

Figure 7-2: Magnetic Structure of the a) AF1 (commensurate) and b) AF2 (incommensurate) Phases (from Kimura *et al.*[10] with permission).

As seen from magnetization measurements, the susceptibility continues to increase above the Néel temperature T_{N2} of 230 K, which would be atypical behavior for paramagnetism.[38] Superparamagnetism and a spin-glass state from surface spins have been ruled out as the cause for this observed behavior.[32] Neutron experiments have failed to detect paramagnetism in bulk CuO even at temperatures as high 550 K[35] but have shown that antiferromagnetism persists above T_{N2} in a 1D form.[2-4, 16-17, 39] This is thought to occur through the very large superexchange interactions along the $[10\bar{1}]$ direction having an exchange constant in the range of 35-73 meV,

which is much larger than exchange constants of other ionic antiferromagnets (typically less than 10 meV).[17, 31, 37, 39]

More recently, multiferroic behavior, which is the coexistence of magnetism and ferroelectricity, has been discovered within the AF2 state of bulk CuO.[10] Due to the competing interactions involved in spiral-phase-induced ferroelectricity, multiferroicity is typically only observed below about 40 K making it inaccessible to practical technological applications.[10-11] The relatively high temperature of multiferroicity in CuO (230 K) has spurred many recent investigations.[10-12, 19-20] Because CuO is a core component of many high-temperature superconductors, understanding the origins of its multiferroic behavior could lead to a greater understanding of superconductivity and even drive the discovery or creation of superconductors with higher critical temperatures than current materials. The high-temperature multiferroic behavior of CuO could also be used in sensors, memory devices, and magnetoelectric devices.[40]

All of the physical properties discussed above have been extensively investigated for bulk CuO, but there have been minimal investigations of nanoscale CuO.[31-33, 41-43] This paper will present heat capacity, susceptibility, and temperature dependent XRD data on nanoscale CuO that has not been reported previously in the literature thus providing an extensive investigation on the magnetic and structural properties of CuO nanoparticles. We will show that structural features common to nanoparticles are responsible for extending the magnetic and ferroelectric temperature ranges by creating stronger ferromagnetic and antiferromagnetic competition through increased exchange interactions along the various directions.

7.2 Experimental

7.2.1 Synthesis and Characterization

CuO nanoparticles were prepared using a solvent deficient method developed by Woodfield *et al.*[44] in which 53 g of $Cu(NO_3)_2 \cdot 2.5H_2O$, 38 g of NH_4HCO_3, and 10 mL of H_2O were ground together in a mortar and pestle for approximately 1 min. The formed precursor was rinsed with about 0.5 L of distilled H_2O and then calcined in air at 250 °C for 1 h.

Transmission electron microscopy (TEM) imaging was carried out using several techniques (see Figure 7-3). The bright field image (Figure 7-3a) shows ellipsoidal crystallites that are highly agglomerated into much larger particles. The high-resolution image (Figure 7-3b) shows that the sample is highly crystalline as lattice fringes are abundantly observed. This figure also shows the presence of a secondary CuO particle size of about 5 nm, though these particles represent only a small fraction of the sample. Diffraction techniques were also used, and the absence of any pronounced amorphous background intensity in the acquired diffraction pattern (Figure 7-3c) shows the high degree of crystallinity. The hollow cone dark field image (Figure 7-3d) shows that the particles are about 20 nm in diameter, though the slightly ellipsoidal shape introduces uncertainty to this value.

The amount of surface-adsorbed water was determined by thermogravimetric analysis (TGA) using a Netzsch STA-409 PC. Prior to the TGA measurements, the sample was dried in a vacuum oven (p = 16.2 kPa) at 100 °C for about 3 h to remove all loosely bound physisorbed water that would be removed during the heat capacity measurements under high vacuum. The TGA measurements were performed under a helium atmosphere with temperatures of 20-900 °C using a heating rate of 3 °C min^{-1}. A buoyancy correction was made by measuring the empty crucible under the same conditions and subtracting this from the measured data. The weight loss

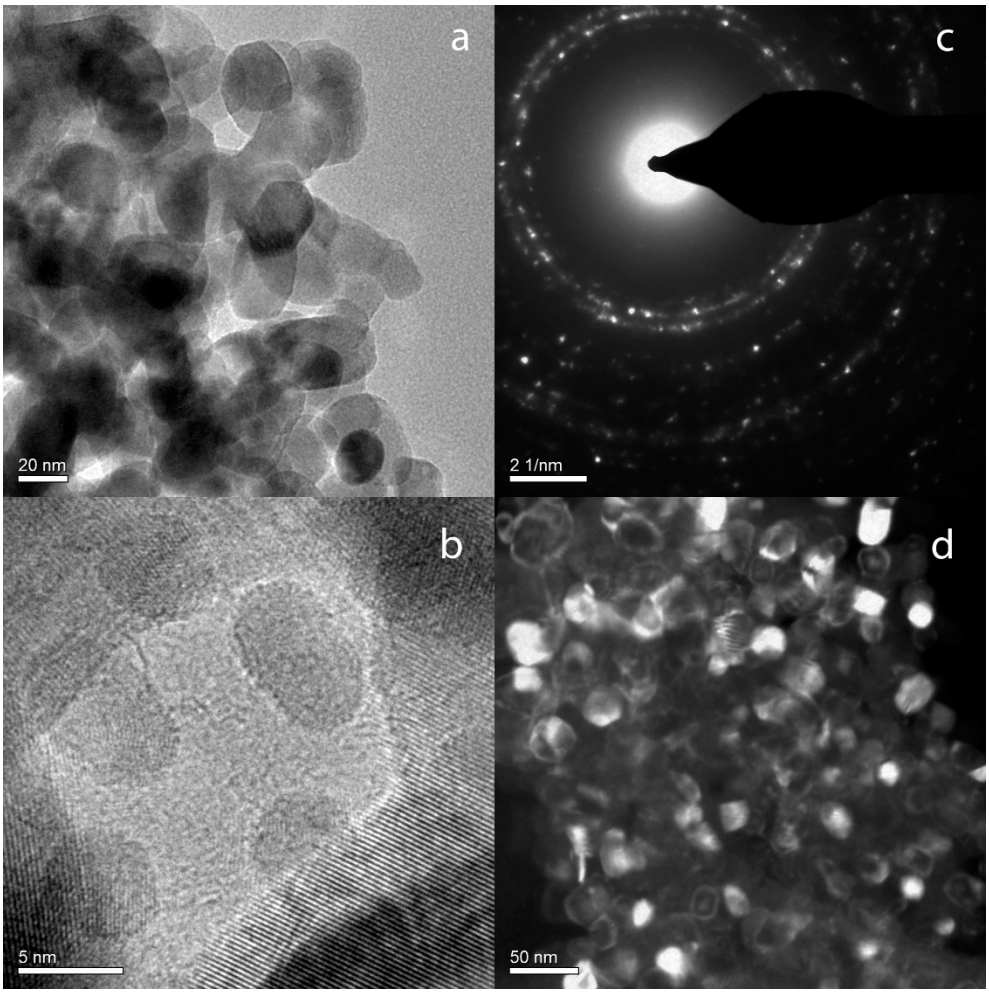

Figure 7-3: TEM Images and Diffraction Patterns of CuO Nanoparticles. a) bright field, b) high-resolution, c) diffraction pattern, d) hollow cone dark field.

at the inflection point of about 500 °C (see Figure 7-4) was attributed to the desorption of chemisorbed water, and the amount of water was determined to be 0.050 ± 0.004 moles of H_2O per mole of CuO. The TGA-DSC data presented in Figure 7-4 show that nanoscale CuO is reduced at about 800 °C.

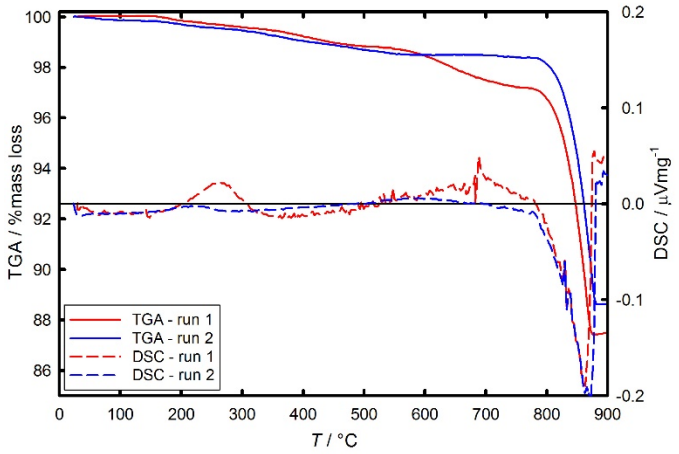

Figure 7-4: TGA-DSC Data of CuO Nanoparticles Showing Mass-loss Due to Water Desorption up to about 500 °C and Reduction above about 800 °C. The left axis gives the percent mass and is represented with solid lines. The right axis gives the DSC data and is represented with dashed lines. The solid black line corresponds to 0 µV·mg^{-1} for the DSC axis. red – run 1; blue – run 2.

7.2.2 Magnetometry

Magnetization curves from 5-400 K were acquired on a Quantum Design Physical Property Measurement System (PPMS) using the vibrating sample magnetometer (VSM) option. The sample was cooled in zero field to about 5 K, and the magnetic moment as a function of temperature was measured in various external field strengths: 0, 50, 100, 1,000, 10,000, and 50,000 Oe. Susceptibility was determined from the relationship $\chi = (\mu/2.84)^2/T$.

7.2.3 X-ray Diffraction

Phase purity was confirmed with X-ray diffraction (XRD) using a PANalytical X'Pert Pro X-ray diffractometer with a Cu Kα radiation source (λ = 0.15418 nm) operating at 45 kV and 40 mA. Data were recorded over a *2θ* range of 20-125° with a scanning rate of 0.01°·s^{-1}. Only monoclinic CuO was observed; however, a Reitveld refinement of this data reveals that significant lattice vacancies are present.[45] Particle size was determined to be about 16 nm using

the Scherrer formula, which is slightly smaller than the sizes obtained from the TEM images, but since the XRD data analyze significantly more particles than the TEM imaging, we will consider the particles to be 16 nm in diameter.

XRD data were also acquired at various temperatures from 90-700 K in order to determine the lattice parameters as a function of temperature. Data above room temperature were collected on the PANalytical X'Pert Pro powder X-ray diffractometer using an Anton Paar HTK 1200N heating stage. Data were collected every 25 K from 300-700 K using the same parameters as described above.

To measure the XRD data below room temperature, we used a single crystal (SC) Bruker diffractometer equipped with a cold finger as described previously.[45] In brief, the powder sample was uniformly compacted into a polyamide capillary having an inner diameter of 0.012 mm, and the ends of the capillary were sealed with clay due to its amorphicity. The sample was mounted on the SC-XRD, and data were collected at temperatures from 90-295 K over 2θ scanning angles of 20-130°. Data were collected about every 25 K below 195 K and about every 15 K from 195-295 K.

7.2.4 Heat Capacity Calorimetry

Heat capacities were measured from 2-400 K using the Quantum Design PPMS. To prepare the sample for measurement, about 9 mg of the dried sample mixed with high purity copper (mass fraction 0.9995) were pressed into a small disk.[46] Correction measurements were performed before each sample measurement to account for the Apiezon N grease used for mounting the sample at low temperatures (below 300 K) and the Apiezon H grease used for mounting the sample at high temperatures (above about 250 K). After each of these correction measurements the sample was attached to the PPMS puck, and the heat capacity was measured.

The heat capacity of the copper contribution was subtracted using data from Stevens and Boerio-Goates.[47] These data have an estimated uncertainty of ± 0.02·C_p° for 2 < T/K < 10 and ± 0.01·C_p° for 10 < T/K < 300.[46]

7.3 Results/Discussion

7.3.1 Magnetization

Magnetic susceptibility measurements were performed on the nanoscale CuO sample at various external field strengths and are shown in Figure 7-5. The data show a minimum at about 100-150 K, a sharp up-turn as temperature decreases towards 0 K, and an increase towards an apparent maximum above 400 K. Several small features are observed at various temperatures, but we believe these are due to noise in the data.

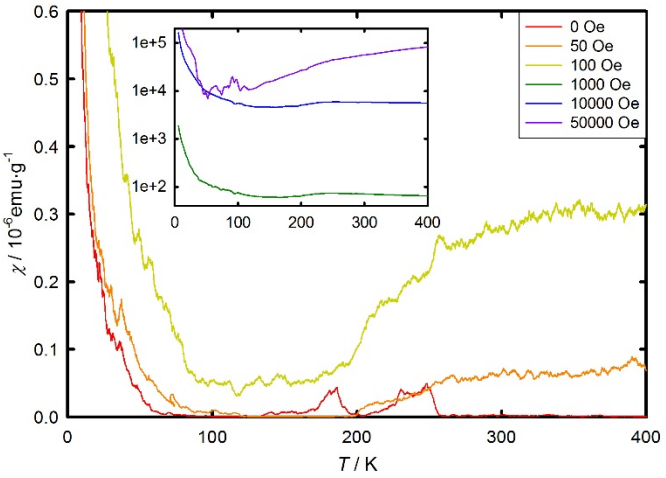

Figure 7-5: ZFC Gram Susceptibility of Nanoscale CuO as Determined from VSM Measurements. Data were taken under various external magnetic fields: red – 0 Oe; orange – 50 Oe; yellow – 100 Oe; green – 1,000 Oe; blue – 10,000 Oe; purple – 50,000 Oe. Note the log scale on the inset.

Although this data does not follow the traditional Curie-Weiss behavior, these trends and features have been observed several times before for both bulk and nanoscale CuO, and Figure 7-6 shows our measured susceptibility data (at 100 Oe scaled by a factor of 5) relative to literature data for bulk[1, 3-4, 11, 29] and nanoscale[31] CuO. We note that the susceptibility data of our nanoscale CuO collected in fields of 100 Oe or less are significantly lower in magnitude than the literature data of bulk and nanoscale CuO; conversely, our data collected in fields of 1,000 Oe or more are significantly higher in magnitude. Perhaps this discrepancy is due to the use of VSM as opposed to other magnetization techniques. Additionally, the up-turn at low temperatures in our data is much more prominent and larger in magnitude compared to the literature data as well. Other than the difference in magnitude of the susceptibility and the large up-turn at low temperatures, our data have the same general trends as the literature.

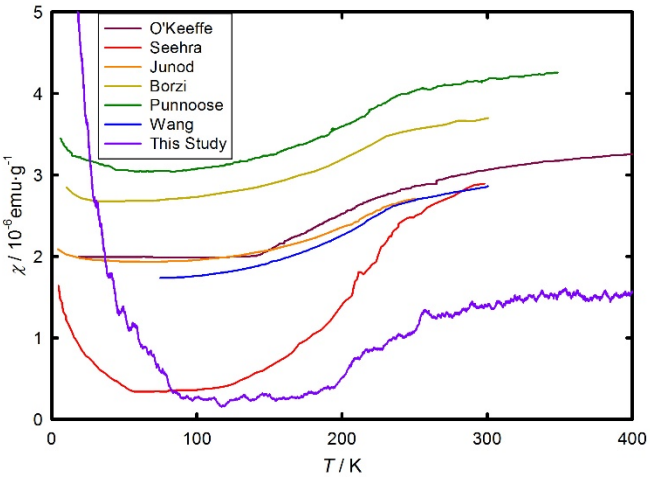

Figure 7-6: Comparison of the Susceptibility Data of Nanoscale CuO Presented Herein (100 Oe data scaled by a factor of 5) to Data Obtained from Various Literature Studies of Bulk and Nanoscale CuO.[1, 3-4, 11, 29, 31]

The low-temperature upturn in our susceptibility data is similar to that of other bulk and nanoscale CuO samples and has been attributed to small particle size[1] and non-ideal

stoichiometry such as oxygen vacancies,[30] though the underlying cause of the up-turn from both size and stoichiometry effects is the same: paramagnetic sites on the particle surface or around vacancies. The larger up-turn in our sample is likely caused by the presence of both of these sources of paramagnetic centers (small particle size and non-ideal stoichiometry) in our nanoscale CuO sample. A large concentration of paramagnetic sites would also explain why the magnitude of the antiferromagnetic susceptibility tends to be lower than the literature.

An alternate explanation for the large up-turn in our nanoscale CuO could be the presence of stronger ferromagnetic interactions, which yield a similar feature in the susceptibility to that observed in our susceptibility data in Figure 7-5. Small particle sizes and lattice vacancies have been shown to create a small ferromagnetic contribution in both bulk and nanoscale CuO.[31-33] The superexchange interactions along [101] and [010] are known to be weakly ferromagnetic;[2] therefore, the presence of ferromagnetism at low temperatures in nanoscale CuO would likely be caused by changes in Cu–O–Cu bond lengths and angles that enhance the exchange interactions in these directions.

7.3.2 XRD Lattice Parameters

The XRD data of nanoscale CuO at temperatures from 90-700 K are shown in Figure 7-7. The high-temperature data (Figure 7-7a) show a weaker signal-to-noise ratio than the low-temperature data (Figure 7-7b), but the instrumental broadening of the low-temperature data is more significant as seen by the broader peaks, which is caused by using transmitted X-rays as opposed to reflected X-rays. These data show that the sample is highly crystalline and phase pure over the entire temperature range. A subtle shift towards sharper and more defined peaks at higher temperatures suggests that the particles are becoming more crystalline or larger, which would reduce peak broadening from microstrain and size effects.

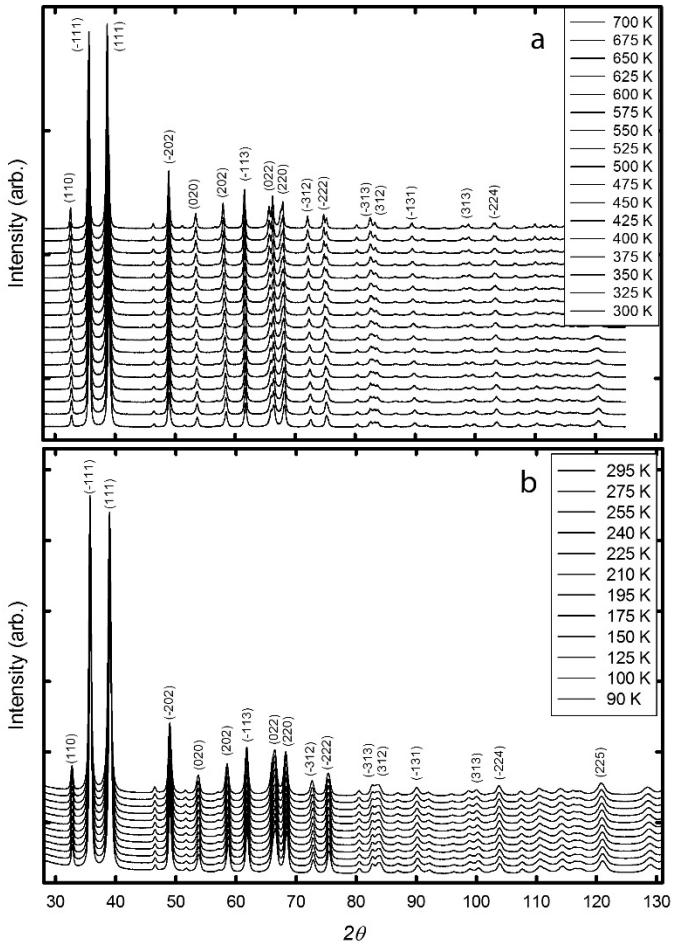

Figure 7-7: XRD Data of Nanoscale CuO at Various Temperatures from 90-700 K. a) high-temperature data (300-700 K) collected on the powder diffractometer. b) low-temperature data (90-295 K) collected on the single-crystal diffractometer. Data (offset for clarity) increase in temperature from bottom to top as shown in the legends.

We have performed a Rietveld refinement on the data shown in Figure 7-7 to obtain lattice parameters at the various temperatures, which are shown in Figure 7-8, and we note that our data are in good agreement with the literature data collected at room temperature for bulk and nanoscale CuO.[4, 11, 13-14] To the best of our knowledge, though, this is the first investigation to show the progression of lattice parameters as a function of temperature for either bulk or nanoscale CuO. Although there are no phase transitions in which lattice parameters change

abruptly, changes in the slope of the data at various temperatures are apparent. We also note that these changes occur at different temperatures for each of the different lattice parameters.

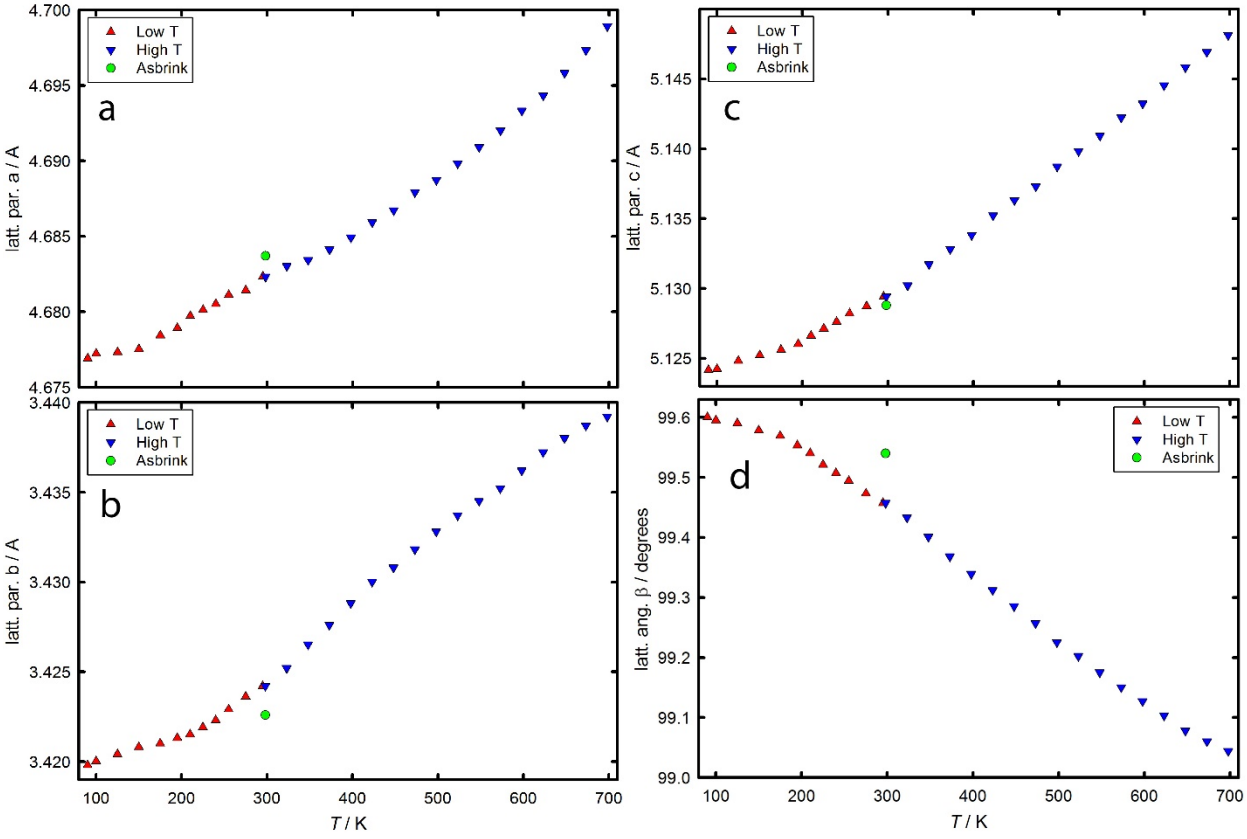

Figure 7-8: XRD Lattice Parameters of Nanoscale CuO at Vvarious Temperatures from 90-700 K as Determined from a Rietveld Refinement of the Data Shown in Figure 7-7. a) parameter *a*, b) parameter *b*, c) parameter *c*, d) parameter *β*. red triangles – low-temperature data. blue inverted triangles – high-temperature data. Units are in Å. Literature data (green circles) taken from Asbrink and Norrby.[13]

The lowest temperature shift in lattice parameters occurs along the *a* axis at about 150 K. A shift in *β* occurs at about 170 K and in *c* at a slightly higher temperature of 195 K. The shift along the *b* axis occurs at the highest temperature of about 220 K. Other possible changes occur

at about 300 and 400 K though these changes in slope are much more ambiguous and appear to occur over a wider temperature range than the slope changes at lower temperatures.

The changes in the *a*, *b*, and *c* lattice parameters at 150, 195, and 220 K, respectively, correspond to those of several other observed properties in bulk and nanoscale CuO. The shift in expansion of the *a* axis around 150 K appears to correspond to the minimum in magnetization. Charnaya *et al.* observed a decrease in T_{N1} to about 190 K in nanoscale CuO embedded in glass,[42] which could be related to the shift in the *c* axis observed in this investigation. The change that occurs along *b* is also similar to the traditional T_{N2} observed at about 230 K. It is apparent that these shifts in lattice parameters and the corresponding structure are caused by the magnetic properties.

The relationship between structure and magnetic properties in bulk CuO has been established previously.[20, 48-50] Competition between ferromagnetic and antiferromagnetic interactions is known to cause structural distortions and even phase transitions;[51] therefore, the presence of these distortions in the lattice parameters of nanoscale CuO suggests that ferromagnetic behavior is significant and competes with the antiferromagnetic behavior. The presence of this strong ferromagnetic-antiferromagnetic competition in nanoscale CuO would therefore be expected to be different from the competition in bulk CuO since smaller particles tend to have larger unit cells (for metal oxides) due to reduced electrostatic forces cause by surface dipoles,[52-53] and these changes in the unit cell parameters affect the Cu–O–Cu bond angles that are highly correlated to the strength of the exchange interactions.[17, 37]

7.3.3 Heat Capacity Analysis

The measured heat capacity data are shown in Figure 7-9 for the low temperature and high temperature segments. Because the data of the two temperature segments were collected

using a different grease and addenda measurement, there was a slight offset of the high-temperature data from the low-temperature data. To correct for this offset, the high-temperature data that tend to have greater uncertainty were scaled by 1 % to match the low temperature data. Although the data for the two segments were collected with a 55 K overlap range (250-305 K), the temperature at which the two segments aligned in terms of heat capacity and the first derivative of the heat capacity data was taken as 295 K where deviations between the two sets of data were smallest. Data from the low-temperature segment above 295 K and from the high-temperature segment below 295 K were not used.

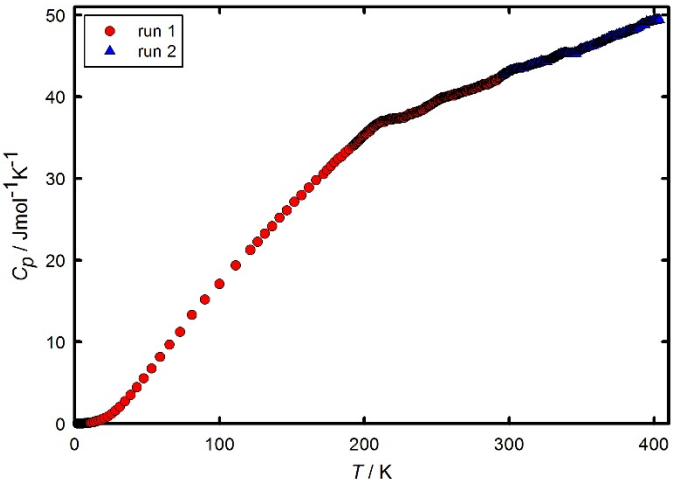

Figure 7-9: Raw Heat Capacity Data of CuO Nanoparticles. red circles – run 1 (low-temperature data); blue triangles – run 2 (high-temperature data).

Figure 7-10 below shows how our heat capacity data of nanoscale CuO compare with data found in the literature for bulk CuO. Data are shown just around the observed T_{N1} and T_{N2} bulk CuO transition temperatures since the literature data do not extend much higher in temperature. The somewhat noisy and diffuse data of Millar show a broad transition peaked at about 230 K.[21] The data of Junod *et al.* are the most precise and show distinct and sharp

transitions at 215 K, 230 K, and 235 K, though the transition at 235 K is attributed to the silicone grease used to mount the sample.[4] The data by Seehra *et al.* show two broad transitions that overlap having maxima at about 217 K and 230 K.[3] In general, the literature data of bulk CuO show a distinct first-order transition at about 213 K and a broader transition at about 230 K.

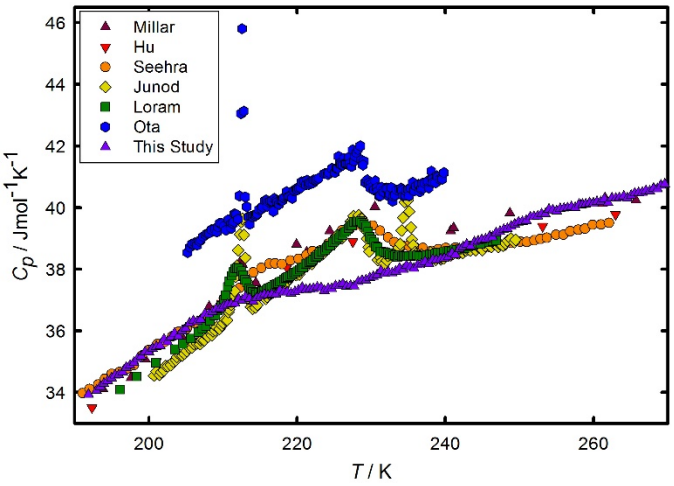

Figure 7-10: Heat Capacity Data of Nanoscale CuO from 180 to 320 K Compared to Data of Bulk CuO from the Literature. maroon triangles – Millar.[21] red inverted triangles – Hu *et al.*[22] orange circles – Seehra *et al.*[3] yellow diamonds – Junod *et al.*[4] green squares – Loram *et al.*[2] blue hexagons – Ota *et al.*[27] purple triangles – this study.

Our data, however, show very broad transitions at temperatures quite different from the bulk transitions. As can be seen in Figures 7-9 and 7-10, our data show four subtle transitions at about 210, 250, 300, and 330 K. To understand the heat capacity data and the transitions more fully, we analyzed the heat capacity data and subtracted the lattice heat capacity from the total heat capacity to reveal just the magnetic heat capacity.

7.3.3.1 Heat Capacity Data Fitting

Prior to analysis of the heat capacity data, we first corrected for the amount of water present on the surface of the CuO nanoparticles as well as the difference between the measured C_p and the more theoretically important C_v. The correction from C_p to C_v is quite simple and involves the use of expansion parameters, which we have done using the values and methods others have used for bulk CuO, specifically, $C_V = C_p - AC_p^2T$, where A equals 1.35×10^{-6} J·mol^{-1} [1] assuming a linear expansion coefficient at 300 K of 10^{-5} K^{-1}.[2, 4, 54] This correction resulted in a change of less than 1 % below 200 K and a maximum change of 2.6 % at 400 K.

The correction for water tends to be much less straightforward. We have recently summarized and discussed various surface-adsorbed water heat capacity models that have been published in the literature.[55] A recent investigation using neutron techniques derived the heat capacity of the CuO surface-adsorbed water.[56] Although this water model might appear to be the best representation for the water on our CuO samples, that study involved a sample with ten times more water than ours suggesting that they measured mostly physisorbed water; whereas, we measured only chemisorbed water. Because of this, we chose to use the "inner TiO_2" water model, which has proven to be applicable to several similar systems involving only chemisorbed water.[55]

After these corrections, the low temperature (T < 10 K) heat capacity data were fit to several theoretical functions that provide information on the various contributions to the heat capacity. The best fitting function was determined from the percent root mean square deviation (%RMS) and a plot of the deviation of each point from the fitting function. The fit that was physically meaningful had the lowest %RMS, and had random deviations was selected as the best fit.

The heat capacity data below 10 K were fit to the sum of theoretical functions:

$$C_{low\,T} = \gamma T + B_3 T^3 + B_5 T^5 \quad (7\text{-}1)$$

where the γ term represents the contribution from lattice vacancies[45] or 1D antiferromagnetic spin waves,[4] and the B_3 and B_5 terms represent the harmonic-lattice expansion.[57] These low-temperature fit parameters and their corresponding %RMS are given in Table 7-1.

Table 7-1: Low-temperature (T < 10 K) Heat Capacity Fit Parameters

γ / mJ·mol^{-1}·K^{-2}	0.489
B_3 / mJ·mol^{-1}·K^{-4}	0.102
B_5 / mJ·mol^{-1}·K^{-6}	-1.29E-4
%RMS	3.26

Samples that are antiferromagnetic also have a T^3 dependence; therefore, to distinguish between the lattice and antiferromagnetic T^3, the Debye temperature, which can give the lattice contribution, must be known. The B_3 coefficient shown in Table 7-1 is not significantly different from that derived from the bulk CuO Debye temperature of 390 K (0.07 mJ·mol^{-1}·K^{-4}) from Junod *et al*.[4] The antiferromagnetic T^3 term is typically ten to twenty times larger than the phonon T^3 term;[54] therefore, this B_3 term does not appear to show any significant antiferromagnetic contribution below 10 K, which is similar to other low-temperature heat capacity investigations.[4, 24]

7.3.3.2 Magnetic Transitions

The magnetic heat capacity transitions of our nanoscale CuO sample (with the water contribution subtracted) were determined by subtracting the lattice contribution from the total heat capacity, as has been done by Junod *et al.* and Loram *et al*., using the bulk CuO lattice data

determined from neutron experiments.[2, 4] Figure 7-11 shows the magnetic heat capacity transitions of our nanoscale CuO as well as bulk CuO data from Junod *et al.*[4] and Loram *et al.*[2]

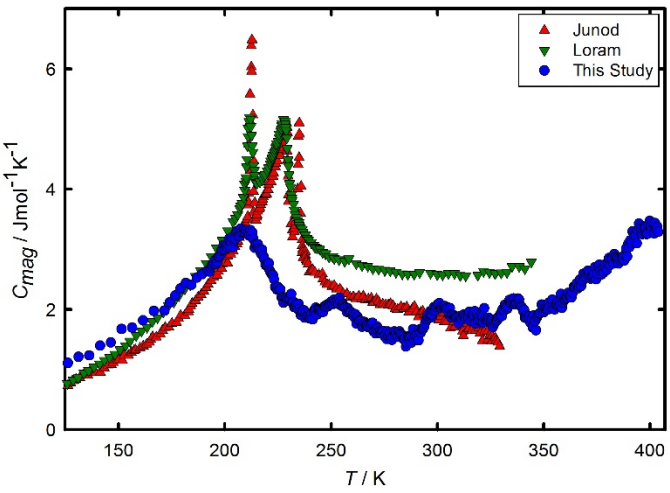

Figure 7-11: Magnetic Heat Capacity Transitions of Our Nanoscale CuO Sample from 125-405 K in Comparison to the Magnetic Heat Capacity Transitions of Bulk CuO from the Literature. red triangles – Junod *et al.*;[4] green inverted triangles – Loram *et al.*;[2] blue circles – this study.

As seen in Figure 7-11, the magnetic heat capacity data of our nanoscale CuO show four transitions, three of which occur at temperatures that are higher than the transitions reported by Junod *et al.* and Loram *et al*.[2, 4] The transitions in our nanoscale CuO are much more visible after the lattice has been subtracted (compare to Figures 7-9 and 7-10). The high-temperature "tail" of the transition in the bulk CuO data of Junod *et al.* decreases with increasing temperature,[4] but the tail in the bulk CuO data or Loram *et al.* levels off and appears to increase above about 300 K.[2] In our nanoscale CuO sample, the tail increases significantly above the fourth transition at about 350 K. Loram *et al*. attributed this tail above T_{N2} to 1D magnetism since a large tail is a result of a lower dimensionality.[4]

Thermodynamic data at the transition temperatures were generated by fitting the data in Figure 7-11 with a cubic spline function and integrating. The entropies and enthalpies of the transitions as well as the transition peak temperatures are given in Table 7-2. The entropies of these transitions can be used to identify the dimensionality of the magnetic character since the entropy at T_{N2} is predicted to be about $0.3R$ ln 2 (1.73 J·mol^{-1}·K^{-1}) for a 1D magnetic system and about $0.12R$ ln 2 (0.69 J·mol^{-1}·K^{-1}) for a 2D system.[2, 4] Because our entropies (> $0.5R$ ln 2) are significantly higher than either of these values and are closer to those of a 3D, spin ½ Heisenberg antiferromagnet,[58] we believe that the competing ferromagnetic interactions are more significant for these nanoparticles and cause an increase in the entropy of the transitions.

Table 7-2: Magnetic Transition Temperatures, Entropies, and Enthalpies

T / K	$\Delta_o^T S_{trans}^o$ / J·mol^{-1}·K^{-1}	$\Delta_o^T H_{trans}^o$ / J·mol^{-1}
208.6	2.6 ± 0.5	270 ± 50
251.9	3.1 ± 0.6	380 ± 80
302.6	3.4 ± 0.7	460 ± 90
335.9	3.6 ± 0.7	530 ± 100

As seen in Table 7-2, the nanoscale CuO sample has peaks at 208.6, 251.9, 302.6, and 335.9 K. Only the peak at 208.6 K resembles the transition between the AF1 and AF2 phases in in the bulk CuO phases. As such, the transition from incommensurate to 1D antiferromagnetism at 230 K is not observed, though it is reasonable to assume that this transition is manifest in the higher temperature transitions; however, neutron experiments on the magnetic properties at these temperatures is necessary to definitively determine the state of the magnetic order between the transitions. Although it has been shown that external magnetic fields do not induce changes in the temperature ranges of multiferroicity,[11] Rocquefelte *et al.* have used density functional theory

and Monte Carlo calculations to show that at high pressures, the multiferroic state of CuO can extend from 230 K up to about 300 K.[59] Because the higher pressures would affect the lattice parameters and cause this increase in the multiferroic temperature range, it is reasonable to suggest that our sample, having multiple lattice distortions, also has an extended range of multiferroicity or of the AF2 phase.

The number of transitions observed in the heat capacity data of nanoscale CuO does not correspond to those determined for bulk CuO that report only two, although Villarreal *et al.* have reported that the transition at 230 K actually consists of two transitions very close in temperature making a total of three transitions.[19] Competition between antiferromagnetic and ferromagnetic interactions in bulk CuO are known to cause the multiple transitions associated with the AF1 and AF2 states;[29, 34, 37] therefore, it is reasonable to assume that changes in the degree of magnetic competition could induce changes in those transitions, and the non-cooperative shifts in lattice parameters could result in additional regions of ferroic order and therefore more transitions.

7.4 Conclusions

From magnetization measurements it was shown that nanoscale CuO exhibits similar susceptibility to that of bulk with the most significant differences being the higher concentration of paramagnetic centers in the form of either surface sites or lattice vacancies as well as stronger ferromagnetic interactions. The XRD data revealed that the CuO lattice parameters do not increase smoothly with temperature but rather have several critical temperatures at which their slope changes significantly; furthermore, these changes in the lattice parameters occur at different temperatures for each of the different parameters. Because these temperatures are similar to known magnetic transitions, we have shown how each magnetic region is related to structural features along the different axes. Heat capacity data revealed that the traditional

transitions observed in bulk CuO are significantly altered in nanoscale CuO. The temperature ranges of the various magnetic and ferroelectric domains increase to higher temperatures, and new domains were observed.

We have shown that structural features in the CuO lattice unique to nanoparticles can induce changes in the multiferroic AF2 state. Specifically, the structure of the lattice and the various Cu–O–Cu bond distances and angles are significant in forming competing ferromagnetic and antiferromagnetic interactions. This competition causes the multiferroicity to appear at different temperatures. From an applications viewpoint, this investigation shows that CuO nanoparticles could be a possible candidate for room temperature multiferroic devices.

REFERENCES

1. O'Keeffe, M.; Stone, F., The Magnetic Susceptibility of Cupric Oxide. *Journal of Physics and Chemistry of Solids* **1962**, *23*, 261-266.

2. Loram, J.; Mirza, K.; Joyce, C.; Osborne, A., Specific-Heat Evidence for Quasi-1d Magnetic Order in Cuo. *EPL (Europhysics Letters)* **1989**, *8*, 263.

3. Seehra, M. S.; Feng, Z.; Gopalakrishnan, R., Magnetic Phase Transitions in Cupric Oxide. *Journal of Physics C: Solid State Physics* **1988**, *21*, L1051.

4. Junod, A.; Eckert, D.; Triscone, G.; Müller, J.; Reichardt, W., A Study of the Magnetic Transitions in Cuo: Specific Heat (1-330 K), Magnetic Susceptibility and Phonon Density of States. *Journal of Physics: Condensed Matter* **1989**, *1*, 8021.

5. Zhou, K.; Wang, R.; Xu, B.; Li, Y., Synthesis, Characterization and Catalytic Properties of Cuo Nanocrystals with Various Shapes. *Nanotechnology* **2006**, *17*, 3939.

6. Chauhan, D.; Satsangi, V.; Dass, S.; Shrivastav, R., Preparation and Characterization of Nanostructured Cuo Thin Films for Photoelectrochemical Splitting of Water. *Bulletin of Materials Science* **2006**, *29*, 709.

7. Bao, Q.; Li, C. M.; Liao, L.; Yang, H.; Wang, W.; Ke, C.; Song, Q.; Bao, H.; Yu, T.; Loh, K. P., Electrical Transport and Photovoltaic Effects of Core–Shell Cuo/C60 Nanowire Heterostructure. *Nanotechnology* **2009**, *20*, 065203.

8. Wadia, C.; Alivisatos, A. P.; Kammen, D. M., Materials Availability Expands the Opportunity for Large-Scale Photovoltaics Deployment. *Environmental Science & Technology* **2009**, *43*, 2072-2077.

9. Gao, X.; Bao, J.; Pan, G.; Zhu, H.; Huang, P.; Wu, F.; Song, D., Preparation and Electrochemical Performance of Polycrystalline and Single Crystalline Cuo Nanorods as Anode Materials for Li Ion Battery. *The Journal of Physical Chemistry B* **2004**, *108*, 5547-5551.

10. Kimura, T.; Sekio, Y.; Nakamura, H.; Siegrist, T.; Ramirez, A., Cupric Oxide as an Induced-Multiferroic with High-Tc. *Nature materials* **2008**, *7*, 291-294.

11. Wang, F.; Zou, T.; Liu, Y.; Yan, L.-Q.; Sun, Y., Persistent Multiferroicity without Magnetoelectric Effects in Cuo. *Journal of Applied Physics* **2011**, *110*, 054106.

12. Babkevich, P.; Poole, A.; Johnson, R. D.; Roessli, B.; Prabhakaran, D.; Boothroyd, A. T., Electric Field Control of Chiral Magnetic Domains in the High-Temperature Multiferroic Cuo. *Physical Review B* **2012**, *85*, 134428.

13. Åsbrink, S.; Norrby, L.-J., A Refinement of the Crystal Structure of Copper (Ii) Oxide with a Discussion of Some Exceptional Esd's. *Acta Crystallographica Section B: Structural Crystallography and Crystal Chemistry* **1970**, *26*, 8-15.

14. Brese, N.; O'Keeffe, M.; Ramakrishna, B.; Von Dreele, R., Low-Temperature Structures of Cuo and Ago and Their Relationships to Those of Mgo and Pdo. *Journal of Solid State Chemistry* **1990**, *89*, 184-190.

15. Wu, W.; Hiraoka, N.; Huang, D.; Huang, S.; Tsuei, K.; van Veenendaal, M.; van den Brink, J.; Sekio, Y.; Kimura, T., Effective Orbital Symmetry of Cuo: Examination by Nonresonant Inelastic X-Ray Scattering. *Physical Review B* **2013**, *88*, 205129.

16. Yang, B.; Tranquada, J.; Shirane, G., Neutron Scattering Studies of the Magnetic Structure of Cupric Oxide. *Physical Review B* **1988**, *38*, 174.

17. Yang, B. X.; Thurston, T. R.; Tranquada, J. M.; Shirane, G., Magnetic Neutron Scattering Study of Single-Crystal Cupric Oxide. *Physical Review B* **1989**, *39*, 4343-4349.

18. Gmelin, E., Cupric Oxide-Cuo: Its Structural, Electrical, Thermal and Magnetic Properties. *Indian Journal of Pure and Applied Physics* **1992**, *30*, 596-608.

19. Villarreal, R.; Quirion, G.; Plumer, M.; Poirier, M.; Usui, T.; Kimura, T., Magnetic Phase Diagram of Cuo Via High-Resolution Ultrasonic Velocity Measurements. *Physical review letters* **2012**, *109*, 167206.

20. Rebello, A.; Winter, Z. C. M.; Viall, S.; Neumeier, J. J., Multiple Phase Transitions in Cuo Observed with Thermal Expansion. *Physical Review B* **2013**, *88*, 094420.

21. Millar, R. W., The Heat Capacities at Low Temperatures of "Ferrous Oxide," Magnetite and Cuprous and Cupric Oxides. *Journal of the American Chemical Society* **1929**, *51*, 215-222.

22. Hu, J.-H.; Johnston, H. L., Low Temperature Heat Capacities of Inorganic Solids. Xvi. Heat Capacity of Cupric Oxide from 15 to 300 K. 1. *Journal of the American Chemical Society* **1953**, *75*, 2471-2473.

23. Kellogg, H. H., Thermodynamic Properties of the Oxides of Copper and Nickel. *Journal of Chemical & Engineering Data* **1969**, *14*, 41-44.

24. Junod, A.; Eckert, D.; Triscone, G.; Muller, J.; Reichardt, W., Specific Heat (1–330k), Magnetic Susceptibility (5–250k) and Phonon Dos of Cuo: A Study of the Magnetic Transitions. *Physica C: Superconductivity* **1989**, *162*, 478-479.

25. Gmelin, E.; Köbler, U.; Brill, W.; Chattopadhyay, T.; Sastry, S., Magnetic Specific Heat and Susceptibility of Cupric Oxide (Cuo) Single Crystals. *Bulletin of Materials Science* **1991**, *14*, 117-123.

26. Ota, S.; Gmelin, E., Magnetic Phase Transitions and Specific Heat of Single Crystalline Cupric Oxide. *Journal of Thermal Analysis and Calorimetry* **1992**, *38*, 635-640.

27. Ota, S. B.; Gmelin, E., Incommensurate Antiferromagnetism in Copper(Ii) Oxide: Specific-Heat Study in a Magnetic Field. *Physical Review B* **1992**, *46*, 11632-11635.

28. Wang, B.-X.; Zhou, L.-P.; Peng, X.-F., Surface and Size Effects on the Specific Heat Capacity of Nanoparticles. *International Journal of Thermophysics* **2006**, *27*, 139-151.

29. Borzi, R.; Stewart, S.; Punte, G.; Mercader, R.; Zysler, R.; Tovar, M., History-Dependent Magnetic Properties in Pure and Zn-Doped Cupric Oxide. *Solid state communications* **2001**, *117*, 311-314.

30. Bizette, H.; Tsaï, B., Susceptibilite Magnetique De L'oxyde Cuivrique Cuo. *Comptes Rendus Hebomadaires des Seances de L Academie des Sciences* **1955**, *241*, 182-188.

31. Punnoose, A.; Magnone, H.; Seehra, M.; Bonevich, J., Bulk to Nanoscale Magnetism and Exchange Bias in Cuo Nanoparticles. *Physical Review B* **2001**, *64*, 174420.

32. Bisht, V.; Rajeev, K.; Banerjee, S., Anomalous Magnetic Behavior of Cuo Nanoparticles. *Solid State Communications* **2010**, *150*, 884-887.

33. Rehman, S.; Mumtaz, A.; Hasanain, S. K., Size Effects on the Magnetic and Optical Properties of Cuo Nanoparticles. *J Nanopart Res* **2011**, *13*, 2497-2507.

34. Mekata, M.; Yaguchi, N.; Takagi, T.; Sugino, T.; Mitsuda, S.; Yoshizawa, H.; Hosoito, N.; Shinjo, T., Successive Magnetic Ordering in Cufeo2–a New Type of Partially Disordered Phase in a Triangular Lattice Antiferromagnet–. *Journal of the Physical Society of Japan* **1993**, *62*, 4474-4487.

35. Forsyth, J. B.; Brown, P. J.; Wanklyn, B. M., Magnetism in Cupric Oxide. *Journal of Physics C: Solid State Physics* **1988**, *21*, 2917.

36. Ain, M.; Menelle, A.; Wanklyn, B.; Bertaut, E., Magnetic Structure of Cuo by Neutron Diffraction with Polarization Analysis. *Journal of Physics: Condensed Matter* **1992**, *4*, 5327.

37. Koo, H. J.; Whangbo, M. H., Magnetic Superstructures of Cupric Oxide Cuo as Ordered Arrangements of One-Dimensional Antiferromagnetic Chains. *Inorganic Chemistry* **2003**, *42*, 1187-1192.

38. Housecroft, C. E.; Sharpe, A. G., *Inorganic Chemistry*; Pearson, 2012.

39. Shimizu, T.; Matsumoto, T.; Goto, A.; Yoshimura, K.; Kosuge, K., Magnetic Dimensionality of the Antiferromagnet Cuo. *Journal of the Physical Society of Japan* **2003**, *72*, 2165-2168.

40. Ortega, N.; Kumar, A.; Scott, J.; Katiyar, R. S., Multifunctional Magnetoelectric Materials for Device Applications. *Journal of Physics: Condensed Matter* **2015**, *27*, 504002.

41. Viano, A.; Mishra, S. R.; Lloyd, R.; Losby, J.; Gheyi, T., Thermal Effects on Esr Signal Evolution in Nano and Bulk Cuo Powder. *Journal of Non-Crystalline Solids* **2003**, *325*, 16-21.

42. Charnaya, E.; Lee, M.; Tien, C.; Pak, V.; Formus, D.; Pirozerskii, A.; Nedbai, A.; Ubyivovk, E.; Baryshnikov, S.; Chang, L., Magnetic and Dielectric Studies of Multiferroic Cuo Nanoparticles Confined to Porous Glass. *Journal of Magnetism and Magnetic Materials* **2012**, *324*, 2921-2925.

43. Dar, M. A.; Kim, Y. S.; Kim, W. B.; Sohn, J. M.; Shin, H. S., Structural and Magnetic Properties of Cuo Nanoneedles Synthesized by Hydrothermal Method. *Applied Surface Science* **2008**, *254*, 7477-7481.

44. Woodfield, B. F.; Liu, S.; Boerio-Goates, J.; Liu, Q.; Smith, S. J. Preparation of Uniform Nanoparticles of Ultra-High Purity Metal Oxides, Mixed Metal Oxides, Metals, and Metal Alloys. US 8,211,388 B2, Jul. 3, 2012.

45. Schliesser, J. M.; Woodfield, B. F., Lattice Vacancies Responsible for the Linear Dependence of the Low-Temperature Heat Capacity of Insulating Materials. *Physical Review B* **2015**, *91*, 024109.

46. Shi, Q.; Boerio-Goates, J.; Woodfield, B. F., An Improved Technique for Accurate Heat Capacity Measurements on Powdered Samples Using a Commercial Relaxation Calorimeter. *The Journal of Chemical Thermodynamics* **2011**, *43*, 1263-1269.

47. Stevens, R.; Boerio-Goates, J., Heat Capacity of Copper on the Its-90 Temperature Scale Using Adiabatic Calorimetry. *The Journal of Chemical Thermodynamics* **2004**, *36*, 857-863.

48. Kuz'menko, A.; Van der Marel, D.; Van Bentum, P.; Tishchenko, E.; Presura, C.; Bush, A., Infrared Spectroscopic Study of Cuo: Signatures of Strong Spin-Phonon Interaction and Structural Distortion. *Physical Review B* **2001**, *63*, 094303.

49. Himmetoglu, B.; Wentzcovitch, R. M.; Cococcioni, M., First-Principles Study of Electronic and Structural Properties of Cuo. *Physical Review B* **2011**, *84*, 115108.

50. Dai, D.; Koo, H.-J.; Whangbo, M.-H., Investigation of the Incommensurate and Commensurate Magnetic Superstructures of Licuvo4 and Cuo on the Basis of the Isotropic Spin Exchange and Classical Spin Approximations. *Inorganic chemistry* **2004**, *43*, 4026-4035.

51. Tristan, N.; Zestrea, V.; Behr, G.; Klingeler, R.; Büchner, B.; von Nidda, H. K.; Loidl, A.; Tsurkan, V., Spin Frustration and Magnetic Exchange in Cobalt Aluminum Oxide Spinels. *Physical Review B* **2008**, *77*, 094412.

52. Ghosh, M.; Karmakar, D.; Basu, S.; Jha, S.; Bhattacharyya, D.; Gadkari, S.; Gupta, S., Effect of Size and Aspect Ratio on Structural Parameters and Evidence of Shape Transition in Zinc Oxide Nanostructures. *Journal of Physics and Chemistry of Solids* **2014**, *75*, 543-549.

53. Ahmad, M. I.; Bhattacharya, S., Size Effect on the Lattice Parameters of Nanocrystalline Anatase. *Applied Physics Letters* **2009**, *95*, 1906.

54. Gopal, E. S. R., *Specific Heats at Low Temperatures*; Plenum Press New York, 1966; Vol. 227.

55. Schliesser, J. M.; Huang, B.; Sahu, S. K.; Navrotsky, A.; Woodfield, B. F., Experimental Heat Capacities, Excess Entropies of Mixing, and Magnetic Properties of Bulk and Nano (1-X)Fe3o4-Xco3o4 and (1-X)Fe3o4-Xmn3o4 Spinel Solid Solutions. *Journal of Physical Chemistry C* **2016**.

56. Spencer, E. C.; Ross, N. L.; Parker, S. F.; Olsen, R. E.; Woodfield, B. F., Inelastic Neutron Scattering Studies of Hydrated Cuo, Zno and Ceo 2 Nanoparticles. *Chemical Physics* **2013**, *427*, 66-70.

57. Phillips, N. E., Low-Temperature Heat Capacity of Metals. *Critical Reviews in Solid State and Material Sciences* **1971**, *2*, 467-553.

58. de Jongh, L. J.; Miedema, A. R., Experiments on Simple Magnetic Model Systems. *Advances in Physics* **1974**, *23*, 1-260.

59. Rocquefelte, X.; Schwarz, K.; Blaha, P.; Kumar, S.; van den Brink, J., Room-Temperature Spin-Spiral Multiferroicity in High-Pressure Cupric Oxide. *Nat Commun* **2013**, *4*.